Exciting with Quantum Light

Juan Camilo López Carreño

Advisors

Dr. Elena del Valle Reboul
Prof. Dr. Fabrice P. Laussy

Committee

Prof. Dr. Gerard Nienhuis..... Universiteit Leiden, The Netherlands
Dr. Johannes Feist.....Universidad Autónoma de Madrid, Spain
Dr. Diego Porras Torre..... Instituto de Física Fundamental CSIC, Spain
Dr. Jan Sperling.....Universität Paderborn, Germany
Dr. Niccolo Somaschi..... Quandela, France

Doctoral Thesis

Dissertation presented for the degree of
Doctor of Philosophy

In the subject of
Physics

Departamento de Física Teórica de la Materia Condensada
Facultad de Ciencias
Universidad Autónoma de Madrid

November 22, 2019

Cover picture: "*Perro semihundido*", by Francisco Goya.

The author can be contacted at juclopezca@gmail.com
This Thesis can be found on the web at http://camilopez.org/wiki/Thesis

Life should not be a journey to the grave with the intention of
arriving safely in a pretty and well preserved body, but rather
to skid in broadside in a cloud of smoke, thoroughly used up,
totally worn out, and loudly proclaiming "Wow! What a Ride!"

— Hunter S. Thompson

The Universe is made of stories, not of atoms.

— Muriel Rukeyser

Success is a journey, not a destination.
It requires constant effort, vigilance and reevaluation.

—Mark Twain

El ejecutor de una empresa atroz debe imaginar que ya la ha cumplido,
debe imponerse un porvenir que sea irrevocable como el pasado

— Jorge Luis Borges

PREFACIO

¿Cuándo comenzó todo esto? ¿En qué momento decidí que era esto lo que quería? Seguramente la decisión la hice con el subconsciente, comenzando a querer hacer un Doctorado sin saber muy bien todo lo que eso implica. Desde muy joven me atrajeron las matemáticas. Pero las matemáticas con sentido, aplicadas a cosas de la vida real. Nunca me gustaron las demostraciones que mis colegas del departamento de al lado me pedían hacer durante la carrera. Más de una noche la pase en vela tratando de demostrar teoremas de álgebra que nunca más me volví a encontrar. Pero la Física! La Física, el Universo, la Luz... estas cosas son hermosas, y parecía que nunca tenía suficiente de ellas, podría pasarme días y días, y el tiempo se me escurría de entre las manos, y yo con una sonrisa porque estaba haciendo lo que me gustaba. Así, al final de los cinco años de carrera en Bogotá, lo tenía clarísimo: mi camino tenía que transcurrir por un Doctorado. No tanto por el hecho de ser Doctor. Siendo de un país donde "*Doctor*" es cualquier idiota con un poquito de poder, no hay nada que repudie más que ese título. Pero veía en hacer un doctorado el paso obligado en la vida académica. Así, comencé a soñar con Europa, y aunque siempre había pensado que iría a Alemania, terminé en Madrid. Y es que la vida es eso lo que pasa mientras estás ocupado haciendo planes, ¿no?

Estando "afuera" entendí lo que mis profes muchas veces nos dijeron: para hace un doctorado, realmente hay que querer hacerlo. Hacer el trabajo y estudiar es fácil. Al fin y al cabo es lo que nos gusta hacer. Es el ambiente en el que hay que hacer ese trabajo lo que no es sencillo. Por más reconfortante que fuera el trabajo, hacer el doctorado fue también escoger una vida solitaria en la que no es sencillo encontrar un lugar al que llamar hogar. En muchas ocaciones he tenido la sensación de ser el *otro*, el *diferente* (que es simplemente una consecuencia de ser inmigrante) y con el paso del tiempo de dejar de ser de ninguna parte. Ahora soy colombiano porque eso es lo que dice mi pasaporte, pero ya ni allá siento que encajo. Soy de todas partes, pero a la vez de ninguna. Este era el precio que había que pagar para la recompensa académica. A esto es a lo que se referían esos profes. Luego, el asunto es saber si se tiene la piel lo suficientemente gruesa como para soportarlo y mantener la esperanza de que un día esa sensación se vaya o que deje de importarte. Todo esto mientras tienes la presión de escribir un paper. Así, escribir la Tesis en un reto. Al menos así lo fue para mí. Fue el momento en el que tuve que enfrentarme, tal vez por primera vez y completamente solo, a todas las inseguridades y preguntas transcendentales que había estado poniendo debajo de la alfombra durante muchos años. Fue el momento en el que todo el esfuerzo que había hecho para llegar hasta aquí parecía insignificante a comparación de lo que quedaba por hacer. Tanto así que más de una vez me pasó por la cabeza dejarlo todo y huir. Pero, ¿a dónde? Seguramente el miedo de no saber la respuesta a esta última pregunta es más grande que el de enfrentarme a mi mismo, porque aquí sigo, a las tres de la mañana de un Jueves en Wolverhampton, como bien lo dijera Hemingway, sangrando estas líneas.

Por supuesto, no todo son tristezas. Tal vez lo que pasa es que son las que más se recuerdan, cuando uno se pone a mirar hacia atrás con nostalgia. Pienso que hacer la Tesis forja el carácter y quiero pensar que ahora soy una persona más fuerte emocional e intelectualmente. Además, durante estos años he ido a lugares y he conocido a personas increíbles (al final, todo se trata de las personas!) por las que no puedo más que agradecer a la Vida por haberlas puesto en mi camino. Ahora lo que queda es ver quién gana este pulso: si la Tesis o yo. A lo mejor ambos. A lo mejor ninguno. A lo mejor sucede como decía García Marquez: uno nunca acaba un texto, uno lo abandona.

Wolverhampton, Octubre de 2019

AGRADECIMIENTOS

Para escribir estos agradecimientos he tenido que hacer un repaso de los últimos cinco años de mi vida, y madre mía, ¡vaya montaña rusa! No pretendo hacer una lista interminable, y espero que nadie que este leyendo estos versos sienta que me he olvidado de él o ella. Como nunca hay que olvidarse del sitio del que uno viene, empezaré por agradecer a Herbert, quien me guió desde que era muy joven y de cierta manera me llevo de la mano durante los primeros pasos del camino que estoy recorriendo ahora.

A mis amigos más cercanos, Camila y Alejandro, quienes a su manera me han apoyado a lo largo de este camino. Desde que terminamos el colegio, Camila tomó un camino muy diferente al mío, pero nuestra amistad ha superado las pruebas del tiempo y la distancia, y hemos logrado mantenernos cerca. Pienso que una amistad así de grande ya nunca se va a romper (no se me ocurre ningún motivo para que eso ocurra). Con Alejandro las cosas son especiales: a pesar de que escogimos caminos muy diferentes en la física, pienso que el hecho de estar viviendo las mismas situaciones (o al menos muy parecidas), hace que nos entendamos muy bien, al punto que hayamos podido establecer nuestro propio principio de incertidumbre (que afortunadamente para los dos, ¡resultó que no era cierto!). Estar lejos de la gente y de los lugares que nos son familiares no es sencillo, y si no fuera por el soporte social de ustedes dos, todas las cosas hubieran sido muy diferentes.

A Carlos, a quien siempre he admirado (¡te lo dije en Moscú, hace ya más de cuatro años, cuando regresábamos al hotel!) y de quien parece que no termino de aprender. Desde nuestro viaje a Japón, cuándo di mi primera charla en una conferencia, lo considero como un amigo más que como a un compañero de trabajo. Así, espero que al leer estas palabras se le pase toda la molestia que le haya podido causar que me haya tomado tanto tiempo obtener resultados con el Bundler.

A los chicos y chicas del laboratorio en Lecce: Antonio, Lello, Rosana, Lorenzo, Dario, Milena, Paolo y, por supuesto, Dani les debo tres de los mejores meses de la tesis. Con voi ho imparato l'italiano, a mangiare bene, a godermi la vita, e abbiamo anche pubblicato un articolo. Cos'altro possiamo chiedere? Grazie raggazi!

A Daniele le debo una mención muy especial en esta tesis. Con su generosidad gigantesca me acogió por tres meses en su laboratorio y, junto con Rocío y Lucía, me hizo sentir bienvenido en su hogar. Más que un jefe o un director de grupo, en él encontré un amigo y aunque a veces me queje un montón sobre él (a lo mejor estás son noticias nuevas para tí, Daniele) y por más que a veces me sienta agobiado al trabajar con él, le tengo mucha admiración y me siento afortunado de poder haber compartido espacio y tiempo a su lado.

Hacia Fabrice y Elena no tengo palabras suficientes para agradecerles todo lo que han hecho por mí y todo lo que me han enseñado. Qué lejos parece aquella tarde en Medellín en la que me convencieron que me convenía más hacer física teórica y me ofrecieron irme con ellos a Madrid para hacer la Maestría. Aunque nunca me había planteado ir a España a estudiar, pienso que haberlos encontrado en mi camino y haber decidido irme con ustedes son de las mejores cosas que me han pasado en la vida. Estando en el C-V hemos forjado una relación que va mucho más allá de la que un estudiante tiene con sus directores de tesis. Ustedes me abrieron las puertas hasta de su casa, literalmente, ¡llegando hasta el punto de que viví en su casa casi seis meses! Con ustedes he aprendido muchísimas cosas, que van desde ser un científico y un académico hasta sobre como van las cosas en esta vida que hemos elegido tener. A Fabrice tengo que agradecerle todo lo que he crecido bajo sus alas y sobre todo que me haya brindado una oportunidad inigualable y me haya hecho parte de la aventura de ir a Wolverhampton a comenzar el departamento de física desde cero. No siempre ha sido fácil, pero él ha encontrado la manera de hacerme enfocar en los aspectos positivos de las situaciones, de manera que hemos podido continuar con nuestro camino. También con Elena he aprendido muchísima física, y pienso que todavía una infinidad de cosas que aprender de ella. Pero también con ella he podido compartir mis alegrías y penas, encontrando siempre en ella un gran apoyo. Eso es

invaluable. Si Fabrice y Elena son mis padres científicos, entonces Julia es de cierta manera una hermanita por transitividad. Más o menos he visto como ha ido creciendo, desde sus primeros días en Tres Cantos hasta sus primeros días de cole en Wolverhampton (pienso que guardando las proporciones, la Juge es mucho más valiente que cualquiera de nosotros), pasando por aquella noche en el tren a San Petersburgo cuando dijo '*ma-má* por primera vez. Sin importar que tan agobiado estuviera, después de hablar o jugar con ella, o después de leerle un cuento, me dejaba una sensación de tranquilidad. Seguramente compartir esas cosas con ella hacía que pusiera las cosas en contexto, y que viera que las preocupaciones en mi cabeza no son tan grandes como parecen.

Mi familia también tiene mérito—aunque sea por pura proximidad—en que esta tesis se esté terminando. La alegría con la que me recibían en Colombia cada vez que regresaba me daba un poco de fuerzas para poder volver a irme y continuar trabajando. Se que a la abuelita Myriam y a la Nona Alcira les hará mucha ilusión que su nieto haya terminado la tesis y esté cumpliendo uno de mis sueños. También se que el Nono Demetrio le hubiera dado mucha ilusión leer estos párrafos. De cierta forma sé que, allí donde sea que esté, él está festejando conmigo este éxito.

Mis papás han sido la única constante durante estos años. Y es sabido que a los físicos (y yo ahora ya me estoy graduando como uno) nos gustan las cosas que se conservan. Esta tesis es también de ustedes y deben tener la seguridad de que si no fuera por el apoyo que me han dado desde el comienzo—desde aquella tarde en que salieron los resultados del examen de admisión de la nacho, diciendo que había entrado a física en vez de ingeniería (¡ahora no me puedo ni imaginar el infierno que hubiera sido haber estudiado una ingeniería!) y solo puedo estar agradecido con la aleatoriedad cósmica de que las cosas hayan sido como son—nada de esto hubiera sido posible. ¿A quién se le hubiera pasado por la cabeza haberme acolitado viajes a conferencias en Europa cuando todavía estaba en la carrera? Pienso que solo a Ustedes y, viéndolo en retrospectiva, ¡todavía me parece una locura!

A la Bebici le debo que escribir esta tesis no sea una tortura, y aunque no ha sido fácil, ella ha estado a mi lado para consolarme cuando me sentía desfallecer. Desde que nos conocimos mi vida se ha llenado de colores y alegría. Estando contigo he llenado de fuerzas y he visto cómo se han renovado mis ganas por seguir trabajando. Soñando una vida juntos, en la que también están incluidos I., L. y E., todos los sacrificios y las decisiones que me han traído hasta aquí cobran sentido. Ahora entiendo porque sucedían las cosas que antes me parecían fortuitas: es que teníamos que encontrarnos aquí. ¡Precisamente en Wolverhampton!

Para mis papás,
María Stella y Luis Demetrio.

CONTENTS

LIST OF FIGURES

LIST OF TABLES

ABSTRACT

ENGLISH

A two-level system—the idealization of an atom with only two energy levels—is the most fundamental quantum object. As such, it has long been at the forefront of the research in Quantum Optics: its emission spectrum is simply a Lorentzian distribution, and the light it produces is the most quantum that can be. The temporal distribution of the photon emission displays a perfect antibunching, meaning that such a system will never emit two (or more) photons simultaneously, which is consistent with the intuition that the two-level system can only sustain a single excitation at any given time. Although these two properties have been known for decades, it was not until the advent of the *Theory of Frequency-filtered and Time-resolved Correlations* that it was observed that the perfect antibunching is not the end of the story: the correlations between photons possess an underlying structure, which is unveiled when one retains the information about the color of the photons. This is a consequence of the Heisenberg uncertainty principle: measuring perfect antibunching implies an absolute knowledge about the time at which the photons have been emitted, which in turn implies an absolute uncertainty on their energy. Thus, keeping some information about the frequency of the emitted photons affects the correlations between them. This means that a two-level system can be turned into a versatile source of quantum light, providing light with a large breadth of correlation types well beyond simply antibunching. Furthermore, when the two-level system is driven coherently in the so-called *Mollow regime* (in which the two-level system becomes dressed by the laser and the emission line is split into three), the correlations blossom: one can find every type of statistics—from antibunching to super-bunching—provided that one measures the photons emitted at the adequate frequency window of the triplet. In fact, the process of filtering the emission at the frequencies corresponding to N-photon transitions is the idea behind the *Bundler*, a source of light whose emission is always in bundles of exactly N photons.

The versatility of the correlations decking the emitted light motivates the topic of this Dissertation, in which I focus on the theoretical study of the behaviour that arises when physical systems are driven with quantum light, i.e., with light that cannot be described through the classical theory of electromagnetism. As the canon of excitation used in the literature is restricted to classical sources, namely lasers and thermal reservoirs, our description starts with the most fundamental objects that can be considered as the optical targets: a harmonic oscillator (which represents the field for non-interacting bosonic particles) and a two-level system (which in turn represents the field for fermionic particles). We describe which regions of the Harmonic oscillator's Hilbert space can be accessed by driving the harmonic oscillator with the light emitted by a two-level system, i.e., which quantum steady states can be realized. Analogously, we find that the quality of the single-photon emission from a two-level system can be enhanced when it is driven by quantum light. Once the advantages of using quantum, rather than classical, sources of light are demonstrated with the fundamental optical targets, we turn to the quantum excitation of more involved systems, such as the strong coupling between a harmonic oscillator and either a two-level system—whose description is made through the Jaynes-Cummings model—or a nonlinear harmonic oscillator—which can be realized in systems of, e.g., exciton-polaritons. Here we find that the statistical versatility of the light emitted by the Mollow triplet allows to perform Quantum Spectroscopy on these systems, thus gaining knowledge of its internal structure and dynamics, and in particular to probe their interactions with the least possible amount of particles: two. In the process of exciting with quantum light, we are called to further examine the source itself. In fact, there is even the need to revisit the concept of a single-photon source, for which we propose more robust criterion than $g^{(2)}$. We also turn to toy-models of the Bundler so as to use it effectively as an optical source. We can then

study the advantages that one gets and shortcomings that one faces when using this source of light to drive all the systems considered on excitation with the emission of a two-level system. Finally, we go from the continuous to the pulsed regime of excitation, which is of higher interest for applications and comes with its own set of fundamental questions.

ESPAÑOL

El sistema de dos niveles—la idealización de un átomo constituido por solo dos niveles—es el sistema cuántico más fundamental que existe. Así, ha estado desde siempre en la vanguardia de la investigación sobre la Óptica Cuántica: su espectro de emisión está dado simplemente por una distribución Lorentziana, y la luz que produce es tan cuántica como es posible. La manera en la que los fotones emitidos por este sistema están perfectamente anti-agrupados (antibunched), lo que quiere decir que este sistema nunca emitirá más de un fotón simultáneamente, lo cual es consistente con el hecho de que el sistema solo puede mantener una excitación en cada instante de tiempo. Aunque estas dos propiedades son conocidas desde hace décadas, no ha sido sino hasta la llegada de la *Teoría de Correlaciones filtradas en frecuencia y resueltas en tiempo* que se observó que el anti-agrupamiento perfecto no es el final de la historia: las correlaciones entre los fotones están investidas por una estructura subyacente, que es desvelada cuando uno retiene la información sobre el color de los fotones emitidos. Esto es una consecuencia del principio de incertidumbre de Heisenberg: medir un anti-agrupamiento perfecto implica el conocimiento absoluto del tiempo en el que los fotones fueron emitidos, lo que a su vez supone la completa incertidumbre sobre su energía. De esta manera, al obtener un poco de información sobre la frecuencia en la que los fotones han sido emitidos, uno afecta las correlaciones entre ellos. Esto significa que un sistema de dos niveles puede convertirse en una versátil fuente de luz cuántica, capaz de proveer luz con un gran rango de correlaciones, yendo mucho más allá del simple anti-agrupamiento. Es más, cuando el sistema de dos niveles es excitado coherentemente en el llamado *régimen de Mollow* (en el que el sistema de dos niveles es vestido por el laser, y su línea de emisión se divide en tres), las correlaciones florecen: uno puede encontrar todos los tipos de estadísticas—desde anti-agrupamiento hasta super-agrupamiento—dado que uno mida los fotones emitidos a las frecuencias adecuadas del triplete. De hecho, el proceso mediante el cual se filtra la emisión a las frecuencias que corresponden a transiciones de N fotones es la idea detrás del *Bundler*, una fuente de luz cuya emisión siempre ocurre en manojos de N fotones.

La versatilidad de las correlaciones que acompañan a la luz emitida es la motivación para el tema de esta Disertación, en la que me enfoco en el estudio teórico del comportamiento que surge cuando sistemas físicos son excitados mediante luz cuántica, i.e., con luz que no puede ser descrita mediante la teoría de electromagnetismo clásica. Como el canon de excitación usado en la literatura está restringida a fuentes clásicas, es decir láseres o reservorios térmicos, nuestra descripción comienza con los objetos más fundamentales que se pueden considerar como objetivos ópticos: un oscilador armónico (que representa el campo de partículas bosónicas no interactuantes) y un sistema de dos niveles (que en cambio representa el campo de partículas fermionicas). Describimos cuales son las regiones del espacio de Hilbert del oscilador armónico que pueden ser accedidas cuando este es excitado por la luz emitida por un sistema de dos niveles, i.e., qué estados cuánticos se pueden obtener como estados estables. De manera análoga, encontramos que la calidad de los fotones individuales emitidos por un sistema de dos niveles se puede mejorar cuando este es excitado mediante luz cuántica. Una vez demostradas las ventajas de usar luz cuántica, en vez de luz clásica, mediante los objetivos ópticos más fundamentales, consideramos la excitación cuántica de sistemas más elaborados, como el acoplo fuerte entre un oscilador armónico y, o un sistema de dos niveles—cuya descripción se hace mediante el modelo de Jaynes-Cummings—o un oscilador armónico no lineal—que, por ejemplo, se puede encontrar en sistemas de polaritones excitónicos. Así, hemos visto que la versatilidad de la estadística de la emisión del triplete de Mollow hace posible la implementación de Espectroscopia cuántica sobre estos sistemas, pudiendo de esta manera obtener información de su estructura interna y dinámica, y en particular sondear sus interacciones con el menor número de partículas posible:

dos. En el proceso de excitar mediante luz cuántica, hemos tenido que examinar la fuente en sí. De hecho, incluso hay necesidad de revisar el concepto de fuente de fotones individuales, para el que hemos propuesto un criterio más robusto que la $g^{(2)}$. También hemos considerado modelos sencillos para describir el Bundler para poder usarlo de manera eficaz como fuente óptica. Así, podemos estudiar las ventajas y desventajas con las que uno se enfrenta al usar esta fuente de luz para excitar todos los objetivos con un sistema de dos niveles. Finalmente, vamos del régimen de excitación continua al de excitación pulsada, el cual es de gran interés para aplicaciones y que además viene con sus preguntas fundamentales particulares.

1 PRELIMINARIES

Out of darkness cometh light

1.1 LIGHT

1.1.1 *'Civilizational' background*

According to the Bible, Light was created right after Heaven and Earth:

> [1]*In the beginning God created the heaven and the Earth.*
> [2]*And the Earth was withouth form, and void; and darkness was upon the face of the deep. And the Spirit of God moved upon the face of the Waters.*
> [3]*And God said, Let there be light: and there was light.*
> [4]*And God saw the light, and it was good; and God divided the light from the darkness.*

From a scientific point of view, the Universe began with the so-called *Big Bang*. What happened before is unknown, and Stephen Hawking even said that such a question is futile, as the concept of time only has physical meaning *after* the Big Bang. Conversely, what happened after is quite clear: a tiny fraction of a second after the Bang (approximately 10^{-34} s), the Universe started a process of *inflation* by which it increases its size over 90 times, going from sub-atomic scales to the size of a tennis ball almost immediately. After the inflation, the expansion of the Universe continued, but at a slower rate. During the first three minutes, the temperature reduced from 100 nonillion (10^{32}) to a billion (10^{9}) Kelvin, and protons and neutrons were able to collide and stick together to form deuterium, an isotope of Hydrogen. The fusion process generates gamma radiation (high energy photons), which constitutes the first appearance of light in the Universe. However, at this point the Universe was so hot, that it was mainly made of a dense plasma of electrons, protons and neutrons, which scattered light like in the fog on a cold night. About 380 000 years after the Big Bang (which is 13.7716 billion years ago), matter cooled down enough for the first atoms to form and the plasma gave way to a transparent gas, which let loose the first flash of light of the Universe. This is the earliest light that we can see. The evidence of such a burst of light is the so-called *Cosmic Microwave Background Radiation*, which was first measured (by accident) by Arno Penzias and Robert Wilson in 1964. Since then, large efforts from space agencies have made possible to have a full-sky map of this radiation. The latest of these images, shown in Fig. 1.1, was obtained by the Planck satellite.

Of course, these measurements were not the first contact that Humans had with Light. Ancient communities had a close relation with light, which still dictate our vital cycles. We are more active during the daylight hours than during night-time (in fact, only about 20% of the mammals are diurnal), and the cycle of the Earth around the Sun rules the times for planting and harvesting crops, as well as other agricultural activities. People knew these facts from their

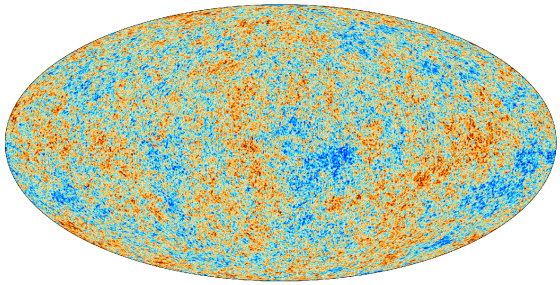

Figure 1.1: Cosmic background radiation showing the fluctuation in the temperature (shown in different colors and with a range of ± 200 μK) that took place during the lifetime of the Universe. Image taken from the ESA's Planck satellite.

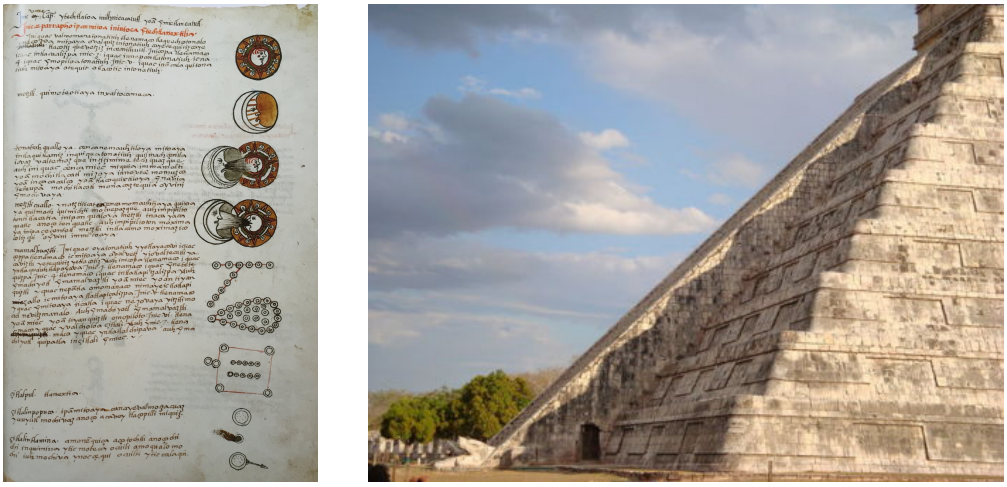

Figure 1.2: Códice Matritense (Codex of Madrid) recording the birth and death of the moon, according to the cosmogony of the Aztec civilization (left). Light permeated the indigenous society to such a degree, that their architecture were filled of symbolism. In the pyramid of Chichen Itza (made by the Mayans), at the sunset of the Equinox, the stairs that lead to the temple are illuminated by the sun in such a way that one can identify a serpent *crawling down* from the temple (right). The pyramid has four staircases, and each of them has 91 steps. Thus, the sum of all the steps plus the temple on top of the pyramid is equal to 365: the number of days in a solar year.

experience, and transmitted them orally, even before the dawn of Science. They also endowed light with mystical properties. For instance, the Egyptians believed that day and night were ruled by the act of vision of Ra, the god of the Sun: whenever its eye was open, there was day, and when its eye was closed, there was night. Various indigenous people on the northern hemisphere gave different interpretations to the phenomenon of *northern lights*: the Inuit of Canada and Greenland, the Saami in Sweden, Finland and Russia, and other tribes in Siberia believed that the northern lights were the souls of the people who died through loss of blood (regardless of the specifics of their deaths). For the Aztecs, life was a gift from the Sun, and it was through the illumination that beings became alive. This had a deep relation with their understanding of the days, months and years. The days were the constant struggle between life (represented by the blue color of the sky during the day) and death (represented by the blood red of the sunrise and the purple of the sunset). The months were linked through the cycles of the moon, which they understood perfectly and which are recorded in the *Códice Matritence* (Codex of Madrid, shown in Fig. 1.2):

1. *Cuando la luna nuevamente nace, parece como un arquito de alambre delgado, aún no resplandece, y poco a poco va creciendo, (When the moon is reborn, it looks like a thin arch of wire, it still doesn't shine, and little by little it starts to grow)*
2. *a los quince días es llena, y cuando ya lo es, sale por el oriente. (fifteen days later it is full, and once it is, it rises from the east)*
3. *A la puesta del sol parece como una rueda de molino grande, muy redonda y muy colorada, (At the sunset, it looks like a huge wheel from a windmill, rounded and maroon)*
4. *y cuando va subiendo se para blanca y resplandece; aparece como un conejo en medio de ella, y si no hay nubes, resplandece como el sol a medio día; (and when it rises, it stays white and shiny; a sort of rabbit appears on it, and when there are no clounds, it shines like the midday sun)*

5. *y después de llena cumplidamente, poco a poco se va menguando hasta que se va a hacer como cuando comenzó; (and right after reaching its apex, little by little it shrinks until it becomes like when it started)*
6. *dicen entonces, ya se muere la luna, ya se duerme mucho. (and they say, the moon is going to die, the moon is going to sleep)*
7. *Esto es cuando sale ya con el alba, y al tiempo de la conjunción dicen: "ya es muerta la luna" (Then, when the sun rises, and at the time of the conjuction, they say: "the moon is dead")*

Every empirical observation that the Aztecs made on the luminosity was defined by tonalities, which in turn were related to the processes of life and death. The Mayans, on the other side, were gifted astronomers and their relation with light and the sun permeated all of their activities. In particular, one can still see the way in which they used the shape of their pyramids to announce important dates of the calendar, such as the Equinoxes. In Chichen Itza, the light that the sun shines towards the pyramid makes the illusion of a serpent crawling down to Earth (cf. Figure 1.2), letting them know that the soil is ready for planting (in March) and harvesting (in September).

The earliest formal studies on the nature of light can be attributed to the Greek. Their school of natural philosophy bloomed with the the work of many great minds such as Democritus, Epicurus, Plato and Aristotle, and their first approach to light was to understand vision. Democritus believed that the air between the object and the eye contracted and was stamped with the details of the object. Thus, in a sort of propagation, the air reached the eye and the vision was completed. Conversely, Epicurus believed that we are able to see objects, because they are sending "atoms" to our eyes (and he explained that the objects didn't run out of atoms, because they were readily replenished by other particles). Plato and his followers thought that the eyes emitted rays of light, which, after being scattered, allowed us to perceive the size, color and shape of the objects.

During the golden age of the Islamic science, many of the Greek theories were debunked and the understanding of light and vision was deepened. Al-Kindi followed the steps of Euclid—who used geometry to understand the phenomena of reflection, refraction and the appearance of shadows—and studied the shadow cast by several opaque objects, to prove experimentally that light travels in straight lines. Furthermore, together with ibn-Sina (known in the occidental world as Avicenna), he argued that light could not emanate from the eyes, as it would have to fill an infinite amount of space everytime we open our eyes. The culmination of optics in the Arab world was carried by the prolific Abu Ali al-Hasan ibn al-Hasan ibn al-Haytham, known

Euclid Alhazen Descartes

Figure 1.3: Light has always been a chief topic of scientific enquiries, even when Science itself was not yet a fully-fledged discipline or method. The primitive theories of light relied on the mathematical apparatus then available, namely, geometry, with results discovered over and over, in the hands of Euclid (300BC), Alhazen (c. 1000) and Descartes (c. 1650) as some of the most significant thinkers of their respective eras.

in the west as Alhazen, who is often regarded as the greatest physicist between Archimedes and Newton. His most important contribution to the field of Optics was his *Book of Optics* (Kitab-al Manzir), in which he tackled the nature of light, the physiological aspects of the eye and the vision, as well as they way in which lenses and mirrors can bend and focus the light. He proved that the theory of the light emanating from the eye was wrong, and that instead light was emanating from sources. He did this through a simple experiment in a dark room: on one of the walls he made a small hole. Outside of it, he placed a pair of lanterns at different heights, which cast a spot of light inside the dark room. When he covered one of the lanterns, he saw the spot of light inside the room disappear. Thus, he concluded that light was coming from the lantern, rather than from the eyes. Based on this experiment, he invented the first pinhole camera and explained why the image in it was inverted.

Light has played a fundamental role not only in Science but also throughout the history of Art: from the mere consideration of how different colors mixed together gave the impression of different environments, to being the center of attention of a work of art. In ancient Egypt, the masks of the pharaohs were tainted with gold to highlight their divinity. In the Christian world, it was not the faces but the regions around the people (such as the halos) that were enlightened to give the sense of superiority and holiness. With the advent of the Renaissance and the mastering of light by the Italian school, led by da Vinci and Caravaggio, the world met the *chiaroscuro*, a technique with which light and shadows are blended, giving the paintings a completely new dimension (cf. Fig. 1.4, left). In the 17^{th} century, light is no longer a tool for the artist to highlight a specific region of the work, but it becomes rather a central figure. This is particularly noticeable in the work of Vermeer, in which light not only is the key subject but it also brings volume to the painting. With the onset of the impressionism, light is completely reinvented and the objects are not what is painted but what is interpreted by the beholder. In the modern times, some painters have perfected the use of light and masterpieces from which light appears to leave the canvas have been created. Hosted by the Hermitage in St. Petersburg and by the Museo del Prado in Madrid, Ivan Aivazovsky's "*The Black Sea at Night*" and Joaquín Sorolla's "*Niños en la playa*", shown in Fig. 1.4, are perfect examples of the mastery of light in paintings.

1.1.2 *Modern description: Maxwell equations*

The scientific revolution started with the Polish astronomer and mathematician Mikołaj Kopernik (Nicolaus Copernicus in Latin). Before Newton's theory of gravitation, the heliocentric model of the Universe theorized by Copernicus was difficult to accept (even though it simplified a lot

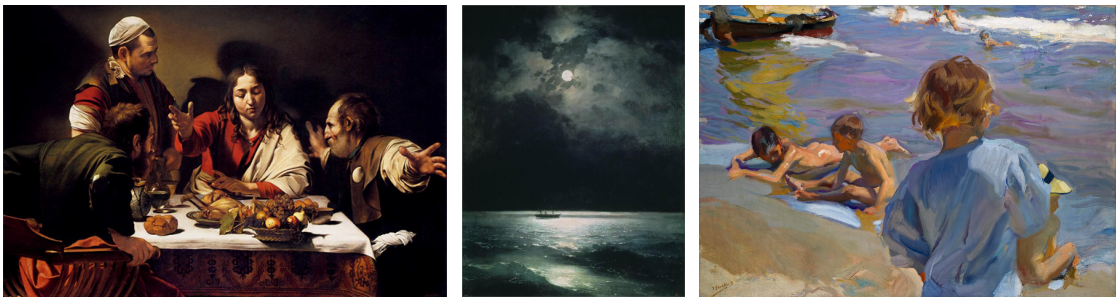

Figure 1.4: On the left is Caravaggio's "*The supper at Emmaus*" (1601), which epitomizes the *chiaroscuro* technique, using the light to point us to the important characters of the work. At the center, is Ivan Aivazovsky's "*The Black Sea at Night*" (1879), in which the light from the moon appears to be coming out of the canvas and thus illuminating the room. On the right is Joaquín Sorolla's "*Niños en la playa*" (1916), whose mastery of light almost makes you feel like you are in the Mediterranean coast witnessing this scene.

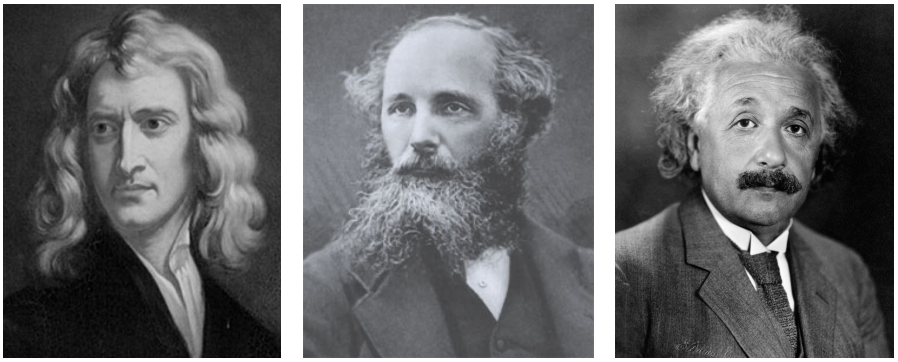

Newton Maxwell Einstein

Figure 1.5: The greatest minds of modern Science have also pondered on the nature and properties of light. Newton (1642-1727) championed the corpuscular theory of light, despite ample opposition (and evidence) and gathered a huge amount of fundamental results in his treatise Opticks, from ray-optics to the naming of the colors in the rainbow. Maxwell (1831-1879) put together in a closed and consistent form the equations of electricity and magnetism, out of which he identified light as an electromagnetic wave. This is widely regarded as one of the greatest intellectual feats and the first great unification of Physics. Einstein (1879-1955) orchestrated the coup-de-théâtre that brought back the corpuscular theory of light to the foreground, making a decisive step towards Quantum Mechanics, which interpretation he would later challenge with his concept of 'element of reality' through the so-called EPR correlations.

the calculations of the orbits of the planets). Although Copernicus died before his theory was published (his ideas were held as heretic by the Catholic church), it was the spark that lit the way towards the development of the European Science. The beginning of this revolution was more fruitful in the protestant countries, where the influence of Rome and the Catholic church was weaker. Living in Germany, Johannes Kepler became interested in astronomical events, and while making an observation of an eclipse with a pin-hole camera, he noticed that the image of the moon as seen through the camera was larger than when it was observed directly. Kepler understood that such an important feature was due to the size of the pin-hole, and his thorough study of it yielded a theory of the radiation propagating through apertures, based on the fact that rays of light travel in straight lines. In the mean time, the French school of optics was led by Descartes, who derived the laws of reflection and refraction of light (although the credit of the discovery is often given to Willebrord Snellius, who derived these laws using trigonometry), and by Pierre de Fermat, who developed Snell's law using the principle of least time, according to which the propagation of light takes place along the path that makes it reach the final point in the least amount of time.

On the other shore of the English Channel, Isaac Newton was developing the theory of gravitation, for which he had to invent calculus, but he also made large contributions to the field of optics. He showed that color was a property of light and not of the medium in which it propagates, and using a prism he established that white light, like the one that comes from the sun, is in fact a superposition of all the colors. Then, he demonstrated that the light of a single color was not split again when passing through a prism, and that recombining all the colors yielded again white light. Studying the way in which lenses and mirrors worked, he was able to design a telescope operating in reflection (up to then, all the telescopes were fabricated to operate in refraction), which suffered much less chromatic aberration. The idea was so clever, that modern telescopes are merely more precise versions of the newtonian telescope.

Newton also theorized about the nature of light. He was an advocate of the *corpuscular* nature of light, thus believing that it was made of minuscule corpuscles, as opposed to matter, which was made of larger particles. However, even at that time, there was evidence that light behaved as waves. Huygens published an oscillatory theory of light in his *Traité de la lumière* (Treatise on light), which was supported by Romer's experiment showing that light propagates at a finite

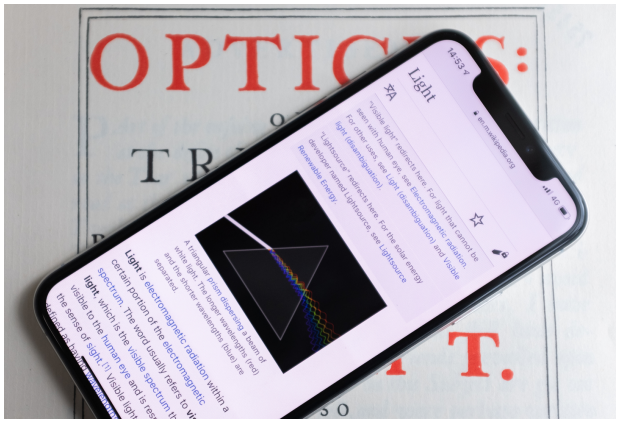

Figure 1.6: When classic meets modern. Below is the cover page of Newton's *Opticks*, in which is developed the theory of optics, including the dispersion of light by which a beam of white light can be decomposed into the seven colours of the rainbow. On top, one of the marvels that technology can achieve with Light, with a display made of OLEDs (organic light emitting diodes), with a pixel density of 448 pixels per inch.

speed. However, it was not until the beginning of the nineteenth century that Young showed that light behave as a wave, thus supposedly proving Newton wrong. In the words of Young:

> … when a beam of homogeneous light falls on a screen in which there are two very small holes or slits, which may be considered as centers of divergence, from whence the light is diffracted in every direction. In this case, when the two newly formed beams are received on a surface placed so as to intercept them, their light is divided by dark stripes into portions equal, but becoming wider as the surface is more remote from the apertures, so as to subtend very nearly equal angles from the apertures at all distances, and wider also in the same proportion as the apertures are closer to each other. The middle of the two portions is always light, and the bright stripes on each side are at such distances, that the light coming to them from one of the apertures, must have passed through a longer space than that which comes from the other, by an interval which is equal to the breadth of one, two, three, or more of the supposed undulations, while the intervening dark spaces correspond to a difference of half a supposed undulation, of one and a half, of two and a half, or more.

By repeating this experiment, Young was able to connect the color of light to the wavelength of the undulations, and was able to identify approximately the wavelength of the seven colors that according to Newton composed white light.

It was the industrial revolution, and the experiments with electricity and magnetism that the theory of electromagnetism took its final form. The works of André-Marie Ampère, Charles-Augustin de Coulomb and Michael Faraday laid the basis of the theory, which James Clerk Maxwell unified with his famous set of four equations

$$\nabla \cdot \vec{E} = \frac{\rho}{\epsilon_0}\,, \qquad \nabla \cdot \vec{B} = 0\,, \tag{1.1a}$$

$$\nabla \times \vec{E} = -\frac{\partial \vec{B}}{\partial t}\,, \qquad \nabla \times \vec{B} = \mu_0 \vec{J} + \mu_0 \epsilon_0 \frac{\partial \vec{E}}{\partial t}\,, \tag{1.1b}$$

where $\vec{E}$ (resp. $\vec{B}$) is the electric (resp. magnetic) field, ρ is the density of electric charges, $\vec{J}$ is the density of currents, and ϵ_0 and μ_0 are the permittivity and permeability of free space, respectively. A simple algebraic manipulation, taking the curl of Eqs. (1.1b), using the vector identity $\nabla \times (\nabla \times \vec{A}) = \nabla(\nabla \cdot \vec{A}) - \nabla^2 \vec{A}$, and assuming that there are no sources of charges or currents, yields a pair of wave equations for the electric and magnetic field

$$\nabla^2 \vec{E} = \frac{1}{c^2}\frac{\partial^2 \vec{E}}{\partial t^2}\,, \qquad \text{and} \qquad \nabla^2 \vec{B} = \frac{1}{c^2}\frac{\partial^2 \vec{B}}{\partial t^2}\,, \tag{1.2}$$

where $c = 1/\sqrt{\epsilon_0 \mu_0}$ is the velocity at which these waves propagates, i.e., the speed of light, thus settling the nature of light as waves. After Maxwell unified the theory of electromagnetism and

predicted that light propagated as a wave, a large effort was put all across Europe to either demonstrate of refute the prediction. After only twenty four years, in 1888, a doctoral student of Helmholtz, Heinrich Hertz, built in his laboratory the first radio wave transmitter, thus demonstrating the reality of the electromagnetic waves.

Maxwell's equations (cf. Eq. (1.1)) constitute the full description of Light according to the classical theory. However, by the end of the 19th century, evidence started to pile up suggesting that not all observations were compatible with the classical theory, and that there was a need for a new theory—Quantum Mechanics—which would change Physics forever.

Technology could nevertheless develop tremendously based mainly on the classical theory alone and the quantum character of Light has mainly remained a question of fundamental interest. However, with the advent of the information age, where performance and efficiency are never enough and the barrier of classical physics are quickly approached, the emergence of quantum light in all aspects of human endeavors becomes every day more perceptible.

1.1.3 *Light in our lives*

In our contemporary world, light is all around us. Even during the night. We are naturally drawn towards shiny objects, and we now have a myriad of bright displays battling for our attention: computers, televisions, advertisements, mobile phones, tablets. A short stroll down Shinjuku in Tokyo, Piccadilly Circus in London, or Times Square in New York, would suffice to see how far we have come from the early days in which light had a mystic component. Light is so abound around us, that many youngster have never had the chance to see the Milky Way on a cloudless night, simply because there is so much artificial light blinding us. The Starlink project of SpaceX has even launched a series of satellites into orbit to provide internet connection in a fashion similar to GPS, making it accessible anywhere on Earth. One problem with this is that the satellites are visible and, when there are enough of them, we will not be able to see the real stars anymore, but an uncanny mesh of artificial ones.

On a more relatable scale, the screens of our mobile phones, omnipresent, shining on our faces are there reminding us that the world keeps on revolving around us, and it has become practically impossible to disconnect from it. Understanding the relationship between light and electromagnetic fields has revolutionized technology. The advent of the Internet, initially thought of as a clever way to share large amounts of information collected from the experiments at CERN (Centre Européen de la Recherche Nucléaire), has become global and now it enables us to know, in a fraction of a second, what is happening on the other side of the Earth. The information, represented by a stream of zeroes and ones, is encoded into light and then travels vast distances, across continents and oceans, by fiber optic cables.

All these electronic devices require energy to work, and the 21^{th} century came together with the alerts of global warming. We are using too many dirty energy sources (fossil fuels, coal, gas, among others) which are changing the climate and in the long term they will end up reducing

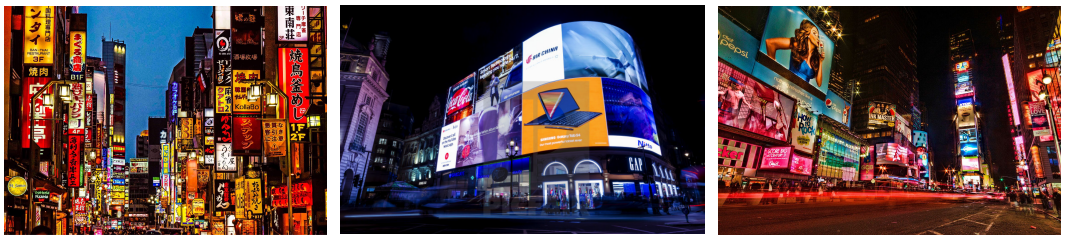

Shinjuku, Tokyo | Piccadilly Circus, London | Times Square, New York City

Figure 1.7: Light pollution in metropolises: Shinjuku in Tokyo (left), Picadilly Circus in London (center) and Times Square in New York City (right) are only the most brilliant examples of the magnitude of the light pollution that brightens our nights.

our quality of life. Thus, a part of the scientific community is facing the problem of making *green* energy sources as available and efficient as the ones we are currently using. One of the most obvious sources of (free) energy is right in front of us, and for millennia has captivated us: the Sun. Nature is wise, and evolution has made plants very efficient at capturing and converting light from the Sun into useful energy for their sustenance. The eyes of fishes living in the deepest regions of the oceans have evolved in such a way that they are able to catch single photons, and recent research by Tinsley et al. (2016) shows indications that the human eye is also able to observe single photons. In comparison, the most efficient solar panels available to date reach a 23% of efficiency, which is somewhat far away from the 30% nominal efficiency that according to Stryer (1981) is obtained by the photosyntetic process. Thus, one upcoming task for scientists is to achieve or exceed such a level of efficiency of detection and manipulation of light, using artificial materials.

1.2 QUANTUM LIGHT

1.2.1 *Quantum Mechanics brings Photons*

The dawn of the 20$^{\text{th}}$ century has been crucial to Physics. The classical theory of Electromagnetism, one of the most beautiful theories that the human mind has developed, was not able to account for the thermal emission of an ideal emitter (a simple black box). The classical equation predicted that the intensity of light emitted at ultraviolet wavelengths (less than 400 nm between consecutive maxima of the wave) was diverging. Clearly, this could not be right, as it implies that matter would radiate all its energy until it reaches the absolute zero, and the problem was coined as the "*ultraviolet catastrophe*". Max Planck deduced an expression for the spectral distribution of the intensity which fitted nicely with the experimental results. However, to write it, he had to make an unfounded assumption: the electromagnetic energy can only be emitted or absorbed in bundles—which he called quanta—of energy, namely

$$E = nh\nu\,, \tag{1.3}$$

where E is the electromagnetic energy, n is an integer number, h is a constant of proportionality—which later became known as "*Planck's constant*"—and ν is the frequency of the wave.

At around the same time, Hertz noticed that when a beam of light was directed onto a metal plate, it induced some sparks: there was an electrical current induced by the incoming light. This, however, was not surprising, as by then it was known that electrons in metals are easy to detach from the atoms, provided that you gave them enough energy. What puzzled Hertz was that in different materials, the sparks began to appear at different "threshold" frequencies. Furthermore, Hertz noticed that increasing the brightness of the beam produced more electrons (a larger current) without increasing their energy, while increasing the frequency of the beam increased the energy of the electrons without increasing their amount. This became known as the *photoelectric effect*, and it was not until a few years later that Einstein (1905) managed to explain it: He realized that Planck's assumption on the quantization of the energy of light was not merely a mathematical trick to make the equation fit the experiment, but that it was rather the true nature of light. In fact, according to Einstein, light is not a wave but a stream of particles whose energy is related to their frequency ν through Planck's relation, $E = h\nu$. Thus, the explanation of the photoelectric effect was reduced to a problem of elastic scattering: if the photon that impinges onto the metal has enough energy—or equivalently, a frequency above the threshold for excitation—it could collide with an electron of one of the atoms and detach it.

Einstein's understanding of light and the elegantly simple explanation of the photoelectric effect were the main reason for which he received the Nobel prize in 1921 (although by then he had also explained the Brownian motion, he had stated the equivalence between mass and energy, and he had developed the special and general theories of relativity, all recognized as "services to theoretical Physics" in his Nobel nomination). Furthermore, by realizing that Planck's hypothesis was in fact a physical reality, Einstein brought to life the Photon—the

quantum of light—which brings another proof of the quantized character of Nature, and is the central physical object of this Thesis.

The 20$^{\text{th}}$ century watched the birth and quick development of Quantum Mechanics. While the first part of the century was devoted to the understanding of atoms, the scientific efforts turned to the study of the way in which electromagnetic fields interact with matter. These efforts quickly led Schawlow and Townes (1958) to the development and fabrication of the Maser, which used the newly discovered (also by Einstein) stimulated emission to generate a highly coherent beam of light. Such a coherence made the beam almost monochromatic and allowed it to propagate through long distances without dispersing. While the energy of the light emitted by the maser corresponded to the microwaves, some years later Maiman (1960) built for the first time such a device emitting light in the visible range of the electromagnetic spectrum. The latter was coined as the *Laser*, changing the M of Maser (coming from *Microwave*) for an L (corresponding to *Light*, as visible light is what people commonly recognize as Light). We are now already at the stage where the concepts of interest in this Thesis can be brought to critical analysis and further developed, so we move on to the parts of the theory that are required to obtain the results that I will present in the subsequent chapters. From this point onward, the discussion will be consequently more detailed.

1.2.1.1 *Formalism*

The dynamical aspect of quantum mechanics can be studied in different ways, depending on the mathematical objects that encode the temporal dynamics. The state of a quantum object is written down as a wavefunction, noted as $|\psi(\mathbf{r},t)\rangle$, which describes the density of probability to find the quantum object at the position $\mathbf{r}$ in space at time t. When the quantum object is subjected to a Hamiltonian with an operator $\hat{H}$ (we have used the $\hat{}$ notation to highlight that the object is an operator), its wavefunction evolves according to the time-dependent Schrödinger equation

$$i\hbar\partial_t |\psi(\mathbf{r},t)\rangle = \hat{H} |\psi(\mathbf{r},t)\rangle \ . \tag{1.4}$$

where $\hbar = h/2\pi$ is the reduced Planck constant. Formally, the wavefuction of the quantum object is a vector within the *Hilbert space* of the system. There, one also finds the operators associated to the object, among which are the so-called "*observables*", whose mean values can be measured directly in an experiment. For instance, the mean value of the Hamiltonian operator, $\langle\hat{H}\rangle$, is the average energy of the object. The formal solution to Schrödinger equation for a time-independent Hamiltonian can be obtained by integrating Eq. (1.4):

$$|\psi(\mathbf{r},t)\rangle = \exp(-i\hat{H}t/\hbar) |\psi(\mathbf{r},0)\rangle \ , \tag{1.5}$$

where $|\psi(\mathbf{r},0)\rangle$ is the state of the system at the initial time $t = 0$. Once the wavefunction in Eq. (1.5) is obtained, we have all the information about the quantum object, and we can compute all the probabilities that we deem relevant: given an operator $\hat{O}$ on the Hilbert space of the quantum object, the mean value of the operator at time t is given as

$$\langle\hat{O}\rangle(t) = \langle\psi(\mathbf{r},t)| \hat{O} |\psi(\mathbf{r},t)\rangle \ , \tag{1.6}$$

where $\langle\psi(\mathbf{r},t)| = |\psi(\mathbf{r},t)\rangle^\dagger$. Note that in Eq. (1.6) all the information about the dynamics of the system is encoded in its wavefunction $|\psi(\mathbf{r},t)\rangle$. This is referred to as the *Schrödinger picture* of Quantum Mechanics.

Manipulating Eq. (1.6) by replacing the wavefunction by its definition, given in Eq. (1.4), we find

$$\begin{aligned}\langle\hat{O}(t)\rangle &= \langle\psi(\mathbf{r},t)| \hat{O} |\psi(\mathbf{r},t)\rangle \ , \\ &= \langle\psi(\mathbf{r},0)| e^{i\hat{H}^\dagger t/\hbar}\hat{O}e^{-i\hat{H}t/\hbar} |\psi(\mathbf{r},0)\rangle \ , \\ &= \langle\psi(\mathbf{r},0)| \hat{O}(t) |\psi(\mathbf{r},0)\rangle \ ,\end{aligned} \tag{1.7}$$

where we have defined the operator $\hat{O}$ as a function of time as $\hat{O}(t) = e^{i\hat{H}^\dagger t/\hbar}\hat{O}e^{-i\hat{H}t/\hbar}$, which is the formal solution to the *Heisenberg equation* for the operator $\hat{O}$:

$$i\hbar\partial_t\hat{O} = [\hat{H}, \hat{O}]\,, \tag{1.8}$$

where $\hat{H}$ is the Hamiltonian operator in Eq. (1.4) and $[\hat{H}, \hat{O}] \equiv \hat{H}\hat{O} - \hat{O}\hat{H}$ is the commutator. Note that in Eq. (1.7) the mean value is computed through the initial condition of the wavefuction, and all the temporal dependence is in the operator rather than in the wavefunction. This is referred to as the *Heisenberg picture* of Quantum Mechanics, and is completely equivalent to the Schrödinger picture.

In the descriptions above, we have assumed that the Hamiltonian that rules the dynamics of the system is independent of time. However, this is not always the case. In particular, one of the Hamiltonians that we will used extensively throughout this Thesis, describing the excitation of a quantum object by a coherent field (such as the one generated by a classical laser), is time-dependent. It is given by

$$H_a = \hbar\omega_a a^\dagger a + \hbar\Omega_a(e^{-i\omega_L t}a^\dagger + e^{i\omega_L t}a)\,, \tag{1.9}$$

where ω_L is the resonance frequency of the coherent field, which drives with intensity Ω_a a quantum field with natural frequency ω_a described with the so-called "*annihilation* operator" a. This is the ladder operator of the harmonic oscillator (see Feynman (1998) for an excellent introduction), which upgrades in the context of "second quantization" to the operator that subtracts one particle from the field. Its hermitian conjugate, $a^\dagger$, is consequently the *creation* operator, that adds a particle. Second quantization is the quantum formalism that describes systems with a varying number of particles, a trademark of quantum field-theory in general and of optics in particular, where photons get constantly created and absorbed. The time-dependent Hamiltonian in Eq. (1.9) makes the evolution of the state of the system more complex than in Eq. (1.5). We can suppress the temporal dependence by transforming the Hamiltonian in Eq. (1.9) into a frame that rotates with the same frequency at which the laser is driving the system. To do so, we need to split the Hamiltonian in two components:

$$H(t) = H_0 + V(t)\,, \tag{1.10}$$

where H_0 is completely independent of time, whereas all the temporal dependence is kept on the term $V(t)$. In agreement with the Schrödinger picture, the evolution of a wavefunction due to the time-independent Hamiltonian H_0 is given by

$$|\psi(t)\rangle = U_0(t,0)\,|\psi(0)\rangle\,, \tag{1.11}$$

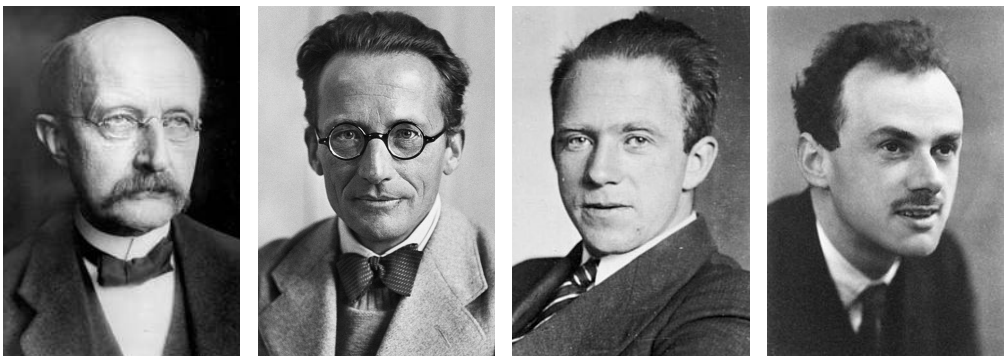

Planck Schrödinger Heisenberg Dirac

Figure 1.8: The fathers of quantum mechanics. Plank (1858-1947) solved the ultraviolet catastrophe making the assumption that the energy of the electromagnetic field could only be transmitted in bundles of energy, thus introducing the concept of quantization. After Einstein's theory for the photoelectric effect, Schrödinger (1887-1961) and Heisenberg (1901-1976) developed (independently) the formalism of Quantum Mechanics. Dirac (1902-1984) extended it to account for relativistic effects.

where $U_0(t,0) = e^{-iH_0 t/\hbar}$ propagates the wavevector $|\psi(t)\rangle$ in time, and satisfies the differential equation

$$i\hbar\partial_t U_0(t,0) = H_0 U_0(t,0)\,. \tag{1.12}$$

However, this function does not take into account the time-dependent part of the Hamiltonian, and as such it does not describe accurately the evolution of the system.

Conversely, we may define a new state vector $|\Psi(t)\rangle$ as some rotation of the state vector $|\psi(t)\rangle$, namely

$$|\Psi(t)\rangle \equiv R(t)\,|\psi(t)\rangle \qquad \text{and} \qquad |\psi(t)\rangle = R^\dagger(t)\,|\Psi(t)\rangle\,, \tag{1.13}$$

where $R(t)$ is a function still to be determined. Taking the temporal derivative of Eq. (1.13) we obtain (for simplicity, we drop the explicit temporal and spatial dependence of the operators and wavefunctions)

$$\begin{aligned} i\hbar\partial_t\,|\Psi\rangle &= i\hbar\partial_t\,(R\,|\psi\rangle)\,,\\ &= i\hbar(\partial_t R)\,|\psi\rangle + i\hbar R\partial_t\,|\psi\rangle\,,\\ &= i\hbar(\partial_t R)R^\dagger\,|\Psi\rangle + RH\,|\psi\rangle\,,\\ &= i\hbar(\partial_t R)R^\dagger\,|\Psi\rangle + RHR^\dagger\,|\Psi\rangle\,,\\ &= \left[i\hbar(\partial_t R)R^\dagger + RHR^\dagger\right]|\Psi\rangle\,, \end{aligned} \tag{1.14}$$

which is a Schrödinger equation for the wavevector $|\Psi\rangle$ with a modified Hamiltonian $\tilde{H} = i\hbar(\partial_t R)R^\dagger + RHR^\dagger$. The choice of the function $R(t)$ depends on the specificities of each system. This transformation is commonly referred to as the *interaction* or *Dirac picture* of Quantum Mechanics. For the Hamiltonian in Eq. (1.9) the transformation that removes the temporal dependence is $R(t) = e^{i\hbar\omega_L t a^\dagger a}$, and the Hamiltonian in the rotating frame becomes

$$\tilde{H}_a = \hbar(\omega_a - \omega_L)a^\dagger a + \hbar\Omega_a(a^\dagger + a)\,. \tag{1.15}$$

With the formalism that we have introduced above the description of the temporal evolution of a quantum system is limited, since the propagator of the state is given by the Hamiltonian only, which, being always an *hermitian* operator, cannot describe dissipative processes. To include such effects into the description, we need to upgrade the wavefunction of the system to a "*density matrix*" ρ. If the state of the system is pure (that is, it can be written as a wavefunction), then the density matrix of the state is given by the tensor product between the *ket* ($|\psi\rangle$) and the *bra* ($\langle\psi|$) associated to the system: $\rho = |\psi\rangle\langle\psi|$. As such, the dynamics of the density matrix is deduced directly from Schrödinger equation (1.4):

$$\begin{aligned} \partial_t\rho &= (\partial_t\,|\psi\rangle)\langle\psi| + |\psi\rangle(\partial_t\langle\psi|)\,,\\ &= -\frac{i}{\hbar}H\,|\psi\rangle\langle\psi| + \frac{i}{\hbar}\,|\psi\rangle\langle\psi|\,H\,,\\ &= -\frac{i}{\hbar}H\rho + \frac{i}{\hbar}\rho H\,,\\ &= \frac{i}{\hbar}[\rho, H]\,, \end{aligned} \tag{1.16}$$

which is known a the *Liouville–von Neumann equation*. This equation describes the system assuming that all the degrees of freedom are taken into account. However, in general it is impossible to satisfy such a condition. A realistic description of a quantum system needs to take into account that the system is not isolated from the rest of the Universe, but rather that it is in contact with it. Therefore, there exists a larger Hamiltonian that describes the complete dynamics of the system of interest with the rest of the environment. Such a Hamiltonian has three contributions

$$H = H_S + H_R + H_{S+R}\,, \tag{1.17}$$

where H_S describes the dynamics of the systems on its own, H_R describes the dynamics of the environment on its own, and H_{S+R} describes the coupling between the system and the

environment. Obtaining the solution for the wavefunction as in Eq. (1.5) becomes intractable since the number of degrees of freedom of the environment increases. However, even though we are taking into account all the degrees of freedom, we are still only interested in the dynamics of the system. Thus, if the state of the system plus environment (that we will refer to as $A \otimes R$) is given by a density matrix $\Lambda(t)$, then we will be interested only in the reduced density matrix, that we obtain by tracing *all* the degrees of freedom from the environment, thus defining

$$\rho(t) = \mathrm{Tr}_{\mathrm{R}}[\Lambda(t)]\,. \tag{1.18}$$

In this way, if $\hat{O}$ is an operator in the Hilbert space of our system, then the mean value of the operator is given by

$$\langle \hat{O} \rangle(t) = \mathrm{Tr}_{S\otimes R}[\hat{O}\Lambda(t)] = \mathrm{Tr}_{\mathrm{S}}\{\hat{O}\,\mathrm{Tr}_{\mathrm{R}}[\Lambda(t)]\} = \mathrm{Tr}_{\mathrm{S}}[\hat{O}\rho(t)]\,. \tag{1.19}$$

The objective is now to obtain an equation for the reduced density matrix $\rho(t)$ with the properties of the environment entering in the description only as parameters. The details on how to get to the equation governing the reduced density matrix are textbook material, and are particularly well explained by Carmichael (2008). The result that one obtains is that the dynamics of the reduced density matrix is given by a so-called *Master equation* of the type (from here onward, we set $\hbar = 1$):

$$\partial_t \rho = i[\rho, H] + \frac{1}{2}\sum_k \mathcal{L}_{L_k}\rho\,, \tag{1.20}$$

where we have used the notation

$$\mathcal{L}_{L_k}\rho \equiv \left(2L_k^\dagger \rho L_k + L_k^\dagger L_k \rho + \rho L_k^\dagger L_k\right)\,. \tag{1.21}$$

In Eqs. (1.20-1.21), the operators L_k are typically referred to as the *jump operators* of the system, and they are responsible for changing the state of the system by, e.g., removing or adding particles. Note that there is no issue with the conservation of energy, as the particles that are removed or added come from or go to the environment (which we have traced out). Equation (1.20) is commonly referred to as the *Master equation in the Lindblad form*, and to get there two important approximations had to be made:

1. *The Born approximation:* We assume that at the time $t = 0$, there are no correlation between the system and the environment, so that $\Lambda(0) = \rho(0)R_0$, where R_0 is an initial environment density operator. At later times, the interaction between the system and the environment induces correlations between them. However, we assume that the environment is large enough to be unperturbed by the system (while the latter is clearly affected by the former!), so that at any given time $\Lambda(t) = \rho(t)R_0$.

2. *The Markov approximation:* While it may be reasonable from physical arguments that the state of our system depends on the history of the state, if the environment with which the system is in contact is itself in thermal equilibrium, we also do not expect it to preserve the minor changes induced in it by the interaction with the system for too long. At least not long enough to change significantly the future evolution of the system. In other words, we assume that if Γ_i and Γ_j are operators of the environment, then their correlations are localized in time: $\langle \Gamma_i(t)\Gamma_j(t')\rangle_{\mathrm{R}} \propto \delta(t - t')$, where δ is the Dirac delta function.

Together, these two conditions are known as the *Born-Markov approximation*, and it relies on the existence of two scales of times: a slow one for the dynamics of the system and a rapid one describing the correlations of the environment.

As an application, let us consider a harmonic oscillator driven by a laser. The Hamiltonian describing this system is given by Eq. (1.9), which in the frame that rotates with the frequency of the laser becomes the Hamiltonian in Eq. (1.15). Considering that the harmonic oscillator

is in contact with an environment, to which it can lose photons at a rate γ_a, we can write the master equation in the lindblad form, as in Eq. (1.20):

$$\partial_t \rho = i[\rho, H_a] + \frac{\gamma_a}{2}\mathcal{L}_a\rho\,, \tag{1.22}$$

where H_a is the Hamiltonian in Eq. (1.15) and $\mathcal{L}_a\rho$ is as in Eq. (1.21). In the steady state, obtained when the left-hand side of Eq. (1.22) equals zero, the harmonic oscillator is found in a pure state commonly referred to as a "*coherent state*". Using the basis of Fock states $|k\rangle$—with k an integer which describes the number of particles contained in the field—the coherent state reads

$$|\alpha\rangle = e^{-|\alpha|^2/2}\sum_k \frac{\alpha^k}{\sqrt{k!}}\,|k\rangle\ . \tag{1.23}$$

The parameter α is a complex number, which for the coherent state of the harmonic oscillator described through the master equation (1.22) is given by

$$\alpha = -\frac{2i\Omega_a(\gamma_a - 2i\Delta_a)}{\gamma_a^2 + 4\Delta_a^2}\,, \tag{1.24}$$

where we have used the notation $\Delta_a = (\omega_a - \omega_\mathrm{L})$ for the detuning between the laser and the oscillator. Furthermore, since the coherent state in Eq. (1.23) is an eigenstate of the annihilation operator a with eigenvalue α, i.e., $a\,|\alpha\rangle = \alpha\,|\alpha\rangle$, it is straightforward to show that the mean population—the average number of photons—of the harmonic oscillator is given by

$$n_a = \langle a^\dagger a\rangle = \langle\alpha|\,a^\dagger a\,|\alpha\rangle = |\alpha|^2 = \frac{4\Omega_a^2}{\gamma_a^2 + 4\Delta_a^2}\,. \tag{1.25}$$

1.2.1.2 *Cascaded Coupling*

Now that we have laid the grounds to describe quantum objects through the master equation, we turn to the description of the excitation of a quantum object using the light emitted by another quantum system, which is the central theme of this Thesis. Usually, when one considers the coupling between two quantum systems, the description is done through an interaction Hamiltonian. In the second quantization formalism, such a Hamiltonian reads in its most simple form:

$$H_I = g(c_1^\dagger c_2 + c_2^\dagger c_1)\,, \tag{1.26}$$

where c_1, c_2 are annihilation operators describing the particles of the coupled system, and g is their interaction strength. If the particles described by c_i have a decay rate γ_i, and are freely evolving with a Hamiltonian H_i, $i = 1, 2$, the master equation describing the dynamics of this system is:

$$\partial_t \rho = i[\rho, H_1 + H_2 + H_I] + \frac{\gamma_1}{2}\mathcal{L}_{c_1}\rho + \frac{\gamma_2}{2}\mathcal{L}_{c_2}\rho\,, \tag{1.27}$$

where $\mathcal{L}_c\rho$ is defined in Eq. (1.21). Depending on whether the coupling H_I or the dissipation γ_i dominates, one speaks of strong or weak coupling, respectively. If one of the two systems, say, 1, is itself excited externally, for instance being driven by a laser, or merely being given a non-vacuum initial condition, then one has a crude picture of system 1 exciting system 2. This is a fairly accurate description in the weak-coupling limit where the dynamics becomes directional and irreversible, simply because excitation are dissipated by system 2 before they can cycle back to system 1.

The coupling between quantum systems does not have to be reversible: it can instead correspond to the scenario of a source and its target. In this case, there is a deep asymmetry between the coupled systems. For instance, one can remove the target from the beam of the source, which leaves the latter unaffected while the former passes from being irradiated to the vacuum. Note that such an asymmetry does not have to hold on logical grounds. In fact,

in electronics, while an ideal source should not be affected by the circuit it powers, in reality, there is a load and every component affects all the others to some extent. In photonics, the picture of a flying qubit, left to propagate long enough before it meets its target, makes it intuitively clear that it should be possible to forbid back-action. This could also be realized by taking advantage of the fast-growing field of chiral optics developed by, e.g., Petersen, Volz, and Rauschenbeutel (2014), Gonzalez-Ballestero et al. (2015), Pichler et al. (2015), Coles et al. (2016), Mahmoodian, Lodahl, and Sorensen (2016), Guimond et al. (2016), Lodahl et al. (2016), and Gonzalez-Ballestero et al. (2016).

Gardiner (1993) and Carmichael (1993b) treated (independently) the problem of quantum excitation without feedback in two consecutive Letters in the Physical Review. This achieved to set up a formalism—named the "*cascaded formalism*" by Carmichael—that allows to excite a system (which we will call the "target") by an other (the "source") without back-action from the target to the source. This permits to think separately of the quantum source, which properties can be independently studied and then directed onto a target. For historical accuracy, let us mention that the problem was first contemplated by Kolobov and Sokolov (1987), who tackled it by providing all the correlations of the exciting quantum field. This was recognized as an overkill by Gardiner (1993) and Carmichael (1993b) (Gardiner had made prior attempts along these lines). They proposed instead to model the quantum source dynamics as well as the response of the target, even if only the latter is of interest.

Despite the conceptual importance of quantum excitation, there have been a moderate follow-up of this cascaded formalism, which I believe is a deep and far-reaching contribution to the problem of light-matter interaction. Even though it became textbook material (see the last chapter from Gardiner and Zoller (2000)'s book) and generated a sizable amount of citations, few texts do actually fully exploit the idea. Gardiner and Parkins (1994) (the formalism is sometimes also named after these two authors) undertook a more thorough analysis of various types of non-standard statistics of the source and Cirac et al. (1997) used it to describe perfect transmission in their proposal for a quantum network, but overall, the core of the literature using the formalism focuses on specialized particular cases, such as driving with squeezed light by Smyth and Swain (1999) and Messikh, Tanaś, and Ficek (2000). Typically, the discussion is then held at the level of correlations from a quantum state (namely a squeezed state), as opposed to dynamical correlations from a quantum source. The other studies, already evoked, turned to approximate or indirect approaches, quite similar to the earlier attempts before the cascaded formalism was set up. The reasons for this is certainly a mix between convenience of using well-known and established formalism and the as-yet unclear advantages of the alternative one.

The derivation of the cascaded coupling requires the usage of the so-called *input-output formalism*, the details of which are given by Gardiner and Zoller (2000). First, the equations of

Gardiner Carmichael

Figure 1.9: Gardiner (1942) and Carmichael (1950) developed (separately) the formalism of cascaded excitations, which readily allows the description of the excitation of an optical target by the emission of a quantum object.

motion are expressed in the quantum Langevin form, thus allowing to set the output field of one of the systems (the source) as the input field for the other (the target). This can be brought to a master equation type of description, with both coherent and Lindblad terms that contrive to direct the flow of excitation from the source to target only. This makes all the operators of the source independent from those of the target, while in turn those depend on operators of the source. The generic case where the source (resp. target) is described by the Hamiltonian H_1 (resp. H_2) and has a decay rate γ_1 (resp. γ_2) is then ruled by the following master equation:

$$\partial_t \rho = i[\rho, H_1 + H_2] + \frac{\gamma_1}{2}\mathcal{L}_{c_1}\rho + \frac{\gamma_2}{2}\mathcal{L}_{c_2}\rho - \sqrt{\gamma_1\gamma_2}\left([c_2^\dagger, c_1\rho] + [\rho c_1^\dagger, c_2]\right). \tag{1.28}$$

The source must also be excited, which can be done either by an incoherent or by a coherent (classical) type of excitation. The incoherent excitation is described simply by adding the Lindblad term $(P_{c_1}/2)\mathcal{L}_{c_1^\dagger}\rho$ to Eq. (1.28). The coherent excitation, however, requires a subtler description, for which one uses the input–output formalism again. The coupling between a coherent field and the system (that latter will be used as the source of quantum excitation) happens through an input channel for the said system. If such an input channel is the only one available to excite the source, then it follows that the only output channel from the source also contains the coherence of the driving field. In this case, the target of the quantum excitation is *also* driven by the coherent field, and its dynamics is given by Eq. (1.28) setting $H_1 = \omega_1 c_1^\dagger c_1 - i\sqrt{\gamma_1}\mathcal{E}(c_1^\dagger - c_1)$, and $H_2 = \omega_2 c_2^\dagger c_2 - i\sqrt{\gamma_2}\mathcal{E}(c_2^\dagger - c_2)$, i.e., the dynamics is ruled by the master equation:

$$\begin{aligned}\partial_t \rho = i\left[\rho, \omega_1 c_1^\dagger c_1 + \omega_2 c_2^\dagger c_2 - i\sqrt{\gamma_1}\mathcal{E}(c_1^\dagger - c_1) - i\sqrt{\gamma_2}\mathcal{E}(c_2^\dagger - c_2)\right] + \\ + \frac{\gamma_1}{2}\mathcal{L}_{c_1}\rho + \frac{\gamma_2}{2}\mathcal{L}_{c_2}\rho - \sqrt{\gamma_1\gamma_2}\left([c_2^\dagger, c_1\rho] + [\rho c_1^\dagger, c_2]\right),\end{aligned} \tag{1.29}$$

where $\mathcal{E}$ is the amplitude of the coherent field driving the source. Note that the effective driving intensity, i.e., $\Omega_1 = \sqrt{\gamma_1}\mathcal{E}$, depends on the decay rate of the system that is being excited, in agreement with the fact that a system that cannot emit cannot be excited either. To prevent the target to be also driven by the coherent field that drives the source, one can use another input (and their corresponding output) channel to excite the source (and also the target). Each of these channels couples with an amplitude $\epsilon_i \leq 1$, with the condition that $\sum_k \epsilon_k = 1$, the sum being over all the input channels. In this case, and considering only two input channels (with amplitudes ϵ_1 and $\epsilon_2 = 1 - \epsilon_1$) as well as only one input channel for the target (with amplitude 1), the dynamics of the system is given by Eq. (1.28) with $H_1 = \omega_1 c_1^\dagger c_1 - i\sqrt{\epsilon_1\gamma_1}\mathcal{E}(c_1^\dagger - c_1)$, $H_2 = \omega_2 c_2^\dagger c_2$, and replacing the coupling strength $\sqrt{\gamma_1\gamma_2}$ by $\sqrt{(1-\epsilon_1)\gamma_1\gamma_2}$ in the second line of Eq. (1.28), i.e., the dynamics is now ruled by the master equation:

$$\begin{aligned}\partial_t \rho = i\left[\rho, \omega_1 c_1^\dagger c_1 + \omega_2 c_2^\dagger c_2 - i\sqrt{\epsilon_1\gamma_1}\mathcal{E}(c_1^\dagger - c_1)\right] + \\ + \frac{\gamma_1}{2}\mathcal{L}_{c_1}\rho + \frac{\gamma_2}{2}\mathcal{L}_{c_2}\rho - \sqrt{\epsilon_2\gamma_1\gamma_2}\left([c_2^\dagger, c_1\rho] + [\rho c_1^\dagger, c_2]\right),\end{aligned} \tag{1.30}$$

where $\epsilon_2 = 1 - \epsilon_1$. The additional input channel to the source makes the coupling between the coherent field not as efficient as when there is only one input channel, thus reducing the effective driving intensity. For the target, although the coupling strength is also reduced, now the driving is uniquely due to the emission from the quantum source.

Putting Eq. (1.28) in the Lindblad form contributes a Hamiltonian part. The formalism thus corresponds to a quantum coherent coupling, allowing the description of continuous wave (cw) and resonant excitation of quantum states. Importantly, in contrast to the Hamiltonian coupling in Eq. (1.26), the coupling strength is now fixed by the decay rate of the source and of the target. An infinitely-lived target cannot be excited. The stronger one wishes to make the coupling between a source and its target, the stronger has to be their (geometric) mean dissipation. This imposes some fundamental constrains on external driving (or driving without

feedback). In contrast, the Hamiltonian coupling sets the coupling strength and decay rates independently. While it would therefore appear that the Hamiltonian coupling has the upper hand, and that one should strive for the standard strong-coupling regime, we will show in the following chapters that the cascaded architecture can be superior to the other types of coupling in some cases and depending on the end purpose.

Finally, as a closing comment on the cascaded formalism—which I will use in this form following the literature—it is interesting to point out that the Lindblad form (1.20) is complete enough to actually also describe such asymmetric source/detector scenarios. Indeed, I have recently shown with Downing et al. (2019) that the cascaded case is a particular case of the Lindblad equation when one considers that a pair of quantum objects can be coupled through both a Hamiltonian (which yields a coherent coupling) and a reservoir (which, conversely, yields an incoherent coupling). The relative phase between these two types of couplings leads to a quasi-chiral behaviour, from which the cascaded formalism is recovered when the feedback from one of the systems is completely blocked.

We have now introduced the overall background of light in its quantum setting, up to the technical details required to describe it theoretically. We will now focus on another central aspect of this Thesis, which is also for that matter another aspect of the quantum theory of light, namely, photon correlations. This starts with a beautiful and stunning discovery from one of the lesser-known heroes of Science.

1.2.2 *Hanbury Brown*

Robert Hanbury Brown (cf. Fig. 1.10) was a British physicist and astronomer. Born in 1916 in India to an army officer, he returned to England at the age of 8 to attend school. Early in his youth, he changed the elementary school for the Brighton Technical College, where he obtained a Bachelor's degree in Electrical Engineering. It was the second half of the 1930s, and England still had the memories of the German Zeppelin raids (the first of which took place over London in April, 1915) stuck in its mind. Thus, a large effort was devoted to the development of technologies that would help to prevent future air raids; specially those taking place at night when the pilots could not locate enemy aircrafts simply by looking at the sky. A possible solution was to use radars—a secret technique introduced in the United Kingdom by Robert Watson-Watt, and which consisted in using radio waves (electromagnetic waves whose wavelength is of the order of meters) to transmit information across large distances—to find the

Figure 1.10: Robert Hanbury Brown (1916-2002) pioneered the experiments involving correlations between photons. He developed an observatory in the Australian desert, in which he placed an interferometer of radio waves (right). The detectors were placed on top of a circular railing, with 94 m of radius, which enabled the astronomers to vary easily the distance between the detectors, and thus measure the correlations in the light coming from distant stars. A new theory of light was needed to account for Hanbury Brown's genius intuition.

position of planes while in the air. Although the normal career path for a scientist would have been to pursue a PhD degree, Hanbury Brown was recruited to work for the government in the development of technologies involving the radar. In particular, his work focused on how to optimize the emission and reception of radio signals, in such a way that they could be used by RAF airplanes to locate other planes while flying. Naturally, this posed great difficulties and many approaches were taken before finding the best way to incorporate radars into planes. Thanks to Hanbury Brown and his team's effort, many air raids were prevented or neutralized when the second World War broke. By the end of the war, Hanbury Brown was one of the world's experts in radio waves, and he turned his "*peacetime*" activity to Bernard Lovell's radio astronomy group at the University of Manchester. While trying to measure the angular size of radio stars (emitting light with wavelengths in the scale of meters), he and Cyril Hazard developed a radio interferometer. With it, they were able to measure the distance between the two detectors at which the signal from the stars lose its coherence. As the angular size becomes smaller, the required separation to lose such a coherence increases, to the point at which it becomes impractical to measure. Then, as Hanbury Brown (1991) recounts:

> This problem worried me for weeks and I could think of nothing else, until one night in 1949 I suddenly thought:
>
> > *If the radiation from a discrete source in the sky is picked up at two different places on Earth, is there anything else besides the phase and the amplitude of the signals which we can compare to find the mutual coherence?*
>
> And into my mind came quite clearly the image of a man looking at the "noise-like" signal received from a radio source on a cathode-ray tube. Supposing, I thought, there was another man many miles away looking at another identical cathode-ray tube, would he see the same noise-like signal? If in fact there is a similarity between what the two men see, could it perhaps, be used as a measure of mutual coherence?

Working out the theory, he realized that he was on the right track, and that if the radiation received in the two places is mutually coherent, then the fluctuations in intensity of the signal are also correlated. He then designed an interferometer for the intensity, rather than for the amplitudes, and started making measurements.

Before designing enormous radio telescopes to look at the stars, he wanted to make sure that his idea—backed by Richard Twiss' calculations—was correct, and that they would not be wasting time and money in a void enterprise. Hanbury Brown and Twiss (1956a) made a simple experiment in which they measured the correlations of the light emitted by a high-pressure mercury arc, observing that the light was indeed correlated. The results of the paper caused a big controversy, with Brannen and Ferguson (1956) reporting a null experiment, without being able to reproduce the observed correlations. Quickly after that, Hanbury Brown and Twiss (1956b) showed that the observation was correct, but that Brannen and Ferguson (1956)'s setup was not sensitive enough, and it would take them about a thousand years to obtain an equivalent accuracy in the correlations with their setup. Still, even though the results were sound, Hanbury Brown and Twiss had trouble getting funding to build the large radio telescope. In fact, the idea was so revolutionary and the result so unexpected, that at some point Hanbury Brown was literally thrown a copy of Dirac's *Quantum Mechanics* to his face and was suggested to look at page 14, where Dirac stated that *interference between two different photons can never occur*. About this, Hanbury Brown (1991) wrote:

> To me the most interesting thing about all this fuss was that so many physicists had failed to grasp how profoundly mysterious light really is, and were reluctant to accept the practical consequences of the fact that modern physics doesn't claim to tell us what things are like *in themselves* but only how they *behave*.

Time and more precise measurements proved Hanbury Brown and Twiss right. The intensity interferometer, now known as the *Hanbury Brown-Twiss* interferometer, has since been used

in a myriad of experiments, including Kimble, Dagenais, and Mandel (1977)'s measurement, in which the observation of photon antibunching proved the quantum nature of light, and now the Hanbury Brown and Twiss effect is routinely observed in countless laboratories across the world. More importantly, the Hanbury Brown and Twiss effect was the starting point for the modern, i.e., quantum theory of light. This was already recognized by early advocates of Hanbury Brown's cause, prominently by Purcell (1956) who understood that "far from requiring a revision of quantum mechanics, [it] is an instructive illustration of its elementary principles". Indeed, Purcell identified the intensity correlations as the results of bosonic fluctuations from indistinguishable particles (he also predicted the opposite tendency for electrons). In this view, intensity correlations result from the tendency of two indistinguishable particles to clump together in their observables (in time, space, etc.) The effect can also be accounted for classically, as discussed for instance by Baym (1998). The full formalization to cover all cases (including those with no classical counterpart) came in the form of what is now known as Quantum Optics.

1.2.3 *The birth of Quantum Optics*

The discovery of correlation in the intensity of light by Hanbury Brown was made with so-called thermal light, namely from light emitted by a chaotic source (a star; note that Hanbury Brown was still calling it "coherent light", in the sense of spectrally filtered). At the same time, the laser was providing a new type of light, and this also came with its own type of correlations. There was a need to describe all this, especially as the Laser quickly became a fundamental tool for research, taking a central role in laboratories across disciplines, from Physics to Chemistry, Biology and even to Medical sciences. The description of the light emitted by a laser was in principle within the dominion of the theory laid by Dirac as part of the *Quantum Theory of Fields*. More to the point, the development of the theory to describe the electromagnetic field generated by the laser was formulated independently by E. C. George Sudarshan and Roy J. Glauber. Sudarshan (1963) published a paper where he showed that the light emitted by a laser could be described both through a semiclassical theory or a fully quantum mechanical one, and that these two descriptions would be analogous. There, he introduced the so-called "*diagonal representation*" and showed that *any* state of light, classical or quantum, could be expressed in such a diagonal form:

$$\rho = \int P(\alpha) \left|\alpha\right\rangle \left\langle\alpha\right| d^2\alpha \,, \tag{1.31}$$

where ρ is the density matrix of an arbitrary state of light, $P(\alpha)$ is a kernel that needs to be determined, and $|\alpha\rangle$ is a coherent state, as defined in Eq. (1.23). Here, ρ is diagonal in the basis of coherent states. A couple of months later, Glauber (1963) published a paper criticizing Sudarshan results and introducing another version of the representation, which he coined the "P-representation" (as the diagonalization of the state consists in obtaining the $P(\alpha)$ function),

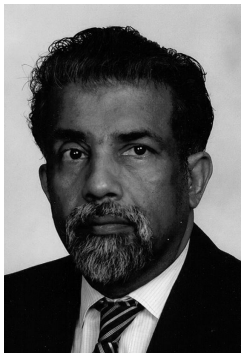

Sudarshan

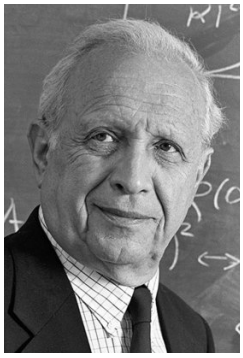

Glauber

Figure 1.11: Sudarshan (1931-2018) and Glauber (1925-2018) built on the work of Dirac to develop a theory that describes the electromagnetic field generated by a laser. Their work was the seed that later blossomed into the field of quantum optics. This breakthrough was the main reason why Glauber was awarded the physics Nobel prize in 2005 (to the annoyance of Sudarshan).

and it is only recently that it has been re-named as the "Glauber–Sudarshan representation" to acknowledge Sudarshan's contribution.

The light emitted by a laser can be represented through a coherent state. Using the Sudarshan-Glauber formalism, a coherent state with amplitude β can be written as in Eq. (1.31) with $P(\alpha) = \delta(\alpha - \beta)$, where δ is the Dirac function. Although coherent states can be expressed through a quantum formalism, they are of a classical nature, i.e., they can be fully described with the classical theory of electromagnetism of Maxwell. Nevertheless, these classical states can be used as a benchmark for the "quantumness" of other states of light. The comparison is made through the correlations between the photons that compose the light field. Such a comparison was formalized by Glauber (1963), who used the second quantization of the light field to define the "Nth-order correlation function":

$$g^{(N)}(t_1, t_2, \cdots, t_N) = \frac{\langle a^\dagger(t_1)a^\dagger(t_2)\cdots a^\dagger(t_{N-1})a^\dagger(t_N)a(t_N)a(t_{N-1})\cdots a(t_2)a(t_1)\rangle}{\langle a^\dagger(t_1)a(t_1)\rangle\langle a^\dagger(t_2)a(t_2)\rangle\cdots\langle a^\dagger(t_N)a(t_N)\rangle}, \tag{1.32}$$

for which we have assumed that the times t_k are in increasing order, namely $t_1 < t_2 < \cdots < t_N$. This quantifies the correlation between N photons emitted at those times. The correlation functions defined in Eq. (1.32) describe, to order N, how close the fluctuations of the field are to those of a coherent (and classical) field. A particular case of Eq. (1.32) that we will use repeatedly throughout the Thesis, and which is widely used across Quantum Optics, is the second-order correlation function, obtained by setting $N = 2$:

$$g^{(2)}(t, t+\tau) = \frac{\langle a^\dagger(t)a^\dagger(t+\tau)a(t+\tau)a(t)\rangle}{\langle a^\dagger(t)a(t)\rangle\langle a^\dagger(t+\tau)a(t+\tau)\rangle}, \tag{1.33}$$

where we have set $t_1 = t$ and $t_2 = t + \tau$, because in the steady-state condition, the correlations do not depend on the initial time t, but only on the delay τ between photons. Furthermore, the delayed correlation (1.33) gives us the information regarding the temporal structure with which the photons are emitted by the system. According to the behaviour of these correlations we can classify the emission in three categories:

1. If $g^{(2)}(\tau) < g^{(2)}(0)$, the emission is *bunched*, as the photons are emitted preferably close to each other.
2. If $g^{(2)}(\tau) = 1$, the emission is uncorrelated and it behaves like a coherent source of light.
3. If $g^{(2)}(\tau) > g^{(2)}(0)$, the emission is *antibunched*, as the photons tend to be emitted far from each other. This scenario is specially relevant, as no classical state can display antibunching.

As the long time-delay limit of *all* the second-order correlation function in the steady-state has to be 1—since the photons emitted with a very large delay between them are not correlated anymore—sometimes the language is twisted and people refer to $g^{(2)}(0) > 1$ as bunching and to $g^{(2)}(0) < 1$ as antibunching. This classification of quantum correlations, first impulsed by the insights and observation of Hanbury Brown ($g^{(2)}(0) = 2$ for thermal light, regardless of its origin), is the modern definition of optical coherence (no correlation). This will be a central quantity for the rest of the text so we now proceed to go from the textbook material as reviewed above to the state-of-the-Art description of these quantities, at which point we will be prepared to enter into the main results of the Thesis per se.

1.2.4 *The observer in Quantum Mechanics*

A fundamental aspect of Quantum Mechanics is the fact that the state of an object does not have a physical reality, until it is measured (see alson Hanbury Brown's comment on pages 17–18). The state of light in which photons are emitted by a quantum object is not an exception. Photon correlations, as introduced by Glauber in Eq. (1.32), being the central quantities in

Quantum Optics, require such a careful consideration of the role of detection. To start with, these correlations, which arise fully from a theoretical viewpoint, assume two conditions that no experimental setup can satisfy, namely, when computing the correlations of Eq. (1.32) we assume that: i) the detector measures the time at which each photon arrives with an infinite precision, and ii) the detector collects the light from *all* the emission spectrum of the source. Eberly and Wódkiewicz (1977) raised this issue early on with regard to the spectrum itself, that is, at the single-photon level, and concluded that a realistic description of the light field requires the addition of the physics of the detection process into the theoretical model. This point becomes increasingly relevant as the source that provides the light is more quantum. The connection between the quantum system that emits light and what the detector receives is typically done through the input-output formalism developed by Collet and Gardiner (1984), Gardiner and Savage (1984), and Yurke (1984), with which one assumes that an operator from the inside of the cavity (say, an annihilation operator a) is coupled to a continuum of extended modes, with annihilation operators A_ω (where the subindex ω indicates the frequency of the mode). Therefore, using the Heisenberg picture (cf. Section 1.2.1) we can compute the power spectrum of the output field as a time-dependent correlator that counts the photons of frequency ω_1 that are emitted at some time T_1:

$$S^{(1)}(\omega_1, T_1) = \langle A^\dagger_\omega(T_1) A_\omega(T_1)\rangle \,, \tag{1.34}$$

which reduces to the well-known Wiener-Khintchine theorem

$$S_a(\omega) = \frac{1}{\pi}\frac{1}{n_a}\Re\int_0^\infty \langle a^\dagger(0)a(\tau)\rangle e^{i\omega\tau}\, d\tau \,. \tag{1.35}$$

This theorem, however, does not arise from the analysis of an experimental situation, and in principle, it only applies to stationary processes. In this light, Eberly and Wódkiewicz (1977) tackled the problem of finding a generalized version of the power spectrum, with the properties that one would like to have from such a quantity, e.g., the facts that it must be positive, regardless of the amount of time in which one collects the light (or compute the correlations) and that the quantity only has physical meaning for times *after* it has been emitted from the source. Thus, they provide another expression, to which they refer as the *physical spectrum*, in which they take into account the time- and frequency uncertainty simultaneously: they show that this can be done simply by making a convolution with the (Lorentzian) detector response function, $e^{-\Gamma t}$, instead of a simple Fourier transform of the time auto-correlation, which then becomes

$$S^{(1)}_{\Gamma_1}(\omega_1, T_1) = \frac{\Gamma_1}{2\pi}\iint_\infty^{T_1} dt'_1 dt'_4\, e^{-(\Gamma_1/2)(T_1-t'_1)} e^{-(\Gamma_1/2)(T_1-t'_4)} e^{i\omega_1(t'_4-t'_1)} \langle a^\dagger(t'_1)a(t'_4)\rangle \,, \tag{1.36}$$

where Γ_1 can be interpreted as the linewidth of the detector. Furthermore, Eberly and Wódkiewicz (1977) show that the physical spectrum in Eq. (1.36) reduces to the Wiener-Khintchine theorem in the limit in which the timescale τ_0 of the fluctuations over the signal, and the correlation time τ_1 of the emission satisfy the relation $\tau_1 \gg \Gamma_1^{-1} \gg \tau_0$.

The extension of including the detection process to photon correlations was impulsed by Arnoldus and Nienhuis (1984) and Knöll, Weber, and Schafer (1984), in which development was obtained the expressions allowing for two detectors to have different linewidths Γ_1 and Γ_2. However, what these expressions had on generality they missed in simplicity, and because of that, the authors had to restrain actual computations to the simplest case. A few years later, Knöll and Weber (1986), Knöll, Vogel, and Welsch (1986), and Cresser (1987) arrived to the final expression for the correlations as measured by two detectors (and which has a clear resemblance to its single-detector counterpart shown in Eq. (1.36)):

$$\begin{aligned} S^{(2)}_{\Gamma_1\Gamma_2}(\omega_1, T_1; \omega_2, T_2) = \frac{\Gamma_1\Gamma_2}{4\pi^2}\iint_\infty^{T_1} dt'_1 dt'_4\, e^{-(\Gamma_1/2)(T_1-t'_1)} e^{-(\Gamma_1/2)(T_1-t'_4)} e^{i\omega_1(t'_4-t'_1)} \times \\ \times \iint_\infty^{T_2} dt'_2 dt'_3\, e^{-(\Gamma_2/2)(T_2-t'_2)} e^{-(\Gamma_2/2)(T_2-t'_3)} e^{i\omega_2(t'_3-t'_2)} \left\langle \mathcal{T}_-\left[a^\dagger(t'_1)a^\dagger(t'_2)\right] \mathcal{T}_+\left[a(t'_3)a(t'_4)\right]\right\rangle \,, \end{aligned} \tag{1.37}$$

where we have defined $\mathcal{T}_+$ and $\mathcal{T}_-$ to order in time a product of operators with the latest time on the far left and far right, respectively. This quantity is the density of joint photon detections at frequencies ω_1 and ω_2, at the respective times t_1 and t_2, with detectors of width Γ_1 and Γ_2.

Both the physical spectrum Eq. (1.36) and its two-photon counterpart (1.37) can be interpreted in two equivalent ways: either as the result of placing detectors (one and two respectively) with a given integration time, or as filtering the output with an interference filter (i.e., whose lineshape is Lorentzian), the output of which is left for another detector (ideal and infinite-bandwith, this time). These two pictures are actually equivalent since the detector is performing a filtering and, conversely, the filtering still requires ultimately a detector (this time an ideal and infinite broad-band one). This is therefore mainly a question of terminology, and throughout the text, we will be using either one or the other types of language (i.e., a filter, or a detector). Of course, one can also consider putting physical detectors post-filtering, or cascading filters, or considering still other configurations. There too, different physical pictures would be described with the same formalism.

What equations (1.36) and (1.37) show is that the resolution in the time at which the photons are emitted is linked, through the Heisenberg uncertainty principle, to the resolution in the frequency of the photons. Such a limitation does not forbid to observe an object whose photons display a perfect antibunching, or to observe a perfectly monochromatic source of light. What it implies, however, is that one cannot observe these two properties *simultaneously*. One relevant illustration of the leap into "what photons are" as opposed to "how they behave" is the recent report of Nguyen et al. (2011) and of Matthiesen, Vamivakas, and Atatüre (2012) who claimed to have observed a source of single photons with an ultra-narrow spectral profile. The idea behind it is simple: consider the resonant excitation of a two-level system with a laser. In the limit in which the intensity of the laser is weak, the photoluminescence of the two-level system is given by two components: a Lorentzian with a width given by the decay rate of the two-level system, and a narrow line centered at the frequency of the two-level system. The former comes from the photons that are absorbed and later re-emitted by the two-level system, while the latter is the contribution of the photons from the laser that are merely scattered by the two-level system. If the intensity of the driving is weak enough, the emission of the two-level system is dominated by the scattered photons, and one could argue that the source is spectrally narrow. On the other hand, given that the emitter is a two-level system, the emitted photons display perfect antibunching. Thus, one has a monochromatic source of single photons. However, in both papers the observation of the emission spectrum and of the photon correlations were performed in different experiments and even using different setups. In chapter 3, I will show how a theory of this effect which includes self-consistently the effect of detection leads us to the opposite conclusion that only one or the other characteristic (antibunching or narrow linewidth) can be obtained. Actually, using the homodyning concept introduced by Vogel (1995), I will show how such an effect can be realized after all, but with the need of including the impact of the detection.

1.2.5 *Frequency-resolved photon correlations*

From the two-photon physical spectrum (1.37) follows straightforwardly the frequency-resolved second-order correlation function, obtained by normalizing it with the square of Eq. (1.36):

$$g^{(2)}_{\Gamma_1\Gamma_2}(\omega_1, T_1; \omega_2, T_2) = \frac{S^{(2)}_{\Gamma_1\Gamma_2}(\omega_1, T_1; \omega_2, T_2)}{S^{(1)}_{\Gamma_1}(\omega_1, T_1)\, S^{(1)}_{\Gamma_2}(\omega_2, T_2)}\,. \tag{1.38}$$

This is the counterpart of Eq. (1.32) but for photons filtered beforehand, as sketched in Fig. 1.12. While such a configuration is a trivial step experimentally, this is a daunting task theoretically. To compute the correlations as in Eq. (1.38) one needs to consider all the possible time-ordering domains, and once these have been selected, one has to perform six integrals. Naturally, such a task becomes harder as the temporal structure of the system described by the annihilation

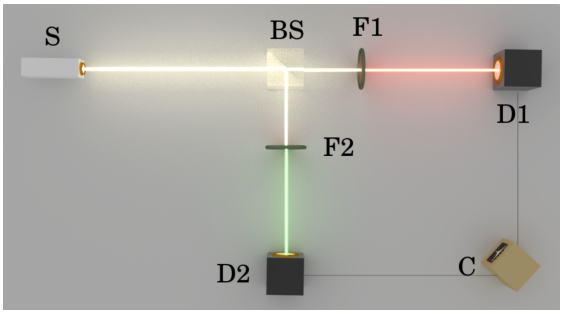

Figure 1.12: Scheme for the measurement of frequency-resolved photon correlations: the signal (S) is directed towards a beam splitter (BS), after which the pair of beams passed through filters (F) with different spectral linewidths. Then, the filtered emission goes to the detectors (D), where the signal is collected and the correlations are computed. The figure is taken from Carlos Sánchez Muñoz (2016)'s doctoral thesis.

operators a becomes more involved. Furthermore, although Eq. (1.37) can be easily generalized to account for N photons from a conceptual point of view, it becomes intractable to even write down the expression to compute, and its actual computation becomes hopelessly complicated even for the simplest problems, already at the three-photon level.

Recently, del Valle et al. (2012) found a simple way of computing the N-photon correlations (not merely to second order), without the huge effort of computing cumbersome integrals after considering multiple time orderings and integration domains. The method consists of including the description of the detectors directly in the master equation governing the dynamics of the quantum system under study, with a coupling of the type:

$$H_I = \varepsilon(a^\dagger \xi + \xi^\dagger a)\,, \tag{1.39}$$

where a and ξ are the annihilation operators of the quantum system and the detector, respectively. To solve the already mentioned reversibility problem between a source and its target (a detector), del Valle et al. (2012) ultimately take the limit $\varepsilon \to 0$ of the system. It will become clear shortly why in their case this limit can be taken. Considering the free energy of the detector—given by $H_\xi = \omega_\xi \xi^\dagger \xi$, thus setting the central frequency at which the detector collects the light—the full description of the system *plus* detector is then given by the master equation

$$\partial_t \rho = i[\rho, H_a + H_\xi + H_I] + \frac{\gamma_a}{2}\mathcal{L}_a\rho + \frac{\Gamma_\xi}{2}\mathcal{L}_\xi\rho\,. \tag{1.40}$$

Here H_a is the Hamiltonian governing the internal dynamics of the system, which has a decay rate given by γ_a, H_I is as given in Eq. (1.39), and Γ_ξ is the linewidth of the detector. The generalization to N detectors, all of them with different frequencies, is then straightforward:

$$\partial_t \rho = i\left[\rho, H_a + \sum_{k=1}^{N}\left\{\omega_{\xi_k}\xi_k^\dagger\xi_k + \varepsilon(a^\dagger\xi_k + \xi_k^\dagger a)\right\}\right] + \frac{\gamma_a}{2}\mathcal{L}_a\rho + \frac{1}{2}\sum_{k=1}^{N}\Gamma_{\xi_k}\mathcal{L}_{\xi_k}\rho\,, \tag{1.41}$$

where Γ_{ξ_k} is the linewidth of the kth detector, which collects the light at the frequency ω_{ξ_k}. Therefore, the Nth-order frequency-filtered correlation function of the system is given simply by

$$g^{(N)}_{\Gamma_{\xi_1}\dots\Gamma_{\xi_N}}(\omega_{\xi_1},\dots,\omega_{\xi_N};t_1,t_2\dots t_N) = \lim_{\varepsilon\to 0}\frac{\langle\xi_1^\dagger(t_1)\xi_2^\dagger(t_2)\cdots\xi_{N-1}^\dagger(t_{N-1})\xi_N^\dagger(t_N)\xi_N(t_N)\xi_{N-1}(t_{N-1})\cdots\xi_2(t_2)\xi_1(t_1)\rangle}{\prod_{k=1}^{N}\langle\xi_k^\dagger(t_k)\xi_k(t_k)\rangle}\,, \tag{1.42}$$

where we have assumed that the times t_k are in increasing order, namely $t_1 < t_2 < \cdots < t_N$. This generalizes the photon correlations defined by Glauber (1963) and shown in Eq. (1.32). In particular, the zero-delay Nth-order frequency-filtered autocorrelation (for which we use only one detector with linewidth Γ_ξ and centered at ω_ξ) reduces to

$$g^{(N)}_{\Gamma_\xi}(\omega_\xi) = \frac{\langle\xi^{\dagger N}\xi^N\rangle}{\langle\xi^\dagger\xi\rangle^N}\,. \tag{1.43}$$

Interestingly, since both the numerator and denominator of the right-hand side of Eqs. (1.42)–(1.43) vanish to the same order in ϵ, one can obtain the exact results for the left-hand side of these equations as the limit $\epsilon \to 0$. In this way, the frequency-filtered time-resolved photon correlations can be obtained bypassing the cascaded formalism of Section 1.2.1.2. On the other hand, if one is interested in, for instance, the *filtered* average occupation of the system, one would obtain zero as these quantities are directly proportional to the coupling strength, which is infinitesimal. These frequency-filtered observables are also of experimental interest. They are required to measure, e.g., the quantum state of the system, that I have defined with Zubizarreta Casalengua et al. (2017), where the unnormalized correlations are used to obtain the probability distribution that the excitations follow within the system. To avoid getting trivial results stemming from the vanishing coupling, we need to develop a new theory, which is one of the results presented in this Thesis. Namely, one needs to turn to the Gardiner and Parkins (1994)'s formalism of cascaded driving presented in Section 1.2.1.2, but upgrading it with the frequency degree of freedom. Although these two approaches to obtain the frequency-filtered correlations come from different perspectives, I will show in Chapter 2 that the two methods are completely equivalent, as far as the correlators are concerned, and the only distinction between them is a technical one: when using the formalism of cascaded driving, the population of the detector can grow arbitrarily, and thus the Hilbert space needs to be truncated adequately. Another qualitative distinction arises when one needs to consider not correlators but observables. The steady-state solutions of most quantum optical systems can be tackled using the master equation formalism that we introduced in Section 1.2.1 and using del Valle et al. (2012)'s theory of frequency-resolved photon-correlations to include the frequency degree of freedom. However, the results obtained in this way correspond to a statistical—or similarly a stochastic—average, and the observables correspond to what one would obtain when repeating the measurement enough times. However, looking at such types of averages blurs the information about the individual realizations, which we need to study, e.g., the temporal structure between photons with different frequencies. As it should be useful to go beyond mean values and get access to time series for a variety of purposes, one could turn to the Quantum Monte Carlo technique applied to color-resolved photons. Ceperley and Alder (1986) developed a quantum version of the classical method, and later on Mølmer, Castin, and Dalibard (1993) modified it to simulate the dynamics of a quantum object through the evolution of its wavefunction. In Chapter 2, I will indeed upgrade and apply the quantum-jump Monte Carlo technique to the case of filtered emission, that is to say, as applied to a stream of photons going through an interference (i.e., Lorentzian) filter. This can turn a simple system into a versatile, tunable quantum source, with applications such as sources with variable statistics, as demonstrated by Dory et al. (2017), or quantum spectroscopy in the schemes proposed by Mukamel and Dorfman (2015) and Kazimierczuk et al. (2015), or by myself, as I will discuss in detail in Chapter 7.

1.2.6 *Resonance Fluorescence & the Mollow triplet*

The concepts introduced above can be ideally illustrated with a particular case which is both simple and important, namely, resonance fluorescence. From a practical point of view, resonance fluorescence is the result of coherent excitation impinging onto a two-level system. Since the early works of Wu, Grove, and Ezekiel (1975), Kimble and Mandel (1976), Agarwal (1976), Kimble, Dagenais, and Mandel (1977), Apanasevich and Kilin (1977), Cohen-Tannoudji and Reynaud (1977), Groove, Wu, and Ezekial (1977), Jakeman et al. (1977), and Arnoldus and Nienhuis (1984), a large breadth of papers have been published studying various aspects of it. In fact, the literature is so large, and the topic so fundamental, that it has long been textbook material (cf. the book of Allen and Eberly (1987)). Using the master equation formalism introduced in Section 1.2.1, the equation governing the dynamics of a coherently driven two-

level system—which energy levels can be noted as $|g\rangle$ and $|e\rangle$ for its ground and excited states, respectively—with annihilation operator $\sigma = |g\rangle\langle e|$, is:

$$\partial_t \rho = i[\rho, H_\sigma] + \frac{\gamma_\sigma}{2}\mathcal{L}_\sigma \rho\,, \tag{1.44}$$

where γ_σ is the rate at which the two-level system emits photons spontaneously. The Hamiltonian H_σ in Eq. (1.44) is in the rotating frame, and is given by

$$H_\sigma = (\omega_\sigma - \omega_{\mathrm{L}})\sigma^\dagger\sigma + \Omega_\sigma(\sigma^\dagger + \sigma)\,, \tag{1.45}$$

where ω_σ is the natural frequency of the two-level system, which is driven by laser of frequency ω_{L} and intensity Ω_σ. In the steady-state, when the left-hand side of Eq. (1.44) is equal to zero, the observables of the two-level system become simple. For instance, its population is given by

$$n_\sigma = \frac{4\Omega_\sigma^2}{\gamma_\sigma^2 + 4\Delta_\sigma^2 + 8\Omega_\sigma^2}\,, \tag{1.46}$$

where $\Delta_\sigma = \omega_\sigma - \omega_{\mathrm{L}}$ is the detuning between the laser and the two-level system. Note that the population of the two-level system has an upper bound, 1/2, which means that the coherent excitation does not yield a population inversion in the two-level system. The upper limit is only reached when the laser and the two-level system are in resonance, and the rate at which the laser excites the two-level system is much larger than its decay rate: this induces Rabi oscillations in the two-level system, which average out as a mean population of 1/2.

Other observables vary depending on the strength of the driving as compared to the emission rate of the two-level system. When the driving is very weak, namely $\Omega_\sigma/\gamma_\sigma \ll 1$, which is also commonly referred to as the *Heitler (1944)* regime, the emission spectrum (given by Eq. (1.35) replacing the operator a by σ and assuming $\omega_\sigma = \omega_{\mathrm{L}} = 0$) becomes

$$S_\sigma(\omega) = (1 - K_2)\delta(\omega) + K_2\frac{1}{\pi}\frac{\gamma_\sigma/2}{(\gamma_\sigma/2)^2 + \omega^2}\,, \tag{1.47}$$

where $K_2 = 8\Omega_\sigma^2/\gamma_\sigma^2$ and δ is the Dirac delta function. The emission spectrum in Eq. (1.47) is simply the superposition of a delta peak centered at the frequency of the laser—originating from the photons that come from the laser and are elastically scattered by the two-level system—and a Lorentzian peak of width γ_σ—which stems from the luminescence (fluorescence) of the two-level system. The coexistence of these two contributions is the basis for our theory of a sub-natural linewidth single photon source, which I will discuss in detail in Chapter 3. Furthermore, the second-order correlation function of the photons, as defined in Eq. (1.33), has a simple form

$$g_\sigma^{(2)}(\tau) = \left(1 - e^{-\gamma_\sigma\tau/2}\right)^2\,, \tag{1.48}$$

Figure 1.13: Some of the pioneers of the theory of frequency-resolved photon correlations, in particular from resonance fluorescence. With their respective co-authors and over decades, they established the correct theory providing increasingly accurate descriptions of the correlations in the light emitted from the various peaks of the Mollow triplet.

which displays a perfect anticorrelation between photons emitted simultaneously.

The opposite regime, where the intensity of the laser is commensurable with the decay rate of the two-level system, brings us into the so-called *Mollow (1969)* regime. There, the emission spectrum is the celebrated Mollow triplet, shown in Fig. 1.14(a) and given by

$$S_\sigma(\omega) = \frac{1}{\pi}\frac{\gamma_\sigma^2}{\gamma_\sigma^2+8\Omega_\sigma^2}\delta(\omega) + \frac{1}{2\pi}\frac{\gamma_\sigma/2}{(\gamma_\sigma/2)^2+\omega^2} + \\ + \frac{1}{4\pi}\frac{3\gamma_\sigma/4}{(3\gamma_\sigma/4)^2+(\omega+\beta/4)^2}\left[\frac{8\Omega_\sigma^2-\gamma_\sigma^2}{8\Omega_\sigma^2+\gamma_\sigma^2} + \frac{\gamma_\sigma}{\beta}\frac{40\Omega_\sigma^2-\gamma_\sigma^2}{8\Omega_\sigma^2+\gamma_\sigma^2}\left(\omega+\frac{\beta}{4}\right)\right] + \\ + \frac{1}{4\pi}\frac{3\gamma_\sigma/4}{(3\gamma_\sigma/4)^2+(\omega-\beta/4)^2}\left[\frac{8\Omega_\sigma^2-\gamma_\sigma^2}{8\Omega_\sigma^2+\gamma_\sigma^2} + \frac{\gamma_\sigma}{\beta}\frac{40\Omega_\sigma^2-\gamma_\sigma^2}{8\Omega_\sigma^2+\gamma_\sigma^2}\left(\omega-\frac{\beta}{4}\right)\right], \quad (1.49)$$

where we have used the notation $\beta^2 = 64\Omega_\sigma^2 - \gamma_\sigma^2$. The spectrum is now composed of four terms: the first one is still the contribution from the elastically scattered photons, which yields a Dirac delta. The other three terms correspond to Lorentzians that form a triplet, which received the name of Mollow (1969), who was the first to find its correct analytical expression. The central peak of the triplet has a linewidth of γ_σ, while the two lateral peaks have a linewidth of $3\gamma_\sigma/2$. Moreover, the intensity of the central peak is twice the intensity of either lateral peak. This can be easily understood in terms of the dressed-atom picture proposed by Cohen-Tannoudji and Reynaud (1979), Reynaud (1983), and Dalibard and Reynaud (1983): In the limit $\Omega_\sigma \gg \gamma_\sigma$, the energy levels of the two-level system become dressed by the laser, thus forming an infinite ladder of excitation manifolds. Each manifold consists of a pair of states $|\pm\rangle$, formed by a superposition of the bare states $|g, n+1\rangle$ and $|e, n\rangle$, where "g" and "e" correspond to the "ground" and "excited" states of the two-level system. Then, both transitions $|+\rangle \to |+\rangle$ and $|-\rangle \to |-\rangle$ have the same energy and constitute the emission from the central peak. Similarly, the lateral peaks are the result from the transitions $|+\rangle \to |-\rangle$ and $|-\rangle \to |+\rangle$, respectively. This in shown in Fig. 1.15(c).

The second-order correlations reflect the Rabi oscillations induced by the laser, and become as follows:

$$g_\sigma^{(2)}(\tau) = 1 - e^{-3\gamma_\sigma\tau/4}\left[\cos\left(\frac{\beta\tau}{4}\right) + \frac{3\gamma_\sigma}{\beta}\sin\left(\frac{\beta\tau}{4}\right)\right]. \quad (1.50)$$

The photon correlation in the Heitler regime (1.48) is a particular case of Eq. (1.50), recovered in the limit $\Omega_\sigma \to 0$. These two cases are shown in Fig. 1.14(b). Note that the expression in Eq. (1.50) describes the correlations between photon pairs without specifying the frequency at which these photons are emitted. The Mollow triplet is, however, a perfect example where one would naturally inquire about the correlations between photons emitted from each of the

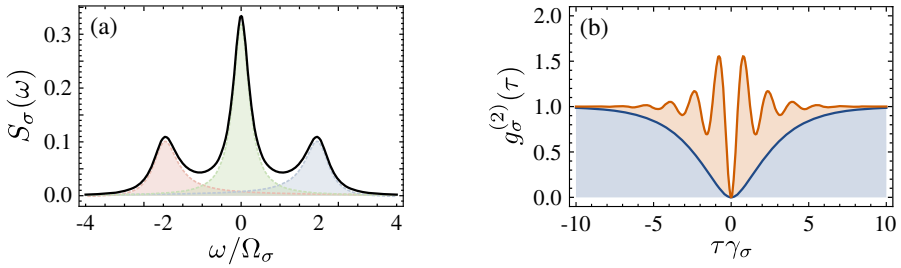

Figure 1.14: Properties of resonance fluorescence. (a) The emission spectrum of the two-level system in the Mollow regime, highlighting the contribution from each term of Eq. (1.49) with a different color. (b) Second-order correlation function of the emission from a two-level system in the Heitler regime (blue line, obtained in the limit $\Omega_\sigma \to 0$ and showing no oscillations) and from the Mollow triplet (orange line, obtained for $\Omega_\sigma = 2\gamma_\sigma$).

three peaks, as well as about the cross-correlations between photons emitted from different peaks. In fact, measuring frequency-resolved correlations from quantum systems has been pursued for almost three decades, starting with Apanasevich and Kilin (1977)'s theoretical prediction and Aspect et al. (1980)'s observation that the photons coming from the peaks of the Mollow triplet displayed strong correlations. However, despite the huge efforts of well renowned theoreticians, in particular from Cohen-Tannoudji and Reynaud (1979), Reynaud (1983), and Dalibard and Reynaud (1983), the description remained approximate, namely, it focused on the spectral peaks, which correspond to the real transitions—in the sense of transitions that arise between the dressed states of the Mollow triplet. Here lies the power of the theory developed by del Valle et al. (2012): since the frequency at which the detectors collect the light is completely free, it gives access to the full underlying structure of the quantum system, that is revealed when mapping correlations at all frequencies. We refer to this structure as the *two-photon spectrum* (2PS). Already with the most fundamental quantum object—a two-level system—González-Tudela et al. (2013) showed that the emitted photons are strongly correlated when the frequency is taken into account, and further Sánchez Muñoz et al. (2014b) demonstrated that such correlations violate Cauchy-Schwarz inequalities. The 2PS of the two-level system driven incoherently is fairly simple, as shown in Fig. 1.15(a): The autocorrelation of the photons emitted at the same frequency, which lie on the principal diagonal of the figure, tend to be bunched (approaching $g^{(2)}_\Gamma \to 2$ in the limit $\Gamma \to 0$) and the intensity of the bunching increases as the frequency gets farther away from the central frequency of the emission. González-Tudela et al. (2013) explained how this is the result of the photon indistinguishability, rather than from

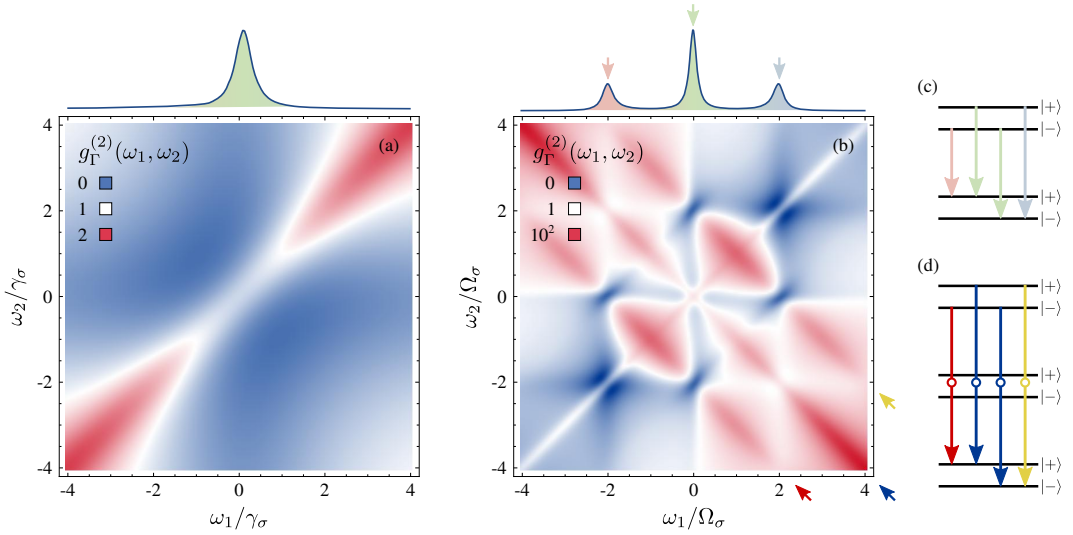

Figure 1.15: Spectral lineshape and two-photon spectrum (2PS, density plots) of a two-level system, showing the correlations between photon pairs with all the combination of frequencies. (a) The incoherently driven two-level system emits photons with a Lorentzian profile, and the 2PS has a simple structure: pairs of photons with the same frequency, located on the diagonal of the density plot, display higher values (even bunching) due to their indistinguishability. (b) The Mollow triplet (spectral lineshape) has a richer structure in its two-photon spectrum, that rises from all the different transitions between manifolds on the ladder of dressed states (right). The one- and two-photon transitions in the ladder are indicated by arrows of corresponding colors. Of particular interest, the two-photon "leapfrog processes" indicated by the red, blue and yellow arrows give rise to strong bunching antidiagonals. In both cases the linewidth of the filter is set to $\Gamma = \gamma_\sigma$. The results in (a) are obtained with an incoherent driving rate $P_\sigma = \gamma_\sigma$, whereas the results in (b) are obtained by driving the 2LS resonantly with the laser pumping rate $\Omega_\sigma = 5\gamma_\sigma$. The Rabi frequency, Ω_+ (which in the case $\omega_\sigma = \omega_L$ is equal to $2\Omega_\sigma$), gives the splitting in each manifold and correspondingly, the position of the side peaks of the Mollow triplet. The energy of one laser-photon, ω_L, is taken as a reference for the variables.

any internal structure of the system, which means that it is present in every 2PS. Outside of the diagonal, the cross-correlations display the expected antibunching (due to the fermionic character of the two-level system), passing through uncorrelated emission in the transition to the indistinguishability bunching. Changing the excitation to a coherent source with enough strength to reach the Mollow (1969) triplet regime, we observe a richer structure blossom, shown in Fig. 1.15(b): in this case, the indistinguishability bunching is overcome by the strong correlations resulting from photon pairs which emission is aided by a virtual transition that "jumps over" one manifold of excitation (one pair of energy levels, labelled as $|\pm\rangle$), as the ones shown in red, blue and yellow arrows on Fig. 1.15(d). The photons emitted through these virtual processes satisfy the equation

$$\tilde{\omega}_1 + \tilde{\omega}_2 = 2\lambda\Omega_\sigma \qquad \text{for} \qquad \lambda = \{-1, 0, 1\}\,, \tag{1.51}$$

where $\tilde{\omega}_i = (\omega_i - \omega_L)$, and they are highly correlated, as shown by the deep red lines on the antidiagonals marked by the red ($\lambda = -1$), blue ($\lambda = 0$) and yellow ($\lambda = 1$) arrows in the density plot of Fig. 1.15(b). In a process akin to purification, the price to pay for enhancing these correlations is the reduction of the emission rate of the photons satisfying Eq. (1.51), with the exception of the photons emitted in resonance to the two-level system. This places the Mollow triplet—one of the most fundamental yet richest quantum systems—as a versatile source of quantum light, able to provide photons with statistics ranging from perfectly sub-Poissonian (that is, with $g_a^{(2)}(0) = 0$) to super-Poissonian (with $g_a^{(2)}(0) \gg 2$) passing from the statistics of a coherent source (for which $g_a^{(2)} = 1$ regardless of time). The following chapters are devoted to using this versatility to excite other quantum systems.

1.3 SOURCES & TARGETS

This Thesis is about Exciting with Quantum Light. At such it requires to worry about the Exciting source on the one hand and about the Excited target on the other hand. One natural question is whether it is advantageous to excite objects with the emission of quantum sources instead of classical ones. This problem is as important as it is fundamental, as it would require to revisit every regime of excitation that has been considered with classical light—like the incoherent light emitted by a thermal reservoir or the coherent light emitted by a laser—applied to an even larger range of optical targets. Since using every possible quantum source and looking at its effect on every possible system is impractical, we will focus on the most fundamental cases. Namely, for the source of quantum light, we will consider the emission of a two-level system, itself being driven into the Mollow (1969) regime. The different types of correlations in the various frequency windows introduced above and further discussed in Chapter 4, will make this fundamental case largely sufficient on its own to investigate these questions at a fundamental level. Even variations, introduced below, arise as particular cases or straightforward extensions. For the targets of the quantum excitation, we will first consider the most simple yet fundamental objects: a bosonic and a fermionic field, as well as the result of their strong coupling.

1.3.1 *Single and Multi-photon sources*

At this stage of technology, quantum light is foremost the one provided by single-photon sources. In fact, their long coherence time and lightweight make photons very appealing to implement logical quantum gates, which would then lead to the development of an universal quantum computer. However, to get to that point it is paramount to be able to generate and manipulate arbitrary quantum states of light, and the first step is the generation of the one-photon Fock state $|1\rangle$. Dynamically, this implies that we need a source of light with a long list of properties. Among them, one would like that the probability that the source emits more than one photon at any given time is zero (which implies a complete suppression of the second-order correlation function, given in Eq. (1.33)), that any two photons emitted by the source are indistinguishable

(which can be measured in a Hong, Ou, and Mandel (1987) experiment), and that the emission takes place in a periodic way. While computing these quantities is straightforward, one should take into account the consideration about detection discussed previously: the properties of the emitted photons only become real when they are observed, either by a detector or by another quantum object. Thus, the correlation between photons, their indistinguishability and all other properties related to the temporal structure of the emission, need to be considered in the light of the Theory of frequency-filtered and time-resolved correlations of del Valle et al. (2012). In Chapter 3, I will discuss in detail how indeed the photon correlations observed by an object with a finite temporal or spectral resolution are affected.

The next step towards the realization of arbitrary states of light is the implementation of sources able to generate Fock states of N photons. For instance one needs such an N-photon source to test for quantum supremacy and performing experiments similar to the Boson Sampling, proposed by Aaronson and Arkhipov (2011) and later measured with few photons by Broome et al. (2013), Crespi et al. (2013), Spring et al. (2013), Tillmann et al. (2013), and Loredo et al. (2017). In a laboratory, a source of N photons can be built from single-photon sources, using techniques such as multiplexing: a stream of single photons—emitted, for instance, by a nonlinear crystal through spontaneous parametric downconversion or by a two-level system driven with pulsed laser—is made to enter an optical circuit to collect the individual photons and keep them organized in time. Pittman, Jacobs, and Franson (2002) first introduced this technique to generate a source of single photons on "pseudodemand", and later Kaneda et al. (2015) demonstrated that the technique could be used to obtain a source of heralded single photons. Increasing the number of photons, however, also increases its complexity, and generating a source of N photons becomes a tedious task. Conversely, one can turn to more exotic sources that provide a large but fixed number of photons without requiring any special optical technique. Sánchez Muñoz et al. (2014a) showed that the emission from a two-level system driven in the Mollow triplet regime can provide such an N-photon source, sketched in Fig. 1.16, at an elementary—and therefore robust—level. Keeping the dressed-atom picture in mind, in which the energy levels of the driven two-level system are given by an infinite ladder of excitations (cf. Fig. 1.15), and strongly coupling a cavity in resonance to the N-photon transition, jumping over $N-1$ intermediate manifolds of excitation, one finds that the emission of the cavity consists predominantly of bundles of N photons.

In chapter 4, I will build on the source of N-photon bundles and study the ways in which the emission can be obtained in a more general way. Considering the correlations between single photons at frequency ω_1 and bundles of photons with frequency ω_2, and looking for the pair of frequencies for which the zero-delay correlations are the strongest, will put the foundation for a new class of heralded N-photon sources.

1.3.2 *Bosons, Fermions and Polaritons*

After discussing the sources of quantum light and how their properties vary when the observer of light has a finite temporal and spectral resolution, we will move on to study the effects

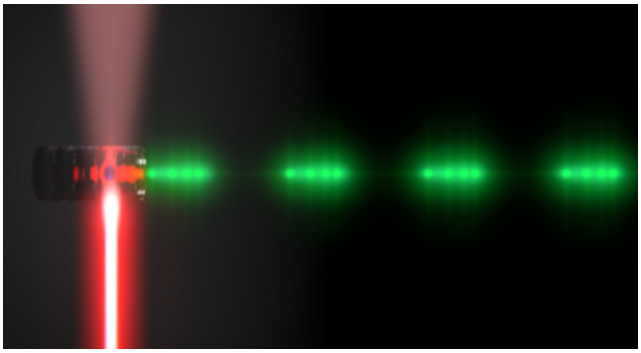

Figure 1.16: Artistic representation of the N-photon emitter proposed by Sánchez Muñoz et al. (2014a). The light of a laser is sent onto a quantum dot embedded in a microcavity. When the frequency of the cavity is detuned the right amount from the quantum dot, the emission of the system is given by bundles of N photons (in this case $N = 4$).

on optical targets. In Chapter 5, I will focus on the bosonic targets, modelled as a harmonic oscillator, and in Chapter 6, I will tackle the excitation of a fermionic target, modelled as a two-level system. In Chapter 8, I will change the source of the quantum excitation from the Mollow triplet to the source of N-photon bundles of Sánchez Muñoz et al. (2014a) and to a two-level system operating in a regime of pulsed excitation. I will use the emission of these two sources, and study their effect on both a bosonic and a fermionic field, thus becoming the counterparts of Chapters 5 and 6. The bosonic and fermionic targets being so fundamental, they need little more introduction. Maybe the next optical target to consider in terms of how fundamental it is, after bosons and fermions, would be the so-called polaritons, which are a quantum superposition of boson with i) fermions (Jaynes-Cummings physics) or ii) weakly interacting bosons. The latter case will play an important part in this Thesis following my collaboration with one of the leading experimental groups working with these objects, which has pioneered some studies of exciting polaritons with quantum light following my (López Carreño et al. (2015)) theoretical proposal in that direction.

The first experimental observation of polaritons was made by Weisbuch et al. (1992) with a cavity containing seven quantum wells (although the best observation was obtained using only five of them), displaying an anticrossing, commonly referred to as *Rabi splitting*, by shifting the energy of the driving laser. In the observation, it was clear that the energies at which the light was emitted from the microcavity were not those of the bare cavity nor the bare excitons, but rather at two different frequencies, which are now referred to as the *lower* and *upper polariton branches*. A typical dispersion relation from a polariton system is shown in Fig. 1.17: panel (a) shows the real image as observed in the laboratory, with the bright regions indicating the emission of light; panel (b) shows the breakdown of the energies that play a role in the figure, with the bare modes (the energy of the photonic mode and of the excitons) in dashed lines, and the polariton branches in solid lines. The energy difference between the upper and lower polariton branches at normal incidence ($k = 0$), shown in panel (b) as $\hbar g$ is given by the strength of the Rabi coupling, i.e., the energy with which the photons and the excitons are bounded. Theoretically, polaritons can be seen simply as coupled oscillators when exciting a single mode or as coupled fields when involving a significant spread in momentum space. They have enjoyed a considerable activity due to their strong interactions at high densities, in which case they opened new directions in fundamental aspects of condensed-matter optics including Bose-Einstein condensation, superfluidity and even superconductivity. For a more

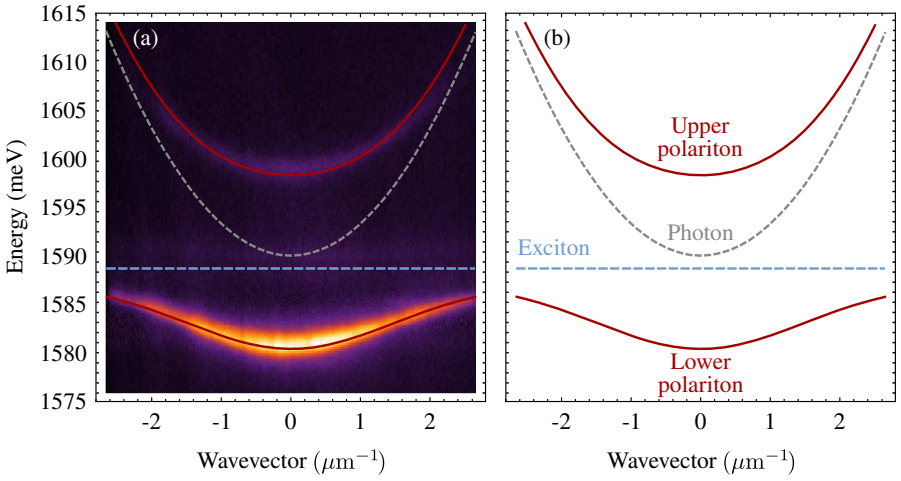

Figure 1.17: A typical polariton dispersion. (a) Luminescence spectrum in momentum space, as observed experimentally, with the bright regions corresponding to zones where light is emitted. (b) Dispersion relation as obtained from the Hamiltonian describing the polaritons. For the experimental image the Rabi splitting was $\hbar g = 8.7$ meV.

detailed coverage, I refer to Kavokin et al. (2017)'s textbook on the topic. While the upper and lower polariton branches have the same relevance in terms of energy, the upper branch suffers much more from dephasing, which reduces the lifetime of the upper polaritons. This has been studied in great details by Dominici et al. (2014), in a paper where I contributed a quantum optical theory of polaritons using the formalism introduced previously. Therefore, most of the experiments related to polaritons are performed using the light emitted from the lower polariton branch. In Chapter 7, I will use the Mollow triplet and the versatility of the statistics from the light emitted at various frequency regions of the triplet to propose an implementation of quantum spectroscopy to tackle the most important question of this field (such as determining the strength of the polariton-polariton interaction).

1.4 SUMMARY OF THE CONTENTS & PUBLISHED PAPERS

In summary, the rest of the Thesis is organized as follows:

- In chapter 2, I will discuss the results of López Carreño, del Valle, and Laussy (2018), in which I put together the formalism of Cascaded systems, developed by Gardiner (1993) and Carmichael (1993b), and the Theory of Frequency-Filtered and Time-Resolved Correlations, developed by del Valle et al. (2012). Thus, I adapt the Quantum Monte Carlo algorithm of Mølmer, Castin, and Dalibard (1993) and Mølmer and Castin (1996) to include the effect of the detection on the statistics of the photons emitted by quantum systems.

- In chapter 3, I will discuss the results of López Carreño et al. (2016a), López Carreño et al. (2018), and López Carreño et al. (2019), in which I consider the sources of single photons in the context of frequency-resolved correlations. Given that the photon antibunching is spoiled when the process of observation is taken into account, I will consider several criteria to rank sources of light, according to how well they maintain their single-photon character after the emission is observed.

- In chapter 4, I will discuss the results of López Carreño, del Valle, and Laussy (2017), in which I turn to sources of N photons following the steps of Sánchez Muñoz et al. (2014a). Using the emission from resonance fluorescence when it is filtered at the adequate frequencies, I will propose a mechanism that allows us to develop a source in which the emission of a bundle of N photons is heralded by a single photon at another frequency.

In chapters 5–7, I will use the light emitted from a two-level system driven itself in the so-called Mollow (1969) regime, which González-Tudela et al. (2013) have found to have a rich structure in its temporal correlations. I will take advantage of this structure to broaden the limits of the quantum states that can be reached by three types of systems:

- In chapter 5, I will discuss the results from López Carreño and Laussy (2016), where I consider the excitation of a harmonics oscillator, which could be interpreted as photons, polaritons or even plasmons. Studying the excitation of the harmonic oscillator, I will chart the regions of the Hilbert space that are accessible only through the excitation with Quantum Light. In particular, I will disprove the commonly-used criterion, $g^{(2)} < 1/2$, to identify single photon sources, showing that there is a myriad of states of the harmonic oscillator that satisfy such a criterion while having an average occupation larger than one.

- In chapter 6, I will discuss the results from López Carreño et al. (2016b), where I consider the excitation of the other fundamental type of particles: Fermions. As an archetype of it, I will study the excitation of a two-level system, which can be realized in a large variety of physical systems, including cold atoms, ions, semiconductor quantum dots, superconducting qubits, among others.

- In chapter 7, I will first discuss the results from López Carreño et al. (2015), where a system of exciton-polaritons is probed by the Mollow triplet, and show as an implementation of quantum spectroscopy how one can extract the polariton-polariton interaction strength. Then, I will discuss the results from Cuevas et al. (2018), in which we used a pair of entangled photons to excite a system of exciton-polaritons. These results were obtained by the laboratory of Dr. Daniele Sanvitto at the CNR-NANOTEC institute in Lecce, and provided the first hard evidence of the quantization of the polariton field, as well as the observation of the effect of the the polariton-polariton interaction at the single-particle level.
- In chapter 8, I change the source of Quantum Light, and instead of a two-level system, I consider the emitter of N-photon bundles proposed by Sánchez Muñoz et al. (2014a).
- In chapter 9, I give an overview of the main results of this Thesis, draw some general conclusions and provide some perspectives, with a succinct description of follow-up works currently in progress.

These results gave rise to the following publications:

1. Ultrafast Control and Rabi Oscillations of Polaritons
   L. Dominici, D. Colas, J. P. Restrepo Cuartas, M. de Giorgi, D. Ballarini, G. Guirales, **J. C. López Carreño**, A. Bramati, G. Gigli, E. del Valle, F. P. Laussy & D. Sanvitto,
   Physical Review Letters **113**, 226401 (2014)

2. Exciting Polaritons with Quantum Light
   J. C. López Carreño, C. Sánchez Muñoz, D. Sanvitto, E. del Valle & F. P. Laussy
   Physical Review Letters **115**, 196402 (2015)
   Selected as "Editor's Suggestion"

3. Excitation with quantum light. I. Exciting a harmonic oscillator
   J. C. López Carreño & F. P. Laussy
   Physical Review A **94**, 063825 (2016)
   Featured in *Physics*

4. Excitation with quantum light. II. Exciting a two-level system
   J. C. López Carreño, C. Sánchez Muñoz, E. del Valle & F. P. Laussy
   Physical Review A **94**, 063826 (2016)
   Featured in *Physics*

5. Criterion for Single Photon Sources
   J. C. López Carreño, E. Zubizarreta Casalengua, E. del Valle & F. P. Laussy
   ArXiv:1610.06126 (2016)

6. Structure of the harmonic oscillator in the space of n-particle Glauber correlators
   E. Zubizarreta Casalengua, **J. C. López Carreño**, E. del Valle & F. P. Laussy
   Journal of Mathematical Physics **58**, 062109 (2017)

7. Photon Correlations from the Mollow Triplet
   J. C. López Carreño, E. del Valle & F. P. Laussy
   Laser and Photonics Reviews **11**, 1700090 (2017)

8. First observation of the quantized exciton-polariton field and effect of interactions on a single polariton
   Á. Cuevas, **J. C. López Carreño**, B. Silva, M. de Giorgi, C. Sánchez Muñoz, A. Fieramosca, D. G. Suárez Forero, F. Cardano, L. Marrucci, V. Tasco, G. Biasiol, E. del Valle, L. Dominici, D. Ballarini, P. Mataloni, F. P. Laussy, F. Sciarrino & D. Sanvitto
   Science Advances **4**, eaao6814 (2018)

9. Frequency-resolved Monte Carlo
J. C. López Carreño, E. del Valle & F. P. Laussy
Scientific Reports **8**, 6975 (2018)

10. Joint subnatural-linewidth and single-photon emission from resonance fluorescence
J. C. López Carreño, E. Zubizarreta Casalengua, F. P. Laussy & E. del Valle
Quantum Science and Technology **3**, 045001 (2018)

11. Impact of detuning and dephasing on a laser-corrected subnatural-linewidth single-photon source
J. C. López Carreño, E. Zubizarreta Casalengua, F. P. Laussy & E. del Valle
Journal of Physics B: Atomic, Molecular and Optical Physics **52**, 035504 (2019)

12. Quasichiral interactions between Quantum Emitters at the Nanoscale
C. A. Downning, **J. C. López Carreño**, F. P. Laussy, E. del Valle & A. I. Fernández-Domínguez
Physical Review Letters **122**, 057401 (2019)

2

FREQUENCY-RESOLVED MONTE CARLO

Wiener wrote in his autobiography that he had ideas similar to the ones I later proposed as the Monte Carlo method. He says vaguely that he found no response when he talked to someone and so dropped the matter.

— Stanisław Ulam
Adventures of a Mathematician

2.1 CLASSICAL MONTE CARLO

Ulam (1991) wrote in his autobiography on the genesis of the technique at the core of this chapter:

> The idea for what was later called the Monte Carlo method occurred to me when I was playing solitaire during my illness. I noticed that it may be much more practical to get an idea of the probability of the successful outcome of a solitaire game (like Canfield or some other where the skill of the player is not important) by laying down the cards, or experimenting with the process and merely noticing what proportion comes out successfully, rather than to try to compute all the combinatorial possibilities which are an exponentially increasing number so great that, except in very elementary cases, there is no way to estimate it. This is intellectually surprising, and if not exactly humiliating, it gives one a feeling of modesty about the limits of rational or traditional thinking. In a sufficiently complicated problem, actual sampling is better than an examination of all the chains of possibilities.

Since then, the Monte Carlo method has been used in a large variety of topics to tackle diverse problems. For instance, Rogers (2006) has reviewed the role that the method has had in the research on medical physics, such as the impact that radiation has on tissues. The academic efforts in this topic led to the development of the software *GEANT4*, that allows the simulation of the passage of particles through matter and which is routinely used at CERN to test the performance of gamma- and X-ray detectors. Badano and Kanicki (2001) and Mesta et al. (2013) have used the Monte Carlo method to analyze the structure of organic materials to make them work as light-emitting diodes. Furthermore, Glasserman (1994) has laid the prospects that the Monte Carlo method has in finance, such as the analysis and prediction of financial time series, which is particularly relevant for the stock markets. While the list of applications could go on for pages, I now focus to the Quantum Monte Carlo methods, which I will show have the potential to describe a large breadth of quantum optical problems.

2.2 QUANTUM MONTE CARLO

If there is a field of Science that involves "exponentially growing numbers" that can only be accessed through "sampling", this is indeed quantum physics. The computational complexity, also combinatorial in nature (everything can happen), is at the core of the theory. Furthermore, sampling is inescapable in the real world, where one can only perform a finite amount of measurements (or observations) that will turn the deterministic but abstract wavefunction into a probability distribution function, of which the end user only gets one result at a time. Theorists have the luxury to access perfect averages, but these are derived quantities, which can be misleading (the average position of the first excited state of a particle bound in a symmetric

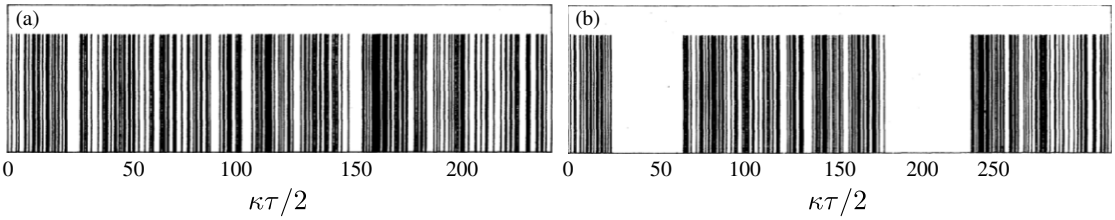

Figure 2.1: The way in which an atomic system emits its photons can be modified by the presence of a metastable energy level. In the panels, the emission of a photon is indicated by a vertical line. The two panels show the emission in absence (a) and in presence (b) of a metastable state. In the latter, one can clearly identify the temporal regions where the emission of light (and lack of it) alternate. This is captured by a Monte Carlo simulation in a way that is not straightforward from standard quantum mechanical averages. This figure is an adaptation from Zoller, Marte, and Walls (1987).

potential is at a point where it is never to be found). In fact, it can be enlightening for theorists to get closer to the experimental reality by striving to access single realizations as well, out of which to compute derived quantities, such as observables.

Ceperley and Alder (1986) showed that the Quantum Monte Carlo technique has ramifications in several fields related to quantum physics. In the context of interest in this Thesis, that of quantum optics, several methods have been developed in the early 90s (Plenio and Knight (1998) have written a detailed review). Of these, the quantum jump approach, developed in the late 80s by Zoller, Marte, and Walls (1987) and Carmichael et al. (1989) and simplified further in the mid 90s by Dalibard, Castin, and Mølmer (1992) and Mølmer and Castin (1996), is particularly appealing as it links the wavefunction collapse to the emission of a photon. Assuming an ideal detector that covers the full 4π solid angle surrounding the emitter, this allows to perform a computer experiment of photo-detections. The need for such sampling techniques was indeed chiefly motivated by going beyond averages, namely, in the so-called intermittency problem (that describes the switching on and off of the emission of a lambda system driven coherently), where the system remains for long periods of time in unstable regions, which are concealed by the averaging, as shown in Fig. 2.1. From such "clicks" (as we will call a detected photon), one can for instance compute the Glauber correlation functions $g^{(n)}$, introduced in Eq. (1.32), but one can also compute less easily accessible quantities such as exclusive probability densities, e.g., detecting the next photon at a time τ after one detection, with no other photon in between ($g^{(2)}$ assumes any photon rather than the next one), or distributions of time delays between nearest neighbours, probabilities to detect any given number or even configuration of photons in a time window, or any other type of binning "experiment".

2.2.1 *Formalism*

We will focus on the Quantum Monte Carlo algorithm, outlined by Mølmer, Castin, and Dalibard (1993), to simulate the dynamics of an open quantum system. This method allows to observe individual quantum trajectories that the system undergoes, and which are washed out by the master equation, as the latter gives the stochastic average of many such individual trajectories. Furthermore, this technique provides the evolution of a wavefunction—rather than a density matrix, as required by a description through the master equation (1.20)—which is particularly useful, and computationally preferable, when the Hilbert space of the quantum system is very large.

Given that the quantum system is governed by the interplay between a Hamiltonian H and dissipative processes—which are associated to jump operators L_k defined in Eqs. (1.20-1.21)—the implementation of the method demands to define a non-Hermitian Hamiltonian as

$$\tilde{H} = H - \frac{i}{2}\sum_k L_k^\dagger L_k\,, \tag{2.1}$$

which rules the deterministic dynamics of the wavefunction. Then, the task is to obtain the state of the system at a time $t + \delta t$, given that we know the state of the system at a previous time t. The probability that during the interval of time between t and $t + \delta t$ the system undergoes a quantum jump, induced by the operator L_k, is given by

$$p_k = \delta t \, \langle \psi(t) | \, L_k^\dagger L_k \, | \psi(t) \rangle \, , \tag{2.2}$$

where $|\psi(t)\rangle$ is the state of the system at time t. Afterwards, we draw as many random numbers r_k (between zero and one) as there are quantum jump operators, and compare them with the probabilities p_k computed in Eq. (2.2). If we find that $r_k < p_k$ for some k, the system makes a quantum jump and the state of the system becomes

$$|\psi(t + \delta t)\rangle = \frac{L_k \, |\psi(t)\rangle}{\langle \psi(t) | \, L_k^\dagger L_k \, | \psi(t) \rangle} \, . \tag{2.3}$$

In case there are more than one k for which $r_k - p_k < 0$, we have to design a strategy to select the operator that makes the jump. For instance, one can select the operator for which the difference $p_k - r_k$ is the largest. If, on the other hand, we find that $r_k > p_k$ for all k, there is no quantum jump and the state of the system evolves as

$$|\psi(t + \delta t)\rangle = \frac{\exp(i \tilde{H} \delta t) \, |\psi(t)\rangle}{\langle \psi(t) | \exp(i \tilde{H}^\dagger \delta t) \exp(i \tilde{H} \delta t) \, |\psi(t)\rangle} \, . \tag{2.4}$$

The choice of the time step δt for the simulations needs to be taken in such a way that: i) the probabilities in Eq. (2.2) are always well below one, and ii) the physical observables are converged (which can be verified using other numerical methods, or simply decreasing δt). In fact, Mølmer, Castin, and Dalibard (1993) showed that the method outlined above is completely equivalent to solving the master equation, given that we take averages over many realizations and in the limit in which the time step is sufficiently small, i.e., in the limit $\delta t \to 0$.

2.2.2 *Incoherently driven two-level system*

We will first illustrate the technique on a two-level system, with annihilation operator σ, which is the simplest system in quantum physics and one of great relevance in this Thesis. Starting with the free Hamiltonian

$$H_\sigma = \omega_\sigma \sigma^\dagger \sigma \, , \tag{2.5}$$

for a two-level system with free energy ω_σ, and Liouvillian

$$\partial_t \rho = i[\rho, H_\sigma] + \frac{\gamma_\sigma}{2} \mathcal{L}_\sigma \rho + \frac{P_\sigma}{2} \mathcal{L}_{\sigma^\dagger} \rho \, , \tag{2.6}$$

describing the incoherent driving at a rate P_σ and an inverse lifetime of the two-level system γ_σ, one finds from standard quantum optical techniques that the steady state emission rate and second-order correlation function are simple quantities, namely

$$n_\sigma = \frac{P_\sigma}{\gamma_\sigma + P_\sigma} \, , \qquad I = \gamma_\sigma n_\sigma = \frac{\gamma_\sigma P_\sigma}{\gamma_\sigma + P_\sigma} \qquad \text{and} \qquad g^{(2)}(\tau) = 1 - \exp[-(\gamma_\sigma + P_\sigma)\tau] \, , \tag{2.7}$$

which predicts, in particular, that the two-level system displays perfect antibunching at zero delay, namely $g^{(2)}(0) = 0$. A Monte Carlo simulation, using the technique explained in Section 2.2.1, is shown in Fig. 2.2. The upper panel shows the fluctuations in the detection times of a million photons from such a source. As such, this realizes a random walk, similar to a random (Poissonian) process, and at large timescales there is nothing noticeable. On the short timescale, however, one can observe clear correlations of antibunching, as shown in the series of clicks indicated by blue ticks in Fig. 2.2(c). Namely, photons tend to repel each other and

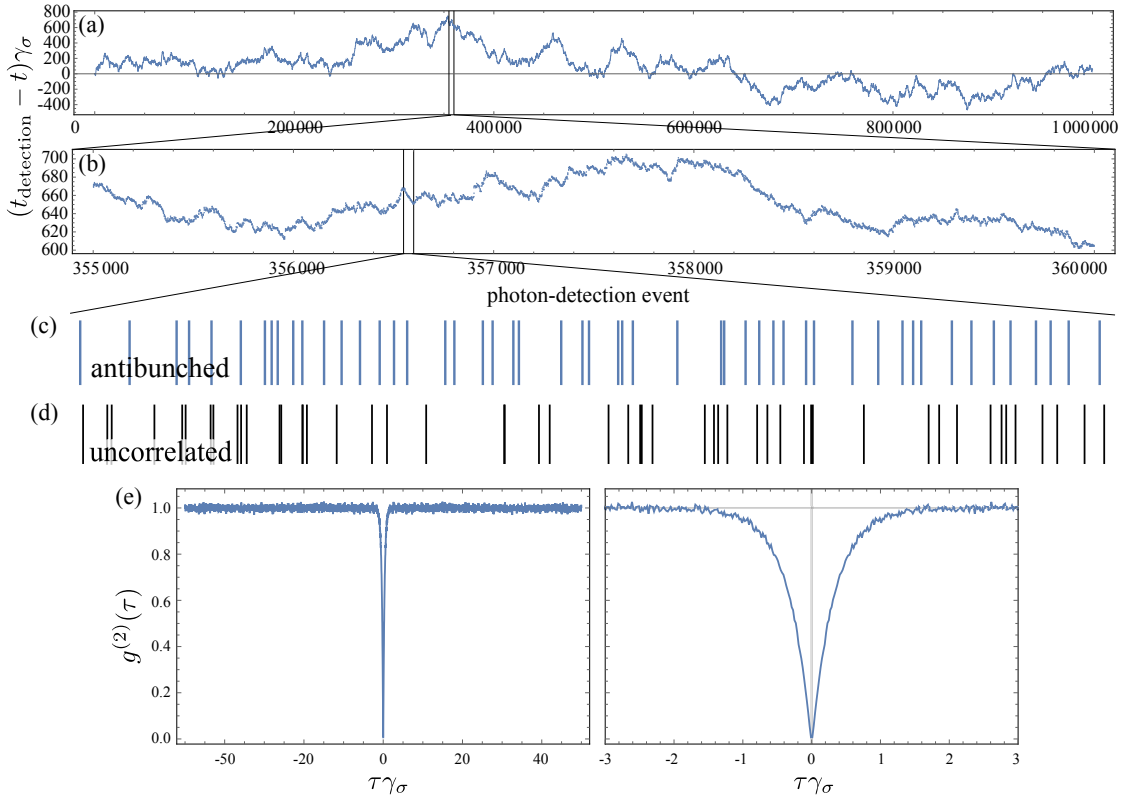

Figure 2.2: Monte Carlo method on a two-level system. (a) Times of emission for 1 000 000 recorded photons as compared to their mean emission rate, exhibiting a classical random walk. (b) Zoom of (a) in the highlighted window. (c) Zoom of (b) in the highlighted window, with detected photons now displayed in absolute time rather than relatively to their mean emission time. Locally, one can observe a structure in their statistical distribution, with a tendency of ordering and mutual repulsion. This becomes obvious when comparing with uncorrelated photons with the same emission rate, shown in (d). The latter exhibit Poisson bursts. (e) Intensity correlations $g^{(2)}(\tau)$ computed from the one million points, in two timescales, featuring a clear antibunching. The inverse lifetime of the two-level system sets the time unit.

appear more orderly than if they would be uncorrelated, as is the case of the second series of photon detections, shown for comparison with black ticks in Fig. 2.2(d). The uncorrelated series exhibits the counter-intuitive "Poisson clumping" or "Poisson burst" effect, which was made famous by von Bortkiewicz's horse kicking casualties in the Prussian army and still of recurrent appearance in the media as intuition repels the notion that a burst of accidents in, say, a hospital, is a natural random process rather than negligence. The strongly-correlated character of the two-level system emission becomes clear and compelling when computing intensity correlations $g^{(2)}(\tau)$ from the clicks, defined as the density of probability of finding two photons with a time difference τ. Specifically, from the times of detection t_i, we compute $t_i - t_j$ for all $1 \leq i \leq N$ with N the total number of detected photons (here $N = 10^6$) and compare the density of time differences to that from uncorrelated clicks with the same intensity. Note that in a typical experiment, a first photon starts a timer and a second stops it, and a distribution of the time difference between successive photons is used as a good approximation. In our case, we compute the exact correlations by collecting all the time differences within the correlation window of interest. This is shown for $|\tau| \leq 50/\gamma_\sigma$ in Fig. 2.2(e), left. One sees an overall plateau, indicating that photons have the same distribution for long-time separations as if they were emitted by a Poisson process (randomly). But one also observes a clear dip at $\tau \approx 0$, indicating that at such close distances, photons behave very differently than uncorrelated ones, namely, the occurrence of small time delays is strongly suppressed. This is better resolved in Fig. 2.2(e), right. Such a behaviour defines antibunching, $g^{(2)}(0) < g^{(2)}(\tau)$, with coincidences, i.e.,

simultaneous detection of two photons, less likely to occur than other closely spaced detections, with perfect suppression of coincidences when $g^{(2)}(0) = 0$. Since these correlations wash out at long times, one has $\lim_{\tau\to\infty} g^{(2)}(\tau) = 1$. The time it takes to reach this plateau is the second-order coherence time. We do not need to overlap these results of the Monte Carlo signal with the theory curve, Eq. (2.7), since, with one million points, it is exact to within the plot accuracy. Beside the statistical noise, that starts to be apparent for $\tau > 1/(2\gamma_\sigma)$, the Monte Carlo data provides a smooth curve in the window of strong correlations. In our simulation, the Δt was $0.01/\gamma_\sigma$ and the binning size was taken twice as large, corresponding to the two closely-spaced vertical lines on the right panel of Fig. 2.2(e), bounding $g^{(2)}(0)$ from below due to this small uncertainty. With a binning size equal to the Monte Carlo timestep, one recovers the perfect antibunching at the origin, although on two grid points, so also producing a small error (the result would be perfect only in the limit of vanishing timesteps).

2.3 IMPACT OF FREQUENCY-FILTERING

These results provide the background for our approach in the filtered signal. We now turn to the question of what happens to the emitted photons if a filter is interposed on their way to the detector? This does not simply subtract a fraction, it also redistributes those that make it through, to provide them with possibly very different statistical properties, as we now discuss in more details.

While the quantum Monte Carlo method has been amply used to compute the power spectrum as well as time-series of photon emission (see the works of Dum et al. (1992), Marte et al. (1993), Mølmer, Castin, and Dalibard (1993), Garraway, Kim, and Knight (1995), Hegerfeldt and Plenio (1996), Plenio (1996), and Schack, Brun, and Percival (1996)), its combined use for both time *and* energy-resolved photons has, to the best of my knowledge, not been provided before in both a practical and exact form. The first attempt in this direction was made by Tian and Carmichael (1992), who considered the behaviour of an optical cavity containing one atom. The cavity energy is resonant to a transition of the atom, so that the description of the dynamics can be done through the Jaynes-Cummings model. Although the cavity could be thought as a filter for the emission of the atom, the coupling between the two objects is not weak enough and one can see the presence of the cavity in the observables of the atom, e.g., the emission spectrum, where lateral peaks (albeit weak) appear on both sides of the Mollow triplet. Also in the early 90s, Carmichael (1993a) considered the Monte Carlo approach within the context of the cascaded formalism, but without connecting it to frequency-resolved correlations. Recently, Sánchez Muñoz et al. (2014b) implemented a Monte Carlo simulation that attempted to take into account the effect that frequency-filtering has on the temporal structure of the photons emitted by the Mollow (1969) triplet. Not only were they interested in the emission from the peaks of the triplet, but also from the frequencies in between, at which Sánchez Muñoz et al. (2014a) predicted an emission of photon pairs. Indeed, the discovery of *leapfrog* emission in general and how these could be further exploited to yield a new type of quantum light, called for further investigations at the Monte Carlo level. In particular, even without frequency filtering, Monte Carlo simulations were central in Sánchez Muñoz et al. (2014a)'s analysis of the purity. In Sánchez Muñoz et al. (2018)'s analysis of bundling with frequency filtering, the lack of an exact Monte Carlo technique prevented them to bring the bundle emission at the same level of scrutiny as in their previous work. I will discuss next the limitations of their approach and, more generally, how to implement an exact and efficient Monte Carlo simulation with frequency-resolution. The technique consists in adapting the Monte Carlo technique to the cascaded formalism. The proof of validity is obtained by showing that the clicks thus generated reproduce the correlations predicted by del Valle et al. (2012)'s theory of frequency-resolved photon correlations. We will apply this technique to the driven two-level system, under both coherent and incoherent emission, at low and large pumping. We will consider both the cases of autocorrelations and cross-correlations. Of course, the same principles could be extended to more than two detectors.

2.3.1 *Formalism*

Sánchez Muñoz et al. (2014b)'s attempt at generating a frequency-resolved Monte Carlo was insightful and provided an excellent first look at this problem. It consisted in placing the cavity at resonance with the sought-after frequency (in particular, at the two-photon transitions) and observing the correlations. However, since the signal at such a frequency is scarce, the simulation was done with the cavity in weak coupling, rather than the vanishing coupling required by the theory. In both cases, involving a cavity sets a problem of optimization: either the coupling is taken to the vanishing limit at the price of reducing the signal available, or the coupling is left weak at the price of obtaining approximate correlations.

In contrast, my approach allows to extract streams of photons from any frequency windows of a quantum source, using all the signal theoretically available and taking into account self-consistently the effect of its filtering, with an exact treatment of its effect on the correlations. This allows to revisit photon-counting experiments with the added energy degree of freedom, that are already challenging without the frequency constrains. The equivalence between spectrally-filtered photo-detection theory and the sensor method was demonstrated by del Valle et al. (2012). Here, I will likewise demonstrate the equivalence between the sensor method and the cascaded formalism, which will also prove, therefore, the equivalence between spectrally-filtered photo-detection theory and the cascaded formalism.

On the one hand, the sensor method "plugs" sensors to the dynamics. Formally, calling σ the annihilation operator of a source and ξ that of a sensor probing it, we can describe their joint dynamics by a Liouvillian equation

$$\partial_t \rho = i[\rho, H_\sigma + \omega_\xi \xi^\dagger \xi + \varepsilon \sigma^\dagger \xi + \varepsilon^* \sigma \xi^\dagger] + \frac{\gamma_\sigma}{2}\mathcal{L}_\sigma \rho + \frac{\Gamma}{2}\mathcal{L}_\xi \rho\,, \tag{2.8}$$

where H_σ is the Hamiltonian that describes the internal dynamics of the source, γ_σ is the decay rate of the source, Γ is the decay rate of the sensor and $\mathcal{L}_c \rho \equiv 2c\rho c^\dagger - c^\dagger c\rho - \rho c^\dagger c$. To describe the dynamics of an arbitrary operator$\xi^{\dagger\mu}\xi^\nu\sigma^{\dagger m}\sigma^n$ under the action of this Liouvillian, we use the notation of del Valle et al. (2012), in which the correlators for the μth and νth powers of the sensor operators $\xi^\dagger$, ξ and all powers of the $\sigma^\dagger$, σ operators are placed within a vector:

$$\vec{w}[\mu,\nu] \equiv (\langle \xi^{\dagger\mu}\xi^\nu\rangle, \langle \xi^{\dagger\mu}\xi^\nu\sigma\rangle, \langle \xi^{\dagger\mu}\xi^\nu\sigma^\dagger\rangle, \cdots, \langle \xi^{\dagger\mu}\xi^\nu\sigma^{\dagger m}\sigma^n\rangle, \cdots)^T\,. \tag{2.9}$$

Then, the master equation (2.8) becomes an equation involving vectors of correlators, as follows

$$\partial_t \vec{w}[\mu,\nu] = \left\{M + [(\mu-\nu)i\omega_\xi - (\mu+\nu)\frac{\Gamma}{2}]\mathbf{1}\right\}\vec{w}[\mu,\nu] + i\varepsilon\mu T_+ \vec{w}[\mu-1,\nu] - i\varepsilon^*\nu T_- \vec{w}[\mu,\nu-1] + O(\varepsilon^2)\,, \tag{2.10}$$

where $\mathbf{1}$ is the unit matrix, $T_\pm$ are normal-ordering superoperators for the σ operators, and the $O(\varepsilon^2)$ notation means that all other terms are of higher order in ε. The matrix M provides the dynamics for the source

$$\partial_t \vec{w}[0,0] = M\vec{w}[0,0] + O(\epsilon^2)\,, \tag{2.11}$$

and is independent of the sensor at the lowest order in ε. At this stage, we do not assume any property of σ or ξ, which could be bosonic (in which case μ, ν, m and n are unbounded) or fermionic (in which case μ, ν, m and n are either 0 or 1). Equation (2.10) can be formally integrated, yielding

$$\vec{w}[\mu,\nu] = i|\varepsilon|\left\{M + [(\mu-\nu)i\omega_\xi - (\mu+\nu)\frac{\Gamma}{2}]\mathbf{1}\right\}^{-1}\left(-e^{i\theta}\mu T_+\vec{w}[\mu-1,\nu] + e^{-i\theta}\nu T_-\vec{w}[\mu,\nu-1]\right) + O(\varepsilon^2)\,, \tag{2.12}$$

where $\varepsilon = |\varepsilon|e^{i\theta}$. This in turn can be solved recursively, down to $\vec{w}[0,0]$ where the equation self-truncates. Each element $\vec{w}[\mu,\nu]$ is found to be, by inspection of Eq. (2.12), of the order $|\varepsilon|^{\mu+\nu}$, to the smallest order in $|\varepsilon|$ (leading when $|\varepsilon| \to 0$). Note that only the absolute value of the coupling can be extracted as a common factor in Eq. (2.12). This results in $(\mu+1)(\nu+1)-1$ nested equations and unknowns in order to compute a given element $\vec{w}[\mu,\nu]$. While these equations

can be solved recursively to obtain analytical expressions, we note that the normalised n-th order correlators, $g_\Gamma^{(n)}$, are ratios of the first component of $\vec{w}[n;n]$ (that is, $\langle \xi^{\dagger n} \xi^n \rangle$) divided by the n-th power of the first component of $\vec{w}[1;1]$ (that is, $\langle \xi^\dagger \xi \rangle$), itself of order $|\varepsilon|^2$, so that in such a ratio ε is cancelled to leading order. Although higher-order terms would spoil this cancellation, they become negligible as the sensor coupling is made smaller. Therefore, in the limit $|\varepsilon| \to 0$, the result becomes exact.

On the other hand, the cascaded formalism, which aims at exciting a target without affecting the source, provides a similar type of cancellation, although not restricted to vanishing coupling. From a causality point of view, it is clear that such a source/detector scenario where only one affects the other can be realized. The source that emitted a photon towards a detector may not even exist anymore by the time the detector is excited. This is achieved formally through interferences that cancel the back-action from the detector to the source. The master equation describing this asymmetric coupling reads

$$\partial_t \rho = i[\rho, H_\sigma + \omega_\xi \xi^\dagger \xi] + \frac{\gamma_\sigma}{2} \mathcal{L}_\sigma \rho + \frac{\Gamma}{2} \mathcal{L}_\xi \rho + \sqrt{\alpha \gamma_\sigma \Gamma} \{ [\sigma \rho, \xi^\dagger] + [\xi, \rho \sigma^\dagger] \} \,. \tag{2.13}$$

The last three-terms of Eq. (2.13) can be re-written in the Lindblad form as

$$\begin{aligned} \frac{\gamma_\sigma}{2} \mathcal{L}_\sigma \rho + \frac{\Gamma}{2} \mathcal{L}_\xi \rho + \sqrt{\alpha \gamma_\sigma \Gamma} \{ [\sigma \rho, \xi^\dagger] + [\xi, \rho \sigma^\dagger] \} = \\ \frac{1}{2} \mathcal{L}_{\hat{o}} \rho + \frac{\chi_1 \gamma_\sigma}{2} \mathcal{L}_\sigma \rho + \frac{\chi_2 \Gamma}{2} \mathcal{L}_\xi \rho + \frac{\sqrt{\alpha \gamma_\sigma \Gamma}}{2} [\rho, \xi^\dagger \sigma - \sigma^\dagger \xi] \,, \end{aligned} \tag{2.14}$$

where $\hat{o} = \sqrt{(1-\chi_1)\gamma_\sigma}\, \sigma + \sqrt{(1-\chi_2)\Gamma}\, \xi$ is the joint decay operator of the whole system, source and detector, and the interpretation of the factor χ_k becomes that of factors that quantify the amount of signal that each part, source and detector, generates on its own and that the joined system generates as a whole. The detector, which must have a finite lifetime to couple to the source, thus also has an intrinsic frequency window with effect of filtering the emission it detects, whence the connection to the sensors formalism. The factor $\alpha = (1-\chi_1)(1-\chi_2)$, for $0 \leq \chi_1, \chi_2 \leq 1$, takes into account that the source can have several decay channels. This is required for instance when only fluorescence is wanted without contamination from another source, e.g., a laser exciting it (experimentally this is typically achieved by detecting at right angle from the exciting beam).

The proof proceeds by showing that $\xi^{\dagger \mu} \xi^\nu \sigma^{\dagger m} \sigma^n$ has the same equation as in the sensor formalism, by computing explicitly the equation for $\partial_t \vec{w}[\mu, \nu]$ in the cascaded formalism, Eq. (2.14). This reads, to all orders in the coupling in this case:

$$\partial_t \vec{w}[\mu,\nu] = \left\{ M + [(\mu-\nu) i \omega_\xi - (\mu+\nu)\frac{\Gamma}{2}] \mathbf{1} \right\} \vec{w}[\mu,\nu] - \sqrt{\alpha \gamma_\sigma \Gamma} \{ \mu T_+ \vec{w}[\mu-1,\nu] + \nu T_- \vec{w}[\mu,\nu-1] \} \,. \tag{2.15}$$

Remarkably, this equation has the same form as Eq. (2.10) with $\varepsilon \to i\sqrt{\alpha \gamma_\sigma \Gamma}$. Even though ε is complex and a vanishing quantity in Eq. (2.10), with higher order corrections, and $\sqrt{\alpha \gamma_\sigma \Gamma}$ is real and finite in Eq. (2.15), both methods provide exactly the same normalised correlators, as these coupling parameters enter in both the numerators and denominators with the same power and cancel out. The result becomes exact for vanishing coupling in the case of sensors and is exact in all cases with the cascaded formalism, regardless of their normalisation. Note as well that θ, the phase of the coupling ε, has an effect on the dynamics only if the Lindblad equation features products of different operators in its dissipative terms, which is the case for the cascaded formalism with $\mathcal{L}_{\hat{o}}$ that brings cross terms of σ and ξ. The sensor formalism, however, has no such joint decay emission and the phase of ε does not play any role, so that ε could have beeen set real. This achieves to prove the mathematical equivalence of the sensor method with the cascaded formalism for the computation of normalized correlators.

Since del Valle et al. (2012)'s sensor formalism has been shown to be equivalent to normalized photon correlations according to photo-detection theory, as discussed for instance by Vogel

and Welsch (2006), the above equivalence of the sensor and cascaded formalisms shows that following the recipe from Carmichael (2008) and applying the quantum Monte Carlo method to the detector realizes a sampling of the emission in the corresponding frequency windows, from which one can reconstruct the frequency-resolved photon correlations. That is to say, this allows us to simulate the photon emission with both time and energy information, which is what we are going to illustrate in the following.

Note that with both Eqs. (2.10) and (2.15), any given correlator $\langle \xi^{\dagger\mu} \xi^{\nu} \rangle$ can be computed exactly (by recurrence) in terms of lower order ones $\langle \xi^{\dagger\mu'} \xi^{\nu'} \rangle$ only, with $\mu' \leq \mu$ and $\nu' \leq \nu$. This means that both methods can be applied using N two-level systems as detectors at different frequencies, in order to compute cross correlations, or with a single harmonic oscillator truncated at N excitations, to compute the Nth order monocromatic autocorrelation function $g^{(N)}$. This is however not sufficient with the cascaded formalism for computing the density matrix (full state) of the detectors or for doing Monte Carlo simulations of the emission. In such cases, one must model the N detectors as harmonic oscillators with a high enough truncation to provide converged results. Such a simulation is conveniently implemented through the quantum-jump approach. The dynamics of the system is thus described by a wavefunction $|\psi(t)\rangle$ that occasionally undergoes a process of "collapsing", attributed to the emission of a photon, that one records in the simulation as a detector would register a click in an experiment. The occurrence of a collapse is decided in each infinitesimal time interval $\delta t \to 0$, where the evolution of the wavefunction is governed by two elements: a non-Hermitian Hamiltonian and random quantum jumps, just like in the method described in Sec. 2.2.1. For the system described by the master equation (2.13), the collapse operators are (cf. Fig. 2.3)

$$L_1 = \sqrt{(1-\chi_1)\gamma_\sigma}\,\sigma + \sqrt{(1-\chi_2)\Gamma}\,\xi\,, \quad L_2 = \sqrt{\chi_1\gamma_\sigma}\,\sigma \quad \text{and} \quad L_3 = \sqrt{\chi_2\Gamma}\,\xi\,, \tag{2.16}$$

whereas the non-Hermitian Hamiltonian is given by

$$\begin{aligned} \tilde{H} &= H_\sigma + H_\xi - \frac{i}{2}\sqrt{\alpha\gamma_\sigma\Gamma}(\xi^\dagger\sigma - \sigma^\dagger\xi) - \frac{i}{2}(L_1^\dagger L_1 + L_2^\dagger L_2 + L_3^\dagger L_3)\,, \\ &= H_\sigma + H_\xi - i\sqrt{\alpha\gamma_\sigma\Gamma}\,\xi^\dagger\sigma - \frac{i}{2}(\gamma_\sigma\sigma^\dagger\sigma + \Gamma\xi^\dagger\xi)\,. \end{aligned} \tag{2.17}$$

In the following sections, we apply the frequency-resolved Monte Carlo method to the emission of a two-level system under various regimes of excitation.

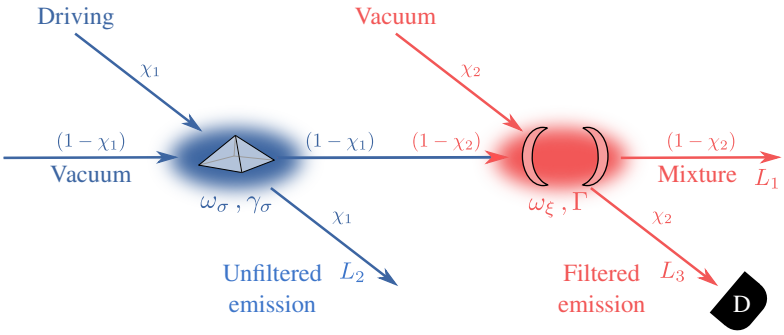

Figure 2.3: Scheme of the setup to measure the frequency-resolved correlations of the light emitted by a source, whose energy is centered at ω_σ and has a decay rate γ_σ. While a fraction of the emitted light goes unfiltered to the open space, to which we refer to as the "unfiltered emission" and which is described by the quantum jumps of the operator L_2 in Eq. (2.16), the remaining fraction is used to weakly drive the sensor, which has frequency ω_ξ and decay rate Γ, which is also the bandwidth of the sensor. The emission from the sensor can also be separated into two streams, depending on whether the emission from the sensor is mixed or not with scattered light from the source (e.g., the emission of the sensor and the scattered light might follow different spatial paths). The case without the scattered light corresponds to the "filtered emission" which can then go to a detector D or a Hanbury Brown setup. It is associated to the operator L_3 of Eq. (2.16), while the mixture of light is described through the operator L_1 of Eq. (2.16).

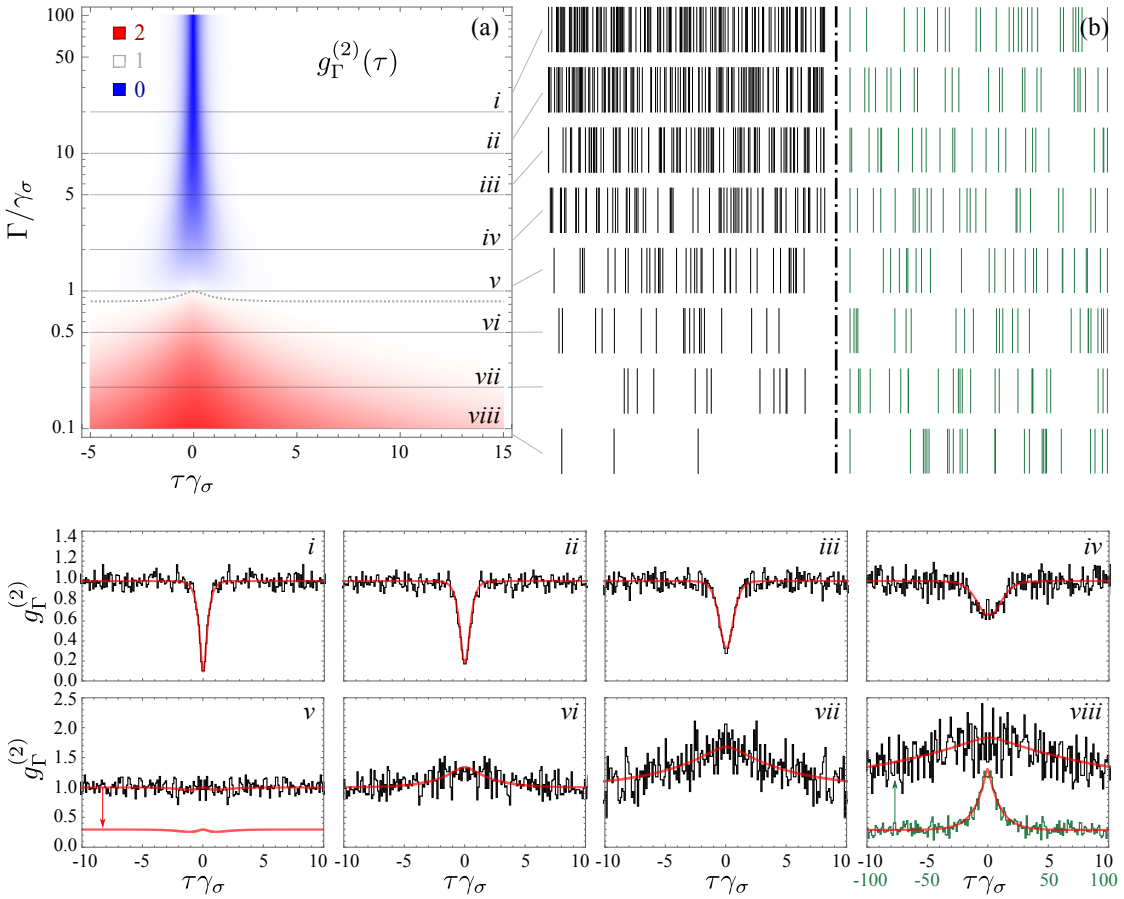

Figure 2.4: Frequency-resolved emission from an incoherently driven two-level system. The number of events (clicks) recorded are close to 10 000 (namely 9976, 9916, 9974, 9927, 9967, 9955, 9860) for the cases *i*–*vii* respectively, and 25 000 for case *viii* to get enough signal for the small timescale comparison to the other filters. (a) The density-plot of the theoretical $g^{(2)}_\Gamma(\tau)$ with the color code indicated (blue for antibunching, red for bunching and white for uncorrelated). Filtering leads to thermalization. The transition is slightly more complex than merely loss of antibunching. The dotted line shows the isoline $g^{(2)}_\Gamma(\tau) = 1$. Monte Carlo simulations have been done for the eight cuts shown. Panel (b) shows samples of clicks in the same time window (black, left) or with rescaling to have the same intensity (green, right). There is a neat transition visible to the naked eye between the two types of photon statistics. Autocorrelation computed from the clicks are shown in the eight panels at the bottom, together with the theory prediction. In panel v, the theory curve is also shown displayed to reveal its fine structure departing from $g^{(2)}_\Gamma(\tau) = 1$. In panel viii, also the case of longer times is shown since thermalization goes together with slowing down of the dynamics. For the density plot $1/\gamma_\sigma$ sets the unit and $P_\sigma = 2\gamma_\sigma$. The clicks correspond to the emission events of the operator L_3 in Eq. (2.16).

2.3.2 *Incoherently driven two-level system*

We now apply the frequency-resolved Monte Carlo method introduced above to the incoherently excited two-level system, which we have already investigated through the standard Quantum Monte Carlo method. The effect of a Lorentzian filter on the statistics of emission of an incoherently excited two-level system has been discussed by del Valle et al. (2018) as is shown in Fig. 2.4(b). The theory predicts thermalization and loss of antibunching with narrowing filtering. The theoretical expression for the delay correlation is given by

$$g^{(2)}_\Gamma(\tau) = 1 - \left(\frac{\Gamma}{\Gamma-\Gamma_\sigma}\right)^2 e^{-\Gamma_\sigma\tau} + \frac{\Gamma_\sigma(\Gamma_\sigma^2 - 3\Gamma\Gamma_\sigma - 2\Gamma^2)}{(\Gamma_\sigma-\Gamma)^2(\Gamma_\sigma+3\Gamma)} e^{-\Gamma\tau} + \frac{2\Gamma_\sigma\Gamma(5\Gamma-\Gamma_\sigma)}{(\Gamma_\sigma-\Gamma)^2(\Gamma_\sigma+3\Gamma)} e^{-(\Gamma_\sigma+\Gamma)\tau/2}, \quad (2.18)$$

where $\Gamma_\sigma \equiv \gamma_\sigma + P_\sigma$ and the detector is resonant to the 2LS. With the frequency resolved Monte Carlo, one can simulate streams of clicks corresponding to spectral filtering, as is shown Fig. 2.4(b) with eight Monte-Carlo simulations of roughly 10 000 clicks each (25 000 for the narrowest filter in case *viii*). Extracts of the recorded clicks are shown, comparing them, 1) in the same time window (black ticks), with effect of having much less clicks for narrower filters, and also 2) when rescaling the unit of time so that the intensities are the same (green ticks). In the latter case, one can compare the statistical distributions, and observe the transition from antibunched clicks (*i*) to thermal ones (*viii*) passing by auxiliary distributions. In the former case, one observes the characteristic antibunching, equally-spaced like distribution of a two-level emitter. In the latter case, one finds the wildly fluctuating thermal (or chaotic) light, with pronounced bunching in the form of long gaps of no emission followed by gusts of emission. This can be differentiated even with the naked eye from the Poisson distribution, whose tendency for "clumping" does not get as dramatic as the thermal case. One can follow the transition neatly from these various sets of clicks, passing by the case of almost uncorrelated light. Since the isoline $g^{(2)}_\Gamma(\tau) = 1$ is not straight (it is shown as a dotted line in the density plot of Fig. 2.4), the passage from antibunching to bunching does not transit through exactly uncorrelated (or coherent light), although the deviation is too small to be appreciated on a small sample. To observe such fine variations, one needs to acquire a large statistical ensemble and condense the correlations in a single object, such as $g^{(2)}_\Gamma$, as is shown in the eight panels at the bottom of Fig. 2.4. The case *v* of close-to-uncorrelated light is also shown separately from the Monte Carlo data to reveal its fine structure. The other cases have a simpler shape of a dip that turns into a hump. The correlation time also changes dramatically, as is observable both from the density plot and the Monte Carlo histograms. As the emission thermalizes, its fluctuations occur on longer timescales. This is the reason for the increased noise in panels *vi*–*viii*. There, one should increase the binning and consider larger time windows, as shown in green for case *viii* that assumes a binning of $\Delta t\gamma_\sigma = 1$ instead of 0.1 for the other cases, and plot the correlations in a time window $|t\gamma_\sigma| \leq 100$ instead of 10, as indicated on the respective axes, recovering the excellent agreement with theory displayed by the antibunched cases.

Now in possession of the statistical data, and with the insurance of its accuracy given its agreement with the theory, it is possible to undertake various types of analysis that would not be so straightforward without these simulations, as has been discussed above. I will not go in this direction now and leave for future works the case of an incoherently excited 2LS. Instead, we now turn to the case of coherent excitation, that presents more features of interest.

2.3.3 *Coherently driven two-level system*

The case of coherent excitation is obtained by complementing the Hamiltonian in Eq. (2.5) with the driving of the two-level system, $\Omega_\sigma(\sigma^\dagger + \sigma)$, and using the master equation (1.44). The case of a filtered coherently driven 2LS is shown in Fig. 2.5. Here as well, there is thermalization and although it only happens when the intensity of the driving laser is larger than the decay rate of the 2LS, i.e., when $\Omega_\sigma > \gamma_\sigma$, it is interesting to consider the effect of filtering and approach it from the Monte Carlo perspective. Taking one slice featuring these oscillations, we collect 10^5 clicks, a small portion of which is shown as ticks at the bottom of Fig. 2.5. Computing the autocorrelations, we find indeed strong oscillations from a very good antibunching with steep bunching elbows, in agreement with the theory. This produces even more pronounced correlations in the photon-detection events, where the spacing appears more regular and between clumps of photons. As far as continuous streams are concerned, this suggests that such strongly-oscillating $g^{(2)}$ do in fact provide more ordered time series than the conventional antibunching of the type of Eq. (2.7). Such questions will be tackled in the next Chapter. We conclude this Section with further comments on the Heitler effect (coherence of the Rayleigh peak), which takes place in the regime of low excitation. While one could try to recover it in the high excitation regime using a narrow filter, one needs to consider several fundamental aspects. First, regarding the emergence of a thermalization similar to that of incoherent driving,

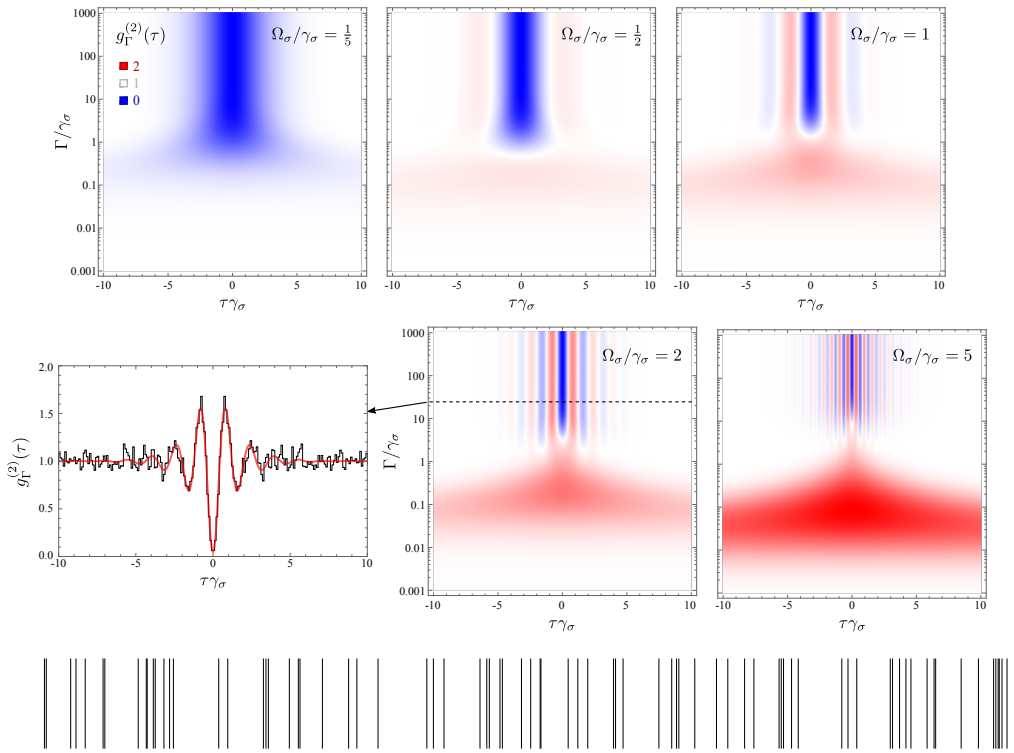

Figure 2.5: Frequency and time-resolved $g^{(2)}_\Gamma(\tau)$ of a two-level system coherently driven, in its transition from the Heitler to the Mollow regime (from left to right). At low pumping, one does not observe thermalization (bunching) with narrowing filters. Higher pumping brings both bunching, similar to the case of incoherent pumping, and oscillations. The bunching is observed only for moderately narrow filtering as extremely narrow filtering goes back to filtering exclusively the Rayleigh peak, with a resurgence of the Heitler effect and uncorrelated (or coherent) emission. Wide filtering overlapping the three peaks captures the Rabi oscillations. A Monte Carlo simulation of the case highlighted with the dashed line is shown through a small sample of clicks (bottom) and the autocorrelation function, compared to the theory prediction. There is a clear structure in the photon clicks, that is unlike any of the cases shown previously. The clicks correspond to the emission events of the operator L_3 in Eq. (2.16).

cf. Fig. 2.4, this is obtained when one enters the Mollow (1969) triplet regime. In this case, luminescence has split into a triplet lineshape and, when filtering at resonance (as is the case here), one filters the central peak alone, which according to Reynaud (1983) corresponds to the spontaneous emission of a photon that leaves the state of the dressed two-level system unchanged. As such, the spontaneously emitted photons react to filtering in a similar way than the incoherently pumped two-level system, hence the observed bunching for narrowing filters linewidths. The similarity is only partial, however, as González-Tudela et al. (2013) showed that in the limit of infinite pumping, instead of thermalization with $g^{(2)}_\Gamma(0) = 2$, the transition is to a super-chaotic state, with $g^{(2)}_\Gamma(0) = 3$ (for the parameters considered here, we find $\max_\Gamma g^{(2)}_\Gamma(0) \approx 2.2$). More strikingly, when filtering well within the central peak, one then isolates the Rayleigh (δ) peak again and reverts to the low-pumping case, with the statistics becoming uncorrelated, as shown in Fig. 2.5. Large filtering windows, on the other hand, collect the emission from all three peaks and reproduce the Rabi oscillations, which is the case selected for the Monte Carlo sampling. We explore in more details the opportunities offered by the Mollow triplet in the next Section.

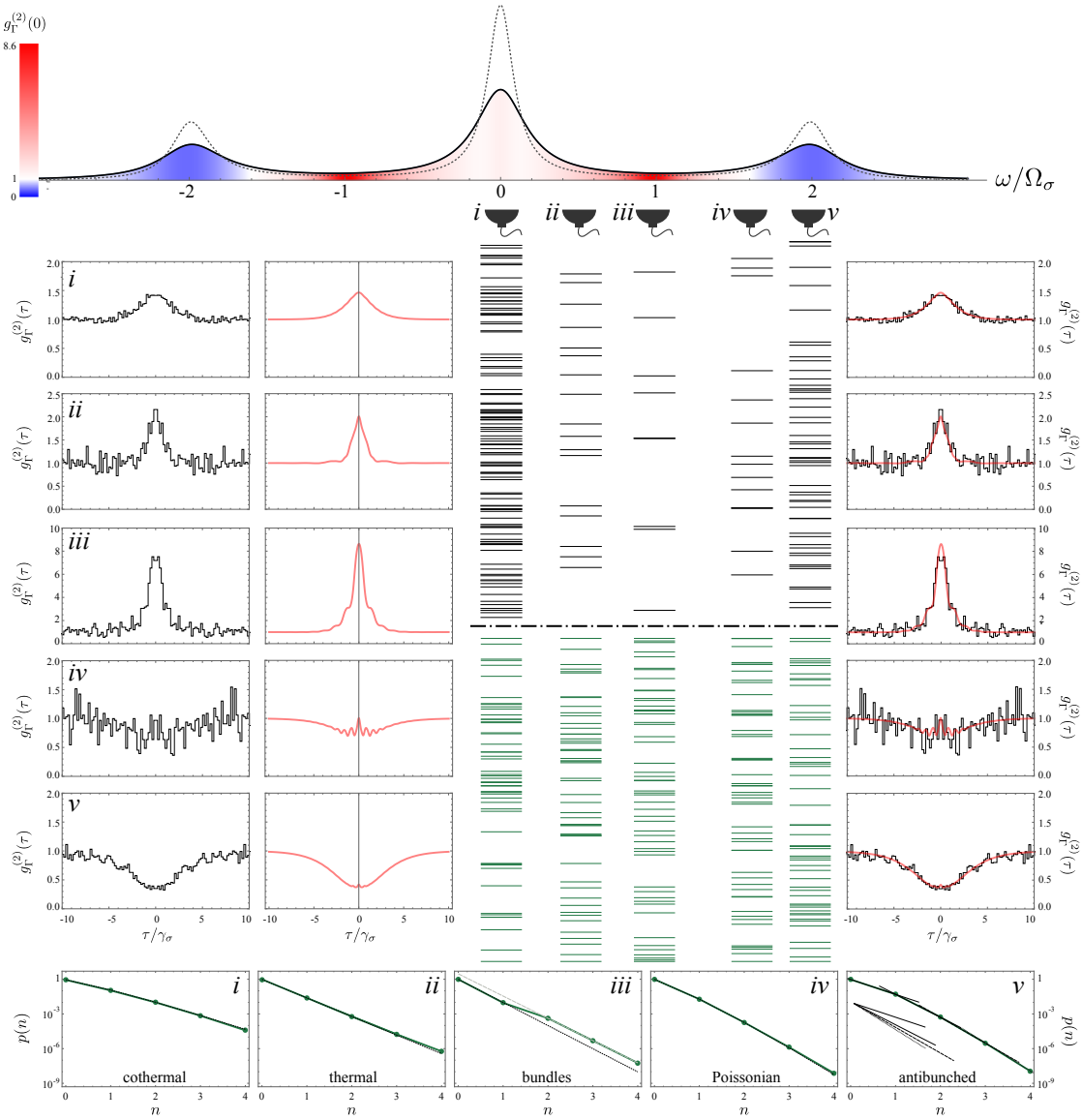

Figure 2.6: Frequency-resolved Monte Carlo simulation of the Mollow triplet in independent frequency windows. The dotted (solid) lineshape is the triplet as detected by an ideal (finite-bandwidth Γ) detector. Sequences of clicks in the frequency windows *i*–*v* have been recorded, with 17241, 22836, 99457, 9112 and 46126 events, respectively. Small samples are displayed, in the same time window (black ticks, up) or with renormalization of time to compare equal intensities (green ticks, bottom). Clear structures are visible even to the naked eye, in particular, the existence of leapfrog emission is obvious. Only one detector has been used, so the streams are not here cross-correlated. The autocorrelations are shown as measured by the Monte Carlo data (left column), as computed by the theory of frequency-resolved photon correlation (2nd column, red) and both superimposed (right column), to show their rich fine structure and the overall agreement. The effective quantum state reconstruction is shown at the bottom, together with fits to fundamental distributions. Panel *v* has its successive emission probabilities brought together to show the exponential extinction of higher photon-numbers. $1/\gamma_\sigma$ sets the unit, $\Omega = 5\gamma_\sigma$ and $\Gamma = \gamma_\sigma$. The clicks correspond to the emission events of the operators L_4 and L_5 in Eq. (2.20).

2.3.4 *Mollow Triplet*

2.3.4.1 *Autocorrelations*

Del Valle et al. (2012)'s theory of frequency-resolved photon correlations revealed strong correlations away from the spectral peaks of the Mollow triplet (cf. Sec. 1.2.6). This is particularly

obvious in the 2PS (Fig. 1.15) where such correlations are revealed as two-photon transition (leapfrogging) straight-lines in the 2D landscape. Such strong correlations are apparent even in autocorrelations, meaning that a single detector positioned at the appropriate frequency (halfway between the peaks in the Mollow triplet) would register highly correlated clicks. We illustrate this in Fig. 2.6 with the statistics of clicks from photo-detection events of the Mollow triplet in frequency windows spanning from the central peak to the side peaks, including various other windows in between, in particular, the leapfrog window. Note that, here as well, the data is for a single-detector observable, that is to say, the different streams shown are not correlated to each other as they have been obtained by the same detector in different runs of the experiment. It would require 5 detectors to obtain the same result but with correct cross-correlations (this is beyond the scope of the present discussion that will go up to two detectors only, but is of course a topic of interest for applications). As we did in Fig. 2.4, we show both ticks in a given time window (in black) and with a rescaling of the unit of time so that their densities are equal (in green). Here as well, the relative emission rates mean that longer integration times are required when collecting away from the peaks. The gain in terms of correlation strengths, however, makes it worthwhile to focus on these regions of reduced emission, in a spirit akin to distillation, as has done del Valle (2013) by trading quantity for quality. The frequency windows have been chosen as they correspond to particular cases of interest:

i Photons from the central peak.

ii Case where $g^{(2)}_{\Gamma}(0) = 2$ (usually attributed to thermal light).

iii Photons from leapfrog emission.

iv Case where $g^{(2)}_{\Gamma}(0) = 1$ (usually attributed to coherent or uncorrelated light).

v Photons from a side peak.

The central peak is partially thermalized, with a $g^{(2)}(\tau)$ that closely resembles the form of thermal fluctuations, $g^{(2)}(\tau) = 1 + \exp(-2|\tau|/\tau_0)$. Upon closer inspection, however, this is an approximation as the exact solution presents small departures, in particular, a differentiable slope at the origin and small ripples that are thinly visible on the theory curve, that we keep separate from the Monte Carlo data for clarity (the quality of their agreement is shown in the rightmost column). Note that the dynamics of coherent driving of a two-level system is considerably more complicated than its incoherent counterpart and we could not find, so far, a general closed-form expression for $g^{(2)}_{\Gamma}(\tau)$ (not even in the case in which $\omega_\xi = \omega_\sigma$). Applying the technique of effective-quantum state reconstruction from the correlators, that I will discuss in detail in the next Chapter, we find that the statistics $p(n)$ fits well with a cothermal distribution with $\approx 80\%$ of thermal emission and $\approx 20\%$ of uncorrelated emission. Overall, the emission of the central peak is thus well described by a mixture of thermal and uncorrelated light. It is, as such, not very interesting per se. Turning now to the second frequency window, *ii*, which features $g^{(2)}_{\Gamma}(0) = 2$, characteristic of thermal emission, one can now see more clearly the deviation from the thermal paradigm, with bulging and tails deforming the correlation function. These are well reproduced by the Monte Carlo statistics and we let the reader decide if their statistical acuity lets them, on the small sample of clicks reported here, observe deviations from the thermal paradigm (cf. Fig. 2.4*viii*).

The most interesting window, *iii*, lies halfway between the central and side peak. This is the frequency at which, following González-Tudela et al. (2013)'s interpretation of the theory, two photons can make a leapfrog process from the state $|+\rangle$ in a given manifold to the state $|-\rangle$ two manifolds below, jumping over the intermediate manifold, cf. the transition highlighted by the yellow arrow in Fig. 1.15(d). These photons are strongly correlated in several ways. From a photo-detection point of view, they should arise as more occurrences of closely-spaced two-photon clicks than if the emission was uncorrelated. In particular, their rate of coincidences should increase, leading to $g^{(2)}_{\Gamma}(0) \gg 2$, or so-called superbunching. This is both predicted

by the exact theory done by del Valle et al. (2012) and González-Tudela et al. (2013) and observed in our Monte Carlo simulations, as seen in Fig. 2.6. Remarkably, even with as few as 9112 clicks collected in the numerical experiment, we can reconstruct a high-quality signal, revealing the fine details of its structure. Note as well that on the real-time series of clicks, out of the nine photons emitted shown here, four came as two-photon bundles (the fifth and sixth clicks are so closely spaced as almost overlapping; other ticks are single-photon events). The small sample of clicks also shows strong ordering, combining equal spacing and gaps of no emission. While the latter is characteristic of thermal emission, the former is typically characteristic of antibunching. This combination can be seen as the selection through filtering of strongly correlated emission from the emitter, rather than tampering from the filters on the statistics: focusing to this frequency windows allows us to detect the two-photon emission events that occurs, from the dressed-atom picture, at this frequency. It would be rewarding to apply this technique to the filtered emission of Sánchez Muñoz et al. (2014a)'s "bundler" that emits the majority, and in some regime, close to 100%, of its light as N-photon emission, specially since Sánchez Muñoz (2016) and Sánchez Muñoz et al. (2018) have found that filtering can considerably boost the purity of the quantum emission. Also further photon-counting characterization would certainly be enlightening, and preliminary investigations show that the percentage of closely-spaced photons is over an order of magnitude higher in *iii* than in the others at the exception of *ii*, as compared to which it is only about 3.8 times larger. We leave further characterizations for future works, but provide a last compelling manifestation of leapfrog emission from the effective quantum state reconstruction approach. This highlights the frequency window *iii* as the most dissimilar one as compared to the others, featuring a neat kink at the probability to have two photons, $p(2)$, showing the relative predominance of two-photon emission.

The fourth frequency window, *iv*, chosen for its $g^{(2)}_\Gamma(0) = 1$ of uncorrelated emission, is also a case that shows strong departures at nonzero τ due to filtering. This is, here again, well captured by the Monte Carlo clicks and is visibly noticeable on the small sample, that features ordered clumps of uncorrelated clicks. With the last window, *v*, we come back to a case well studied in the literature, of antibunched emission, albeit far from perfect ($g^{(2)}_\Gamma(0) \approx 0.42$ and $\min_\tau g^{(2)}_\Gamma(\tau) \approx 0.37$). The fact that the minimum antibunching is not at zero is another manifestation of frequency filtering, thinly visible on the figure as small oscillations, but not reproduced at this level of signal by the Monte Carlo data. Correspondingly, the $p(n)$ shows increasingly suppressed probabilities to get higher number of photons.

2.3.4.2 *Cross-correlations*

We now consider cross-correlations, for which the Mollow triplet is also a particularly suitable lineshape. That is to say, we consider two detectors acquiring data simultaneously. The master equation for two detectors upgrade Eq. (2.14) to:

$$\partial_t \rho = i\left[\rho, H_\sigma + \sum_{i=1,2} \omega_{\xi_i} \xi_i^\dagger \xi_i\right] + \frac{\gamma_\sigma}{2}\mathcal{L}_\sigma \rho + \sum_{i=1,2}\left(\frac{\Gamma_i}{2}\mathcal{L}_{\xi_i}\rho + \sqrt{\alpha_i \gamma_\sigma \Gamma_i}\{[\sigma\rho, \xi_i^\dagger] + [\xi_i, \rho\sigma^\dagger]\}\right), \quad (2.19)$$

with ξ_1, ξ_2 the two detectors. The factors $\alpha_1 = \chi_0(1-\chi_2)$ and $\alpha_2 = (1-\chi_0-\chi_1)(1-\chi_3)$, satisfying simultaneously $0 \leq \chi_0, \chi_1, \chi_2, \chi_3 \leq 1$ and $\chi_0 + \chi_1 \leq 1$, take into account the several decay channels of the source: a fraction χ_1 into free space, a fraction χ_0 to the detector ξ_1 and the remaining fraction $(1-\chi_0-\chi_1)$ to the detector ξ_2. In analogy with the case of a single detector, the system described by the master equation (2.19) has five collapse operators:

$$L_1 = \sqrt{\chi_0\gamma_\sigma}\,\sigma + \sqrt{(1-\chi_2)\Gamma_1}\,\xi_1\,, \quad L_2 = \sqrt{(1-\chi_0-\chi_1)\gamma_\sigma}\,\sigma + \sqrt{(1-\chi_3)\Gamma_2}\,\xi_2\,, \quad L_3 = \sqrt{\chi_1\gamma_\sigma}\,\sigma\,,$$
$$L_4 = \sqrt{\chi_2\Gamma_1}\,\xi_1 \quad \text{and} \quad L_5 = \sqrt{\chi_3\Gamma_2}\,\xi_2\,, \quad (2.20)$$

and its associated non-hermitian Hamiltonian becomes

$$\tilde{H} = H_\sigma + H_{\xi_1} + H_{\xi_2} - i(\sqrt{\alpha_1\gamma_\sigma\Gamma_1}\,\xi_1^\dagger\sigma + \sqrt{\alpha_2\gamma_\sigma\Gamma_2}\,\xi_2^\dagger\sigma) - \frac{i}{2}(\gamma_\sigma\sigma^\dagger\sigma + \Gamma_1\xi_1^\dagger\xi_1 + \Gamma_2\xi_2^\dagger\xi_2)\,. \quad (2.21)$$

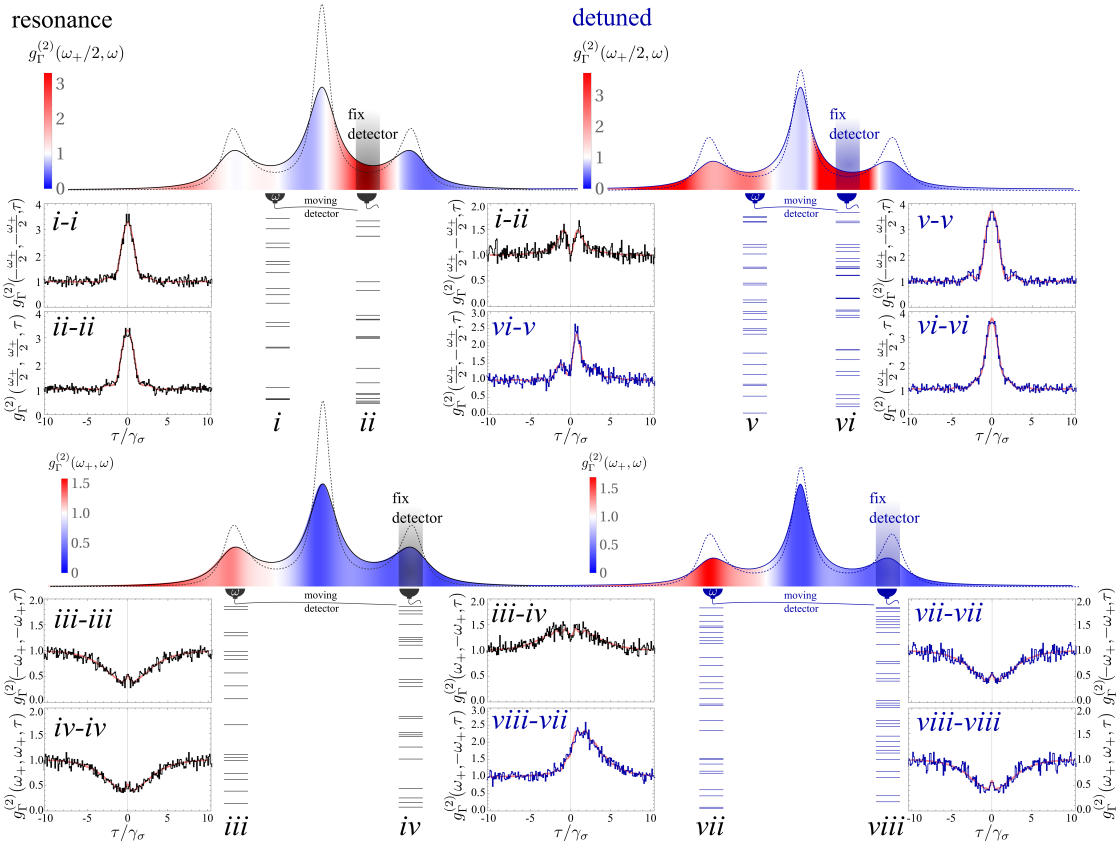

Figure 2.7: Frequency-resolved Monte Carlo simulation of the Mollow triplet in dual frequency windows. The case on the left (right) is for driving the two-level system at resonance (with detuning $\Delta = 1.5\gamma_\sigma$). The dotted (solid) lineshape is the triplet as detected by an ideal (finite-bandwidth Γ) detector. The color code within the spectra is for one filter kept fixed at a leapfrog window (top case) or at a sideband (bottom case). Sequences of clicks have been recorded in the windows *i* and *ii* and *iii* and *iv*, the two groups being independent (that is, clicks between, e.g., *i* and *iii* are not correlated). Small samples are displayed, with renormalization of time to compare equal intensities between the two groups (time is the same within each group). Strong correlations of photons with different frequencies are clear, in particular, the simultaneity of leapfrog emission and their heralding character with detuning are obvious. The cross-correlations are shown as measured by the Monte Carlo data (left column) and as computed by the theory of frequency-resolved photon correlation (2nd column, red). $1/\gamma_\sigma$ sets the unit, $\Omega = 5\gamma_\sigma$, $\Delta = 1.5\gamma_\sigma$ and $\Gamma = \gamma_\sigma$. The clicks correspond to the emission events of the operators c_4 and c_5 in Eq. (2.20).

As for the case of autocorrelations, one could similarly demonstrate the equivalence between cross-correlations to any orders as computed through the frequency-resolved photon correlations and those obtained through Eq. (2.19) above. Also, as was done before for single frequency windows, by applying the Monte Carlo techniques to the detectors, one can thus obtain simulated photon emissions, this time in two frequency windows. Computing the correlations from this raw data provides a numerical version of the theoretical correlations. This is shown in Fig. 2.7 for the joint emission of the two sidebands on the one hand, and then of the two leapfrog windows on the other hand, both when driving the two-level system at resonance or with a detuning.

While we considered a small subset only of the possible autocorrelations in Fig. 2.6 for the Monte Carlo data, we could still provide a comprehensive theoretical result at least for $g^{(2}_\Gamma(0)$ through the color-coded spectrum. For cross-correlations, however, this would require a 2D plot to reproduce the entire two-photon correlation spectrum predicted by González-Tudela et al. (2013). Instead, we consider here the case where one detector is fixed and the other one sweeps the rest of the spectrum, providing the cross-correlations. We then place the other detector for

Monte Carlo sampling at the location of interest. As before, we show raw photon emission, but with no time-rescaling as the respective frequencies chosen have similar intensities. We also compare two-photon correlations computed from this data (black and blue lines, at resonance and with detuning respectively) with the theoretical result (red lines). The main difference between these cases and the previous ones is that the two streams of photons are now correlated as the detectors are measuring simultaneously. If restricting to one stream only, we recover the previous cases, so in Fig. 2.7, panels *i*-*i* and *ii*-*ii* on the one hand, as well as *iii*-*iii* and *iv*-*iv* on the other hand, can be found in Fig. 2.6 (in panels *iii* and *v* respectively). The two cases have different parameters, since with two detectors, the simulation is more computer intensive and we chose a case that provides more emission between the peaks. One can check however how the qualitative shapes of the correlations remain the same. At resonance, both streams provide the same type of correlations, but with detuning, they could be different. This is indeed the case for the leapfrog emission, and small departures can be observed between *v*-*v* and *vi*-*vi*, both in the theoretical line and the Monte-Carlo generated data: the oscillations are more marked for the low-energy window and a depletion is indeed visible in *vi*-*vi* that disappeared in *v*-*v*. The side peaks, however, feature similar correlations. This shows again the typical richer dynamics away from the peaks.

Both at resonance or with detuning, what is of interest when detecting in different windows simultaneously is their cross-correlations, as shown in the central column of Fig. 2.7 with panels *i*-*ii*, *vi*-*v*, *iii*-*iv* and *viii*-*vii*. There are now clear features in these cross-correlations, whereas the same procedure applied to the streams of the previous cases features no correlations, i.e., one obtains flat lines. At resonance, the cross-correlations are symmetrical in time. The side peaks correlations feature tiny oscillations which are however too small to be observed with the amount of signal we acquired in the numerical experiment, and they are hidden by its fluctuations. With detuning, they can and do become time-asymmetrical, as shown in panels *vi*-*v* and *viii*-*vii*. In such cases, the order of detection matters, and in both cases, the detection on first detector, *vi* or *viii*, respectively, makes it more likely to later detect (with around $1/\gamma_\sigma$ delay) a photon on the second detector, *v* and *vii*, respectively. The strength of such correlations, less than 3, is still fairly modest to call this heralding, but this is the basis for such a mechanism to be exploited with proper engineering, such as Purcell-enhancement. Like before, our procedure yields correlated streams of photons of different frequencies, that we have just shown through their agreement with the theory of frequency-resolved photon correlations, simulate the actual photon emission from the system. One could use this raw data to compute numerically, e.g., counting or time-delay distributions, otherwise not easily accessible theoretically. Of course, the scheme could in principle be extended to any number of detectors and allow consequently higher orders of correlation to be computed in this way. In the limit of an infinite number of detectors, each with a given frequency and vanishing spectral width, one would thus simulate the ideal emission of the system. With a finite number of detectors with a finite bandwidth, one would simulate its filtered emission. We believe that a complexity analysis of the correlations would allow to use the emission of the two-level system as a simpler platform than the boson sampling protocol, proposed by Aaronson and Arkhipov (2011) to test quantum supremacy by making a laboratory measurement which no classical computer would be able to simulate.

2.3.5 *Controversy*

Decades ago, Apanasevich and Kilin (1977) noted the correlations that exist between photons emitted from resonance fluorescence for the case of transitions obeying $|\pm\rangle \rightrightarrows |\pm\rangle$. While back then the authors overlooked the transitions that follow the rule $|\pm\rangle \rightrightarrows |\mp\rangle$ (which are equally obvious with the dressed atom picture in mind), this was a considerable achievement that foresaw these results with two years of advance on the other experts in a time of burgeoning activity. Now paired with another co-author, Shatokhin and Kilin (2000), Shatokhin and Kilin (2001), and Shatokhin and Kilin (2002), produced another series of noteworthy works on the

problem of photon correlations. Recently, however, Shatokhin and Kilin (2016) have expressed some critics on the leapfrog picture, writing that

> *the concept of the "leapfrog" processes is not justified*, [they] *present an alternative explanation* [based on] *the unnormalized spectral correlation function* [which is] *a true measure of spectral correlations and which exhibits no signatures of the leapfrog transitions*.

From their discussion, one thus understands that the production of strongly-correlated photons away from the peaks, that was predicted by González-Tudela et al. (2013) and others in their wake, is an artifact due to normalization. In principle, one can indeed inflate the vacuum and create what one could regard as an artificial superbunching. In fact, this is the mechanism used by Liew et al. (2016) in their proposal for a bosonic laser. This, however, is not what happens with leapfrog emission, although according to these authors, nothing of interest takes place away from the peaks, what they illustrate by producing a two-photon spectrum remarkably featureless, in contrast to the two-photon spectrum that is rich from photon correlations flourishing away from the peaks. I compare the two versions in Fig. 2.8, showing in panels (a) and (b) the theoretical prediction and its experimental verification by Peiris et al. (2015). On the other hand, the two-photon spectrum proposed by Shatokhin and Kilin (2016) is shown in panel (c) (which displays the correlations as $\langle a^\dagger(\delta_1)a^\dagger(\delta_2)a(\delta_1)a(\delta_2)\rangle - \langle a^\dagger(\delta_1)a(\delta_1)\rangle\langle a^\dagger(\delta_2)a(\delta_2)\rangle$), comparing the two-photon correlations with the product of the photon occupation at each frequency. This non-normalized spectrum is correct but is also less interesting as it merely shows that first-order processes smother second-order ones, as is however well-known and expected. As I have shown above, in contrast, the scarce signal from higher-order processes has stronger correlations than those from first-order processes. This is amply and vividly illustrated through the Monte Carlo simulations below. One can also consider placing a cavity in this "featureless" region when not normalized, and observe how the system then keeps emitting strongly correlated photons but now dominating over the other first-order processes, as has been showed by Sánchez Muñoz et al. (2014a) and Sánchez Muñoz et al. (2018), and which would not happen would the correlation be an artifact due to normalization. The best proof, however, comes from a frequency-resovled Monte Carlo simulation, where the manifestation appears to the naked eye, as shown for instance in Fig. 2.6, where one can see how photons are physically detected as closely-spaced. Indeed, this simulation makes it obvious that the emission in this frequency window suffers from no artifact of post-selection or normalization, but does indeed provide strongly correlated photon streams.

The rest of Shatokhin and Kilin (2016)'s criticisms are merely on semantics, in which case we should clarify, as this is apparently needed, that the dressed-atom picture is, precisely, a "picture", that is, an insightful mental representation that is helpful to visualize the basic mechanism at play, support the intuition and guide further inquiries. This does not preclude exact calculations based on the opaque equations of quantum mechanics. This is possibly why the Mollow triplet is named after Benjamin, not only for his seminal input but also in recognition of the exact expression, although the Cohen Tannoudji and Reynaud approximate picture is the one everybody has in mind when thinking about this problem. We combine both approaches: the sensor technique provides the exact result, while the leapfrog processes provide a physical representation *à la* Cohen Tannoudji *et al.*. Thus, in the same way that resonance fluorescence is not spontaneous emission from the dressed atom, the leapfrog emission is not, strictly speaking, spontaneous emission jumping over intermediate manifolds. This is, instead, a complicated process that involves the laser and the two-level system in a sequence of coherent absorption and emission. In fact, in Chapter 6, I will show how even fluorescence in the low-driving regime does not consist of Rayleigh scattering events but form an intricate interference between emission and absorption, that powers the single-photon emission mechanism by suppressing the fat tails of the Lorentzian and turning the lineshape into a t_2 distribution instead. In the strongly nonlinear regime, a similar dynamics takes place but it becomes forbidding and certainly not even useful to apprehend the problem in these terms. Note that although inspired by the dressed-atom approach of the problem, ultimately, our computations are exact (and in

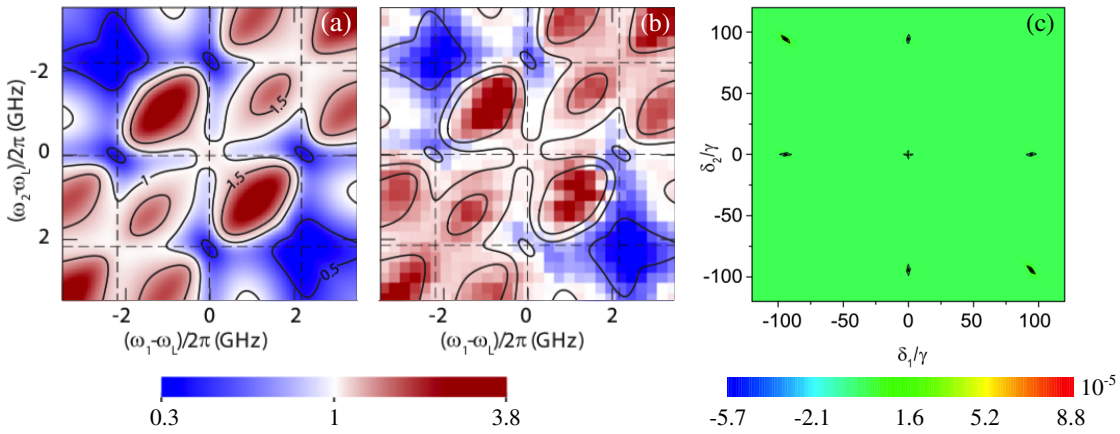

Figure 2.8: Two-photon spectra from the Mollow triplet. (a,b) Prediction made using the theory of del Valle et al. (2012) and experimental observation by Peiris et al. (2015), displaying an outstanding agreement between them. The two-photon emission, the leapfrogs, can be identified in the regions of the principal diagonal in which the cross-correlations are the highest. (c) The unnormalized two-photon spectrum proposed by Shatokhin and Kilin (2016) in which all the features are washed away. The figures are an adaptation from Peiris et al. (2015) and Shatokhin and Kilin (2016). Note that in panels (a-b) the y-axis is inverted, with the positive values on the bottom, while in Panel (c) the axes are in the canonical order, and the comparison should be done with a two-photon spectrum as shown in Fig. 1.15(b).

full agreement with this physical picture). While the dressed atom picture has proven to be extremely fruitful for two photons, the N-dimensional case treated in Chapter 4 will make its usage mandatory. In fact we can easily generalize them to arbitrary photon orders and guess which energies are to be avoided in a N dimensional space to harness the best sought configuration of multi-photon emission, without having to undertake any actual computation. Is the concept therefore not justified and should one only be allowed infinite series of Feynman diagrams? We therefore believe that the comments of Shatokhin *et al.* targeting the leapfrog picture bring very little to their physics, if not in fact muddying it with confused statements and blurring their actual contributions that otherwise concur with our results, and of which we wish to remove nothing, as this approach has its merits.

2.4 CONCLUSIONS

In conclusion, I have presented in this Chapter an efficient and numerically-exact technique to simulate photon emission when taking into account the frequency degree of freedom, and applied it to computer experiments that simulate the photon emission from a two-level system under both coherent and incoherent driving, at both low and large pumping. This approach is based on the Quantum Monte Carlo technique, first introduced by Zoller, Marte, and Walls (1987), Carmichael et al. (1989), Dalibard, Castin, and Mølmer (1992), and Mølmer and Castin (1996), applied to the cascaded formalism developed by Gardiner (1993) and Carmichael (1993a). I have shown how the correlations computed from the raw data of the simulation match with the theoretical results provided by del Valle et al. (2012)'s theory of frequency-resolved photon correlations. In the simplest case, I have confirmed with simulated photon emission how filtering spoils antibunching and turns a two-level system into a thermal source, albeit in a more subtle way than is usually assumed. I have also shown more generally how frequency filtering provides a resource to tailor and engineer photon statistics, in particular thanks to its selection of strongly correlated processes such as "leapfrog" transitions that consist in the simultaneous emission of a photon bundle between two non-contiguous dressed states in the level structure of the system, as has been predicted by González-Tudela et al. (2013). This displays rich and potentially useful features that are captured in the Monte Carlo simulation and that would

be similarly observed experimentally. An apparent shortcoming is that the signal is scarce in frequency windows that are the most strongly correlated. This is however a direct consequence of dealing with the quantum part of the signal: there is less of it. Del Valle (2013) further showed that frequency filtering acts as a process akin to distillation, with the same consequence of providing quality at the expense of quantity. Nevertheless, quantum engineering can come to the rescue and using the oldest trick of cavity QED—Purcell enhancement—Sánchez Muñoz et al. (2014a) found *all* the light of the system to be emitted as strongly correlated bundles of photons. In Chapter 4, I will further expand on this idea and show that using cavities to Purcell-enhance leapfrog processes, one can devise new generations of heralded N-photon sources, or, even more generally, bring the system to emit in any desired distribution of photons. Such configurations remain to be studied in detail and, of course, implemented in the laboratory. The latest work from Peiris, Konthasinghe, and Muller (2017), who are so far leading the laboratory implementation of this emerging branch of quantum optics, focused on the side peaks emission and, although they did observe the predicted effect, they failed to break the barrier of a Bell violation which Sánchez Muñoz et al. (2014b) place at in the leapfrog window. Jogenfors, Cabello, and Larsson (2017) have challenged this proof of nonlocality, arguing that the work of Aerts et al. (1999) shows that such setup can only reach a 50% post-selection. It is easily computed that leapfrog emission would break the Franson limit, but in the light shone by Jogenfors et al. (2015) on the Franson configuration's loophole, the new challenge is to turn to stricter conditions of Bell violations such as Chained Bell's inequalities. While Tomasin et al. (2017) have recently demonstrated this, the tunable statistics from the Mollow triplet and its windows of strong correlations make it a promising platform to further test and advance this line of research. Finally, the combinatorial aspects that quickly make such simple problems numerically forbidding also suggest that a two-level system could be used in the laboratory for tests of quantum supremacy directly from photon detections, without a complex system of beam splitters intervening to bring in the quantum complexity, as demonstrated by Broome et al. (2013) and Crespi et al. (2013). All these results leave much room for further works, and we foresee that frequency-resolved photon correlations will become a major theme of photonics. They are relevant even when they are ignored and awareness of the underlying physics should allow to considerably optimize, tune and expand the range of applications of quantum light sources.

3 SINGLE-PHOTON LIGHT

If a thing is worth doing, it is worth doing well.

— Oscar Wilde

3.1 INTRODUCTION

Over a decade ago, O'Brien, Furusawa, and Vučković (2009) and more recently Aharonovich, Englund, and Toth (2016) as well as Senellart, Solomon, and White (2017) noted that single photon sources (SPS) constitute a basic component of the future quantum technologies. Since then, several groups including Kuhlmann et al. (2015), Somaschi et al. (2016), Ding et al. (2016), Wang et al. (2016), Kim et al. (2016), Daveau et al. (2017), Grange et al. (2017), Schlehahn et al. (2018) or Hanschke et al. (2018) among others, have actively pursued their laboratory implementation and are competing for the delivery of the best emitter with the required characteristics. As has been emphasized by, e.g., Dada et al. (2016), Müller et al. (2016), Eisaman et al. (2011), Santana et al. (2017), He et al. (2017), Loredo et al. (2017), Rodiek et al. (2017), and Schweickert et al. (2018), the desiderata for single photon emitters are both of a fundamental character (such as antibunching, purity, indistinguishability, etc.) and of an applied nature (efficiency, price, brightness, etc.). As numerous routes exist to generate single photons, there is a need to compare different emitters from several platforms and operating through various mechanisms. Since the technology is yet within a developmental phase, the most prized properties are still the fundamental ones. As such, one of the defining characteristics of a SPS is the suppression of multiple-photon events. Already in the early 80's, Paul (1982) identified that photon antibunching, a property that refers to the second-order correlation function, defined in Eq. (1.33), satisfying the relation $g_a^{(2)}(0) < g_a^{(2)}(\tau)$, is a good parameter to characterize the multi-photon suppression. In fact, it has long been known (see for instance the books of Gerry and Knight (2005) or Vogel and Welsch (2006)) that antibunching is a proof of the non-classical character of the field and is commonly used as a criterion for the quantum character of a state. Zou and Mandel (1990) proposed another quantity, which became more popular, although it is fundamentally disconnected from antibunching—since in general none implies the other—and consists on the suppression of zero-delay coincidences as compared to random events, namely $g_a^{(2)}(0) < 1$. This describes sub-Poissonian fluctuations and, of particular interest for SPS, the case $g_a^{(2)} = 0$ corresponds to a field with at most one photon at any given time. For this reason, it has been adopted as the criterion to describe single photon sources. However, a mathematical zero is not a good physical observable. Aiming instead for $g_a^{(2)}(0)$ to be very close to zero would be the natural remedy, and has been the one adopted by the quantum optics community at large. This criterion, however, is misleading for the purpose of comparing—or even identifying—single photon sources (SPS). In this chapter, we aim to both reveal the shortcomings of small but nonzero $g_a^{(2)}$ and to propose a fitting substitute. This will allow us to establish a ranking of the best mechanisms for single-photon generation. Our approach is to first identify what constitutes a perfect SPS and then compute how much do the various candidates depart from it.

3.2 THE ROLE OF DETECTION

3.2.1 *Effective quantum state*

Single photon sources and the light that they provide are only useful when they are shone on other objects. The latter collects the emission, and acts as an observer. As we have seen

in Section 1.2.5, the photon correlations of the detected photons are affected by the finite spectral resolution of the observer. This effect can be illustrated using the light emitted by a two-level system (2LS). In principle, the latter can only emit single photons, as it can only sustain one excitation at every instant in time. In fact, the second-order correlation function of a 2LS, given in Eq. (1.50), vanishes exactly when the delay between the photons is zero. However, as we have seen in Fig. 1.15, an observer with a finite resolution sees a large breadth of correlations, depending on the frequencies at which they are looking. The interplay between the temporal and spectral uncertainty of the observer leads, in particular, to a finite zero-delay photon correlation. In turn, this implies that filtering the emission of a 2LS results in nonzero probabilities $p(n)$ to detect $n \geq 2$ photons. There are various ways to understand this result, and we already mentioned how the filter introduces a time uncertainty that can pile-up consecutive photons. More interestingly, from a quantum mechanical viewpoint, the 2LS can be seen to emit a continuous stream of photons at all the possible frequencies, which amplitudes interfere destructively to result in a single photon upon detection. Trimming the tails spoils the destructive interference and allows more than one photon to reach the detector: the frequencies of the photons are in fact a crucial component when it comes to suppressing multi-photon emission.

Since an observer would detect an effective quantum state of the light emitted by the source, and even if the latter is a 2LS the probability of detecting two (or more) photons simultaneously is non zero, we need to describe the frequency-filtered source as an effective source of its own, with a bosonic annihilation operator s. The detector and the effective source are of course related. On the hand, the normalized photon correlations are identical, since the detector measures faithfully the correlations of the (effective) source, namely

$$g^{(n)} = \frac{\langle s^{\dagger n} s^n \rangle}{\langle s^\dagger s \rangle^n} = \frac{\langle \xi^{\dagger n} \xi^n \rangle}{\langle \xi^\dagger \xi \rangle^n} \,, \tag{3.1}$$

where ξ is the annihilation operator of the detector. On the other hand, the conservation of energy imposes that the emission rates of the two systems must be equal:

$$\gamma_\sigma \langle s^\dagger s \rangle = \Gamma \langle \xi^\dagger \xi \rangle \,, \tag{3.2}$$

where γ_σ and Γ are the decay rates of the source and detector, respectively. Thus, combining Eqs. (3.1) and (3.2) we obtain the relation between the unnormalized correlators:

$$\langle s^{\dagger n} s^n \rangle = \left(\frac{\Gamma}{\gamma_\sigma} \right)^n \langle \xi^{\dagger n} \xi^n \rangle \,, \tag{3.3}$$

from which, as I have shown with Zubizarreta Casalengua et al. (2017), one can derive the probability $p(n)$ of find the effective source occupying the Fock state $|n\rangle$. These probabilities are obtained through a bijective map linking them to the photon correlations as

$$p(n) = \sum_{k \leq n} = \frac{(-1)^{k+n}}{n!(k-n)!} \langle s^{\dagger k} s^k \rangle \,, \tag{3.4}$$

where, although in principle the summation has to be done for k up to infinity, it quickly converges for finite (and usually rather small) number of photons. Note that the photon correlations that enter in Eq. (3.4) are unnormalized. While the sensing method of del Valle et al. (2012) and the cascaded formalism (Sec. 1.2.1.2) are equivalent when one is interested in the *normalized* photon correlations, only the cascaded formalism can provide the average population of the detector $\langle \xi^\dagger \xi \rangle$. Thus, in the following we will use the cascaded formalism, and consider the effective quantum state of a filtered 2LS excited either through an incoherent or a coherent driving.

The dynamics of the system is governed by the master equation (1.28), setting $c_1 = \sigma$ (the fermionic annihilation operator of the 2LS), $c_2 = \xi$ (the bosonic annihilation operator of the

detector) and the decay rates as $\gamma_1 = \gamma_\sigma$ and $\gamma_2 = \Gamma$. While the Hamiltonian for the detector is given by $H_2 = \omega_\xi \xi^\dagger \xi$, the Hamiltonian for the 2LS depends on the driving regime. In the case of incoherent driving $H_1 = \omega_\sigma \sigma^\dagger \sigma$ and the master equation needs to be complemented with the Lindblad term $(P_\sigma/2)\mathcal{L}_{\sigma^\dagger}\rho$ to describe the excitation. In the case of coherent driving, the Hamiltonian of the 2LS is given by Eq. (1.45) and the frequency of the detector needs to be referred to the frequency of the driving laser. Thus, the population of the detector is when the 2LS is driven incoherently is given by

$$\langle \xi^\dagger \xi \rangle = \frac{P_\sigma \gamma_\sigma (\Gamma_\sigma + \Gamma)}{\Gamma_\sigma((\Gamma_\sigma + \Gamma)^2 + \Delta^2)}\,, \tag{3.5}$$

while in the case of coherent excitation it reads

$$\begin{aligned}\langle \xi^\dagger \xi \rangle = \Big[& 2\gamma_{01}\Omega_\sigma^2(\gamma_{10}(\gamma_{11}^2 + 4\Delta^2)^2(\gamma_{12}^2 + 4\Delta^2) + 4\Omega_\sigma^2(\gamma_{10}\gamma_{11}^2\gamma_{12}\gamma_{32} \\ & + 4(2\gamma_{10}^3 + 16\gamma_{10}^2\gamma_{01} + 23\gamma_{10}\gamma_{01}^2 + 8\gamma_{01}^3)\Delta^2 - 16(\gamma_{10} - 2\gamma_{01})\Delta^4) + 32\gamma_{11}(\gamma_{10}^2 + 4\Delta^2)\Omega_\sigma^4)\Big] \Big/ \\ & \Big[(\gamma_{10}^2 + 4\Delta^2)(\gamma_{11}^2 + 4\Delta^2)(\gamma_{01}^2 + 4\Omega_\sigma^2)\{\gamma_{10}^4 + 6\gamma_{10}^3\gamma_{01} + 12\gamma_{10}\gamma_{01}(\gamma_{01}^2 + 2\Delta^2 + 4\Omega_\sigma^2) + \\ & \gamma_{10}^2[13\gamma_{01}^2 + 8(\Delta^2 + 2\Omega_\sigma^2)] + 4[\gamma_{01}^4 + 4(\Delta^2 - 2\Omega_\sigma^2)^2 + \gamma_{01}^2(5\Delta^2 + 8\Omega_\sigma^2)]\}\Big]\,,\end{aligned} \tag{3.6}$$

with $\Gamma_\sigma = P_\sigma + \gamma_\sigma$, $\Delta = (\omega_\sigma - \omega_\xi)$ and $\gamma_{ij} \equiv i\Gamma + j\gamma_\sigma$. For the incoherently driven 2LS, the photon correlations observed by the detector can be written in closed form through the recurrence relation (the case out of resonance is also analytical, but too cumbersome to be written here)

$$g_\Gamma^{(n)} = g_\Gamma^{(n-1)} \frac{n\Gamma_\sigma(\Gamma_\sigma + \Gamma)}{[\Gamma_\sigma + (n-1)\Gamma]\left[\Gamma_\sigma + (2n-1)\Gamma\right]}\,, \tag{3.7}$$

where by normalization $g_\Gamma^{(2)} = 1$. Using these normalized correlations and the average population in Eq. (3.5), we can compute the unnormalized correlations and, using Eq. (3.4), obtain the probability to detect n photons from a 2LS driven incoherently:

$$p(n) = C_n \times {}_1F_2\left(n+1; \frac{2n+1}{2} + \frac{\Gamma_\sigma}{2\Gamma}, n + \frac{\Gamma_\sigma}{\Gamma}; -\frac{P_\sigma}{2\Gamma}\right)\,, \tag{3.8}$$

where ${}_1F_2$ is the generalized hypergeometric function and C_n are coefficients that satisfy the recurrence relation

$$\frac{C_n}{C_{n-1}} = \frac{P_\sigma \Gamma}{[\Gamma_\sigma + (n-1)\Gamma][\Gamma_\sigma + (2n-1)\Gamma]}\,,$$

starting with $C_0 = 1$.

Following the same procedure, one can obtain the expressions for the n-th order correlation function and the probability distribution for the coherently driven 2LS. However, these expressions are too bulky to be written here. Figure 3.1 shows the reconstruction of the quantum state of the filtered emission of a 2LS under the two types of driving: incoherent and coherent. Panels (a) and (b) show the emission spectra of the 2LS and the various frequency windows used for the figure. Filtering the emission makes the observed state of light equivalent to the unfiltered emission from a source with a different—in particular, bosonic—probability distribution, shown in panels (c) and (d), for the incoherently and coherently driven 2LS, respectively. In the former case, we used a large driving intensity, $P_\sigma = 10^2\gamma_\sigma$, so that in the case of perfect detection ($\Gamma/\Gamma_\sigma \to \infty$) the observed quantum state is the Fock state with one photon $|1\rangle$. The application of a filter turns the system from a two-level emitter to a source able to deliver more than one photon at a time, namely, for narrow enough filtering, $p(n) \approx (1-\theta)\theta^n$ for all n, with $\theta \approx 0.01$ for the narrowest filter considered here. We have lost two orders of magnitude for the population but the probability to observe two (resp. three) particles is 1% (resp. 0.01%) of that to observe one only, etc., which effectively shows how filtering a single-photon source

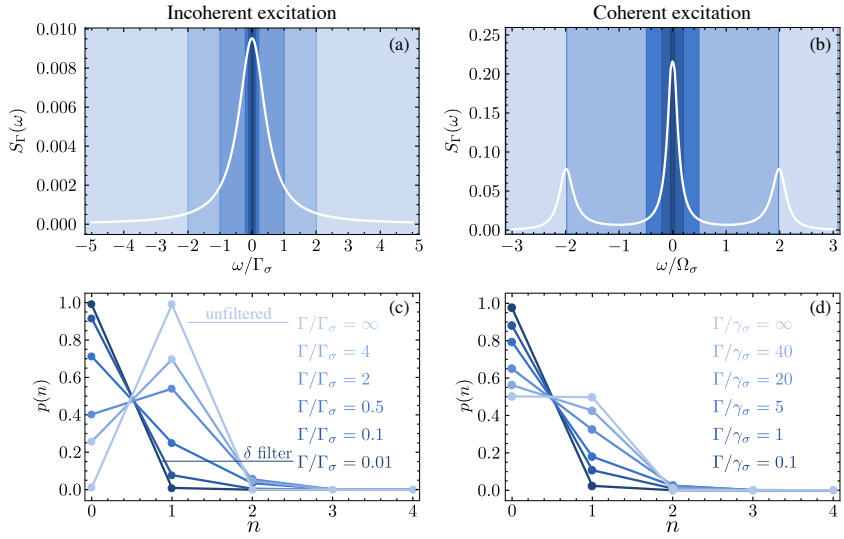

Figure 3.1: Effective quantum state reconstruction from the emission of a frequency-filtered 2LS. (a-b) Emission spectrum of an incoherently and of a coherently driven 2LS, together with several frequency windows that filter the emission. The light filtered in this way is equivalent to the emission of an unfiltered emitter whose quantum state has a distribution $p(n)$ to have n excitations, shown in (c) and (d). For the incoherent driving, case (c), the system is kept in its excited state by large pumping, so that without filtering, one observes a state close to the Fock state $p(n) = \delta_{n,1}$. Filtering leads to thermalization, with preponderance of vacuum but nonzero probability to detect $n > 1$ particles. The same is observed for the coherent driving, case (d), but starting from $p(0) = p(1) = 1/2$ due to the no-inversion of a two-level system in presence of stimulated emission. The figure is obtained with the following parameters: for incoherent excitation, $P_\sigma = 10^2\gamma_\sigma$ (saturating the two-level system). For coherent excitation, $\Omega_\sigma = 5\gamma_\sigma$. The rest of the parameters are as indicated in the figure.

turns it into a black body with nonzero probability to emit n photons. Its population is smaller than without the filter, as the latter is rejecting some photons, but the statistical distribution of those that go through now corresponds to an altogether different quantum state. A similar situation occurs with coherent excitation (when not filtering so much as to isolate the Rayleigh peak), with, for the case shown in Fig. 3.1(d), $\theta \approx 0.025$. In the next section, I will show at which point filtering prevents a single-photon source to emit non-classical states of light, i.e., states that cannot be expressed as a convex mixture of Gaussian state.

3.2.2 *Convex mixture of Gaussian states*

The probability distributions of the filtered 2LS, given in Eq. (3.7) for the incoherent driving and shown in Fig 3.1(c–d) for both types of driving, show that filtering (or, equivalently, using a finite-resolution detector) spoils the photon correlations and the strong quantum character of the source. Filip and L. Mišta (2011) proposed a criterion to identify (truly) quantum states, considering whether they are beyond a convex mixture of Gaussian states (every classical state can be expressed as one such mixture). The criterion of Filip and L. Mišta (2011) for the strong character of a state was given as an upper bound for the probability $p(1)$ of the state being in the Fock state of one photon: No convex mixture of Gaussian states can have this probability larger than $3\sqrt{3}/(4e) \approx 0.477889$. For a 2LS with decay rate γ_σ, excited incoherently at the rate P_σ or excited coherently with an intensity Ω_σ, this is achieved when

$$\frac{P_\sigma}{\gamma_\sigma} \geq \frac{p(1)}{1-p(1)} \approx 0.9153 \qquad \text{or} \qquad \frac{\Omega_\sigma}{\gamma_\sigma} \geq \frac{1}{2}\sqrt{\frac{p(1)}{1-2p(1)}} \approx 1.64368\,. \tag{3.9}$$

There is thus a threshold in pumping to meet this criterion. Higher pumping of course satisfy it even more and in the limit of infinite pumping, the incoherent excitation of a 2LS maintains the pure Fock state $|1\rangle$ in the steady state. This is the most quantum state one can get with respect to a single-particle objective. However, strong pumping is also not good for SPS, as it spoils another important quality: the indistinguishability of the emitted photons. With pumping comes power broadening and photons are emitted with increasingly fluctuating energies. The Fock state $|1\rangle$ emits photons one at a time but at all the frequencies! For the case of coherent driving, increasing the intensity of the driving also makes the state of the emission more quantum, but the emission is again spread over all frequencies (and taking place from three different Lorentzians).

Shortly after Filip and L. Mišta (2011)'s paper, Ježek et al. (2011) showed that considering both the probability of observing the vacuum and a single photons provide a stricter criterion to separate weak classes of quantum states from strong ones. Figures 3.2(a–b) show the probability for the vacuum $p(0)$ and for one-excitation $p(1)$ as a function of the incoherent pumping rate to the 2LS and the filtering linewidth of the detector. The parameter-space that lies on the right of the thick blue line realizes the quantum non-Gaussian states sought for quantum applications, while those on the left can be obtained as convex mixtures of Gaussian states. This confirms that to maintain the quantum character of the source, there is a limit to the filter linewidth. For a pumping rate commensurable with the decay rate, the boundary lies roughly at twice the intrinsic linewidth of the two-level system. Increasing filter bandwidths are required not for higher pumping rates—due to power broadening—but also for vanishing driving, showing that the more scarcely the 2LS is excited, the less quantum it is—due to the deleterious vacuum contribution.

Since the tail events are the main responsible for spoiling the SPS, an emitter whose power spectrum has faster decaying tails than Lorentzian allows to collect more of the photons in a reduced spectral window and thus better preserve its quantum features. The simplest way to achieve this is to turn to coherent driving. In Chapter 6 we will show that in the low intensity regime of the coherent driving, commonly referred to as the Heitler (1944) regime, the processes of absorption and spontaneous emission interfere to yield an emission spectrum with a Student t_2 distribution. This can be further enforced either by turning to quantum rather than classical excitation, in a cascaded scheme of several 2LS in a chain, as I will show

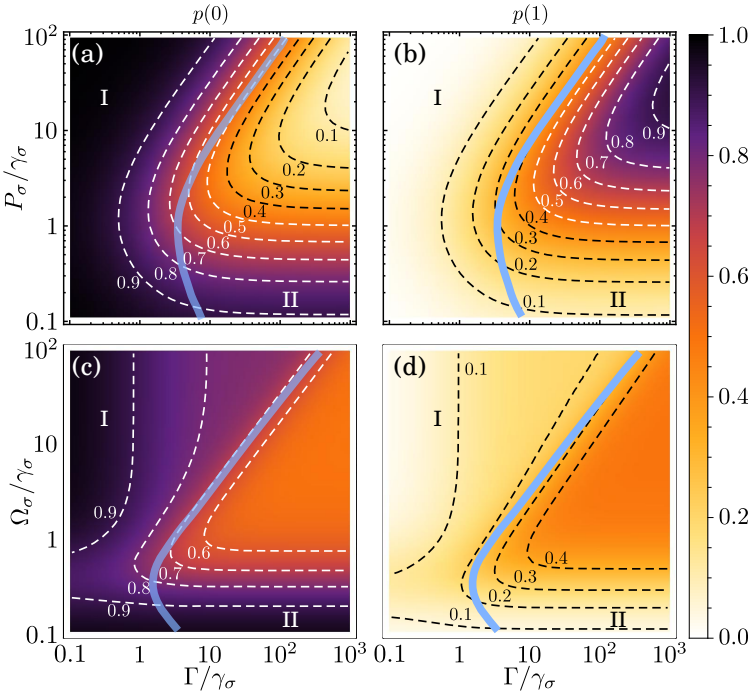

Figure 3.2: Vacuum and single photon probabilities for a frequency-filtered 2LS under incoherent (a & b) and coherent (c & d) excitation. The blue thick contour divides the states that, according to Ježek et al. (2011), exist as a convex mixture of Gaussian states (I) from those that exhibit a strong quantum character (II).

in Chapter 6, or by devising a mechanism that allows the emission of single photons with a spectral width narrower than the natural linewidth of the emitter, as I will show in Sec. 3.3. A drawback of coherent driving is that it forbids total inversion of the 2LS, which, by stimulated emission, is at most half-excited. Therefore, while the $g_\Gamma^{(2)}$ is indeed smaller, the quantum state itself deviates less from convex Gaussian mixtures than under incoherent excitation. This is shown in Figs. 3.2(c–d), which are the counterparts of the above row but for coherent excitation. The probability saturates at $p(1) = 1/2$, which is a considerable impediment to demonstrate a genuine quantum character (e.g., through a negative Wigner function).

The quantum non-Gaussian character of the state, although of great fundamental interest, is clearly not characterizing a SPS (an emitter of N-photon states would also generate non-Gaussian states). The widely used criterion that relies on the second-order correlation function captures the key idea and indeed sets the standard. It presents, however, some subtleties and is frequently mishandled, for instance through a popular criterion $g_\Gamma^{(2)} < 1/2$ that supposedly guarantees the single-photon or single-emitter character of the source. One finds such a misinterpretation in the works of Michler et al. (2000), Verma et al. (2011), di Martino et al. (2012), Lukishova et al. (2012), Palacios-Berraquero et al. (2016), Ishii, Uda, and Kato (2017), Grosso et al. (2017), Lin et al. (2017), Dietrich et al. (2018), and Walker et al. (2018). However, I will show in Chapter 5 that the Hilbert space contains an infinite amount of states with population larger than one, and which still satisfy the condition $g^{(2)} < 1/2$. Although the exact criterion remains $g^{(2)} = 0$, it is surprising that striving for the condition $g^{(2)} \to 0$ leads to incorrect results, as it can be shown that many states have vanishingly small second-order correlation, while also having arbitrarily large third-order correlations. For instance, the state

$$\rho = (297001/300000)\,|0\rangle\langle 0| + (1999/200000)\,|1\rangle\langle 1| + (1/600000)\,|3\rangle\langle 3|\,, \tag{3.10}$$

has $g^{(2)} = 1/10$ and $g^{(3)} = 10$. Thus, considering only the second-order correlation function is not enough to guarantee the single-photon character of a source. Indeed, Filip and L. Mišta (2011) showed that the condition on $g^{(2)}$ alone accommodates as well the weak class of quantum states that consists of convex mixtures of Gaussian states, while single photon sources are pursued for providing stronger quantum resources that allow, e.g., the reconstruction of any other state. From the detected photons, however, the situation is also far from being ideal.

Clearly, in the most general setting, a SPS has to exclude all fanciful designs, possibly deviously conceived fake ones, that would give the illusion of good antibunching through standard $g^{(2)}$ measurements. Brassard et al. (2000) showed that this would open the possibility for photon-number splitting backdoors, which would allow to hack cryptographic protocols by encoding the information in N photon states not detectable at the two-photon level. The conundrum with which we are faced now it the apparent impossibility to observe a source of light that keeps its photon antibunching, while at the same time emitting the photons in a single (or at least narrow) line of frequencies. In the next section, I will develop a theory which, using the homodyning technique brought forward by Vogel (1995), allows to observe simultaneously these two properties.

3.3 SINGLE PHOTONS WITH SUB-NATURAL LINEWIDTH

Recently, Nguyen et al. (2011) and Matthiesen, Vamivakas, and Atatüre (2012) reported the observation of a source of single photons, which spectral width is narrower than the natural linewidth of the emitter. The underlying mechanism is the coherent driving of a 2LS in the Heitler regime. There, the emission spectrum of the 2LS is given by Eq. 1.47, which describes a δ-narrow line sitting on top of a Lorentzian with a width given by the decay rate of the 2LS γ_σ. The delta function term is the Rayleigh peak attributed to the elastic scattering of the laser photons by the 2LS, while Dalibard and Reynaud (1983) showed that the Lorentzian term comes from the actual photon excitation and re-emission. Note that in the linear regime, and particularly in the limit $\Omega_\sigma \to 0$, and excluding second order terms (which involve two-photon states in the detector), the spectrum of emission reduces to the delta function. Furthermore,

since photon correlations of the emitted light are perfectly antibunched (cf. Eq. 1.48), Nguyen et al. (2011) and Matthiesen, Vamivakas, and Atatüre (2012) claimed that they had a source of spectrally ultra-narrow single photons. In fact, if one is interested in the spectral density of isolated one-photon events only, regardless of their time of arrival or their relation to other photons, the source is effectively providing photons as spectrally narrow as the laser (here infinitely narrow making the source perfectly monochromatic). However, if such photons are to be used in temporal relation with others, such as when considering their statistical properties (such as their antibunching), then the second-order part of the spectrum must be taken into account. As we have seen in Section 1.2.6, by having the frequency resolution below the natural emitter linewidth (in order to maintain a narrow spectrum to first order) one filters out part of the incoherent spectrum which determines its statistics. On the other hand, increasing the temporal precision—by increasing the frequency resolution of the detector—broadens the spectrum. As a result, resolving antibunching can be expected to spoil the subnatural linewidth of the source, and vice-versa. Thus, with the setups used in their experiments, these authors cannot observe the two properties simultaneously, which means that an object excited with this light will not observe them either. In the rest of this Section, I will develop a proposal that allows to obtain such a sub-natural linewidth SPS.

3.3.1 *Antibunching in resonance fluorescence and the impact of detection*

We are interested in the low-driving regime of resonance fluorescence, i.e., the Heitler (1944) regime. In this scenario, the emitter is modelled as a two-level system with annihilation operator σ and is driven coherently with a weak laser of intensity Ω_σ. We assume that the laser is exactly at resonance with the two-level transition for simplicity, but everything can be easily generalized to the close-to-resonance case by adding a detuning parameter, as shown by López Carreño et al. (2019). Importantly, we take into account the *physical detection* of resonance fluorescence. This is a central point of our approach as it allows us to consider the physical, self-consistent and complete description of the source. The technical aspects of how to do this were given in Section 1.2.5, and following these ideas our detector is therefore considered as an harmonic oscillator, with bosonic annihilation operator a, which makes the full

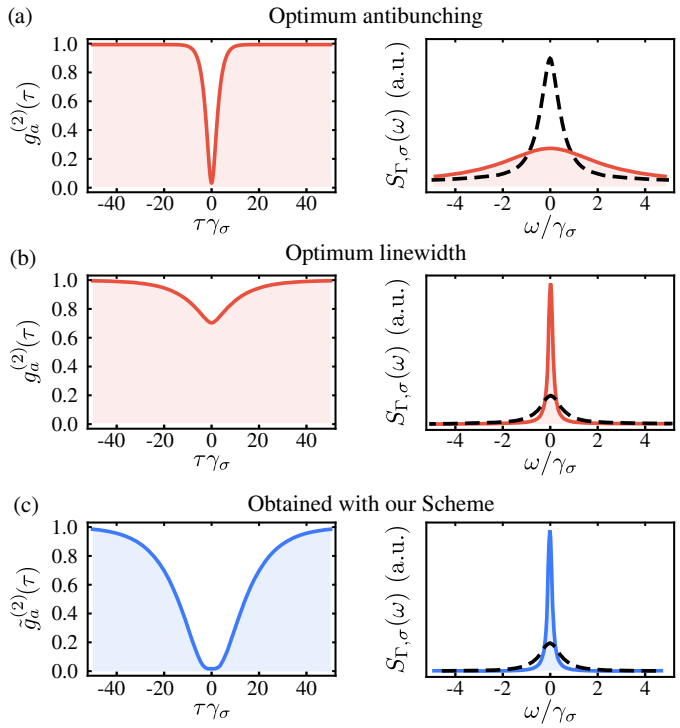

Figure 3.3: Schematics of the effect that filtering has on the emission spectrum and the photon statistics. (a) Using spectrally wide detectos to measure antibunching broadens the spectrum of emission (solid red) as compared to the naturel linewidth of the emitter (dashed black). (b) Using spectrally narrow detectors resolves well in frequency but spoils the antibunching. (c) Using the scheme presented in this Section using narrow detectors, we can have simultaneously perfect antibunching and narrow spectrum (solid blue).

and self-consistent description of filtered resonance fluorescence an easy theoretical problem. Indeed, the master equation describing this complete system is given by Eq. (1.40) with $\xi = \sigma$, $\Gamma_\xi = \gamma_\sigma$ and $\gamma_a = \Gamma$. The Hamiltonian of the system, $H = \Omega_\sigma(\sigma + \sigma^\dagger) + g(a^\dagger\sigma + \sigma^\dagger a)$, describes the laser driving the two-level system (at resonance and with an intensity Ω_σ that we consider to be real without loss of generality) and its coupling to the detector is taken as g (also real). We set the detector at resonance with both the laser and the two-level system.

The effect that filtering has on the photon correlations of the emitted light can be expressed in a quantitative way. Let us consider the Nth-order correlation function, $g_a^{(N)}$, of resonance fluorescence as measured by a detector with both frequency and time resolution (set at resonance with the source). The expressions for a general laser driving strength exist but are bulky (see, for instance Eq. (5.12b) for the case $N = 2$). However, since in this Chapter were are interested in the Heitler regime, it is enough to expand these expressions to the lowest order in the driving, which is, for $\langle a^{\dagger N} a^N \rangle$, to order $O(\Omega_\sigma^{2N})$. This allows us to generalize to all orders the expression for the correlations, which simply reduces to (for $N \geq 2$):

$$g_a^{(N)} = \prod_{k=1}^{N-1} \frac{\gamma_\sigma^2}{(\gamma_\sigma + k\Gamma)^2} \,. \tag{3.11}$$

As expected from del Valle et al. (2012)'s theory, when $\Gamma \to \infty$, this expression recovers the perfect antibunching of the source itself, i.e., when the full emission is being detected without any frequency resolution: $\lim_{\Gamma\to\infty} g_a^{(N)} = g_\sigma^{(N)} = 0$. In the opposite limit of narrow frequency filtering, we recover the result for a coherent field: $\lim_{\Gamma\to 0} g_a^{(N)} = 1$ for all N. With the present semi-classical model for the laser, which has zero linewidth (perfect first-order coherence), we do not recover the expected thermal value for photons of completely undetermined time of emission, i.e., $\lim_{\Gamma\to 0} g_a^{(N)} \neq N!$, because it is impossible to filter inside a laser width when it is itself vanishing, as observed by González-Tudela et al. (2013). For a general intermediate Γ, the perfect antibunching needed for quantum applications is spoiled: $0 < g_a^{(N)} \leq 1$. For instance, when filtering at the natural linewidth of the emitter $\Gamma = \gamma_\sigma$, we obtain a reduction of 25% in the antibunching ($g_a^{(2)} = 1/4$) and $\Gamma = \gamma_\sigma/3$ leads to $g_a^{(2)} = 0.56$. As a consequence, making use of the subnatural spectral width of such a SPS, as done by Nguyen et al. (2011) and Matthiesen, Vamivakas, and Atatüre (2012), which implies detecting its photon with some accuracy in time and frequency, or coupling its output light to an optical element with $\Gamma < \gamma_\sigma$, spoils its statistical properties. In summary, subnatural linewidth and antibunching are in contradiction for resonance fluorescence in its bare form. The system emits photons which one can choose to see, depending on the detection scheme, with the properties of the driving laser or of the emitter, but not simultaneously.

In order to address this discouraging issue, let us dive deeper into the mechanism that yields antibunching in resonance fluorescence when integrating over its full spectrum, with $\Gamma \to \infty$. This can be understood in terms of interfering fields: Mandel (1982) and Carmichael (1985) already knew that the emission of a coherently driven two-level system can be expressed as a superposition of a coherent and a squeezed incoherent field. We apply a mean field procedure and write $\sigma = \alpha + d$, with a mean coherent field $\alpha = \langle\sigma\rangle$ and d an operator for the quantum fluctuations characterized by $\langle d \rangle = 0$. The coherent field is the one that gives rise to the delta function in the spectrum of emission (1.47) while the Fourier transform of $\langle d^\dagger(0) d(\tau)\rangle$ provides the Lorentzian peak, i.e., the incoherent part of the spectrum, that transforms into the Mollow (1969) triplet when the intensity of the driving increases. Working out $g_\sigma^{(2)}$ in term of this decomposition results in four contributions:

$$g_\sigma^{(2)} = 1 + \mathcal{I}_0 + \mathcal{I}_1 + \mathcal{I}_2 \,, \tag{3.12}$$

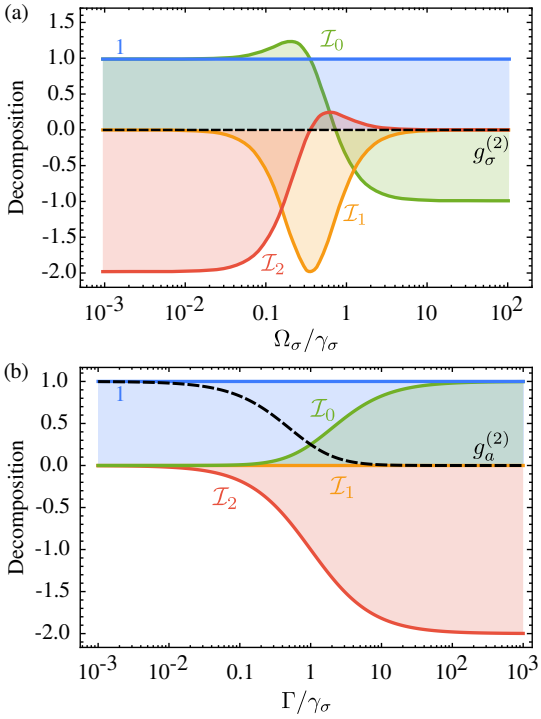

Figure 3.4: (a) Second-order correlation function of the emission from a two-level system (dashed black line) and its decomposition Eq. (3.12) into the four components (solid colored lines) given by Eqs. (3.13a-3.13c), as a function of the laser excitation. Regardless of the driving regime, the total emission fulfills $g^{(2)}_\sigma = 0$. In the Heitler regime, on the left hand side, this is due to a destructive interference at the two-photon level between the coherent and incoherent (squeezed) components of resonance fluorescence. In the strong driving regime, right-hand side, perfect antibunching is due to the dominating sub-Poissonian fluctuations. (b) The same decomposition but now for the filtered emission $g^{(2)}_a$ and as a function of Γ in the Heitler regime ($\Omega_\sigma = 10^{-3}\gamma_\sigma$). In this case, antibunching gets spoiled as the frequency-resolution is increased by filtering, leading to an imperfect compensation of the components. This can however be restored with an external laser.

that grow as powers of α:

$$\mathcal{I}_0 = \frac{\langle d^{\dagger 2} d^2\rangle - \langle d^\dagger d\rangle^2}{\langle n_\sigma\rangle^2} = |\alpha|^2 \frac{6\langle n_\sigma\rangle - 4|\alpha|^2}{\langle n_\sigma\rangle^2} - 1\,, \tag{3.13a}$$

$$\mathcal{I}_1 = 4\frac{\Re(\alpha^*\langle d^\dagger d^2\rangle)}{\langle n_\sigma\rangle^2} = 8|\alpha|^2 \frac{|\alpha|^2 - \langle n_\sigma\rangle}{\langle n_\sigma\rangle^2}\,, \tag{3.13b}$$

$$\mathcal{I}_2 = 2\frac{|\alpha|^2\langle d^\dagger d\rangle + \Re(\alpha^{*2}\langle d^2\rangle)}{\langle n_\sigma\rangle^2} = 2|\alpha|^2 \frac{\langle n_\sigma\rangle - 2|\alpha|^2}{\langle n_\sigma\rangle^2}\,. \tag{3.13c}$$

This decomposition is what one would obtain when performing a $g^{(2)}$ measurement on the output of a beam splitter, that would have σ as the associated output arm operator, with input fields α and d. This is the well known homodyne measurement, first suggested by Vogel (1991) to analyze the squeezing properties of signal d thanks to the controlled variation of a local oscillator α. The numerator of $\mathcal{I}_0$ in the left-hand side of Eq. (3.13a) is the normally ordered variance of the fluctuation intensity, i.e., $\langle :(\Delta n_d)^2: \rangle = \langle :n_d^2: \rangle - \langle n_d\rangle^2$ with $n_d = d^\dagger d$ and $\Delta n_d = n_d - \langle n_d\rangle$. Therefore, having $\mathcal{I}_0 < 0$ indicates sub-Poissonian statistics of the fluctuations, which, in turn, contributes to the sub-Poissonian statistics of the total field σ. The numerator of $\mathcal{I}_1$ in Eq. (3.13b) represents the normally ordered correlation between the fluctuation field-strength and intensity, $\langle d^\dagger d^2\rangle = \langle :\Delta d\, \Delta n_d:\rangle$, to which Vogel (1991) and Vogel (1995) referred to as *anomalous moments*. A squeezed-coherent state has such correlations. The numerator of the last component, $\mathcal{I}_2$, in Eq. (3.13c), can be written in terms of one of the fluctuation quadrature $X = (d + d^\dagger)/2$, in the following way: $4|\alpha|^2\left(\langle :X^2:\rangle - |\alpha|^2\right)$. If this is negative, there is some quadrature squeezing.

The four terms of this decomposition for $g^{(2)}_\sigma$ are shown in Fig. 3.4(a), as a function of the intensity of the driving laser. They always compensate exactly and the final result is, of course, the perfect sub-Poissonian statistics of the two-level system emission. However, as is clear in the figure and has been shown by Carmichael (1985), this compensation occurs in different ways depending on the driving regime:

- In the region of large driving ($\Omega_\sigma \gg \gamma_\sigma$), where the spectrum of the emitter displays a Mollow triplet, we have that $\mathcal{I}_0 = -1$ with $\mathcal{I}_1 = \mathcal{I}_2 = 0$ meaning that antibunching appears

solely due to the sub-Poissonian statistics of the fluctuations, that dominate over the vanishing coherent component $\lim_{\Omega_\sigma \to \infty} \alpha = 0$ (and therefore $d \to \sigma$).

- In the intermediate driving region ($\Omega_\sigma \sim \gamma_\sigma$), it is $\mathcal{I}_1 < 0$ that almost fully compensates the positive contributions of $1 + \mathcal{I}_0$. This is where $\mathcal{I}_0$ changes sign and the fluctuations become super-Poissonian.
- In the Heitler regime ($\Omega_\sigma \ll \gamma_\sigma$) that interests us more particularly, it is the fluctuation squeezing that plays a major role, being this time the one responsible for antibunching, $\mathcal{I}_2 = -(1 + \mathcal{I}_0) = -2$.

Note that in the Heitler regime, $\mathcal{I}_1$ vanishes again. Consequently, resonance fluorescence reaches its maximum squeezing also in this region, an effect that has been confirmed in the emission from ensembles of atoms by, e.g., Slusher et al. (1985), Raizen et al. (1987), Lu, Bali, and Thomas (1998), McCormick et al. (2007), and McCormick et al. (2008), and recently on single atoms by Ourjoumtsev et al. (2011) and quantum dots by Schulte et al. (2015). Another way to understand the origin of antibunching in this region is as an interference between the coherent and incoherent parts of the emission (c.f. Eq. (1.47), since those terms which are either purely coherent (1) or purely incoherent ($\mathcal{I}_0$), are fully compensated by the 50%-50% mixed one, $\mathcal{I}_2$.

One can also compute the decomposition for the filtered second-order correlation function $g_a^{(2)}$ by applying again Eqs. (3.13a-3.13c), now with the detector field operators, that is with $a \to \sigma$, $\langle n_\sigma \rangle \to \langle n_a \rangle$ and $\alpha = \langle a \rangle$. This is shown in Fig. 3.4(b) for the Heitler regime as a function of the filter width Γ. One can see how, with filtering, or equivalently when detection is taken into account, the terms no longer exactly compensate each other and their sum do not add up to exactly $g_a^{(2)} = 0$. Speaking in spectral terms, this is because the filter is leaving out some of the incoherent part that should compensate for the fixed coherent one (the delta function is always fully included in the convolution with the filter centered at $\omega_L = 0$). In the Heitler regime, this is clear when $\Gamma < \gamma_\sigma$, since γ_σ is the width of the (incoherent) Lorentzian peak, as shown in Eq. (1.47).

3.3.2 *Destructive N-photon interference and antibunching restoration*

The decomposition of the filtered second-order correlation function $g_\sigma^{(2)}$ outlined above allows us to determine what is missing in terms of coherent and/or incoherent fractions to produce the perfect antibunching. Since the compensation comes, in part, from a coherent field, and such a field is easy to produce and control in the laboratory (with a laser), one can actually *restore* full antibunching by superimposing to the filtered resonance fluorescence an external coherent field β, making them interfere at a beam splitter, and collecting the new signal for further use or analysis. We can find theoretically the value of β that ensures that the resulting total field, $s = t\,\sigma + r\,\beta$. Here, t and r are the transmission and reflection coefficients of the beam splitter, respectively, taken real and such that $r^2 + t^2 = 1$. Although the emission has been filtered, it still produces perfect antibunching at the output. We will call $\tilde{g}_a^{(2)}$ the second-order correlation function of this filtered signal that is interfered with a correcting external coherent beam, and proceed to show how to cancel it despite the filtering. This, in effect, realises the previously claimed subnatural linewidth SPS proposed by Nguyen et al. (2011) and Matthiesen, Vamivakas, and Atatüre (2012). This becomes possible because the source is not a passive object anymore, that relates time and frequency of its emission merely through the Fourier transform, but includes a dynamical element. We will see in the following that, as a consequence, our source even achieves more than joint subnatural linewidth and antibunching.

The principle for antibunching restoration is simple: since the filtering reduces the incoherent fraction, β should lower (proportionally) the coherent fraction. This is possible for two coherent fields by destructive interferences. That is, given that at resonance $\alpha = -i|\alpha|$, we should find a β of the form $\beta = i|\beta|$ such that the total mean field is reduced to $-i(t|\alpha| - r|\beta|)$. Out of resonance, both α and β have imaginary and real parts but the same idea would apply. This protocol and

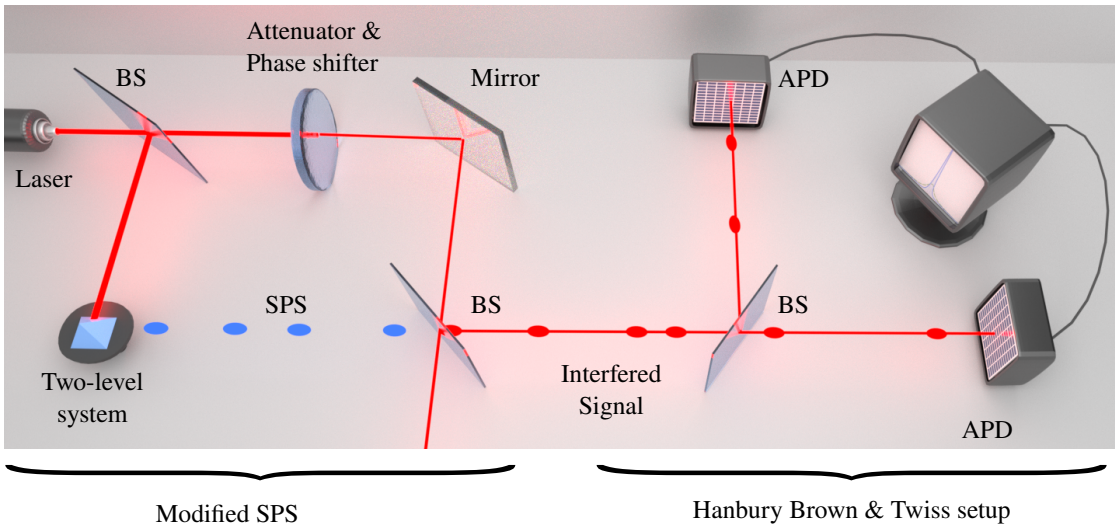

Figure 3.5: Scheme of our proposed setup to generate a SPS for which one can simultaneously measure, in the same experiment and with both time- and frequency-resolving detectors, a narrow spectrum of emission and perfect antibunching. From left to right: part of the excitation laser (red beam) is attenuated and π-phase shifted, to later interfere with the resonance fluorescence signal (blue dots). The right-hand side of the table represents a standard Hanbury-Brown-Twiss setup to measure the second-order correlation of the total signal

the condition for the external β-field are one of the chief results of this text. We now proceed to describe a possible setup to realise this interference and a theoretical model that provides an exact analytical condition.

The simplest and most reliable way to interfere resonance fluorescence with a controlled coherent field is to divert some light from the laser that excites the two-level system in the first place. In this way, one works with the same coherence time of the driving laser and should be immune to slow fluctuations. A possible setup is sketched in Fig. 3.5: The laser beam passes through a first beam splitter, that redirects part of it to the two-level system on one output arm and to an attenuator and a phase shifter on the other output arm. We have not taken into account the first beam splitter of Fig. 3.5 in the calculations for simplicity, but, assuming it is balanced (50:50), doing so would simply rescale the original driving to $2\Omega_\sigma$ in order to obtain the results presented here. The emission of the two-level system (σ) and the attenuated laser (β) are admixed at a second beam splitter. The output constitutes our new antibunched source $s = t\,\sigma + r\,\beta$, which can be further analysed, measuring, for instance, its second-order correlation function in a Hanbury Brown–Twiss setup, as depicted in the figure.

In the theoretical description, we include the detectors in the dynamics to now receive simultaneously the attenuated laser and the emission of the emitter $s = t\,\sigma + r\,\beta$. This is modeled by adding a coherent driving term to the detector $H_a = i\Omega_a(a^\dagger - a)$, substituting $H \to H + H_a$ in the master equation, with $\Omega_a \in \mathbb{R}$. Note that the phase of driving to the detector is fixed to $\beta = i\Omega_a/g$ and the resulting Hamiltonian is then $H + H_a = \Omega_\sigma\sigma + g(t\sigma + ir\Omega_a/g)a^\dagger + \text{h. c.}$ In this way, the detector is effectively performing a homodyne procedure between the light emitted by the two-level system and a coherent field with amplitude $r\Omega_a/(tg)$. Furthermore, our model describes detection self-consistently and allows us to study the joint dynamical properties (in both time and frequency) of the light produced by the superposition. Since we are interested in the low driving limit, we express Ω_a in terms of Ω_σ through a new dimensionless parameter:

$$\mathcal{F} = \frac{r}{t}\frac{\gamma_\sigma\Omega_a}{g\Omega_\sigma}\,. \tag{3.14}$$

We also define $\mathcal{F}' = \mathcal{F}t/r$, which absorbs the dependence on the transmission and reflection parameters of the beam splitter. We take both $\mathcal{F}$ and $\mathcal{F}'$ to be real and positive. With these definitions, $\beta = i\Omega_\sigma \mathcal{F}'/\gamma_\sigma$ and it is clear that $100\mathcal{F}'$ is then the percentage of the laser intensity that finally interferes with resonance fluorescence, while $\mathcal{F}$ is the fraction that is needed to attenuate the laser for the compensation to be effective. The total mean field of the signal that exits the beam splitter towards detection (the right-hand side in Fig. 3.5) reads $\langle s\rangle = t\alpha + r\beta = -i\Omega_\sigma t(2-\mathcal{F})/\gamma_\sigma$.

Next, we solve the new master equation in the Heitler regime, finding that the detected Nth-order correlation function is

$$\tilde{g}_a^{(N)} = g_a^{(N)} \left[\frac{\sum_{k=0}^{N} \binom{N}{k} 2^k (-\mathcal{F}')^{N-k} \prod_{\lambda=1}^{N-k} [1 + (N-\lambda)\Gamma/\gamma_\sigma]}{(2-\mathcal{F}')^N} \right]^2 , \tag{3.15}$$

where $\tilde{g}_a^{(N)}$ is for the compensated signal and $g_a^{(N)}$ is given by Eq. (3.11). Note that all $\tilde{g}_a^{(N)}$ have a divergence at $\mathcal{F}' = 2$, independently of the filtering parameter Γ/γ_σ. This is another type of interference related to superbunching, which lies beyond the scope of the present analysis and is further discussed by Zubizarreta Casalengua et al. (2019). For $N = 2$ the correlation in Eq. (3.15) simplifies to

$$\tilde{g}_a^{(2)} = \left[\frac{4\gamma_\sigma - (4-\mathcal{F}')\mathcal{F}'(\gamma_\sigma + \Gamma)}{(2-\mathcal{F}')^2(\gamma_\sigma + \Gamma)} \right]^2 , \tag{3.16}$$

which becomes exactly zero when the attenuation factor takes the two values

$$\mathcal{F}'_{2,\pm} = 2\left(1 \pm \sqrt{\frac{\Gamma}{\Gamma + \gamma_\sigma}}\right) . \tag{3.17}$$

This result is valid to first (leading) order in Ω_σ, meaning that when the condition (3.17) is fullfilled, $\tilde{g}_a^{(2)} = 0$ with deviations due to higher-order terms in the driving only, so remaining extremely small. The antibunching becomes "exactly zero" only in the limit of vanishing driving. In fact, together with Zubizarreta Casalengua et al. (2017), I have shown that if the second-order correlation function $\tilde{g}_a^{(2)}$ is exactly zero, then also all higher-order terms would satisfy $\tilde{g}_a^{(N)} = 0$ for $N \geq 2$ and provide the ultimate, perfect SPS that emits a Fock state of a single photon. In the Heitler regime, but with a finite signal, the antibunching remains so small as to be well approximated by zero on the figures, in contrast to normal resonance fluorescence.

Note that the protocol outlined above becomes meaningless for two extreme cases: in the limit of broad filters, where we recover perfect antibunching without the interference, $\lim_{\Gamma\to\infty} \mathcal{F}'_{2,-} = 0$, and in the limit of vanishingly narrow filters, where $\lim_{\Gamma\to 0} \mathcal{F}'_{2,\pm} = 2$ and $\tilde{g}_a^{(N)}$ diverges. The latter case means that if the filter is very narrow, compensating for the loss of the incoherent component becomes impossible, as one ends up removing completely the coherent component, thus ending with no signal whatsoever. One can nevertheless reduce the linewidth by over an order of magnitude as compared to the natural linewidth of the emitter, which amply qualifies as a subnatural linewidth.

The two solutions in Eq. (3.17) correspond to two different mean fields that, despite having different phases, lead to the same intensity in the interference signal, $\langle s_\pm\rangle = t\alpha + r\beta_\pm = \pm 2i\Omega_\sigma t/\gamma_\sigma \sqrt{\Gamma/(\Gamma+\gamma_\sigma)}$, and, therefore, both successfully compensate for the incoherent component, recovering perfect antibunching for any given realistic detection resolution Γ. Nevertheless, they are of a very different character: $\mathcal{F}'_{2,+}$ changes the phase of the original mean field, from $\alpha = -i|\alpha|$ to $\langle s_+\rangle = i|t\alpha + r\beta_+|$, while $\mathcal{F}'_{2,-}$ corrects for the intensity maintaining the same phase $\langle s_-\rangle = -i|t\alpha + r\beta_-|$. This manifests in the higher-order correlation functions (3.15): while evaluating them at $\mathcal{F}' = \mathcal{F}'_{2,+}$ does not lead to small values, for $\mathcal{F}' = \mathcal{F}'_{2,-}$ they remain close to zero as well (although in general they do not recover the exact zero). For every N, there are two values, $\mathcal{F}'_{N,\pm}$, that lead to $\tilde{g}_a^{(N)} = 0$, but they do not imply zero values for the other functions in general. Remarkably, for a given N and the parameter $\mathcal{F}'_{N,-}$, there is always a $\Gamma_{N,N'}$

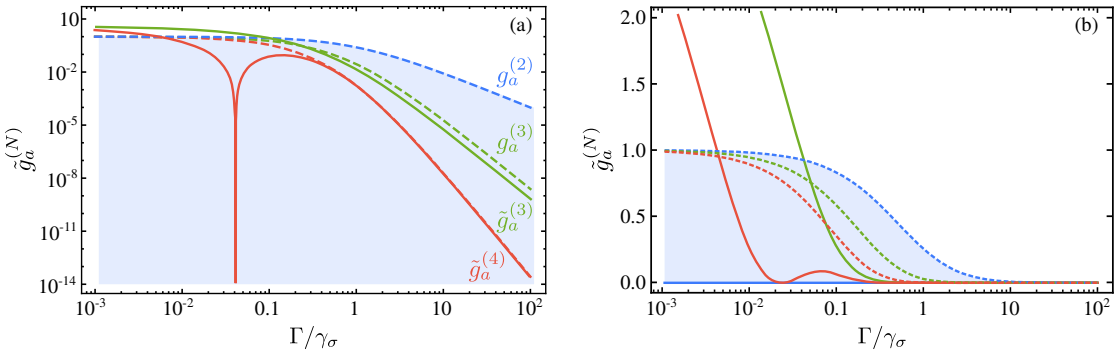

Figure 3.6: Comparison between, on the one hand, the Nth-order correlation function for the filtered light $\tilde{g}_a^{(N)}$ with the interference signal, Eq. (3.15), at the condition of perfect antibunching, $\mathcal{F}' = \mathcal{F}'_{2,-}$ (solid lines), with, on the other hand, the corresponding case $g_a^{(N)}$ without the interference, i.e., normal resonance fluorescence (dashed lines). The main panel is in logarithmic scale and the inset in linear scale. $\tilde{g}_a^{(2)}$ only appears in the linear scale because it is exactly zero for all Γ. Panels (a) and (b) show the lines in Logarithmic and Linear scale, respectively.

for which also the coherence function N' is exactly zero, as long as $N' > N+1$. Therefore, exact zeros are found for pairs of coherence functions, $\{N, N' > N+1\}$, when using this particular pair of parameters $\{\mathcal{F}_{N,-}, \Gamma_{N,N'}\}$. For instance, $\Gamma_{2,4} = \gamma_\sigma/24$ and $\Gamma_{2,5} = (4 \pm \sqrt{13})\gamma_\sigma/12$. Since the antibunching obtained with our scheme is due to interference between coherent and incoherent components and there are only two parameters left in Eq. (3.16), it is reasonable that the condition $\tilde{g}_a^{(N)} = 0$ can be satisfied for two different N, N' simultaneously, obtaining two conditions for $\mathcal{F}'$ and Γ. Note that, by performing a *wavefunction expansion*, following the procedure described by Carmichael, Brecha, and Rice (1991) and Bamba et al. (2011), on the joint state of the emitter and detector, the attenuation fractions in Eq. (3.17) yield a suppression of the two-photon probability in the detector. This has also been observed by Zubizarreta Casalengua et al. (2019), and it corroborates the idea that perfect antibunching is restored due to an interference effect at the two-photon level, that is, involving not only coherently scattered photons but also the incoherent (second order) ones in Eq. (1.47).

In Fig. 3.6, we show the correlation functions for the interfered signal, Eq. (3.15), when the condition for perfect antibunching is met, i.e., $\mathcal{F}' = \mathcal{F}'_{2,-}$, so that $\tilde{g}_a^{(2)} = 0$ (solid lines), and we compare it to the case without the interference, i.e., $\mathcal{F}' = 0$ (dashed lines), which is the case from Nguyen et al. (2011) and Matthiesen, Vamivakas, and Atatüre (2012). We plot the cases $N = 2$ (blue), 3 (green) and 4 (red), as a function of the spectral width of the detector, Γ/γ_σ. Note that the solid blue line does not appear in the main figure, which is in logarithmic scale, because its value is exactly zero to this order in the Heitler regime. This is the main result as compared to $g_a^{(2)}$ which, although it can get relatively small, can do so only for broad linewidths, and loses its antibunching for narrow lines. In stark contrast, the perfect antibunching for the interfered signal remains satisfied even when the filter is much narrower than the natural linewidth of the emitter. On the other hand, the higher-order correlation functions also yield noteworthy results, which we will only briefly discuss. In contrast to $\tilde{g}_a^{(2)}$ which always remain much smaller than its unfiltered counterpart, there are filter linewidths where the interference results in larger higher-order correlations as compared to the standard case. This is clear in the inset of Fig. 3.6 which is in linear scale. If one wants to remain within small values of this higher-order functions, this limits how narrow the filtering can be, though still allowing for considerable improvement. We have also already noted how one is limited by the signal. Finally, even though perfect antibunching remains true for arbitrarily narrow filters in the theory, as $\Gamma \ll \gamma_\sigma$, the system would become unstable under increasingly small variations of the laser intensity: $\lim_{\Gamma\to 0} \mathcal{F}'_{2,-} = 2$, which is a diverging point for $\tilde{g}_a^{(2)}(\tau)$. Zubizarreta Casalengua et al.

(2019) have shown that a small fluctuation in the laser intensity would bring the system from perfect antibunching to a huge superbunching. This could be seen as an advantage, providing a highly tunable quantum photon source that can be switched between antibunching and bunching by slightly adjusting the second laser attenuation. However, this superbunching effect also follows from an interference and is not linked to N-photon emission or other types of structured emission.

A representative filter linewidth for optimal operation can be taken as $\Gamma = \gamma_\sigma/5$, which we also use as the reference case in the following figures, because it is well below the natural emitter linewidth and brings an improvement essentially everywhere, i.e., we find that the interference yields the values $\tilde{g}_a^{(2)} = 0$, $\tilde{g}_a^{(3)} = 0.36$ and $\tilde{g}_a^{(4)} = 0.08$ while without the interference, one gets $g_a^{(2)} = 0.69$, $g_a^{(3)} = 0.35$ and $g_a^{(4)} = 0.14$. Note also the existence of a second local minimum for $\tilde{g}_a^{(4)}$ in Fig. 3.6. We find that there is such a local minimum for all higher-order correlators except the one that immediately follows the one that is exactly cancelled by the interference (i.e., $\tilde{g}_a^{(3)}$ in this case).

Further discussion of the quantum state generated by this interference would lead us too far astray. Furthermore, in the light of the effect that filtering the light has on its statistics, and the way in which the photon correlations can be corrected to restore the antibunching, we now turn to the criteria that can be used to quantify: i) how well the sources provide single photons, and ii) how close they are to being an ideal source of single photons.

3.4 CRITERIA FOR SINGLE PHOTON SOURCES

In the previous two sections we have insisted in how relevant it is to take into account the detection in the description of the emission of light, and how the apparent perfect antibunching from the archetype of SPS can be spoiled by observing it. In this section I will propose two criteria that can be used to characterize SPS and to quantify their single-photon "purity".

3.4.1 *According to the photon correlations*

The discussion that we had in Section 3.2 led us to conclude that when the detection process is taken into account, the suppression of the second-order correlations function is not enough to guarantee the single-photon character of a stream of photons. Conversely, one needs to strive for the suppression of the photon correlations to *all* orders. Thus, we propose a novel criterion to identify and compare usefully SPS which does that. Namely, we propose the N-norm of the vector of correlation functions:

$$\|(g_a^{(k)})\|_N \equiv \sqrt[N]{\sum_{k=2}^{N+1} g^{(k)^N}}\,, \tag{3.18}$$

that quantifies the deviation from the ideal SPS, perfectly antibunched to all orders. The criterion is then that $\|(g_a^{(k)})\|_N$ should be as small as possible (not simply the $g^{(2)}$, which is the 1-norm) for N as high as technically feasible. In the limit $N \to \infty$, the quantity becomes $\|(g_a^{(k)})\|_\infty = \max(g^{(k)})$ and measures the failure of the SPS by the order at which it less suppresses multiple-photon emission.

In Fig. 3.7, we show the result for several popular sources, limiting to the 3-norm (i.e., measuring up to $g_a^{(4)}$), which is enough for the chosen cases that do not engineer scenarios where the SPS breaks for large photon numbers. This is as a function of the spectral filtering bandwidth, that, as already discussed, is a key parameter for photon correlations, and we will describe a realistic experiment. The incoherently driven 2LS sets a useful reference. As the filtering window is enlarged, our measure in Eq. (3.18) indeed decreases. The coherently driven 2LS, in comparison, decreases much faster, and this confirms the known fact that resonant excitation provides better antibunching than the non-resonant case. This is the case at low

driving, since at high driving, the system enters the Mollow (1969) triplet regime, and the photon correlations vary strongly with their frequency, thus spoiling its SPS attributes. The cascading scheme I proposed, in which a 2LS is driven by the emission of another 2LS driven by the emission of a third 2LS, and which I will discuss in details in Chapter 6, is confirmed as a better SPS than under classical resonant driving, although the slope is the same as for the conventional case. The slope, however, can be enhanced through the interferometric scheme that I proposed in Sec. 3.3. This source (shown in Fig. 3.7 as a solid red line) provides the smallest 3-norm down to $\Gamma/\gamma \approx 1/5$, when it is surpassed by the 2LS driven either with a coherent or an incoherent emitter. However, at such a filter width the 3-norm of these three sources is already ≈ 1. Therefore, the source described in Sec. 3.3 is in fact the best SPS of our selection.

A value of this criterion resides in its identification of sources with a strong two-photon antibunching (small $g^{(2)}$) but that fail to higher orders. This the case for instance of a biexciton, i.e., a molecule binding two excitons (electron-hole pairs). It supports two excitons with opposite third component of the angular momentum, with annihilation operators $\sigma_\uparrow$ and $\sigma_\downarrow$. The linearly polarized states of the biexciton system, namely $\sigma_{\mathrm{H,V}} = (\sigma_\uparrow \mp \sigma_\downarrow)/\sqrt{2}$, describe transitions from the exciton to the ground state emitting a vertically and horizontally polarized photon, respectively. To test the biexciton as a SPS, we drive it coherently with a vertically polarized laser of intensity Ω_σ and in resonance with the exciton transition. The Hamiltonian describing the biexciton is given by $H_{\mathrm{B}} = (\omega_\sigma - \omega_{\mathrm{L}})(\sigma_\uparrow^\dagger\sigma_\uparrow + \sigma_\downarrow^\dagger\sigma_\downarrow) - \chi(\sigma_\uparrow^\dagger\sigma_\uparrow\sigma_\downarrow^\dagger\sigma_\downarrow) + \Omega_\sigma(\sigma_{\mathrm{V}}^\dagger + \sigma_{\mathrm{V}})$ where ω_σ is the bare exciton energy (we consider resonant excitons), ω_{L} is the frequency of the driving laser and χ is the bonding energy, so with biexciton energy $2\omega_\sigma - \chi$. The biexciton is described by the master equation Eq. (1.44) replacing H_σ by H_{B}, and with exciton decay rate γ_σ for both polarizations. Figure 3.7 shows that the 3-norm for the biexciton emission saturates above the measure set by the incoherently driven 2LS. This means that, as expected, the biexciton is not a good SPS. Figure 3.7 also shows that the asymmetry in the driving field favors the vertically polarized emission over the horizontally polarized one. In fact, for a large region of values for Γ/γ, the vertically polarized emission of the biexciton is a better SPS than the central peak of the Mollow triplet.

Another striking case is the so-called "polariton blockade" (also known as "photon blockade"), first described theoretically by Verger, Ciuti, and Carusotto (2006) in its conventional version,

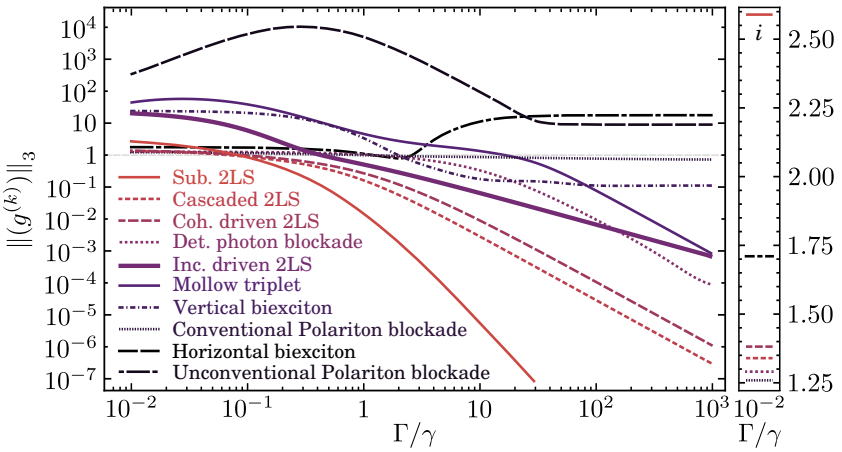

Figure 3.7: 3-norm for several sources of light as a function of their spectral filtering. The incoherently driven 2LS (in the limit of $P_\sigma \ll \gamma_\sigma$) is set as the benchmark for SPS. It is always surpassed by the coherently driven 2LS and the cascaded 2LS as long as $\Omega_\sigma \ll \gamma_\sigma$. The emission of the biexciton (with $\chi/\gamma_\sigma = 40$ and $\Omega_\sigma/\gamma_\sigma = 10$), on the other hand, fails to overcome the benchmark in either polarization. The blockade mechanisms provide better antibunching in the limit of vanishing Γ, but fail as SPS in the opposite limit. Here γ is meant as either γ_σ or γ_a depending on the system. Panel i shows a zoom in linear scale of the limit of $\Gamma/\gamma = 10^{-2}$.

and by Liew and Savona (2010) in its unconventional form. In the former case, antibunching follows from self-interactions (polaritons in this context are essentially strongly interacting photons), while in the latter case, a much stronger antibunching is obtained at vanishing pumping from an interference. Calling a and b the annihilation operators of two polariton modes, the Hamiltonian reads

$$H_{\mathrm{P}} = (\omega_p - \omega_{\mathrm{L}})(a^\dagger a + b^\dagger b) + g(a^\dagger b + b^\dagger a) + U(a^\dagger a^\dagger aa + b^\dagger b^\dagger bb) + \Omega_a(a^\dagger + a)\,, \tag{3.19}$$

where ω_p is the polariton energy, g is the coherent coupling between polaritons (e.g., by tunneling), U is the strength of polariton interaction, γ_a is the polariton decay rate and Ω_a is the intensity of the laser driving one of the polaritons. This Hamiltonian covers both types of blockades depending on the frequency of the excitation and the coherent coupling. Figure 3.7 shows that the conventional polariton blockade (obtained by setting the laser in resonance with the first rung of excitation and $g = 0$ in Eq. (3.19) to keep only polaritons a) behaves differently from the other SPS, as it remains roughly constant as more light is collected. The situation is even more serious for the unconventional polariton blockade that, contrary to a popular belief that made its manifestation actively sought after, performs rather poorly as a SPS, in particular in the configuration where its $g_a^{(2)}$ is very small. Indeed, despite its excellent antibunched $g_a^{(2)}$ emission, it also exhibits a superbunched $g_a^{(k)}$ for $k \geq 3$ and its ∞-norm actually diverges, therefore failing to behave as a SPS for most of the values of U/γ_a, including that where $g_a^{(2)} \ll 1$. Such a distinction between the two types of blockades is shown in Fig. 3.8, comparing all $\|(g^{(k)})\|_p$ for $p = 1, \ldots, 4$ and this time as a function of the interaction strength (normalized to the broadening) U/γ_a. The dashed lines correspond to the conventional blockade and show an essentially converged result regardless of p, indicating that the conventional blockade is a SPS that gets increasingly (albeit slowly) better with increasing nonlinearity. On the other hand, while the unconventional blockade is much better as perceived through the 1-norm (the conventional $g_a^{(2)}$, this is the result hailed in the literature), it is quickly spoiled at the 2-norm level, particularly at the value of U/γ_a that minimizes $g_a^{(2)}$. I have shown with Zubizarreta Casalengua et al. (2019) that it has a range of convergence and is a better SPS than its conventional counterpart (dashed line), but in a different configuration than the one aimed for (dotted line) and this would be overtaken by the conventional blockade for stronger nonlinearities.

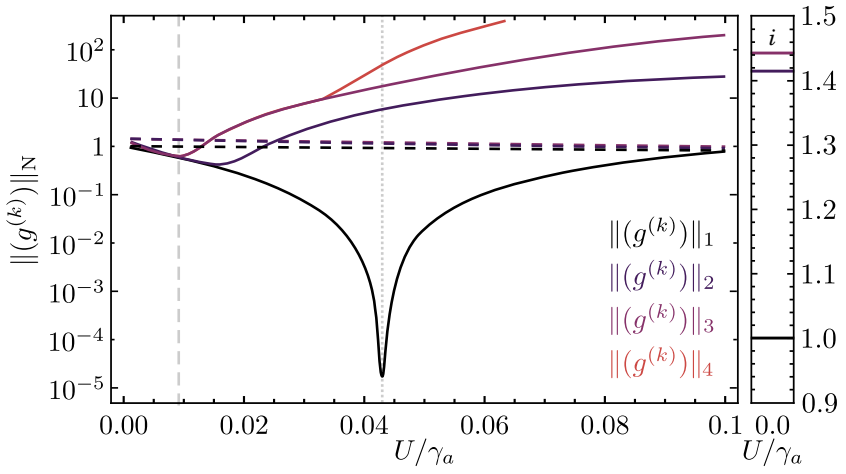

Figure 3.8: Comparison of the $\|(g^{(k)})\|_N$ for the conventional (dashed) and unconventional (solid) polariton blockade (Parameters as taken by Lemonde, Didier, and Clerk (2014), i.e., $\gamma_a = \gamma_b$, $\omega/\gamma_a = 0.275$ and $g/\gamma_a = 3$). The filtered 3-norm in Figure 3.7 is for $U/\gamma_a = 0.0425$ that minimizes $g^{(2)}$. Panels i shows a zoom in linear scale of the limit of $U/\gamma_a = 0$.

With the criterion in Eq. (3.18), one can weight the assets from various approaches. For instance, the bare 2LS presents the shortcoming of emitting in a large solid angle and placing it in a cavity brings several advantages, such as increasing its emission rate by Purcell enhancement, but also for practical purposes, in collecting and directing the light in a focused output beam. One can ask whether this has a cost in other aspects and weakens the suppression of multiple-photon emission as compared to bare SPS. We find with Eq. (3.18) that in the limit of weak-coupling and fast decay rate of the cavity, the impact is negligible, which is a welcome result as this configuration is widespread. More involved designs, such as the one proposed by Müller et al. (2015), can optimize the combination of these aspects in other configurations, for instance the detuned photon blockade proves to remain an excellent coherently driven SPS within a cavity, making such an implementation a serious contender for future applications.

3.4.2 *According to the temporal structure*

Independently of how bright, antibunched or indistinguishable are the photons emitted by any SPS, for many practical applications one would also like to know the time at which the photons are going to be emitted; or equivalently the delay between consecutive photons. For instance, if a SPS emits N photons per second, then, we know that *on average* we will have one photon every $1/N$ seconds. However, the emission rate does not provide any information about the temporal structure of the emission, like its standard deviation of the time-separation between consecutive photons: a laser emitting its photons randomly and a pulsed source emitting its photons equally spaced in time can have the same emission rate, but the standard deviation in the delay between consecutive photons is drastically different. Clearly, having the same emission rate, the source emitting its photons periodically in time is a better candidate for applications, as the emission time of the photons can be predicted. Thus, we can use the standard deviation in the delay between consecutive photons as another criterion to classify sources of single photons. The comparison of the variances is only meaningful when the means (that is, the emission rate) is equal. Therefore, we will use the standard deviation of the times between successive photons normalized to the emission rate as follows:

$$\sigma_2(\tau) = \sqrt{\frac{\left(\sum_{k=1}^{N} \tau_k N/T - 1\right)^2}{N-1}}\,, \tag{3.20}$$

where $\tau = \{\tau_1, \tau_2, \cdots \tau_n\}$ is the collection of all the delays between consecutive photons, N is the total number of photons and T the time it took the source to emit all the photons. The factor N/T is the emission rate of the source, and if the emitted photons are emitted equally spaced in time, then $\tau_k N/T = 1$ for every τ_k and the criterion becomes $\sigma_2 = 0$.

To the best of my knowledge, there is no physical system that naturally provides single photons separated equally in time. However, we can get close to it under controlled conditions by considering a 2LS driven coherently with a $\pi/2$-pulse with a δ-profile. The area of the pulse guarantees that the 2LS is left in its excited state, and the shape of the pulse minimizes the delay between the arrival of the pulse and the excitation of the 2LS. Once the 2LS is excited, it relaxes to its ground state emitting a single photon. This process takes place in the form of spontaneous emission, which is inexorably statistical, and the probability that the photon is emitted at some time t after the 2LS has been excited is given by

$$p_\sigma(t) = \gamma_\sigma\, e^{-\gamma_\sigma t}\,, \tag{3.21}$$

where γ_σ is the decay rate of the 2LS, and $1/\gamma_\sigma$ is the mean time at which the photons are emitted from the 2LS. Even if the 2LS is driven by a series of pulses, each of them separated from the previous one by a fixed time Δt, the delay between two consecutive single photons emitted by the 2LS will not be constant. In fact, the photon emitted from the kth pulse will be emitted at some time $t_k = k\Delta t + \delta t_k$, while the consecutive photon will be emitted at some

other time $t_{k+1} = (k+1)\Delta t + \delta t_{k+1}$, where both δt_k and δt_{k+1} are random variables following the exponential distribution in Eq. (3.21). Thus, the delay between consecutive photons is given by

$$\tau_k = t_{k+1} - t_k = \Delta t + (\delta_{k+1} - \delta_k)\,. \tag{3.22}$$

While Δt is a constant, $(\delta_{k+1} - \delta_k)$ is a random variable following the probability distribution

$$p_\delta(t) = \frac{1}{2\gamma_\sigma} e^{-|t|\gamma_\sigma}\,, \tag{3.23}$$

which standard deviation is $\sqrt{2}$. Using the expression of the delay between consecutive photons in Eq. (3.22) to compute the standard deviation in Eq. (3.20), we find

$$\sigma_2(\Delta t) = \sqrt{\frac{\sum_{k=1}^{N}[(\delta_{k+1} - \delta_k)/\Delta t]^2}{N-1}} = \frac{\sqrt{2}}{\Delta t}\,, \tag{3.24}$$

where we have used $N/T = 1/\Delta t$, and which is the trend for large values of $\gamma_\sigma \Delta t$ in Fig. 3.9(a). In the limit in which the product between the decay rate and the separation between consecutive pulses is very large, the σ_2 criterion becomes increasingly better: as the separation between pulses is increased, the relative uncertainty of the photon emission from the SPS becomes smaller, thus reducing the jitter of the source. Conversely, the behaviour of our criterion changes when the time difference between consecutive pulses is less than $1/\gamma_\sigma$. In such cases, the probability that the 2LS is still in its excited state when another pulse arrives is non-negligible. As a result, the sequence of equally spaced photons is spoiled and the σ_2 goes towards one. The way in which the σ_2-criterion is sensitive to missing photons from the otherwise series of perfectly separated single photons is shown in Fig. 3.9(b) as a function of the percentage of photons removed from the stream. The line shown was obtained directly from a Monte Carlo simulation, and can be fitted exactly with the relation

$$\sigma_2(p_r) = \sqrt{p_r + \sigma_2^2(p_r = 0)}\,, \tag{3.25}$$

where p_r is the percentage of photons removed from the stream and $\sigma_2(p_r = 0)$ is the value of the standard deviation when no photons are removed. Therefore, even if the 2LS is driven by a series of pulses evenly distributed in time, the delay between two consecutive single photons emitted by the 2LS will not be constant.

The discussion above is valid for an ideal source operating in the regime of pulsed excitation. However, ideal sources are seldom realisable in a laboratory. Instead, the best we can aim for is to find the source which most resembles the ideal one. In particular, we focus on the sources working at continuous excitation. In agreement with the results of the previous section, the incoherently driven 2LS is the CW source most similar to an ideal SPS. Figure 3.9(c) shows the normalized variance of the emission time as a function of the intensity of the incoherent driving, for several filtering widths. Independently of the spectral width of the detector, we find that there is always an ideal driving intensity that minimizes the disorder in the emission time of the photons. In fact, when the detector is color blind, the ideal driving rate matches the decay rate, in a configuration that keeps the 2LS with an average occupation of exactly 1/2. However, the ideal rate decreases as the width of the filter is reduced, and the state of the 2LS becomes thermal (cf. Fig. 3.2(a)), as the variance of the emission time of the photons is less affected by the lack of signal than by the large fluctuations of a highly populated thermal state.

3.5 CONCLUSIONS

In summary, we have discussed quantitatively the effect that filtering has on the statistical properties of the light emitted by single-photon sources. We have shown, that the setups proposed by Nguyen et al. (2011) and Matthiesen, Vamivakas, and Atatüre (2012) are not

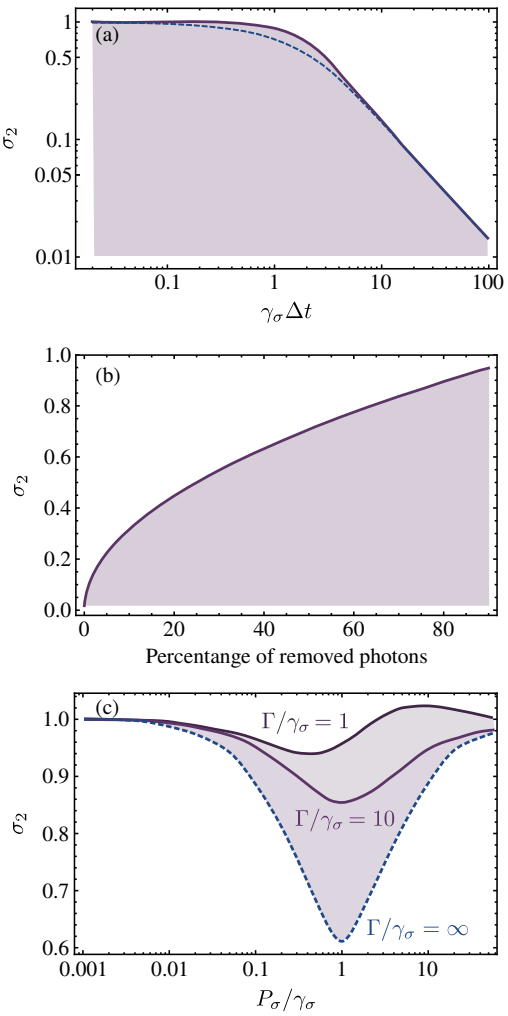

Figure 3.9: Criterion for single photons equally spaced in time σ_2. (a) The jitter of a pulsed 2LS can be reduced arbitrarily, simply by increasing the time between consecutive photons, as compared to the exponential time it takes the 2LS to emits its photons. (b) The criterion is also sensitive to photons missing from the emission, which is comparable to a real detector that misses some of the photons emitted by the source. (c) The CW-source that comes closer to emit its photons in a periodic way is the incoherently driven 2LS, albeit with a minimum $\sigma_2 \approx 0.6$.

actually providing single photons with a ultra-narrow linewidth, because, in their setup, these two properties cannot be measured simultaneously. Nevertheless, we developed a theory which, using the homodyning technique introduced by Vogel (1995), allows the realization of a sub-natural linewidth single photon source. Furthermore, we studied the quantum non-Gaussian character of a 2LS and how filtering and/or finite-detector resolution affects its qualities as a SPS. We proposed a criterion to quantify its performance: the N-norm of the photon correlation functions. For practical purposes, it is convenient and often enough to limit to the 2-norm or 3-norm. On the other hand, we showed that $g_a^{(2)}$ alone (the 1-norm), which is the widespread standard, is not sufficient and can lead to erroneous assessments. We illustrated the criterion with a variety of SPS mechanisms and found that the best realizations are obtained with yet-to-be-implemented SPS (such as the cascaded configuration of two-level systems and the subnatural-linewidth SPS), resonance fluorescence at low driving is the best already existing SPS. We also showed how other sources that appear to be good SPS do actually fail in a stricter sense that could jeopardize quantum information protocols. Beyond a criterion considering the correlations among the photons emitted by the SPS, we further discussed a criterion in the context of the distribution of the temporal separation of consecutive photons. For many practical purposes the ideal SPS is deterministic, in the sense that its photons are emitted at constant intervals. Such an ideal source sets the benchmark with which we can compare realistic sources. We find that in this respect, a two-level system driven with δ-pulses separated by a time larger than its inverse decay rate can get arbitrarily close to the ideal SPS. In the regime of continuous wave excitation, the best source is a 2LS driven incoherently.

4 MULTI-PHOTON LIGHT

No tengo forma de saber si los eventos que
estoy a punto de narrar son efectos o causas

— Jorge Luis Borges

4.1 INTRODUCTION

In the previous chapter, we have seen that the interferences between the absorbed and emitted light from a two-level system (2LS) in the Heitler regime leads to counter-intuitive effects, which Aharonovich, Englund, and Toth (2016) have used to power one of the best mechanisms for single-photon emission. In this Chapter, I will still consider the emission from a 2LS driven coherently by a laser, but this time in the high excitation regime, in which the emission spectrum is the Mollow (1969) triplet, as shown in Section 1.2.6. Such a triplet structure, obtained when considering first-order observables, unfolds into a rich landscape of correlations when one considers second-order observables, as shown in Fig. 1.15(b). Using the dressed atom picture introduced by Cohen-Tannoudji and Reynaud (1977) and Reynaud (1983), and summarized in Section 1.2.6, it is easy to understand the structure of the two-photon spectrum of the Mollow triplet, and in particular the emission of highly correlated photons pairs that takes place at the frequency halfway between the central and the lateral peaks of the triplet. Sánchez Muñoz et al. (2014a) showed that coupling a cavity in resonance with this frequency enhances the emission of these photons pairs. As these photons are the result of a transition through virtual states, the pair of photons are emitted simultaneously and the system becomes a source of two-photon bundles, thus upgrading the fundamental quantum of light to two photons. With sufficient-enough coupling strength to dissipation ratio, the emission from the system consists a 100% of photon bundles. Four years later, Sánchez Muñoz et al. (2018) have shown how to reach this regime in the bad-cavity limit, with system parameters already available as of today.

The objective of this Chapter is twofold. Firstly, I will show that the bundling from the Mollow triplet is not restricted to the case of generate photons, and discuss the implications of considering virtual processes that occur over an arbitrary number of excitation manifolds with no constrain on the photons' frequencies. In particular, I will show that the transitions in which not all the photons have the same frequencies are interesting, as one of the photons from the bundle could be used to herald the emission of the rest of photons from the bundle: thus, one can imagine scenarios in which an N-photon bundle is broken down in such a way that one photon heralds $N-1$, or two photons herald $N-2$ and so on. Secondly, I will show that considering the dressed atom picture sometimes lead to wrong conclusions, as one is more prone to (unwillingly) consider N-photon transitions which become resonant to a real state and lose their correlations. In contrast, I will consider a map of correlations considering a second-order correlation function, similar to Eq. (1.33) defined for individual photons, considering the correlations between a photon of frequency ω_1 and a N-photon bundle of frequency ω_2, thus upgrading the system to a *heralded* source of N-photon bundles.

4.2 LEAPFROG PROCESSES

The transitions that give rise to the antidiagonal lines of superbunching in the 2PS, shown in Fig. 1.15 and described through Eq. (1.51), are a particular case of a general set of transition

involving N photons and $N-1$ excitation manifolds. These photons satisfy the general condition

$$\tilde{\omega}_1 + \tilde{\omega}_2 + \cdots + \tilde{\omega}_N = \Delta\,, \qquad \text{with} \qquad \Delta = \{-\Omega_+, 0, \Omega_+\}\,, \tag{4.1}$$

where $\tilde{\omega}_i = (\omega_i - \omega_{\rm L})$. This is a simple generalization of the expression given in Eq. (1.51) for the case of two photons only but one of great consequences. The parameter Ω_+ is the separation between the central and the lateral peaks of the Mollow triplet and, while in the regime of very high excitation (when $\Omega_\sigma \gg \gamma_\sigma$) the splitting is given by $\Omega_+ \approx 2\Omega_\sigma$, in general it is given by

$$\Omega_+ \equiv \frac{\sqrt{8\Omega_0^2 - 6\gamma_\sigma^2 + \sqrt{9\gamma_\sigma + 16\Omega_0^4 - 24\gamma_\sigma^2(16\Omega_\sigma^2 + \Omega_0^2)}}}{2\sqrt{3}}\,, \tag{4.2}$$

with $\Omega_0^2 \equiv 4\Omega_\sigma^2 + \tilde{\omega}_\sigma^2$. Note that the transitions in Eq. (4.1) can also be satisfied by photons transiting over real states. For instance, there is a strong difference between $|+\rangle \to |\pm\rangle \to |-\rangle$ (a transition that is a cascade between real states) and $|+\rangle \rightrightarrows |-\rangle$ (a leapfrog transition that involves a virtual state). In a cascade between real states, each photon is real and the first transition takes place independently from the second. The correlations are thus of a classical character: the second transition becomes more likely simply because the first one reached the state that allows it to take place. In the other case of a leapfrog transitions, the two photons are emitted simultaneously, with stronger correlations as the joint emission is intrinsic to the process. Thus, also at the N-photon level, the stronger correlations correspond to the transitions in which all the intermediate photons are virtual, in which case we refer to an "N-photon leapfrog".

These leapfrog processes can be singled out from the total emission by spectral filtering, to select the frequencies where the corresponding photons are expected to be emitted. As characteristic of a quantum system, the combinatorics aspect quickly becomes overriding in the description of the phenomenology. At the two-photon level, the picture is fully captured by the two-photon correlation spectrum, shown in Fig. 1.15(b). This case has been widely discussed in the previous Chapters, so I consider directly the next order, for which the standard correlation function was provided for Glauber (1963) for order three (given in Eq. (1.32) for $N = 3$), which, with frequency filtering, becomes $g^{(3)}_{\Gamma_1,\Gamma_2,\Gamma_3}(\omega_1, t_1; \omega_2, t_2; \omega_3, t_3)$, given by Eq. (1.42) by setting $N = 3$. Assuming that the three detectors have the same linewidth and considering the case of coincidences, $t_1 = t_2 = t_3$, we arrive at a 3D correlation spectrum $g^{(3)}_{\Gamma}(\omega_1, \omega_2, \omega_3)$, a section of which is shown in Fig. 4.1 (the details of its computation are given in the next Section). It is not easy to visualize a three-dimensional correlation structure, but we can nevertheless characterize it fairly comprehensively. It consists essentially of leapfrog planes of superbunching, which, following Eqs. (4.1), read at the three-photon level

$$\tilde{\omega}_1 + \tilde{\omega}_2 + \tilde{\omega}_3 = \Delta\,, \tag{4.3}$$

but also, as revealed by the exact calculation, of the families of planes defined by

$$\tilde{\omega}_1 + \tilde{\omega}_2 = \Delta\,, \qquad \tilde{\omega}_1 + \tilde{\omega}_3 = \Delta\,, \qquad \tilde{\omega}_2 + \tilde{\omega}_3 = \Delta\,, \tag{4.4}$$

where in each case Δ is one of the three combinations of initial/final states transitions, i.e., $\Delta = -\Omega_+$ (the red planes in Fig. 4.1(b–e)), $\Delta = 0$ (blue) and $\Delta = \Omega_+$ (yellow). The planes from Eq. (4.3) are the three-photon leapfrogs where all the intermediate photons are virtual, as shown in the upper part of the dressed states ladder in Fig. 4.1(f). The planes from Eqs. (4.4) correspond to three-photon correlations that involve two two-photon leapfrog transitions linked by a cascade, namely, with two photons belonging to one two-photon leapfrog transition while the third comes from another two-photon leapfrog transition. Alternatively, this can be seen as a four-photon leapfrog transition that intersects a real-state, breaking it in two two-photon leapfrog transitions. This is shown in the bottom of the ladder in Fig. 4.1(f). It is at this point that the concept of a "bundle"—the N-photon object issued by a leapfrog transition—becomes handy. The planes in panels (c–e) thus correspond to a bundle-bundle radiative cascade in the

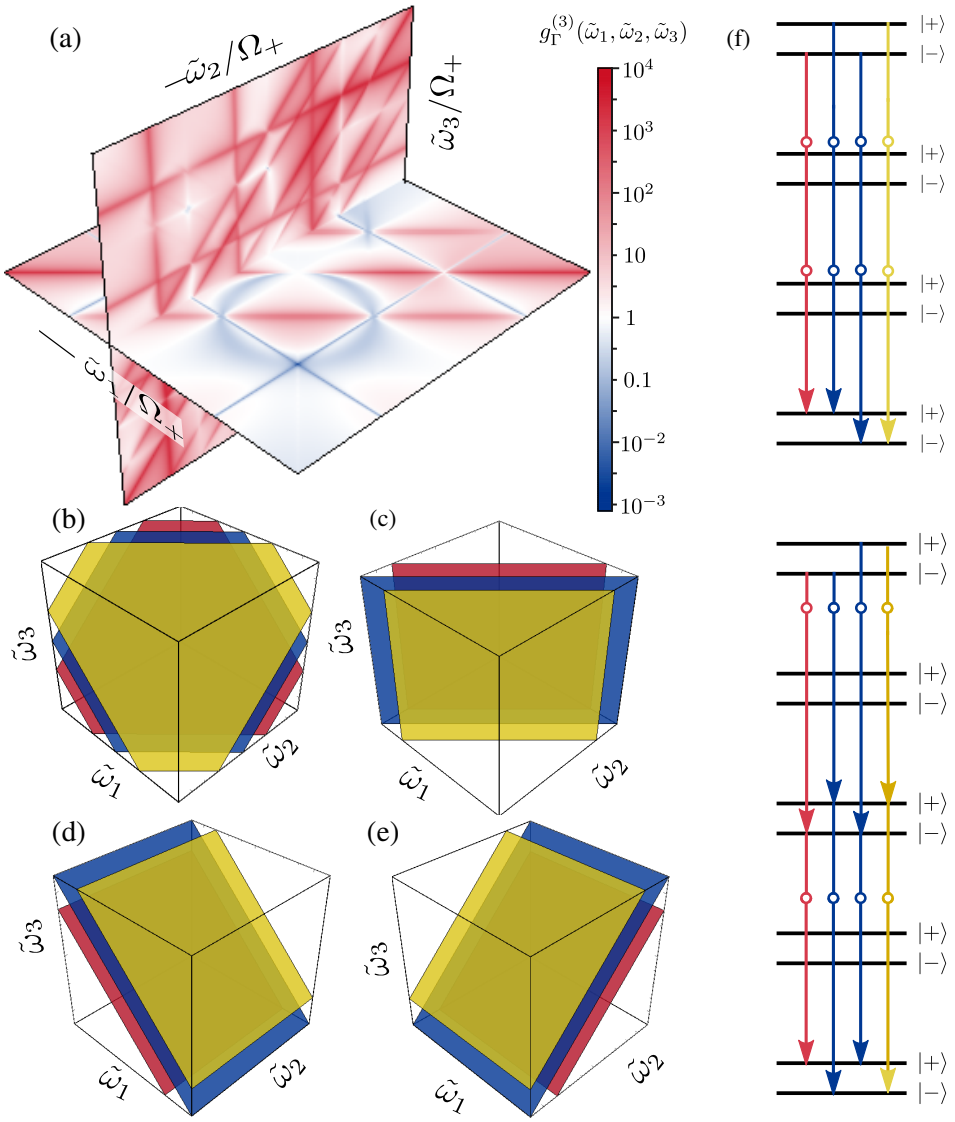

Figure 4.1: High-order correlations from N-photon transitions in the Mollow triplet. (a) The 3$^{\text{rd}}$-order correlation function $g_\Gamma^{(3)}(\omega_1,\omega_2,\omega_3)$ is shown as a two-plane cut in the full-3D structure. The vertical plane is pinned at a leapfrog transition while the horizontal plane is pinned at the central peak. The lines observed are superbunching resonances that result from the intersections with the leapfrog planes given by Eqs. (4.3a)-(4.3d), and displayed in panels (b-e), respectively. The colors correspond to the different values of Δ, namely Ω_+ (shown in yellow), 0 (blue) and $-\Omega_+$ (red). The leapfrog transitions involved are shown in the ladder of dressed states in panel (f). At the top, the three-photon leapfrog, Eq. (4.3a), yield the planes shown in (b). At the bottom of the ladder, the cascades of two two-photon bundles, out of which three photons yield the planes shown in (c-e). Panel (a) was obtained for $\Omega_+ = 300\gamma_\sigma$, $\tilde{\omega}_\sigma = 200\gamma_\sigma$ and $\Gamma = 5\gamma_\sigma$, setting the decay rate γ_σ of the 2LS as the unit.

ladder, the same process as that discussed by Cohen-Tannoudji & Reynaud in the dressed-atom picture, but here for two-photon bundles instead of two single-photons. The plane in panel (b) correspond to a single three-photon bundle transition. The fact that four photons can team up in this way to provide correlations that appear in the three-photon spectrum $g_\Gamma^{(3)}$ is first and foremost a result of the exact computation, that can be understood in terms of leapfrog transitions, which, in turn, can make predictions that exact computations can subsequently confirm, as will be shown later on. The four-photon transitions sketched in Fig. 4.1(f) are the only possible ones to account for the observed leapfrog planes (c-e). If one photon would

correspond to a transition between real states, we would observe lines instead of planes. A four-photon bundle on the other hand would not constrain two frequencies, as is the case of Eq. (4.4) and, beside, Laussy et al. (2012) discussed how a fourth-order process is not detectable by a third-order correlator. Since all the observed resonances are accounted for by the processes highlighted and that, in turn, all these processes produce a resonance in the computed correlation spectrum, we have found a one-to-one mapping between the numerically exact calculations and a simple physical model, and the characterization of the photon correlations is indeed comprehensive. Before turning to these exact calculations, we illustrate how the powerful dressed-atom picture also allows us to make some qualitative statements on the expected behaviours at the bundle level. Specifically, let us consider degenerate N-photon bundles, i.e., with all photons having the same energy. Such bundles need to change the state of the 2LS, for otherwise they break into real-state transitions. There are therefore two types of such degenerate bundles, those with photons of frequency $-\Omega_+/N$ and those with photons of frequency Ω_+/N. Now, for the same reasons as for single photons, one can expect for two bundles of the same type to be antibunched, as the 2LS has changed state, whereas two bundles of a different type will form a cascade and can be expected to be bunched. Note that such a behaviour holds at the level of the bundles rather than at the level of the photons themselves, that should be bunched in all cases. Such "predictions" from the leapfrog picture are confirmed by exact computations.

To get a more quantitative picture, we need to turn to an exact theory of frequency-resolved three-photon correlations, that I will present in next Section. Importantly, this will confirm that the leapfrog transitions in Eqs. (4.3) are the main three-photon relaxation processes.

4.3 THEORY OF FREQUENCY-RESOLVED n-PHOTON CORRELATIONS

The correlations between N photons detected in as many (possibly degenerate) frequency windows as required, without restricting ourselves to the peaks, can be computed exactly with the theory of frequency-resolved correlations outlined in Section 1.2.5. Thus, the two-photon (Fig. 1.15(b)) and three-photon (Fig. 4.1) frequency-resolved correlations can be obtained as particular cases of the general expression given in Eq. (1.42), namely

$$g^{(2)}_\Gamma(\tilde\omega_1,\tilde\omega_2)=\frac{\langle\xi_1^\dagger(\tilde\omega_1)\xi_2^\dagger(\tilde\omega_2)\xi_2(\tilde\omega_2)\xi_1(\tilde\omega_1)\rangle}{\langle\xi_1^\dagger(\tilde\omega_1)\xi_1(\tilde\omega_1)\rangle\langle\xi_2^\dagger(\tilde\omega_2)\xi_2(\tilde\omega_2)\rangle}\,, \tag{4.5a}$$

$$g^{(3)}_\Gamma(\tilde\omega_1,\tilde\omega_2,\tilde\omega_3)=\frac{\langle\xi_1^\dagger(\tilde\omega_1)\xi_2^\dagger(\tilde\omega_2)\xi_3^\dagger(\tilde\omega_3)\xi_3(\tilde\omega_3)\xi_2(\tilde\omega_2)\xi_1(\tilde\omega_1)\rangle}{\langle\xi_1^\dagger(\tilde\omega_1)\xi_1(\tilde\omega_1)\rangle\langle\xi_2^\dagger(\tilde\omega_2)\xi_2(\tilde\omega_2)\rangle\langle\xi_3^\dagger(\tilde\omega_3)\xi_3(\tilde\omega_3)\rangle}\,. \tag{4.5b}$$

We have assumed for brevity only the case where all the filters have the same linewidth, although one can further enhance the correlations by optimizing the filters linewidths to match the width of the selected resonances. The case of different filter linewidths is further discussed by González-Tudela, del Valle, and Laussy (2015) in the case of two-photons, but we will not address it here for N-photons. One can therefore consider in the following that there is still room for further improvement.

A particular case of interest is the autocorrelation $g^{(N)}_\Gamma(\tilde\omega)$ when all the frequencies are degenerate, $\tilde\omega_1=\cdots=\tilde\omega_N$. This corresponds to the correlations, at various orders, of the light passing through a single filter. The cases up to fourth order as computed with the sensors technique are shown in Fig. 4.2. Panel (b) confirms the known results obtained by Aspect et al. (1980), Schrama et al. (1992), and Ulhaq et al. (2012) of antibunching for the side peaks, and also of bunching for the main peak ($g^{(2)}_\Gamma(\tilde\omega=0)\approx 1.05$ with our parameters, see caption). Strikingly in the latter case, it is revealed that, in the full picture, this bunching actually sits in a local minimum and that, although the central peak is indeed bunched, this comes in a region of suppressed bunching, as shown in the inset of Fig. 4.2(b) (zooming in the area indicated by the arrow). This feature is not fully conveyed by the dressed-atom picture. The

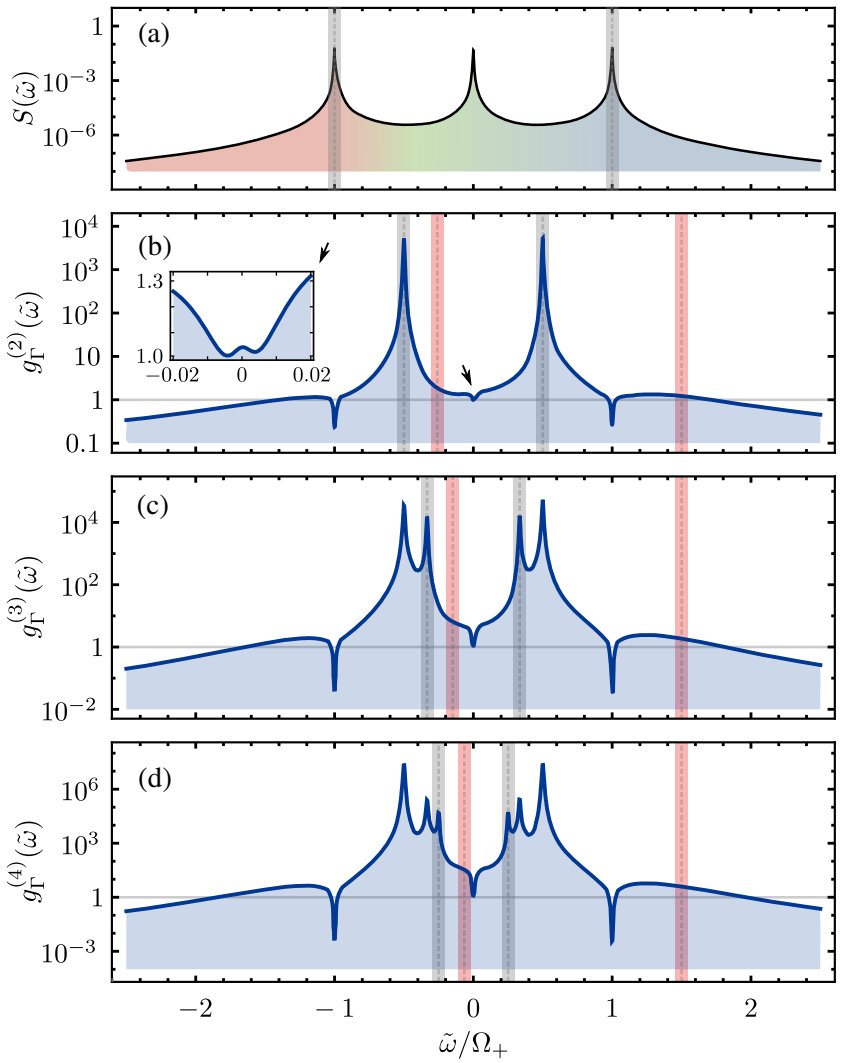

Figure 4.2: Correlations between bundles of N photons. (a) Photoluminescence spectrum of the Mollow triplet, with the configuration of filters that has been proposed for single photon heralding by Schrama et al. (1992), namely, filtering the two side peaks. (b–d) 2, 3 and 4-photon autocorrelation spectrum. The resonances in the photon correlations reveal the frequencies where the same type of heralding but for N-photon bundles can be achieved. Such frequencies, shown here in gray, are given by $\tilde{\omega} = \pm\Omega_+/N$ at order N. In red are shown the even better configuration where the heralding does not involve any transition through a real state. The inset in Panel (b) shows a zoom of the correlations nearby the central peak, marked by an arrow, revealing bunching to sit on a local minimum. The decay rate of the 2LS sets the unit, the splitting of the triplet is set to $\Omega_+ = 300\gamma_\sigma$, the sensors linewidth to $\Gamma = 2\gamma_\sigma$, and the detuning between the laser and the 2LS to $\tilde{\omega}_\sigma = 200\gamma_\sigma$.

most notable feature, however, is one that remained unnoticed until the numerically exact calculations of González-Tudela et al. (2013): the two strong resonances that sit between the peaks. These are the leapfrog correlations. Similar results are generalized when turning to higher orders, as shown in panels (c) (three photons) and (d) (four photons). While the correlation of the peaks retain the same qualitative behaviours, new features thus appear away from the peaks, associated to the leapfrog transitions, successively captured by increasing the order of the correlations. These resonances, at $\pm\Omega_+/N$, pile up toward the central peak, and become increasingly difficult to access individually, as however can be expected from such strongly quantum objects involving a large number of particles.

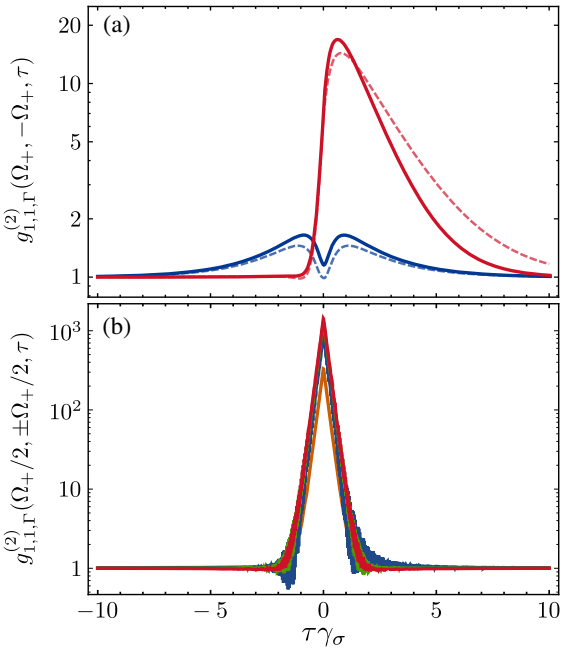

Figure 4.3: Filtered single-photon correlations from the emission of, (a) the opposite sidebands, and, (b) the two-photon leapfrogs. Panel (a) shows the exact behaviour at resonance (solid blue) and with detuning (solid red), and compares it with the approximated expressions given by Schrama et al. (1992), shown as dashed blue and dashed red, respectively. Panel (b) shows the filtered correlations from the same two-photon leapfrog (shown in red at resonance and in green with detuning) and from the leapfrogs at opposite sides of the central peak (shown in orange at resonance and in blue with detuning). The curves essentially overlap, meaning that, thanks to the nature of the leapfrog transition, the choice of configuration in which a two-photon bundle heralds another one is not very important. The decay rate of the 2LS sets the unit, $\Omega_+ = 300\gamma_\sigma$, $\Gamma = 5\gamma_\sigma$ and in the cases with detuning $\tilde{\omega}_\sigma = 200\gamma_\sigma$.

While these cuts in the N^{th}-order correlation spectrum are useful and will be later referred to again—being so-closely connected to degenerate bundles—they provide a very simplified account of the structure of the correlations at the N-photon level. The case for $N = 3$ photons, displayed in Fig. 4.1(b) in two planes that intersect the full 3D spectrum, provides the full picture at this order, on the basis of which one can best exploit the photon emission. We will not discuss the antibunching patterns, whose intersections in the density plot produce in addition to straight lines, also a circular shape which physical origin is interesting but beyond the scope of this Thesis. We will now discuss how intercepting the red superbunching lines in the general three-dimensional space, that originate from the leapfrog planes in panels (b–e) of Fig. 4.1, allows to design a new family of heralded N-photon emitters.

4.4 SOURCES OF HERALDED PHOTONS

With the formalism introduced in previous Sections, it is straightforward to compute the exact frequency-resolved peak-peak correlations studied by Ulhaq et al. (2012). This includes their time-resolved version, beyond the coincidences that we have considered so far. The theory then needs to take proper care of time-ordering, which is however easily achieved with the technique presented in Section 1.2.5. Since we consider here a system in its steady state, only relative time differences $\tau \equiv t_2 - t_1$ are of interest. Some frequency- and time-resolved correlations for the Mollow triplet are shown in Fig. 4.3(a), at both resonance (blue curve) and with a detuning between the 2LS and the laser (red curve). We compare the exact (solid) and approximated (dashed) solutions, obtained through the sensing formalism and the earlier theories, respectively. There is an excellent qualitative if not quantitative agreement. In the case of laser detuning, the asymmetric shape lends itself to heralding purposes, whereby detection of a photon from the high-energy peak correlates strongly with the detection of another photon from the low-energy peak.

The great advantage of the theory of frequency-resolved photon correlations from Section 1.2.5 is that it also allows to compute exactly correlations in more general configurations than those restricted to the peaks. For instance, correlating the photons emitted by the leapfrog processes, by filtering at the corresponding frequencies, one gets the correlation function shown in Fig. 4.3(b), with several notable features, all in line with the quantum nature of these transitions. Namely, the correlations

- are much stronger (about 50 times larger) than those of the photons emitted through real states, as shown in panel (a),
- they have smaller correlation time (and thus yield better time resolutions),
- they do not depend much on detuning,
- they do not depend much on the choice of configuration (degenerate bundles or not), and
- they are symmetric in time.

Note that symmetric correlations are not detrimental for heralding, as the instantaneous character of the emission allows to delay one channel and thus keep the other as the heralding one. One obvious drawback of such strongly-correlated emission is the much reduced signal, since the collection is made away from the peaks. While there are ways to circumvent this limitation, for instance by Purcell-enhancing them with a cavity of matching frequency, as has been done by del Valle (2013), Sánchez Muñoz et al. (2014a), and Sánchez Muñoz et al. (2015), we will remain here at the level of describing the naked correlations. Now that we have shown the new perspectives opened by the leapfrog process at the two-photon level, we focus on more innovative aspects.

4.5 SOURCES OF HERALDED BUNDLES

The powerful dressed-atom picture allows a straightforward generalization of the heralding discussed in the previous Section. One can contemplate the configuration where a photon heralds a bundle in the radiative cascade down the ladder, as shown in case *i* of Fig. 4.4(c). This is the same idea as Ulhaq et al. (2012)'s heralding a single-photon, but now heralding a bundle instead. Even better, however, is to consider a three-photon leapfrog where all photons are virtual, and use one of them to herald the other two, a sketched in case *ii*. Conveniently, one can use the heralding photon to have a different energy from the two other ones, that can be degenerate. One needs a careful analysis, however, since there is room for subtleties in a relaxation process that starts to be complex. As an illustration, case *ii*, that has no real photons, has in fact the same distribution of photon frequencies as case *i*, that transits via a real state. The difference is the initial and final states, $|-\rangle \to |+\rangle \rightrightarrows |-\rangle$ and $|+\rangle \overset{\rightarrow}{\rightrightarrows} |+\rangle$. For this reason, case *ii* turns out to be suppressed as a three-photon leapfrog process, as revealed by the exact calculation. One needs instead to find a case such as *iii* that suffers no such interference with another relaxation in the ladder intersecting with a real state. A quantitative analysis is thus required, and the theory of frequency-resolved photon correlations here again allows us to easily tackle this problem. The relevant correlation is the one that generalizes Eq. (1.42) to the N-th order correlation function of N bundles, with each of them—detected at frequency $\tilde{\omega}_\mu$—being composed of n_μ photons:

$$g^{(N)}_{n_1,\cdots,n_N,\Gamma}(\tilde{\omega}_1,\ldots,\tilde{\omega}_N) \equiv \frac{\langle : \Pi_{\mu=1}^{N} {\xi_\mu^\dagger}^{n_\mu}(\tilde{\omega}_\mu)\xi_\mu^{n_\mu}(\tilde{\omega}_\mu) : \rangle}{\Pi_{\mu=1}^{N}\langle {\xi_\mu^\dagger}^{n_\mu}(\tilde{\omega}_\mu)\xi_\mu^{n_\mu}(\tilde{\omega}_\mu)\rangle}\,, \tag{4.6}$$

where ":" indicates normal ordering, a necessary requirement when two (or more) of the sensors have the same frequency. With this notation, Eq. (4.5a) is the particular case with $N = 2$ and $n_1 = n_2 = 1$. For the simplest extension to Ulhaq et al. (2012)'s paradigm, that is, one photon heralding a two-photon bundle, one therefore deals with

$$g^{(2)}_{1,2,\Gamma}(\tilde{\omega}_1,\tilde{\omega}_2) = \frac{\langle : \xi_1^\dagger(\tilde{\omega}_1){\xi_2^\dagger}^2(\tilde{\omega}_2)\xi_2^2(\tilde{\omega}_2)\xi_1(\tilde{\omega}_2) : \rangle}{\langle \xi_1^\dagger(\tilde{\omega}_1)\xi_1(\tilde{\omega}_1)\rangle\langle {\xi_2^\dagger}^2(\tilde{\omega}_2)\xi_2^2(\tilde{\omega}_2)\rangle}\,. \tag{4.7}$$

Figure 4.4(a) shows this quantity computed for the Mollow triplet and, in (b), the mathematical structure of this photon-bundle correlation spectrum. The "heralding scenario" of one photon,

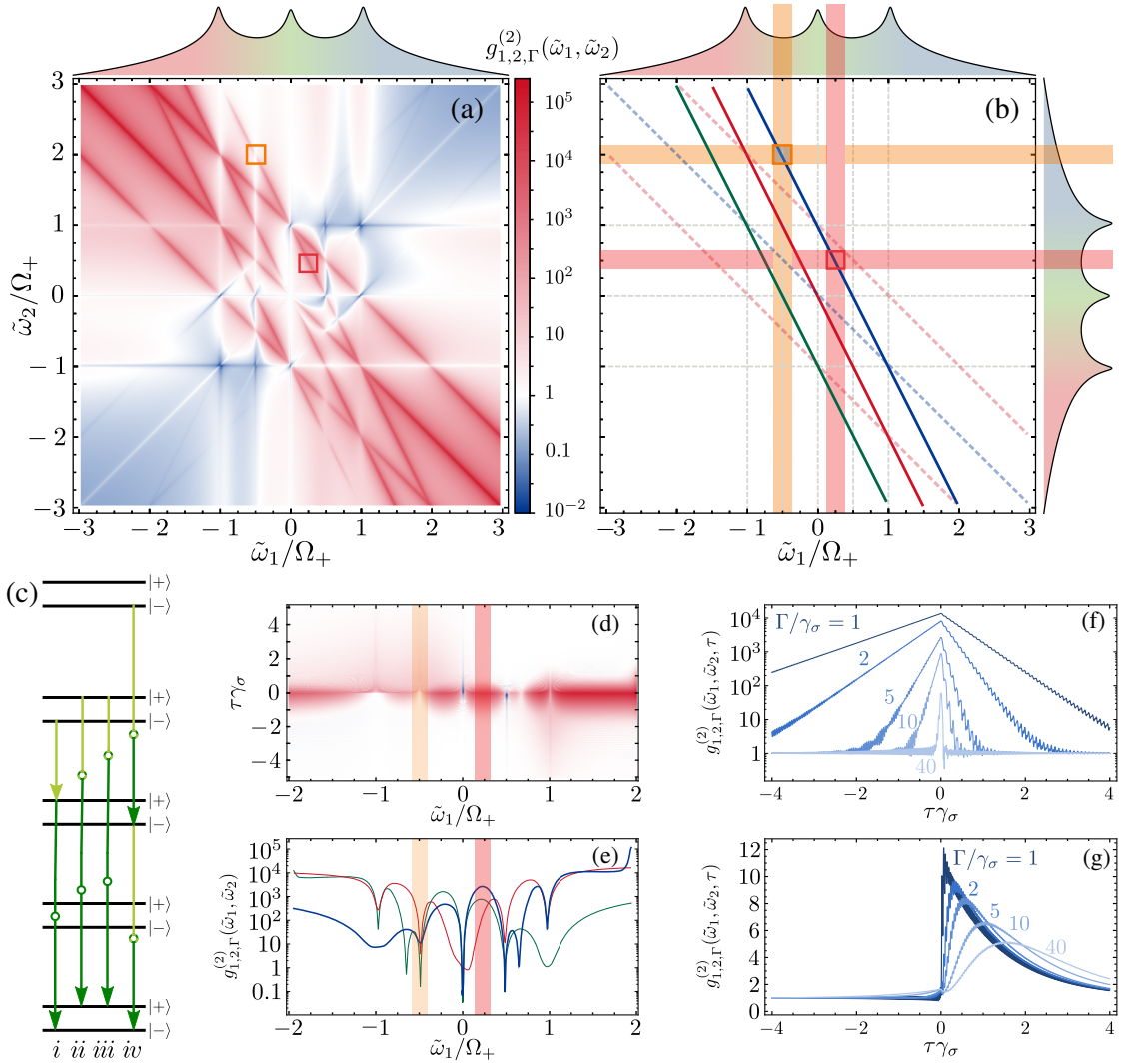

Figure 4.4: Correlations between a single photon and a bundle of two photons. Panel (a) displays the full correlation spectrum $g^{(2)}_{1,2,\Gamma}(\tilde{\omega}_1,\tilde{\omega}_2)$ between a single photon with frequency $\tilde{\omega}_2$ and a bundle of two photons, each with frequency $\tilde{\omega}_1$. The antidiagonals of superbunching are shown in Panel (b): the dashed lines correspond to the transitions $\tilde{\omega}_1+\tilde{\omega}_2=\Delta$, whereas the solid lines correspond to the transitions $2\tilde{\omega}_1+\tilde{\omega}_2=\Delta$. The latter are shown in the ladder of Panel (c) as cases *i*–*iii*, where the dark green arrows represent the two-photon bundles and the light green arrows the single photon. Panel (d) shows the τ-dynamics along the blue antidiagonal of panel (b), while panel (e) shows the correlation intensities for all the solid antidiagonals, with the same color code. Panels (f) and (g) show the time-correlations measured at the frequencies specified by the red and orange filters. Although the correlations in panel (g) have the λ-shape commonly associated to photon heralding, the correlations in panel (f) are much stronger. Note that while the correlations captured by the orange filters, with the two-photon bundle emitted at $\tilde{\omega}_1=-\Omega_+/2$, are bunched, they actually correspond to a local minimum, as seen in panel (e) for the blue line. The global maximum, instead, lies at a frequency with no particular attribute that one would not a priori target without the knowledge of the photon-bundle correlation spectrum. Its frequency is one captured by the red filters. The triplet splitting is $\Omega_+=300\gamma_\sigma$, the detuning between the laser and the 2LS is $\tilde{\omega}_\sigma=200\gamma_\sigma$ and the spectral width of the sensors is $\Gamma=5\gamma_\sigma$, except in panels (f) and (g), where the filter size is specified for each curve.

of frequency $\tilde{\omega}_2$, announcing a two-photon bundle, made of photons of frequency $\tilde{\omega}_1$, follows from Eq. (4.1) with $N=3$ and $\tilde{\omega}_3=\tilde{\omega}_1$, resulting in correlations for $g^{(2)}_{1,2}$ when the condition

$$2\tilde{\omega}_1+\tilde{\omega}_2=\Delta \tag{4.8}$$

is met, with, as before, $\Delta = 0$ or $\pm\Omega_+$. These yield the steeper lines in Fig. 4.4(a), reproduced as solid lines in (b). They correspond to transitions of the type *i–iii* in the ladder of panel (c). The antidiagonals, with the same strength than the three-photon bundles, correspond to transitions of the type *iv* in panel (c), namely, a two two-photon bundle cascade, transiting by an intermediate real state. Two photons from different leapfrogs can have the same frequency, allowing for their detection as an apparent bundle, although actually emanating from different bundles, related by a cascade through a real state. In this case, any of the other photon can be detected as the heralder while the fourth photon is discarded. Although we have shown previously that correlations that involve a real state are weaker than those that only involve virtual states, this is when comparing processes of the same order, i.e., with the same number of photons. Here the two two-photon bundle transition involves a cascade through a real state but is otherwise composed of (two) second-order processes, while the three-photon bundle that does not involve a real state, is a third-order process. All this considered, the exact computation shows that these processes result in correlations of similar strength in the correlation spectrum, as seen in Fig. 4.4. This could be generalized, although the combinatorial explosion of different ways in which N photons can be correlated at the same order would make such a discussion difficult, and I believe that the three-photon case is illustrative of the overall situation. Therefore, coming back to the three-photon bundle, specified by Eq. (4.8), we show in Fig. 4.4(d) the photon-bundle correlations $g^{(2)}_{1,2,\Gamma}(\tau)$ along the leapfrog transitions. We highlight the case $|+\rangle \rightrightarrows |-\rangle$ (blue line in panel (b)), the results being similar for other leapfrogs. The density plot allows to spot where the photon-bundle correlations are the strongest. One sees, as expected, that correlations are smothered when intersecting a real state, even exhibiting antibunching instead of superbunching for the cases $\tilde{\omega}_1/\Omega_+ = 0$ (intersecting with the central peak) and $\tilde{\omega}_1/\Omega_+ = \pm 1/2$ (leapfrogs). Since, by the nature of the leapfrog correlations, they are fairly symmetric in τ and maximum at zero, we can identify the optimum as the local maximum nearby the peaks of $g^{(2)}_{1,2}(\tilde{\omega}_1, (\Delta - \tilde{\omega}_1)/2)$, shown in Fig. 4.4(e). It lies in good approximation between the two depletions in correlations already described. The correlations in time there for various filter sizes are shown in panel (f), reproducing in this photon-bundle scenario the same phenomenology as the photon-photon correlations shown in Fig. 4.3(b). The oscillations that are observed in time are due to the spectral width of the sensors, which detects photon from transitions other than the N-photon leapfrog, causing interferences. Such an oscillatory behaviour can be reduced either by turning to a triplet with a larger splitting, in which the emission from different transitions are further apart, or by using a smaller filter width. The photon-bundle correlations display strikingly the same phenomenology as the photon-photon case of Fig. 4.3. Namely, they are completely symmetric in time, regardless of the size of the bundle, i.e., the cascade emission of N-photon bundles from opposite sides of the Mollow triplet does not have a preferential order. The temporal symmetry can be broken by involving a real transition and detuning the laser from the 2LS. To complete the analogy with Fig. 4.3, we also show in panel (g) the transition that involves a real state transition for the photon heralding the bundle. In this case, the correlation profile shown in (g) is obtained, in clear analogy of Fig. 4.3(a). So one has these two options of heralding a bundle with a photon, would one scenario be better suited than the other and the Mollow triplet can be turned into a tuneable and versatile source of N-photon bundles simply by filtering its emission at the adequate spectral windows.

This physics can be generalized, in principle, to any higher order. Of course, an actual experiment measuring such correlations would be increasingly challenging. Still, for the sake of illustration, we now quickly address the case of four-photon bundles (and parenthetically the general case of N-photon bundles). The leapfrog are then hyperplanes of dimension 3 (N) in an hyperspace of dimension 4 ($N + 1$), which we shall not attempt to represent. Instead, we show the two-bundle correlation spectra, in Fig. 1.15(b). When correlating two bundles of two-photons each, we recover a landscape fairly similar to that of Fig. 1.15. When correlating a photon with the rest of the bundle, we turn to the heralding scenario. The number of possibilities is that given by the integer partition of 3 (N), which is conveniently represented as Young tableaux,

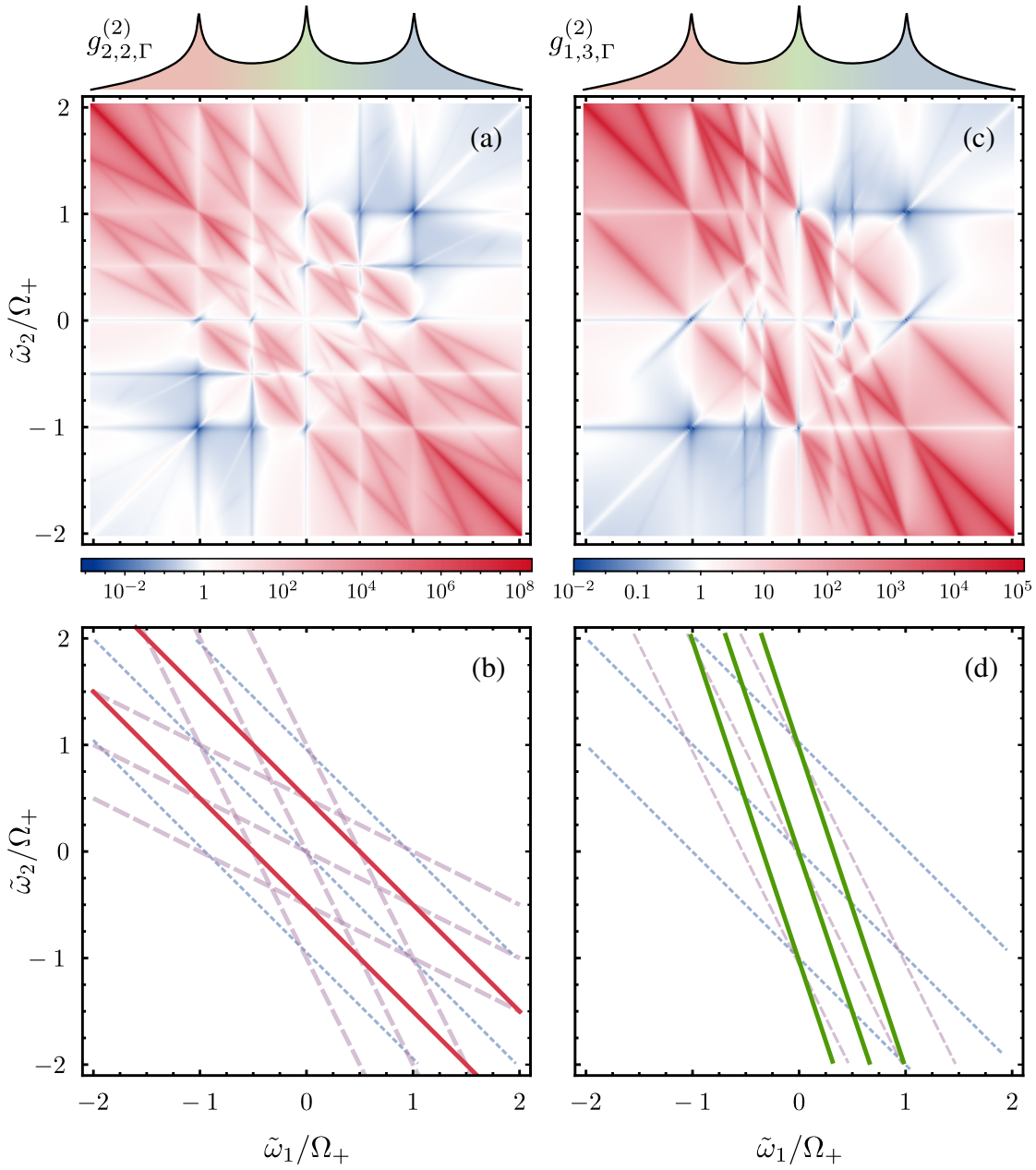

Figure 4.5: Correlations involving four photons. (a) Landscape of correlations between two-photon bundles as given by $g^{(2)}_{2,2,\Gamma}(\tilde{\omega}_1, \tilde{\omega}_2)$. (b) Mathematical structure of the correlations with transitions $\tilde{\omega}_1 + \tilde{\omega}_2 = \Delta$ (shown as dotted blue lines), $\tilde{\omega}_1 + 2\tilde{\omega}_2 = \Delta$ and $2\tilde{\omega}_1 + \tilde{\omega}_2 = \Delta$ (dashed purple), and $2\tilde{\omega}_1 + 2\tilde{\omega}_2 = \Delta$ (solid red), where $\Delta = -\Omega_+, 0, \Omega_+$. (c) Correlations between a three-photon bundle, in which each photon has frequency $\tilde{\omega}_1$, and a single photon with frequency $\tilde{\omega}_2$. (d) Mathematical structure of the correlations with transitions $3\tilde{\omega}_1 + \tilde{\omega}_2 = \Delta$ (shown in solid green) and the transitions described in (b). The decay rate of the 2LS sets the unit, $\Omega_+ = 300\gamma_\sigma$, $\tilde{\omega}_\sigma = 200\gamma_\sigma$ and $\Gamma = 5\gamma_\sigma$.

whose number of rows is the order of the correlation, and with each entry providing the composition of the correlated bundles:

1. $\begin{smallmatrix}\square\\\square\\\square\\\square\end{smallmatrix}$ for $g^{(4)}_{1,1,1,1}$, the standard Glauber correlator $g^{(4)}$,
2. $\begin{smallmatrix}\square\square\\\square\square\end{smallmatrix}$ for $g^{(2)}_{2,2}$, shown in Fig. 4.5(a),

3.  for $g^{(2)}_{1,3}$, shown in Fig. 4.5(b),

4.  for $g^{(3)}_{1,1,2}$.

The non-partitioned case  does not lead to a correlator (it could be understood as normal luminescence). Maybe the most useful configuration is  , with a single photon heralding a N-photon bundle. The case of one photon heralding a 3-photon bundle lies on any of the corresponding leapfrogs shown as the steepest lines in Fig. 4.5(b), with equation $N\tilde{\omega}_1 + \tilde{\omega}_2 = \Delta$ (the case $N = 3$ is the one shown in the figure). While it might be less obvious that other configurations could also be useful, it would not be surprising on the other hand that the need could arise with the boom of quantum technologies. It seems that, in such a case, the Mollow triplet can serve as a universal photon-emitter, able to deliver any requested configuration, e.g., distributing ten photons in a five channel input with two single photons, two two-photon bundles and a four-photon bundle:

 . (4.9)

Would such a profile be required to feed a quantum gate, it is a small technical matter to identify which spectral windows would capture this configuration and filter it out from the total luminescence. Once again, here we do not address specifically the issue of the signal, but only point to the structure of the photon correlations that reside in the Mollow triplet. We highlight as well that, in addition to feeding boson sampling devices, the very combinatorial nature of the emission could allow to test quantum supremacy through photon detection only, without the need of interposing a complex Galton board of optical beam-splitters. Whatever its actual use for practical applications, it is clear that the Mollow triplet overflows with possibilities, so characteristic of strongly-correlated quantum emission.

4.6 CONCLUSIONS

I have shown that the Mollow triplet is a treasure trove of quantum correlations, at all orders and not limited to dressed-state transitions. Specifically, I have shown—based on both qualitative arguments rooted in the structure of the dressed-atom ladder and exact computations made possible by a recent theory of frequency-resolved N-photon correlations—that the emission from the Mollow triplet exhibits its richest potential when dealing with leapfrog transitions, i.e., processes that occur through virtual photons, endowing them with much stronger correlations.

While the focus of photon correlations from the Mollow triplet has been on correlations between two photons from the peaks, following the picture of a radiative cascade between dressed states, our results should encourage the study of correlations from photons away from the spectral peaks, where the emission from a Mollow triplet at the appropriate frequencies can be used as a heralded source of N-photon bundles or, taking full advantage of the scheme, any customisable configuration of photons. At an applied level, including with the use of cavities to Purcell enhance these transitions and turn the virtual processes into real ones, this should allow to develop new types of quantum emitters, of interest for instance for multiphoton quantum spectroscopy following my proposal, which I will discuss in Chapter 7, or to deepen the tests of nonlocality and quantum interferences between correlated photons, as done by Peiris, Konthasinghe, and Muller (2017). My result only scratches the surface of the possibilities that reside in the Mollow triplet, which should be of interest as programmable quantum inputs for future photonic applications.

5 EXCITATION OF A HARMONIC OSCILLATOR

The most exciting phrase to hear in Science,
the one that heralds new discoveries,
is not 'Eureka!' but 'That's funny...'

— Isaac Asimov

5.1 INTRODUCTION

In the previous Chapters, we have introduced various types of quantum light and the importance of the detection in the description of the emission. Now we will discuss the effect that quantum light has on optical targets. For this purpose, we will use the formalism of cascaded coupling, introduced in Section 1.2.1.2. The general problem of excitation with quantum light has obviously numerous ramifications. To the already large variety of optical targets, one now has to combine a very much enlarged set of quantum sources. This literally opens a new dimension to optics. Indeed, classical excitation could arguably be limited to a rather small set of categories:

(a) Incoherent excitation (incoherent pumping, Boltzmann dynamics, thermal baths, equilibrium, etc., cf. Fig. 5.1(a))

(b) Coherent excitation (driving with a laser, cf. Fig. 5.1(b))

Quantum light, on the other hand, encompasses not only the above—if only because it is a more general case that includes classical excitation as a particular case—but also comes with many more and higher degrees of freedom. This did not lead so far, to the best of my knowledge,

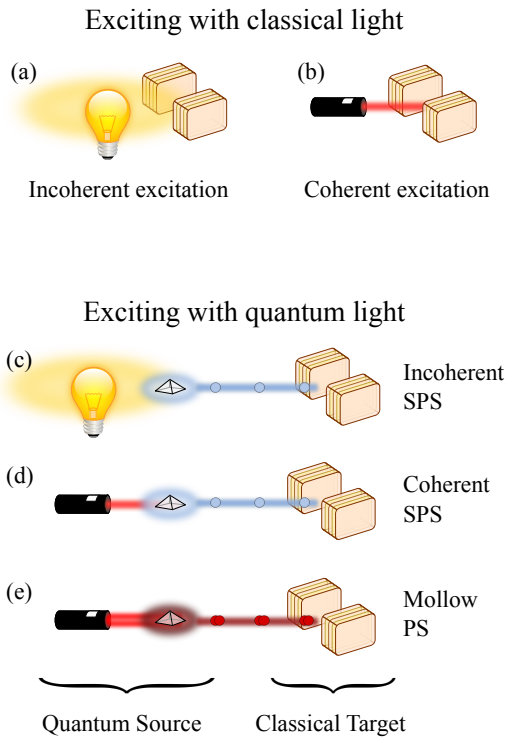

Figure 5.1: Upper part: The two main types of classical excitation. The harmonic oscillator can be implemented by a single-mode cavity, sketched here as two distributed Bragg reflectors facing each other. The single-photon source (SPS) can be implemented by a quantum dot, sketched here as a little pyramid, resembling the geometry that Grundmann, Stier, and Bimberg (1995) observed when growing them by self-assembly. (a) Incoherent excitation, typically corresponding to thermal light. (b) Coherent excitation, typically corresponding to driving the system with a laser. Lower part: Upgrading the classical sources of the upper panel with SPS. (c) is the counterpart of (a), to be referred to as the "incoherent SPS". The coherent case yields two very different types of quantum light at low and high pumping: (d) the coherent SPS and (e) the Mollow PS which can emit more than one photon at a time. Other types of quantum sources and other types of targets constitute the topic of the following texts in the series.

to a comprehensive classification. Tentatively, this could be provided in a first approximation by $g_\sigma^{(2)}$ (antibunching, uncorrelated, bunching, superbunching). Since squeezed states have the correlations of coherent states, however, and they are precisely the type of input that motivated a new formalism, it is clear that this is still far from appropriate. I will approach this general problem by considering:

- the same optical target (here an harmonic oscillator, in the next chapter a two-level system),
- the same type of quantum source (here and in the next chapter, a single-photon source, in chapter 8, an N-photon emitter),
- both coherent and incoherent regimes,
- both low and high pumping regimes.

The single-photon source (SPS) is a good starting point because it is the paradigm of quantum light and is the most common light of this type in the laboratory. Exciting the harmonic oscillator makes the problem both simple and fundamental, so this is also a good starting point. While we have considerably restrained the possibilities, there still remains much to be explored and the following will only address the main results. The two types of excitations aforementioned (a–b) yield quite different types of SPS, that are introduced in the beginning of their respective Sections, and are summarized in table 5.1 . Note that in the table, the bottom row also includes the middle one (which is the limit of small pumping). They are however so distinct qualitatively that it is helpful to think of them as separate sources. As we will show, the middle row (small coherent pumping) leads to the best antibunching in the target.

5.2 PURE QUANTUM STATE IN THE DISSIPATIVE REGIME

We first consider the simplest possible implementation: the excitation of a passive cavity, modelled as a harmonic oscillator, by the output of a weakly driven 2LS evolving according to Eqs. (1.44–1.45). There are only two parameters ruling this configuration: the ratio between the decay rates of the target and the source, γ_a/γ_σ, and the intensity of the driving Ω_σ (also normalized to γ_σ to keep all the variables dimensionless). Figure 5.2 shows the states of the cavity field that can be reached, through (a) the photon statistics (color coded) and population (isolines) as well as (b) the purity of the states measured through $\mathrm{Tr}[\rho^2]$ (zero corresponding to maximally mixed states and one to pure states). The results of the calculation show that a large family of steady-state pure quantum states, i.e., with a wavefunction

$$|\psi\rangle = \sum_{n=0}^{\infty} \alpha_n |n\rangle \ , \tag{5.1}$$

(here $\alpha_n \in \mathbb{C}$ such that $\sum_{n=0}^{\infty} |\alpha_n|^2 = 1$) can be obtained despite the driven-open nature of the system. Many of these states are non-classical, meaning that they sustain quantum superpositions and sub-Poissonian fluctuations, depending on the interplay of quantum pumping and

Source	Pumping	Population n_σ	$g_\sigma^{(2)}(\tau)$	Lineshape	Linewidth
Incoh. SPS	P_σ	Given in Eq. (2.7)	Given in Eq. (2.7)	Lorentzian	γ_σ
Coh. SPS	small Ω_σ	$4\Omega_\sigma^2/\gamma_\sigma^2$	Given in Eq. (1.48)	t_2-distribution	γ_σ
Coh. SPS	large Ω_σ	Given in Eq. (1.46)	Given in Eq. (1.50)	Triplet	$\begin{cases}\gamma_\sigma \text{ (central)} \\ 3\gamma_\sigma/2 \text{ (satellites)}\end{cases}$

Table 5.1: Characteristics of a SPS driven incoherently or coherently. In the latter case, for clarity, we also consider separately the low-driving intensity (middle column) from the general case (right column) that covers all pumpings, to highlight the strong qualitative features of the Mollow regime.

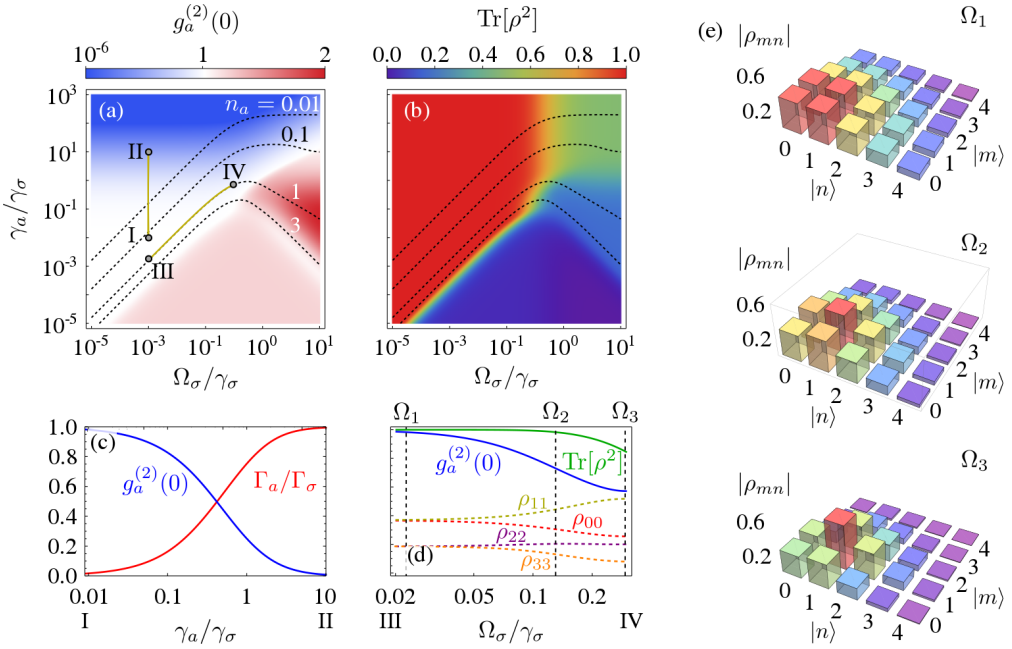

Figure 5.2: Pure quantum states in the steady state. The red area of (b) shows areas where the system is in a pure state. The density plot of $g_a^{(2)}(0)$ in (a) shows that this corresponds to states with $g_a^{(2)} \leq 1$. It is possible to have antibunched mixed states. Four isolines of constant populations are shown on both panels. (c) Antibunching and ratio of the effective linewidths of the target and source along the line I–II, showing a transfer of properties from the source to its target. (d) Antibunching and diagonal elements of the density matrix along the line III–IV. (e) Density matrices for three pumping powers. At Ω_3, the system is in state $|1\rangle$ with more than 60% probability, although not in a pure state anymore.

decay. The cut along the line I–II shows the transition from a regime where the target behaves according to its own classical nature (I) to one where it inherits instead the properties of the quantum source (II). In the former case, where the repetition rate of the emitter is larger than the decay rate of the target, the many excitations that can be accumulated give predominance to the target, which grows a coherent state ($g_a^{(2)} = 1$) and exhibits the same PL spectrum as it would than if excited classically. In the latter case, on the contrary, where the input is sparse, the target simply stores the excitation and reproduces it faithfully. This is the counterpart to the effect described in Chapter 3, in which a 2LS driven in the Heitler regime is the basis to generate single photons with a sub-natural linewidth.

Some interesting scenarios lie in the intermediate region, where the state fed into the cavity mixes characteristics of both its input and its recipient. These states, however, require the concept of mixity that involves statistical averages and the upgrade of the wavefunction (a state vector, given in Eq. (5.1)) to a density matrix

$$\rho = \sum_{n,m=0}^{\infty} \rho_{nm} |n\rangle \langle m| \, . \tag{5.2}$$

Thus, one can create quantum states of the light field with no need of quantum engineering, merely by exciting the system with resonance fluorescence. This realizes what one can refer to as "dissipative Fock state N," defined as a steady state in an open environment qualitatively close to $\rho_{nm} = \delta_{Nn}\delta_{Nm}$, with δ_{kl} a Kronecker delta, as shown in Fig. 5.2(e). Together with the Fock states, we thus can find such steady states with population larger than one and exhibiting antibunching, $g_a^{(2)} < 1$. Also, whenever $g_a^{(2)} < 1/2$, the population is less than unity, thus still satisfying on average this flawed criterion for single-particle excitation, which we have reviewed in Chapter 3. Another cut, III–IV, on the isoline of average population fixed to unity, shows how

antibunching increases as the amplitude of state $|1\rangle$ increases at the expense of vacuum and state $|3\rangle$, keeping the amplitude of state $|2\rangle$ the same, which in practice allows to have quantum control in the steady state. Sánchez Muñoz et al. (2014a) have observed that considering sources with an even higher quantum character, it is possible to reach pure steady-state wavefunctions for the driven harmonic oscillator such that $\rho_{22} > \max(\rho_{11}/2, \rho_{33})$, that is, with less quantum fluctuations for two particles in the steady-state than are normally allowed by spontaneous emission, thereby realizing an effective dissipative Fock state of two particles.

5.3 CHARTING THE HILBERT SPACE

A natural question that is raised when exciting with quantum light is whether this kind of driving increases the space of quantum states accessible to the system being excited. For this, however, we need a road map to characterize all the states at a glance. The Hilbert space is a big place, and Human's capacity of abstraction gives a deceivingly simple picture of it. The canonical basis of Fock states $|n\rangle$ with $n \in \mathbb{N}$ provides a comprehensive and concise map of the states in the harmonic oscillator's Hilbert space $\mathcal{H}_\infty$, writing them as the wavefunction in Eq. (5.1). While this expression is precise, it also fails to provide a qualitative map of the possible states. Beyond Fock states, one needs to keep track of the coherent states from classical physics, as shown in Eq. (1.31), for which $\alpha_n = \alpha^n \exp(-|\alpha|^2)/\sqrt{n!}$ for some complex number α that defines the amplitude and phase of a classical field. The next family of important states can only be described through a density matrix, as in Eq. (5.2). For instance, now we can introduce the thermal states, for which $\rho_{nm} = (1-\theta)\theta^n \delta_{nm}$ for some reduced temperature $\theta \in [0, 1]$. Laussy et al. (2006) showed that these two families can be unified into a larger class of "cothermal" states that interpolate between the two and describe, e.g., single-mode Bose condensates not too far from threshold. From there on, one essentially deals with quantum states of light with popular examples such as Lvovsky (2015)'s squeezed states, Haroche and Raimond (2006)'s cat (and kitten) states, and other less popular states such as Stoler, Saleh, and Teich (1985)'s binomial states or Nieto (1997)'s displaced Fock states. While this zoology of states is familiar to every quantum physicist, it fails to provide the sought mapping of the Hilbert space. In particular, it is restricted to known (and popular) cases and leaves most of Eqs. (5.1–5.2) uncharted.

For the following discussion, I propose to chart the Hilbert space based on important observables of the quantum state, namely, the Nth order correlation function, introduced in Eq. (1.32). Since we are interested in the quantum state of the harmonic oscillator, and not in the way in which the system has reached such a state, the normalization makes the first-order correlation function, $g_a^{(2)}(1)$, to be trivially unity. I therefore use instead the normalization itself, which is an important observable, the population of the state (average number of excitations), n_a, for which we use the notation introduced in Eq. (1.25). Note that to measure (and compute) the corrrelations in Eq. (1.32) we only need the diagonal elements $p(m) = |\alpha_m|^2$, so in this discussion there is no distinction between pure (given by a wavefunction, as in Eq. (5.1)) and mixed (described only through a density matrix, as in Eq. (5.2)) states. In terms of these diagonal elements, the n-th order correlator (defined in Eq. (1.32), and at zero delay) reads:

$$g_a^{(n)} = \frac{\sum_{m=0}^{\infty} m! p(m)/(m-n)!}{\left(\sum_{m=0}^{\infty} m p(m)\right)^n}. \tag{5.3}$$

A convenient mapping of the Hilbert space is to chart it with the n_a and $g_a^{(2)}$ "rulers", that is, tag the possible quantum states through their joint statistical properties and population. The value of $g_a^{(2)}$ allows to tell apart classical from quantum states depending on whether $g_a^{(2)}$ is larger (bunching) or smaller (antibunching) than unity. This is meant in the sense of whether a classical, possibly stochastic, description is possible, or whether some "quantum" features such as violation of Cauchy–Schwarz inequalities or negative probabilities in the phase space are manifest. The population gives another meaning to quantumness, in the sense of few-particle effects vs macroscopic occupation. It is therefore particularly interesting to contrast these two

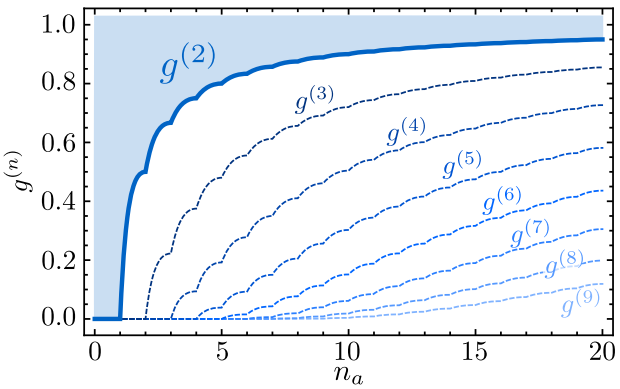

Figure 5.3: Charting the Hilbert space. The shaded area shows the region where a physical quantum state exists with the corresponding joint population and antibunching. It is delimited by the boundary Eq. (5.4) of "Fock duos", defined by Eq. (5.5). Higher order correlators (thin dashed) set other boundaries, also delimited by Fock duos.

attributes and consider, e.g., highly occupied genuinely quantum states. There is a physical limit to such states and for populations $n_a > 1$, some values of antibunching are out of reach. This is expected on physical grounds from familiar features of the Fock states popularly known as being the "most quantum" states, with their $g_a^{(2)}$ tending to one as the number of excitations increases. Also, macroscopic quantum states, such as a BEC, are essentially coherent states in most formulations. Here, I make this notion precise by providing the complete picture, in Fig. 5.3, along with the closed-form expression for the boundary that separates accessible combinations from impossible ones (the proof of this is detailed in Appendix B.1):

$$g_a^{(2)} = \frac{\lfloor n_a \rfloor (2n_a - \lfloor n_a \rfloor - 1)}{n_a^2} \,. \tag{5.4}$$

This boundary is provided by superpositions of contiguous Fock states, i.e., of the type:

$$\sqrt{p(n)}\,|n\rangle + \sqrt{1-p(n)}e^{i\theta}\,|n+1\rangle \,, \tag{5.5}$$

for $n \in \mathbb{N}$, $p(n) \in [0,1]$ and $\theta \in [0, 2\pi[$ an (irrelevant) phase. As already commented, this includes also mixed states of the type $p(n)\,|n\rangle\langle n| + (1-p(n))\,|n+1\rangle\langle n+1|$ and all others with the same diagonal but different off-diagonal elements. I will not make this distinction anymore in the following. I call the states in Eq. (5.5), "*Fock duos*". They set the continuous lower limit of the space of available quantum states in our charted Hilbert space. Their antibunching, Eq. (5.4), is a generalization to non-integer n_a of the formula $g_a^{(2)} = 1 - 1/n_a$ for the Fock state $|n_a\rangle$ to which it reduces for $n_a \in \mathbb{N}$. In particular, it shows that the popular "single-particle criterion" that asserts that $g_a^{(2)} < 0.5$ ensures a one particle state—which is rather widely used in the community, cf. Michler et al. (2000), Dong et al. (2007), Verma et al. (2011), di Martino et al. (2012), and Leifgen et al. (2014)— is wrong, as demonstrated, e.g., for the case $n_a = 1.5$ for which $g_a^{(2)} = 4/9 \approx 0.44$. The generalization to higher orders is straightforward. Namely, the nth-order correlation frontier for real n_a is given by:

$$g_a^{(n)} = \frac{\lfloor n_a \rfloor !}{(\lfloor n_a \rfloor - n)! n_a^n} \left[1 + \frac{n(n_a - \lfloor n_a \rfloor)}{\lfloor n_a \rfloor + 1 - n}\right] , \tag{5.6}$$

which generalizes the Fock state formula $g_a^{(n)} = (1/n_a^n) m!/(m-n_a)!$ valid for integer n_a where it agrees with Eq. (5.6). Interestingly, the lower limit is also set, for all n, by Fock duos (not "n-plets"). One can also consider other charts of the Hilbert space, such as $(g_a^{(2)}, g_a^{(3)})$, this time contrasting two- and three-particle correlations together, but with Zubizarreta Casalengua et al. (2017) we have demonstrated that this space is not bounded, as shown in Fig. 5.4. Since the excitation of an harmonic oscillator by the SPS leads to strong correlations between various $g_a^{(n)}$, we will focus on the $(n_a, g_a^{(2)})$ space.

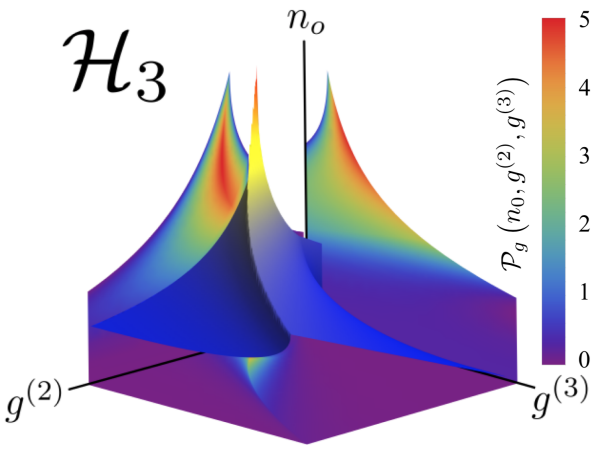

Figure 5.4: The complete distribution for $\mathcal{H}_3$, the Hilbert space for up to three particles, lives in a 3D space, shown here through its upper boundary along with the three projections on 2D spaces. The function $\mathcal{P}_g(n_0, g^{(2)}, g^{(3)})$ gives the density of probability of the states with a set of population, second- and third-order correlation functions. The figure is an adaption of one of my papers with Zubizarreta Casalengua et al. (2017).

5.4 EXCITING WITH AN INCOHERENT SPS

Now that we can conveniently characterize the states of the harmonic oscillator that one can excite, we come back to the dynamical problem of the quantum driving of an harmonic oscillator and how close can one get to the limit set by Eq. (5.4). We first consider the case of excitation with an incoherent SPS, i.e., where the two-level system (2LS) that acts as the source, is itself driven incoherently, as sketched in Fig. 5.1(c). Namely, there is a constant rate P_σ at which the 2LS is put in its excited state, and is otherwise left to decay. The system is thus described by the master equation (1.28), with $c_1 = \sigma$ the 2LS and $c_2 = a$ the harmonic oscillator operators, respectively. The 2LS pumping is described by a Lindblad term $(P_\sigma/2)\mathcal{L}_{\sigma^\dagger}\rho$. Thanks to the absence of feedback, the dynamics is ruled by closed equations which allows us to obtain exact solutions for the observables of interest. Namely, I find that the cavity population n_a and statistics $g_a^{(2)}$ of the target are given by (cf. the upper row of Table 5.1 for the source):

$$n_a = \frac{P_\sigma \gamma_\sigma}{(\gamma_\sigma + P_\sigma)(\gamma_\sigma + P_\sigma + \gamma_a)}, \qquad \text{and} \qquad g_a^{(2)} = \frac{2(\gamma_\sigma + P_\sigma)}{\gamma_\sigma + P_\sigma + 3\gamma_a}. \tag{5.7}$$

Only two parameters are required to describe fully the system:

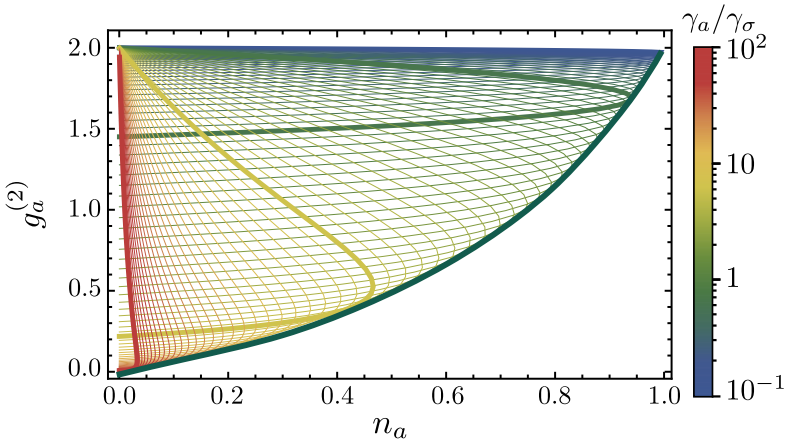

Figure 5.5: Trajectories in the Hilbert space charted by n_a and $g_a^{(2)}$ for the states excited by an incoherent SPS, for various values of γ_a/γ_σ. The implicit parameter is the pumping. Highlighted are the cases $\gamma_a/\gamma_\sigma = 10^{-1}$ (blue), 1 (green), 10 (yellow) and 10^2 (red). The dark green thick envelope shows the closest one can get in this configuration to the ideal antibunching, which is zero. All the states, and only these states, above this line and below $g_a^{(2)} = 2$, are accessible with an incoherent SPS.

- the ratio between the decay rate of the cavity and the leakage rate of the 2LS, γ_a/γ_σ, and
- the intensity (or pumping rate) of the 2LS, P_σ, also normalized to γ_σ to keep the parameters dimensionless.

Eliminating P_σ from Eqs. (5.7) gives the equation for the trajectory in the $(n_a, g_a^{(2)})$ space as function of the parameter γ_a/γ_σ:

$$n_a = \frac{1}{6}\frac{(2-g_a^{(2)})(3g_a^{(2)}(\gamma_a/\gamma_\sigma)-(2-g_a^{(2)}))}{g_a^{(2)}(1+g_a^{(2)})(\gamma_a/\gamma_\sigma)}\,. \tag{5.8}$$

These trajectories in the Hilbert space are plotted in Fig. 5.5. The curves start from the point:

$$\left(n_a = 0, g_a^{(2)} = \frac{2}{1+3\gamma_a/\gamma_\sigma}\right), \tag{5.9}$$

at vanishing pumping, reach a turning point with coordinates:

$$\left(n_a = \frac{2+(\gamma_a/\gamma_\sigma)-2\sqrt{1+(\gamma_a/\gamma_\sigma)}}{(\gamma_a/\gamma_\sigma)^2}, g_a^{(2)} = \frac{2}{3\sqrt{1+\gamma_a/\gamma_\sigma}-2}\right), \tag{5.10}$$

when the rate of driving takes the value $P_\sigma = \sqrt{\gamma_\sigma(\gamma_a+\gamma_\sigma)}$ and converge at $(n_a = 0, g_a^{(2)} = 2)$ at large pumpings, where the source gets quenched. For each value of γ_a/γ_σ, there are two values of pumping that result in the same population but two values of $g_a^{(2)}$. The curve of Eq. (5.8) is fairly constant till the turning point and, from Eq. (5.9), leads to a genuine quantum state (which, e.g., feature antibunching) as long as $\gamma_a/\gamma_\sigma > 1/3$, which means that, with a SPS one can imprint antibunching in a system that has a substantially longer lifetime. The optimum antibunching/population for a given γ_a/γ_σ is achieved slightly earlier than the turning point, namely, when $P_\sigma = \gamma_\sigma$. The envelope of all the curves in Fig. 5.5 is the closest one can get to the Fock-duos limit, and is given by $g_a^{(2)} = 2n_a/(3-2n_a)$. This is the thick dark green line in Fig. 5.5.

The above solution gives an already substantial description of the response of an harmonic oscillator to an incoherent SPS. We can complement it with alternative descriptions that approach the solution from different viewpoints and manifest the advantage of cascaded coupling over other types of excitation. A natural comparison is with the standard Hamiltonian coupling, which is the usual way to couple different systems. For instance, it is convenient to lay out the observables as function of the parameters in 2D density plots, as shown in Fig. 5.6. Panels (a–c) show the photon statistics (color code) and the population of the cavity (isolines) using the (a) cascaded coupling and (b, c) the Hamiltonian coupling. For the later case, we consider two configurations: (b) when the 2LS has the same decay term as when acting as a source in the cascaded scheme, and (c) when the 2LS has no decay term, so that all its excitation is directed towards the cavity, corresponding to the ideal excitation of the cascaded scheme. Interestingly, (a) and (b) types of excitation present a qualitatively similar photon statistics layout, but the topography of the resulting population yields largely differing states, as evident once reported in the $(n_a, g_a^{(2)})$ space, panel (d). The color circles along the isolines mark the points with strongest antibunching (i.e., smallest $g_a^{(2)}$) for a given population. It is seen that for a given signal, the antibunching is significantly larger with the cascaded coupling. In both cases the antibunching is marred before the cavity population reaches one photon on average. At larger populations, the photon statistics of the cavity become bunched, i.e., $g_a^{(2)} = 2$. On can contemplate other configurations but they result in worse results: detuning the cavity from the 2LS leaves the photon statistics unchanged, but reduces the population of the cavity, so the antibunching is lost at even smaller cavity populations. Dephasing the 2LS increases the broadening of the emission peak, but also drives the cavity towards a coherent state faster. Hamiltonian coupling with no decay of the 2LS, case (c), differs qualitatively from the former cases and provides a substantially better antibunching than Hamiltonian coupling with decay of the 2LS. It even becomes better than the cascaded coupling when $n_a \gtrsim 2/3$. This situation can be much improved with the coherent SPS.

5.5 EXCITING WITH A COHERENT SPS

We now consider excitation by a coherent SPS, i.e., when the 2LS that acts as the source is driven coherently by an external laser, as sketched in Fig. 5.1 (d). This driving is described by the Hamiltonian:

$$H_\sigma = \omega_\sigma \sigma^\dagger \sigma + \Omega_\sigma \sqrt{\epsilon_1}(\sigma^\dagger e^{-i\omega_L t} + \sigma e^{i\omega_L t}), \tag{5.11}$$

where ω_σ is the energy of the 2LS, and ω_L and $\Omega_\sigma = \sqrt{\gamma_\sigma}\mathcal{E}$ are the frequency and intensity of the driving laser (which drives a 2LS of decay rate γ_σ with a coherent field of intensity $\mathcal{E}$), respectively. The coefficient $\sqrt{\epsilon_1}$ is put here so that the cavity is driven only by the emission of the 2LS and not by the external laser. The system is otherwise still described by the master equations (1.27) and (1.30), with $c_1 = \sigma$ the 2LS (source) and $c_2 = a$ the harmonic oscillator (target), and reducing the coupling strength by a factor $\sqrt{1-\epsilon_1}$, i.e., the coupling is given by $\sqrt{(1-\epsilon_1)\gamma_a\gamma_\sigma}$. Here again, one can obtain the cavity observables in closed-form, although it

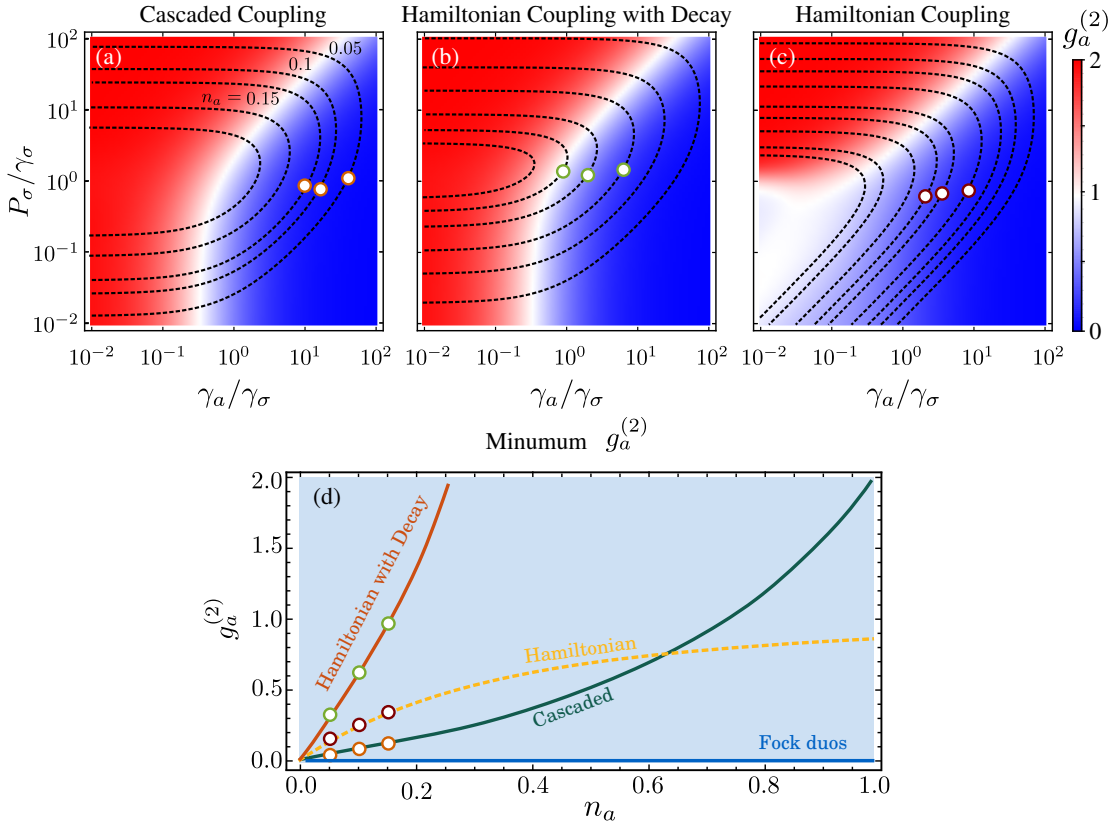

Figure 5.6: Populations (isolines) and $g_a^{(2)}$ (color) of the target excited by an incoherent SPS, through (a) the cascaded coupling or (b,c) the Hamiltonian coupling with (b) and without (c) decay of the 2LS. (d) Minimum $g_a^{(2)}$ that can be reached at a given population for all these cases. The color circles mark the parameters P_σ/γ_σ and γ_a/γ_σ at which the population isoline meets the minimum $g_a^{(2)}$.

takes slightly more cumbersome expressions. At resonance (out-of resonance cases can also be obtained but get even more bulky):

$$n_a = \frac{16(1-\epsilon_1)\gamma_{\widetilde{01}}\Omega_0^2\left(\gamma_{\widetilde{11}}^2\gamma_{\widetilde{12}}+8\gamma_{\widetilde{10}}\Omega_0^2\right)}{\gamma_{\widetilde{10}}\gamma_{\widetilde{11}}(\gamma_{\widetilde{01}}^2+8\Omega_0^2)(\gamma_{\widetilde{11}}\gamma_{\widetilde{12}}+16\Omega_0^2)}\,, \tag{5.12a}$$

$$g_a^{(2)} = \Big\{\gamma_{\widetilde{11}}(\gamma_{\widetilde{01}}^2+8\Omega_0^2)(\gamma_{\widetilde{11}}\gamma_{\widetilde{12}}+16\Omega_0^2)[\gamma_{\widetilde{11}}\gamma_{\widetilde{21}}^2\gamma_{\widetilde{31}}^2\gamma_{\widetilde{12}}\gamma_{\widetilde{32}}+8\gamma_{\widetilde{10}}\gamma_{\widetilde{31}}(17\gamma_{\widetilde{10}}^3+29\gamma_{\widetilde{10}}^2\gamma_{\widetilde{01}}+18\gamma_{\widetilde{10}}\gamma_{\widetilde{01}}^2+$$
$$+4\gamma_{\widetilde{01}}^3)\Omega_0^2+192\gamma_{\widetilde{10}}^2\gamma_{\widetilde{21}}\Omega_0^4]\Big\}\times\left[\gamma_{\widetilde{21}}\gamma_{\widetilde{31}}(\gamma_{\widetilde{11}}\gamma_{\widetilde{21}}+8\Omega_0^2)(\gamma_{\widetilde{31}}\gamma_{\widetilde{32}}+16\Omega_0^2)(\gamma_{\widetilde{11}}^2\gamma_{\widetilde{12}}+8\gamma_{\widetilde{10}}\Omega_0^2)^2\right]^{-1}\,, \tag{5.12b}$$

where I have introduced the notation $\gamma_{\widetilde{ij}} = i\gamma_a + j\gamma_\sigma$ (e.g., $\gamma_{\widetilde{31}} = 3\gamma_a+\gamma_\sigma$), and we have set $\Omega_0 = \sqrt{\epsilon_1}\Omega$. Eliminating Ω_σ^2 from Eqs. (5.12) yields, for a given γ_a/γ_σ, solutions of the type $g_a^{(2)} = (P[3]\pm\sqrt{P[6]})/(P[2]n_a^2)$ where $P[n]$ is an n-th order polynomial of the variable n_a. The $\pm$ terms provide the two branches of the curve as seen in Fig. 5.7(a). The lower branch corresponds to low pumping, where the photoluminescence (PL) of the source is still a single line as shown in the bottom inset, while the upper branch corresponds to high pumping where the PL has split into a Mollow triplet, shown in the upper inset. Each curve starts from the point:

$$\left(n_a = 0, g_a^{(2)} = \frac{1}{(1+\gamma_a/\gamma_\sigma)^2}\right)\,, \tag{5.13}$$

showing that coherent SPS provide a much stronger antibunching than their incoherent counterpart, Eq. (5.9), already at vanishing pumping. At high pumping, in contrast to the incoherent case that vanishes the population of its target, the coherent SPS quenches it to a nonzero value and featuring bunching:

$$\left(n_a = \frac{1-\epsilon_1}{1+\gamma_a/\gamma_\sigma}, g_a^{(2)} = 3\frac{1+\gamma_a/\gamma_\sigma}{1+3\gamma_a/\gamma_\sigma}\right)\,. \tag{5.14}$$

Eliminating γ_a/γ_σ here leads to the curve $g_a^{(2)} = 3(1-\epsilon_1)/[3(1-\epsilon_1)-2n_a]$, which for $\epsilon_1 = 1/2$ simplifies to $g_a^{(2)} = 3/(3-4n_a)$ as shown in thick black in Fig. 5.7(a). The expression for the lower envelope of maximum antibunching, in blue, is too complicated to be derived fully in closed-form but we can find simple asymptotic expressions by series expansion of Eqs. (5.12), namely, $g_a^{(2)} \approx 5n_a^2$ when $n_a \ll 1$ and $g_a^{(2)} \approx 1-1/(3(n_a+5))$ when $n_a \gg 1$. The states thus get close to the ideal Fock limit for large populations, approaching unity as $1/(3n_a)$ rather than $1/n_a$. There is no limit in the population that can be excited in the target by the coherent SPS, in stark contrast to the incoherent SPS that is bounded by unity. Although the accessible states in the $(n_a, g_a^{(2)})$ space remain quite some distance away from the ideal limit, the coherent SPS provides a much better antibunching than its incoherent counterpart, as can be seen by comparing Figs. 5.5 and 5.7. Namely, it is still antibunched when population is unity (with a maximum antibunching slightly over $1/2$) and we have already commented how it allows for arbitrary large populations, that still feature antibunching. This is achieved by exciting at resonance targets of very long lifetimes as compared to the source.

This describes the resonant situation. Since the coherent SPS has a rich spectral structure, it opens new configurations of excitation in the Mollow triplet regime beyond the central peak, such as exciting with a satellite peak (as shown in Fig. 5.7(c)) or with the leapfrog window (Fig. 5.7(b)). In these cases we show the results in log-log plots as only small populations are within reach (unlike the case of resonance) and, in the case of leapfrog excitation, also a huge bunching can be imparted to the target. The envelope of optimum antibunching as obtained in resonance is reported in these panels (also in green) for comparison, showing that these alternative schemes do not enhance antibunching. The excitation with leapfrog processes allows to access new regions of the Hilbert space related to superbunching, so it is a configuration that presents its own interest. This is achieved at the price of small populations. Exciting with a

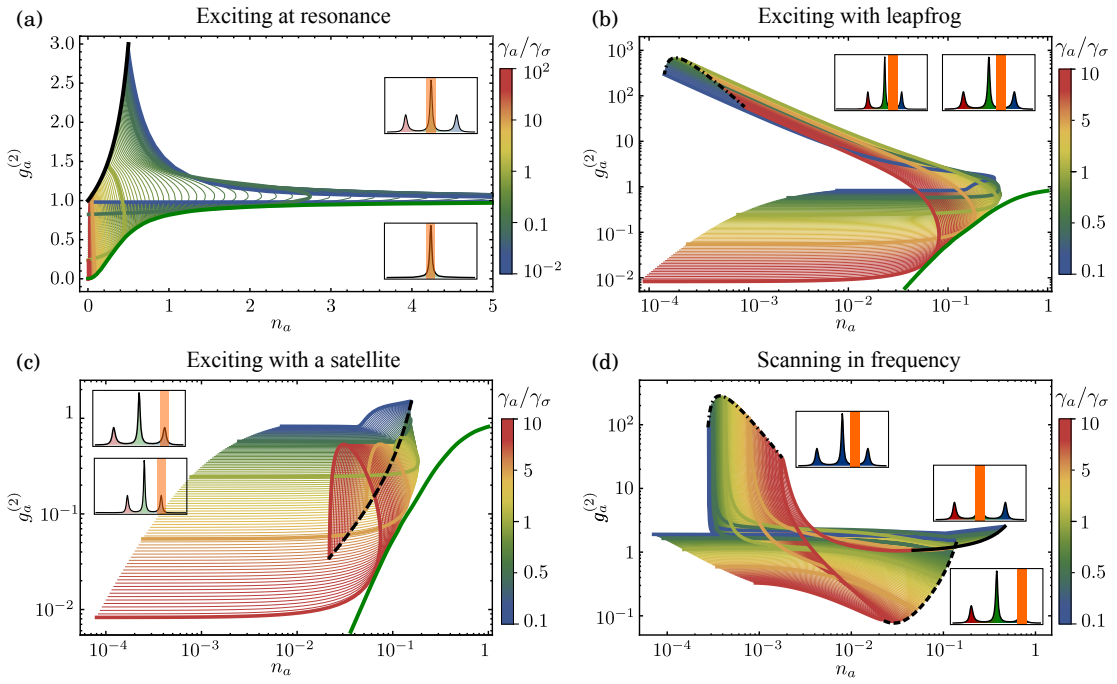

Figure 5.7: Same as Fig. 5.5 but for the excitation from a coherent SPS. In (a,c) the implicit parameter is the pumping to the two-level system and the green line shows the closest one can get from the Fock-duos limit from the case at resonance. In (d) the implicit parameter is the detuning between the source and its target. (a) Exciting at resonance. The optimum antibunching is the envelope in this configuration of the family of curves varying with γ_a/γ_σ. Highlighted are the cases $\gamma_a/\gamma_\sigma = 10^{-2}$ (blue), 10^{-1} (green), 1 (chartreuse), 10 (yellow) and 10^2 (red). (b-d) Exciting in other configurations, namely (b) with the leapfrog processes, (c) with the satellite and (d) as a function of frequency. Highlighted are the cases $\gamma_a/\gamma_\sigma = 10^{-1}$ (blue), 0.5 (chartreuse), 1 (green), 5 (orange) and 10 (red). The dashed-dotted line in panel (b) and the dashed line in panel (c) show the limit of large intensities and are merely a visual aid rather than a physical boundary. They are also shown in panel (d), along with the black solid line for the envelope of the curves at $\omega_a = \omega_\sigma$.

satellite peak also conquers new territories in the $(n_a, g_a^{(2)})$ space not accessible through either the central peak or leapfrog emission in a small region ($n_a \approx 0.6, g_a^{(2)} \lesssim 2$). Panel (d) shows the trajectories when varying the frequency of emission, where the cases just discussed—resonance, leapfrog and satellites—appear as boundaries of the complete picture, thus showing that these configurations already give access to all the accessible states.

We can also compare in the parameter space the coherent SPS with its Hamiltonian counterpart, as we did for the incoherent SPS. This is shown in Fig. 5.8, that is also usefully compared with Fig. 5.6 (incoherent SPS excitation). For the coherent SPS as well, both cascaded and Hamiltonian coupling are qualitatively similar in their statistical layout when the 2LS has a decay term, but also differ notably from the topography of the associated intensities. This is, again, clear on the $(n_a, g_a^{(2)})$ space, with the maximum antibunching that can be obtained for a given cavity population with cascaded coupling (green line) and Hamiltonian coupling (red line). The Hamiltonian coupling with no decay of the 2LS also results in qualitative differences and an enhanced antibunching. However, in this case, the Hamiltonian coupling never comes to surpass the cascaded scheme. Instead, in all the range of population, the antibunching obtained through the cascaded coupling is larger than the one obtained with any type of normal (Hamiltonian) coupling, for a given population. When the cavity is detuned from the 2LS, the antibunching is lost before the cavity's population reaches one photon. Also, when the cavity is in resonance with the leapfrog process emission, the photon statistics of the cavity is superbunched but its population remains well below unity. Including a dephasing rate to the

dynamics of the 2LS increases the broadening of each emission line in the triplet, and even a small dephasing rate spoils the antibunching. Thus, the best antibunching with a coherent SPS is obtained exciting the cavity at low pumping and in resonance with the 2LS, using the cascaded coupling.

One of the departing features of the coherent SPS excitation, is that it allows to populate its target with more than one excitation on average, therefore triggering Bose stimulation effects. There is a phase locking (of 0, as determined by the Hamiltonian) of the incident photons from the quantum source that accumulate while still exhibiting some features of Fock states, in particular being antibunched. A complete picture of the resulting quantum states, beyond the diagonal elements only, is given Fig. 5.9 for the states marked with black circles in Fig. 5.6(f), both through the Wigner representation, Fig. 5.9(a-c), and through their matrix representation, Fig. 5.9(d-f). The Wigner representation exhibits negative values at the origin, a mark of a genuine quantum state with no classical counterpart, for the states with $n_a = 1$ and $n_a = 1.5$. It is, however, positive everywhere for $n_a = 3$, although the state is still antibunched. Also, one can see that the phase uncertainty decreases as the population increases, in agreement with the "classical limit". Moreover, the matrix elements in these cases also satisfy the relation $\rho_{22} > \max(\rho_{11}/2, \rho_{33})$, which means that the fluctuations are smaller than could be expected from rate equation arguments, since two excitations are twice as much likely to decay than one excitation, making the probability to find one excitation only in principle at least twice as large than double occupation.

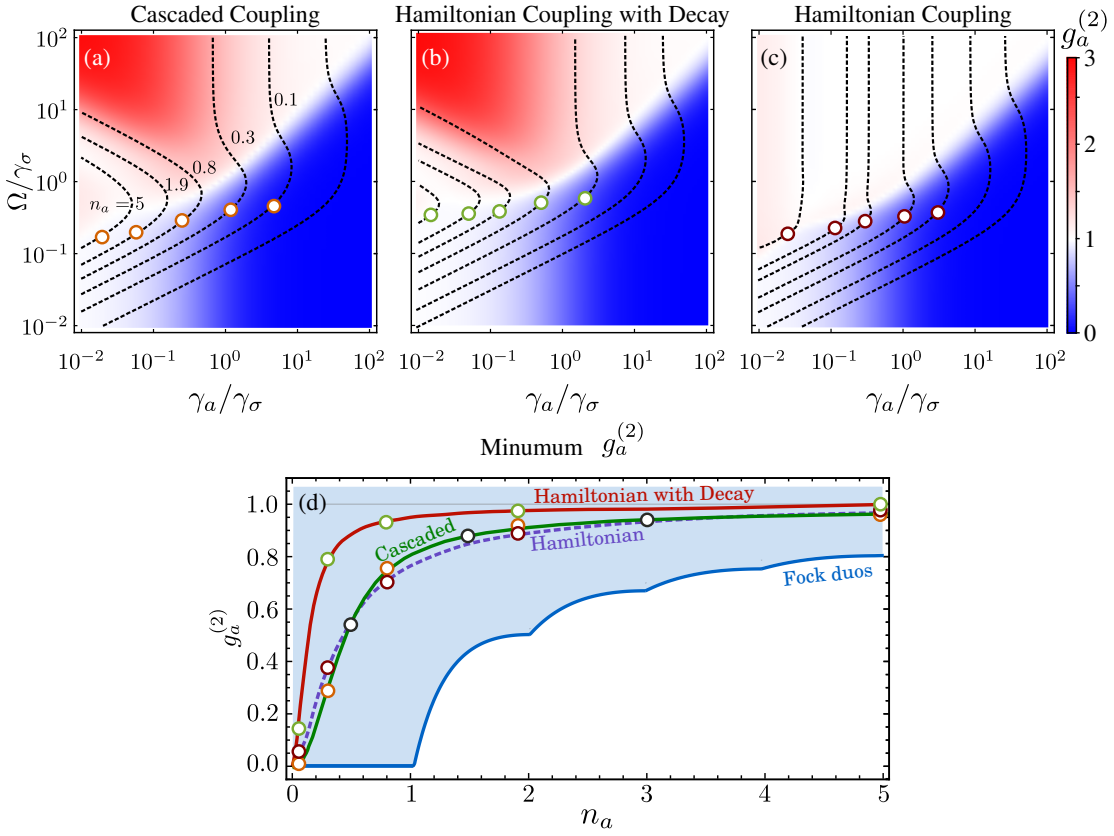

Figure 5.8: Same as Fig. 5.6 but for a coherent SPS, with (a) the cascaded coupling and (b,c) the Hamiltonian coupling with (b) and without (c) decay of the 2LS. (d) Minimum $g_a^{(2)}$ that can be reached at a given population for all these cases. The color circles mark the parameters $\Omega_\sigma/\gamma_\sigma$ and γ_a/γ_σ at which the population isoline meets the minimum $g_a^{(2)}$.

We conclude this Section on driving an harmonic oscillator with the coherent SPS by considering states in the $(g_a^{(2)}, g_a^{(3)})$ space. This is shown in Fig. 5.10 for the most notable configurations of exciting with the central peak of the Mollow triplet or the leapfrog region between the central peak and a satellite. All points are physical on this map, including cases with $g_a^{(2)} \ll 1$ and $g_a^{(3)} \gg 1$ (and vice-versa), although the accessible regions are strongly confined along curves that we can fit in monomial form, leading in good approximation to $g_a^{(3)} \approx 0.2[g_a^{(2)}]^2$ at low pumping (in the antibunching corner) and $g_a^{(3)} \approx 4.5 g_a^{(2)}$ at large pumpings (in the superbunching corner). We indicate positions of popular quantum states such as Fock states, coherent states, thermal states and their combinations. Driving with a SPS spans over great distances in this space, especially when exciting with leapfrog processes, as seen in panel (a) of the figure. This shows, again, how the central peak remains confined essentially to the antibunched corner of the map (excursions to bunching cases are up to $g_a^{(2)} = 3$). Panel (b) is a zoom around small values in linear scale. The leapfrog processes, on the contrary, allow one to reach large joint values of $g_a^{(2)}$ and $g_a^{(3)}$. Interestingly, while the points accessible in the $(n_a, g_a^{(2)})$ space extend over 2D areas, in the $(g_a^{(2)}, g_a^{(3)})$ space they are confined to 1D curves, showing how these correlators are strongly inter-dependent, and thus making the $(n_a, g_a^{(2)})$ representation more prominent.

5.6 VARIATIONS IN THE TYPE OF COUPLING

The comparison between the top rows of Figs. 5.6 and 5.8 shows that the coherent SPS is a much better quantum drive to generate bright antibunching than the incoherent one, even in the region where $n_a < 1$. The coherent SPS exciting the cavity still remains some distance away from the Fock duos boundary, but it gets significantly closer than with the Hamiltonian coupling. We complete our juxtaposition between the two types of coupling, cascaded and Hamiltonian, by comparing with other variations in the way the source couples to its target.

First, we consider another source of decay for the source in the cascaded coupling scheme, i.e., with an extra term $(\gamma_\sigma^*/2)\mathcal{L}_\sigma \rho$ in the master equation, leaving the coupling strength constant and equal to $\sqrt{\gamma_a \gamma_\sigma}/2$. This describes the situation where not all the light that is lost from the

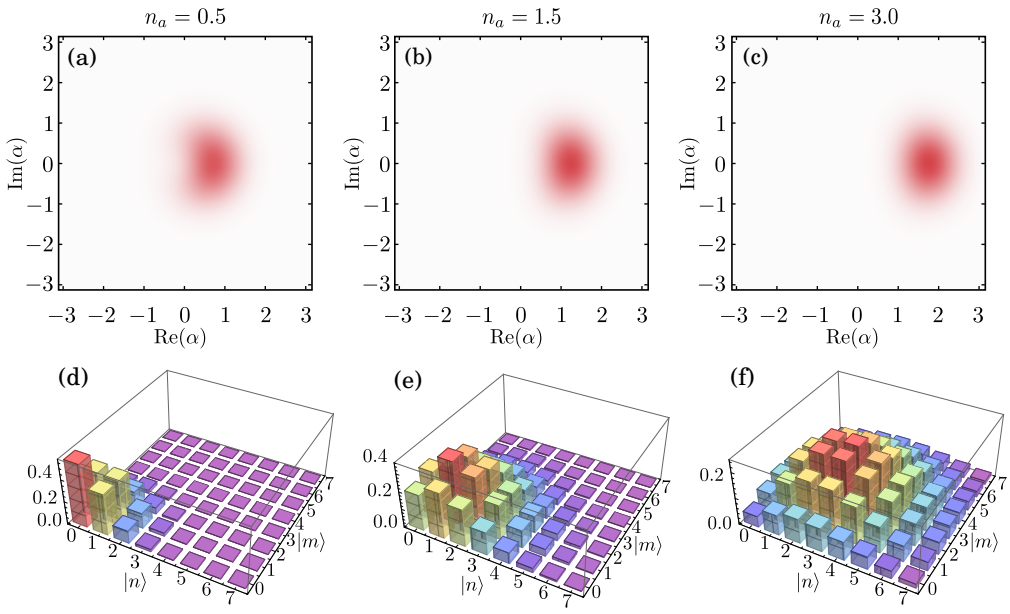

Figure 5.9: Wigner function (a–c) and density matrix (d–f) for the states marked by black circles along the green line in Fig. 5.8(d). These states have populations $n_a = 1$, 1.5 and 3 from top to bottom and all feature antibunching.

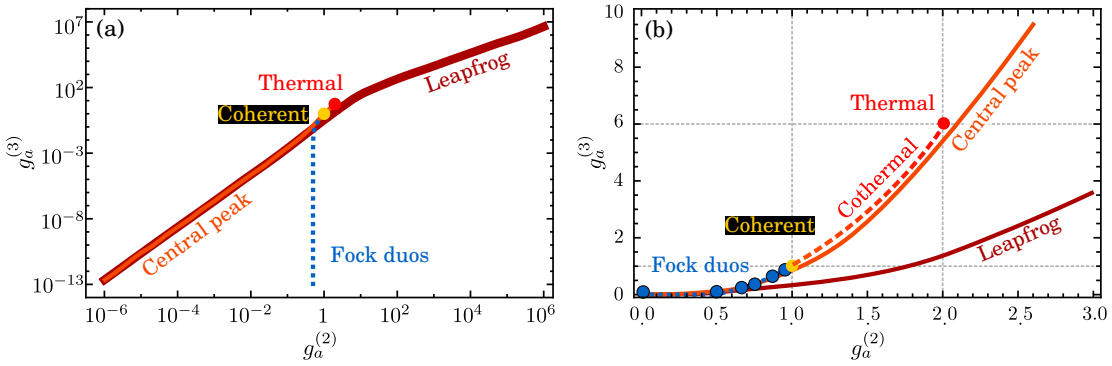

Figure 5.10: States accessible in the $(g_a^{(2)}, g_a^{(3)})$ space by coherent SPS excitation, at resonance with the central peak (orange line) or with the leapfrog emission (red line). The dashed blue line corresponds to the "Fock duos", Eq. (B.1). The same result is shown in both (a) log-log and (b) linear scales.

source is redirected to the target. Figure 5.11(a-b) shows how this other source of decay spoils the antibunching and drives the cavity faster toward a coherent state (for the coherent SPS) or to a thermal state (for the incoherent SPS). At $\gamma_\sigma^* = 10\gamma_\sigma$, the antibunching is worse than that obtained using the Hamiltonian coupling (without any additional dissipative channel). This shows that it is better to minimize losses from the quantum emitter, but that unless these are drastic, the impact is moderately detrimental. Note that the cascaded coupling strength can only be smaller or at most equal to $\sqrt{\gamma_1\gamma_2}$, unlike the statements by Flayac and Savona (2014), who refer to "arbitrary coupling strengths". This leads, otherwise, to unphysical states for the target. Second, in the Hamiltonian coupling, we increase the coupling strength and bring the system into the strong-coupling regime. This is one considerable degree of freedom of the Hamiltonian coupling that is lost when considering some external excitation, since photons that drive the system from outside can couple to it in the first place because it is dissipative. In fact, the more efficient is the source–target coupling, the more dissipative the target has to be. But a dissipative target cannot sustain quantum effects for long, as the states do indeed decay. Therefore there is a compromise for the target's lifetime to allow simultaneously an efficient driving from the source while still allowing to store long enough the imprinted quantum attributes. In the Hamiltonian coupling, however, coupling and decay are independent and one can consider a pure Hamiltonian picture with no decay whatsoever. We will see later in Chapter 8 how one can remedy to this vicious circle to some extent by considering other types of quantum sources. For now, we show that, surprisingly, the cascaded coupling indeed provides a better quantum driving than the Hamiltonian coupling brought in the strong-coupling regime. This is because in the latter case, the reversible process from the "target" back to the "source" acts like an effective decay. This is shown in Fig. 5.11(c,d), where we compare again the maximum antibunching obtained in the configuration of Sec. 5.5 (solid green lines) with a magnified Hamiltonian coupling $\tilde{g} = N\sqrt{\gamma_a\gamma_\sigma}/2$ for various N. For both the coherent and incoherent excitation cases, the antibunching is improved by raising the coupling strength. However, this improvement is still not large enough to overcome the cascaded coupling. As seen in the figure, even for large Hamiltonian coupling strengths, the antibunching obtained with the cascaded coupling (solid green line) is always significantly better. Increasing even further the value of N does not improve the antibunching, but makes it occur at larger $(\Omega_\sigma, \gamma_a)$ values. At this limiting case, the antibunching obtained for the Hamiltonian coupling with the decay of the source coincides with the antibunching for the Hamiltonian without the decay of the source. Therefore, Fig. 5.11(c) shows the optimum antibunching that can be obtained using both the cascaded and Hamiltonian couplings.

Increasing the coupling has a much stronger effect in the case of incoherent excitation, as shown in Fig. 5.11(d). Even a small variation of the coupling strength, $N = 1.5$, changes

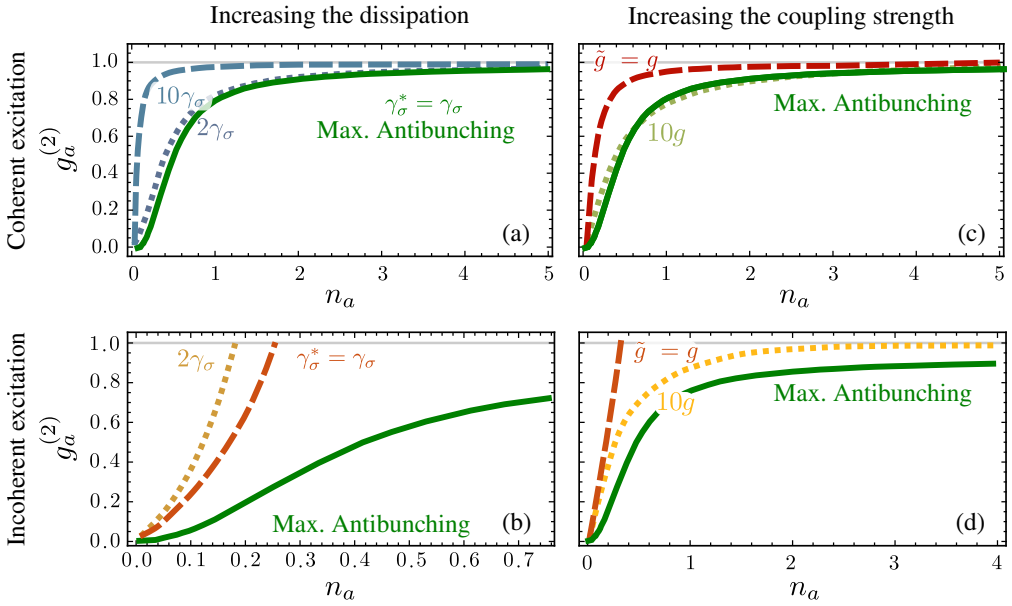

Figure 5.11: Variations in the model. (a, b) Adding a dissipative channel to the source in the cascaded coupling spoils the antibunching. (c, d) Increasing the coupling strength g in the Hamiltonian coupling (with decay in the source) enhances the antibunching until it reaches the one obtained for the Hamiltonian coupling without decay of the source (when $\tilde{g} \approx 10g$). However, the enhancement is never enough to top the antibunching obtained using the coherently driven 2LS and the cascaded coupling.

significantly the curvature of the antibunching curve. For instance, del Valle and Laussy (2011) showed that increasing the value of N makes the system enter the "one-atom laser" regime and the state in the cavity becomes coherent. As for the coherent excitation, the best antibunching saturates with increasing coupling (converging at roughly $\tilde{g} = 10g$), with larger values of the coupling strength merely occurring at larger (P_σ, γ_a) values. Nevertheless, although raising the coupling strength improves the antibunching, and at large $\tilde{g}$ the $g_a^{(2)}$ approaches 1 when the cavity population increases, the best antibunching is still obtained with the cascaded coupling in the coherent excitation regime (green line in Fig. 5.11(d)). Overall, it is therefore established that optimum antibunching is obtained in the cascaded architecture. This could have important consequences in the design of future quantum-optical devices.

5.7 CONCLUSIONS

My analysis of the excitation by a SPS of a quantum harmonic oscillator can be summarized by Fig. 5.12. Here I show again the charting of the Hilbert space of the quantum harmonic oscillator that I have introduced, along with the various areas that can be accessed with a SPS. First, the region I of physical states, shown in light blue, delimited by Fock duos (Eq. (5.5)) according to Eq. (5.4). No state exists that can provide the corresponding joint population and antibunching in the white region. In contrast to popular belief, states do exist in the region above this boundary that satisfy $g_a^{(2)} < 1/2$ and $n_a > 1$ which shows that on mathematical grounds, the criterion $g_a^{(2)} < 1/2$ cannot be used to exclude states with more than one particle. In this region of physical states, the green area can be accessed in the steady state by exciting a cavity with a SPS, provided an adequate γ_a/γ_σ ratio and pumping. The largest span is realized by a coherent SPS (i.e., a 2LS itself driven by a laser) at resonance with its target. This gives access to the light green region II. Not all states are accessible in this configuration, in particular the limit of Fock duos remains some distance away from the driven dissipative case. States of arbitrary populations can be reached with the coherent SPS (by using targets with long enough

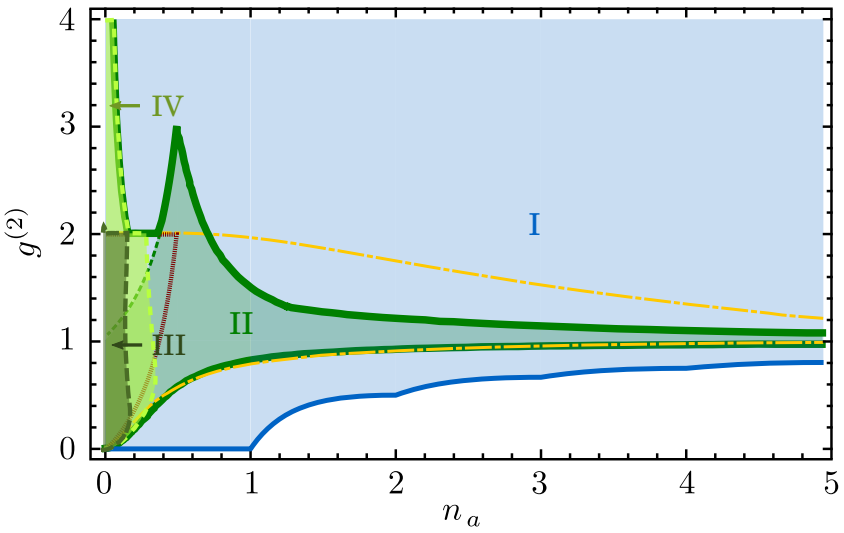

Figure 5.12: Summary of our results: the Hilbert space of an harmonic oscillator charted by the n_a (population) and $g_a^{(2)}$ (second-order correlation function) is accessible for any point in the blue region I (the white region is forbidden). Of this region, the wider span is achieved by exciting with a coherent SPS, covering the green region. This region breaks down into II, the region achieved at resonance between the source and the target, III, that achieved with the excitation from a satellite of the Mollow triplet and IV that achieved with the leapfrog emission. The incoherent SPS covers a smaller region, delimited by the red dotted curve. The Hamiltonian coupling, between the two dotted-dash yellow curves, also covers a large span of the Hilbert space and is neither included nor fully excluded of the SPS area. In particular, the excitation by a SPS allows to provide a stronger antibunching for any given population as compared to a Hamiltonian coupling, although it still remains some distance away from the ideal limit.

lifetimes) that still retain antibunching. One can also realize states of arbitrary high bunching, by using leapfrog emission of the SPS in the Mollow triplet regime. This is the region IV shown in dark green in Fig. 5.12. Exciting with the satellite peaks covers the region III that gives access to a small patch not within reach of II and IV. Other frequencies do not lead to areas not already covered by these cases. The incoherent SPS does not extend this territory either, as it is contained in the area $2n_a/(3-2n_a) \leq g_a^{(2)} \leq 2$, shown in dotted red. Notably, the region accessible by the Hamiltonian regime does not include nor is included by that accessible with the cascaded coupling. They do share some common area. In fact, cascaded coupling reduces to Hamiltonian coupling whenever $g/\gamma_\sigma \ll \gamma_a/\gamma_\sigma$ which, for the cascaded coupling constrain of $g/\gamma_\sigma = \sqrt{\gamma_a/\gamma_\sigma}/2$, provides the criterion $\gamma_a/\gamma_\sigma \gg 1/4$ for which the conventional formalism is enough to describe excitation with no feedback. This criterion allows, for instance, to develop del Valle et al. (2012)'s theory of frequency correlation in a conventional setting without the explicit need of the cascaded formalism to prevent feedback. In other cases, I have shown that cascaded coupling allows, surprisingly, to reach regions of the Hilbert space out of reach of a conventional Hamiltonian dynamics and, in particular, to improve the possible antibunching for a given population.

6 EXCITATION OF A TWO-LEVEL SYSTEM

In an infinite Universe anything can happen

— Douglas Adams

6.1 INTRODUCTION

The two-level system (to which Feynman, Leighton, and Sands (1971) refer to as the "two-state quantum system") is an important type of oscillator in the quantum universe. In some respects, it can be seen as the truly quantum oscillator, with a response at the single-particle level, whereas the (quantum) harmonic oscillator appears instead as a classical oscillator able to sustain non-classical motion. The 2LS, a fundamental object in any case, rose to gigantic proportion with Deutsch (1985)'s insight of quantum computation, that turned it into a "qubit", the elementary piece of information in the physical universe. It then became of primary importance to control the dynamics of a two-level system. To this day, this is achieved mainly with classical laser pulses, thanks to the "pulse-area" theorem shown by Golubev and Kuleff (2014) which states that any desired final state can be obtained with a suitable pulse. Entire textbooks have been written on the topic, one of the best ones by Allen and Eberly (1987), and still did not exhaust it.

In this chapter, we study the excitation of the 2LS (or qubit) when driven quantum mechanically, rather than classically. Here, we focus on the continuous excitation, and leave the pulsed excitation, of particular relevance for state preparation and quantum information processing, for future works. We will show that while the quantum states that can be prepared for a 2LS with the source of quantum excitation are not different than those accessible with the classical excitation, the dynamical emission, on the other hand, can reach new regimes. As an application, we will show how this can be used to engineer better single-photon sources. To a large extent, the problem posed in this Chapter also addresses the fundamental question of what defines strong-coupling. The excitation of a 2LS by light falls largely in the framework of resonance fluorescence, whose most notable manifestation is the so-called Mollow (1969) triplet, which we have already discussed at length in the previous chapters. This occurs when the intense excitation (by a classical laser) of a 2LS dresses its bare states (ground $|g\rangle$ and excited $|e\rangle$) to give rise to new eigenstates from their quantum superposition $|\pm\rangle \equiv (|g\rangle \pm |e\rangle)/2$. The coupling is mediated by the classical laser that, being a c-number parameter, does not directly appear in the structure of the Hilbert space and thus neither in the quantum state. We will discuss in detail the nature of these dressed states when quantizing the excitation field and how various quantum states leads to various results.

The rest of the Chapter is organized as follows. Section 6.2 adapts the formalism which has been amply motivated and introduced in Chapter 5 to the 2LS. In Section 6.3, we study which states of the 2LS are accessible under quantum excitation and we show how, in the continuous driving regime, classical excitation is more suitable than driving by, say, a Single-Photon Source (SPS), in terms of the accessible states in the Bloch sphere. In Section 6.4, we discuss how strong-coupling takes place with the more general case of quantum light as the driving agent. Beyond a new definition for strong-coupling needed to accommodate quantization of the driving light-field, this discussion will also allows us to pinpoint which features are specific to the classical driving by contrasting all the variants of the Mollow triplet under various types of excitation. For instance, we will revisit the mysterious Heitler effect, already mentioned in Chapter 3, whereby the coherent absorption-emission processes in the low driving limit result in photons with the first-order coherence of the source (the laser) and the second-order coherence of the target (the 2LS). As such a source of spectrally narrow antibunched photons is

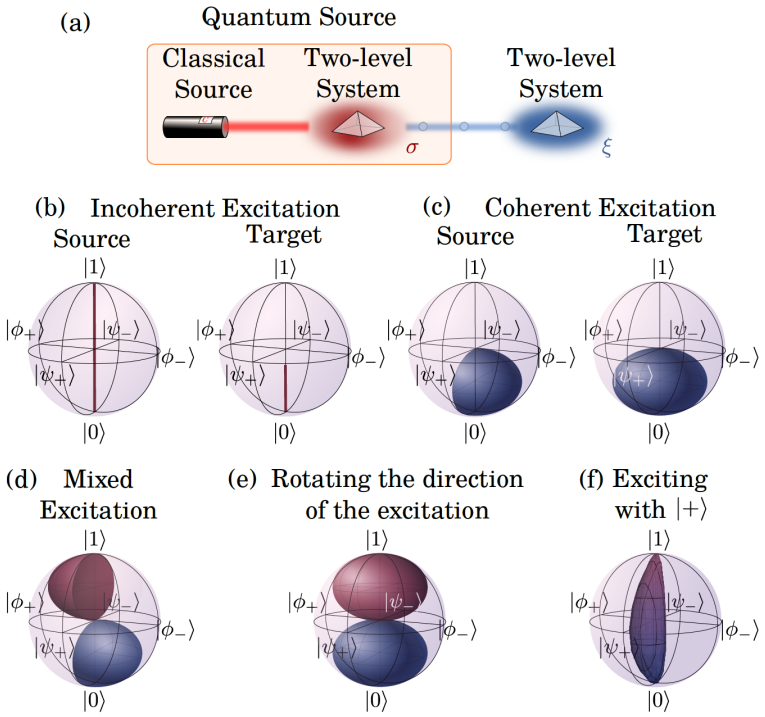

Figure 6.1: (a) A 2LS is driven by the emission of a quantum source. In this particular case, the quantum source is made of a 2LS driven by a classical source. (b-f) Accessible states of the 2LS under different driving configurations, as seen by the accessible volume in the Bloch sphere. The states of the equator of the sphere are $|\psi_\pm\rangle = (|0\rangle \pm |1\rangle)/\sqrt{2}$ and $|\phi_\pm\rangle = (|0\rangle \pm i\,|1\rangle)/\sqrt{2}$. (b) Incoherent excitation: this kind of excitation does not generate coherence in the 2LS, so all the accessible states lie along the z–axis of the Bloch sphere. (c) Coherent excitation: this kind of excitation does not allow the qubit to have a population larger than 1/2, so all the accessible states lie in the south hemisphere of the Bloch sphere. The source 2LS is allowed to go only in one half an the ellipsoid, while the target 2LS can cover the ellipsoid completely. (d) Mixed excitation: under this driving the source 2LS can access a symmetrical region in the north hemisphere of the Bloch sphere. However, the region available to the target 2LS does not increase. (e) Rotating the direction of the excitation of the source 2LS allows it to access the regions otherwise out of reach, thus filling the entire ellipsoid. (f) Exciting with a source that generates the transition $|+\rangle\langle 0|$ allows the source 2LS to access states with mean population 1/2 but not completely mixed.

of high technological interest, the understanding of its underlying principle is important. In Section 6.5, we take advantage of this understanding to design better SPS by turning the target into a source of its own, that excites still another 2LS. We will show how better antibunching can be achieved in this way that overcomes the Rayleigh scattering. Section 6.6 concludes.

6.2 THEORETICAL DESCRIPTION

Like in the previous Chapter, we use the cascaded formalism introduced in Section 1.2.1.2 to described the excitation of a target by a quantum source. However, in this Chapter we focus on a 2LS as the target (with annihilation operator ξ) and consider various sources that will be introduced as they are referred to. Taking for instance another 2LS with annihilation operator σ as the source, as sketched in Fig. 6.1(a), the resulting master equation takes the form of Eq. (1.28) with $c_1 = \sigma$ and $c_2 = \xi$, both following the Pauli algebra. Furthermore, each system has a decay rate γ_c and a Hamiltonian H_c, for $c = \sigma, \xi$. We now proceed to investigate which regions of the Hilbert space of the target 2LS are accessible under various types of driving.

6.3 ACCESSIBLE STATES

While in the previous Chapter we had to introduce a new charting of the harmonic oscillator's Hilbert space to map the states created by quantum excitation, there has long been a comprehensive representation for the two-dimensional Hilbert space of the 2LS: the *Bloch sphere*, which Bengtsson and Życzkowski (2008) have shown to describe unambiguously pure states, since the sphere is a projective space for two complex lines $(\alpha, \beta) \in \mathbf{C}^2$ and pure states of the 2LS are given by the wavefunction:

$$|\psi\rangle = \alpha\,|0\rangle + \beta\,|1\rangle\ . \tag{6.1}$$

The mapping is complete since it also accounts for the phase between the probability amplitudes. Feynman, F. L. Vernon, and Hellwarth (1957) have shown that the quantum dynamics of a 2LS also evolves naturally in this geometry, as it can accommodate mixed states *inside* the Bloch sphere (pure states lie on its surface). Mixed states are expressed by a density matrix, which is also determined by two numbers: the population and the coherence of the qubit:

$$\rho = \begin{pmatrix} 1 - n_\sigma & \langle\sigma\rangle^* \\ \langle\sigma\rangle & n_\sigma \end{pmatrix}, \tag{6.2}$$

where $n_\sigma \equiv \langle\sigma^\dagger\sigma\rangle$, the 2LS population, is such that $0 \leq n_\sigma \leq 1$, and $\langle\sigma\rangle$, the coherence of the qubit, is a complex number. Since the eigenvalues of the density matrix must be non–negative, the coherence of the qubit has an upper bound: $|\langle\sigma\rangle|^2 \leq n_\sigma(1 - n_\sigma)$. The state in Eq. (6.2) is pure if $\mathrm{Tr}(\rho^2) = 1$, i.e., if $|\langle\sigma\rangle|^2 = n_\sigma(1 - n_\sigma)$, in which case the states in Eq. (6.1) and Eq. (6.2) are equivalent, with $n_\sigma = |\beta|^2$ and $\langle\sigma\rangle = \alpha\beta^*$. Thus, any state in the form of Eq. (6.2) is represented in the Bloch sphere as a point with cartesian coordinates:

$$x = 2\mathcal{R}\langle\sigma\rangle \quad y = -2\mathcal{I}\langle\sigma\rangle \quad \text{and} \quad z = 1 - 2n_\sigma\,, \tag{6.3}$$

such that $x^2 + y^2 + z^2 \leq 1$. The amount of vacuum and excitation, often referred to as *population imbalance*, varies along the z-axis. The relative phase between the vacuum and the excited state is given by $\phi = \arg\langle\sigma\rangle$ and varies around the x–y plane.

6.3.1 *Incoherent driving*

To contrast the excitation of a 2LS by quantum light with the usual counterpart of classical excitation, we must first remind (and in some cases possibly derive for the first time) the situation in the latter case. We will see throughout that the need to understand the quantum excitation also teaches us on features of the more familiar classical case.

The expected value of the coherence, $\langle\sigma\rangle$, of an incoherently driven 2LS is zero, so its steady–state density matrix is fully determined by its population:

$$n_\sigma^{\mathrm{inc}} = \frac{P_\sigma}{P_\sigma + \gamma_\sigma}\,, \tag{6.4}$$

where P_σ is the rate of incoherent driving. The accessible states under incoherent excitation cover the entire z–axis, as shown in the Bloch sphere at the left of Fig. 6.1(b). Using this 2LS as a source for another 2LS reduces the span of accessible area. Namely, the steady–state of the target 2LS, also completely determined only by its population, reads:

$$n_\xi^{\mathrm{inc}} = \frac{4n_\sigma^{\mathrm{inc}}\gamma_\sigma(P_\sigma + \gamma_\sigma + \gamma_\xi)}{P_\sigma^2 + (\gamma_\sigma + \gamma_\xi)^2 + 4\Delta_{\sigma\xi}^2 + 2P_\sigma(\gamma_\xi + 5\gamma_\sigma)}\,, \tag{6.5}$$

where γ_ξ is the decay rate of the target 2LS, and $\Delta_{\sigma\xi} = \omega_\sigma - \omega_\xi$ is the detuning between the source and the target. The accessible states are shown in the Bloch sphere at the right Fig. 6.1(b),

and unlike the source 2LS that can be saturated to its excited state by incoherent pumping, the population of the target 2LS lies between $0 \leq n_\xi^{\text{inc}} \leq 0.3535$. The upper bound $0.3535 \approx 7/20$ is obtained in the regime $P_\sigma \approx \gamma_\sigma$ for the source, in which case $n_\sigma^{\text{inc}} = 1/2$, and when $\gamma_\xi \approx \gamma_\sigma$. The reason for this saturation is a type of self-quenching, here induced by the power broadening of the source. This shows clearly the intrinsic limitations of exciting with a 2LS. One can increase the emission rate, but this comes at the expense of other fundamental parameters such as the spectral broadening. In contrast, one can increase the emission rate of a cavity independently of its spectral width.

6.3.2 *Coherent driving*

In the case of coherent classical driving of the source, its population and coherence are given by:

$$n_\sigma^{\text{coh}} = \frac{4\epsilon_1\Omega_\sigma^2}{\gamma_\sigma^2 + 4\widetilde{\omega}_\sigma^2 + 8\epsilon_1\Omega_\sigma^2} \qquad \text{and} \qquad \langle\sigma\rangle^{\text{coh}} = \frac{2\sqrt{\epsilon_1}\Omega_\sigma(2\widetilde{\omega}_\sigma + i\gamma_\sigma)}{\gamma_\sigma^2 + 4\widetilde{\omega}_\sigma^2 + 8\epsilon_1\Omega_\sigma^2}\,, \tag{6.6}$$

where Ω_σ is the rate of coherent excitation, ϵ_1 is the amplitude of the channel through which we drive coherently the source, and $\widetilde{\omega}_\sigma = (\omega_\sigma - \omega_{\text{L}})$ is the detuning between the driving laser and the 2LS. Unlike the incoherent excitation, these states now span a volume in the Bloch sphere, which means that they have some degree of purity, the higher the closer to the ground state. Also, since coherent driving forbids population inversion, this volume is restricted to the southern hemisphere of the Bloch sphere, reaching population $n_\sigma = 1/2$ at most in a maximally-mixed state. Finally, the phase of the driving laser also fixes the phase of the excitation of the 2LS, so only one half of the southern hemisphere is accessible. The final accessible volume is shown in the left Bloch sphere in Fig. 6.1(c). Its boundaries are given by the shell of an ellipsoid with equation:

$$1 = \left(\frac{x}{\sqrt{2}/2}\right)^2 + \left(\frac{y}{\sqrt{2}/2}\right)^2 + \left(\frac{z - z_0}{1/2}\right)^2\,, \tag{6.7}$$

with $z_0 = -1/2$, $|x| \leq \sqrt{2}/2$ and $-\sqrt{2}/2 \leq y \leq 0$.

The expressions for the population and coherence of the target 2LS are not as straightforward as for the source 2LS, and although they can be found in closed form, they are too lengthy to be written here. As an illustration of their complexity, we provide the particular case when the driving laser, the source 2LS, and the target 2LS are in resonance, in which case the population and the coherence of the target 2LS reduce to:

$$\begin{aligned} n_\xi^{\text{coh}} &= 16\epsilon_1\Omega_\sigma^2(1-\epsilon_1)\gamma_{\widetilde{10}} \times \\ &\quad \left[\gamma_{\widetilde{11}}^3\gamma_{\widetilde{21}}\gamma_{\widetilde{12}} + 8\epsilon_1\Omega_\sigma^2(2\gamma_{\widetilde{10}}^3 + 6\gamma_{\widetilde{10}}^2\gamma_{\widetilde{01}} + \gamma_{\widetilde{10}}\gamma_{\widetilde{01}}^2(1-\epsilon_1) + 3\gamma_{\widetilde{01}}^3) + 64\gamma_{\widetilde{01}}\epsilon_1^2\Omega_\sigma^4\right]/N^*\,, \qquad (6.8a) \\ \langle\xi\rangle^{\text{coh}} &= -4i\sqrt{\gamma_{\widetilde{10}}\gamma_{\widetilde{01}}\epsilon_1(1-\epsilon_1)}\Omega_\sigma\gamma_{\widetilde{10}}\left\{\gamma_{\widetilde{11}}^3\gamma_{\widetilde{12}}\gamma_{\widetilde{21}} + 8\gamma_{\widetilde{11}}^2\epsilon_1\Omega_\sigma^2\left[4\gamma_{\widetilde{01}} + \gamma_{\widetilde{10}}(8\epsilon_1 - 3)\right] + \right. \\ &\quad \left. + 128\epsilon_1^2\Omega_\sigma^4\left[\gamma_{\widetilde{01}} + \gamma_{\widetilde{10}}(2\epsilon_1 - 1)\right]\right\}/N^*\,, \qquad (6.8b) \end{aligned}$$

with the normalization constant defined as

$$\begin{aligned} N^* &= \gamma_{\widetilde{01}}\gamma_{\widetilde{10}}^2\gamma_{\widetilde{11}}^3\gamma_{\widetilde{21}}\gamma_{\widetilde{12}} + 8\gamma_{\widetilde{11}}^2\epsilon_1\Omega_\sigma^2\left[2\gamma_{\widetilde{01}}^4 + 7\gamma_{\widetilde{01}}^3\gamma_{\widetilde{10}} + 12\gamma_{\widetilde{01}}^2\gamma_{\widetilde{10}}^2 + 2\gamma_{\widetilde{01}}\gamma_{\widetilde{10}}^3(13 - 10\epsilon_1) + 8\gamma_{\widetilde{10}}^4(1-\epsilon_1)\right] + \\ &\quad + 64\epsilon_1^2\Omega_\sigma^4\left[5\gamma_{\widetilde{01}}^4 + 2\gamma_{\widetilde{01}}\gamma_{\widetilde{10}}^3(23 - 20\epsilon_1) + 3\gamma_{\widetilde{01}}^2\gamma_{\widetilde{10}}^2(21 - 16\epsilon_1) + 2\gamma_{\widetilde{01}}^3\gamma_{\widetilde{10}}(17 - 10\epsilon_1) + 8\gamma_{\widetilde{10}}^4\right] + \\ &\quad + 1024\epsilon_1^3\Omega_\sigma^6\left[\gamma_{\widetilde{01}}^2 + \gamma_{\widetilde{01}}\gamma_{\widetilde{10}}(3 - 2\epsilon_1)\right]\,, \end{aligned}$$

and where we have used the notation introduced in the previous Chapter after Eq. (5.12)have introduced the notation, $\gamma_{\widetilde{mn}}^k \equiv (m\gamma_\sigma + n\gamma_\xi)^k$. Interestingly, while Eqs. (6.8) for the target have a much more complicated form than Eqs. (6.6) for the source, they lead to the same accessible

volume of the type of Eq. (6.7). At such, unlike the case of incoherent excitation, the target suffers no restriction of its accessible region under quantum excitation by a coherent excited 2LS as compared to direct excitation from the coherent source. In fact, since the phase of excitation is not fixed by the source, the accessible volume of the target 2LS is given by the full ellipsoid in Eq. (6.7) with $|y| \leq \sqrt{2}/2$, as shown in the rightmost Bloch sphere of Fig. 6.1(c).

6.3.3 *Mixture of coherent and incoherent driving*

The source 2LS can drive its target from the entire z–axis when driven incoherently to half an ellipsoid in the southern hemisphere when driven coherently. Mixing the two types of excitations allows the source 2LS to access a volume in the northern hemisphere as well, symmetric to the volume accessible by coherent excitation only, as shown in Fig. 6.1(d). The expressions for the population and the coherence in this case are:

$$n_\sigma^{\text{mix}} = \frac{P_\sigma[(P_\sigma+\gamma_\sigma)^2+4\widetilde{\omega}_\sigma^2]+4\epsilon_1\Omega_\sigma^2(P_\sigma+\gamma_\sigma)}{(P_\sigma+\gamma_\sigma)[(P_\sigma+\gamma_\sigma)^2+4\widetilde{\omega}_\sigma^2+8\epsilon_1\Omega_\sigma^2]}, \tag{6.9a}$$

$$\langle\sigma\rangle^{\text{mix}} = \frac{2\sqrt{\epsilon_1}\Omega_\sigma(P_\sigma-\gamma_\sigma)[2\widetilde{\omega}_\sigma+i(P_\sigma+\gamma_\sigma)]}{(P_\sigma+\gamma_\sigma)[(P_\sigma+\gamma_\sigma)^2+4\widetilde{\omega}_\sigma^2+8\epsilon_1\Omega_\sigma^2]}, \tag{6.9b}$$

from which we see that the condition to access the volume in the northern hemisphere, i.e., $n_\sigma \geq 1/2$, is simply that $P_\sigma > \gamma_\sigma$. The northern-hemisphere volume is enclosed by the ellipsoid in Eq. (6.7) with $z_0 = 1/2$, $|x| \leq \sqrt{2}/2$ and $0 \leq y \leq \sqrt{2}/2$.

However, exciting the 2LS with this mixture of drivings (to allow its steady state to reach points in the northern hemisphere away from the axis) does not make it a quantum source able to drive the target 2LS beyond the southern-hemisphere ellipsoid of coherent excitation, shown in Fig. 6.1(c). The expressions for the population and coherence of the target 2LS in this case are analytical as well, but even at resonance and using the compact notation of Eq. (6.8), they are too bulky to be written here. Note that by changing the direction from which the laser drives the source 2LS, or by using waveplates, one can rotate its phase, changing σ for $e^{i\theta}\sigma$ in the master equation (1.28). This variation leaves the population of the source 2LS unchanged, but adds a phase to its coherence. In this way, the source 2LS can span all states in a volume obtained by revolving around the z–axis. The same holds for the case of mixed excitation, and therefore the total accessible volume of the source 2LS is given by two full ellipsoids as shown in Fig. 6.1(e).

Overall, these results show that a 2LS as a source of excitation is no more advantageous than classical sources as far as accessible volumes in the Bloch sphere and in the steady state are concerned. The target is "quantum-enough" not to benefit further from quantum excitation (at least when it comes from a SPS) as compared to classical excitation. We will see later in the Chapter that this is because we consider the target in isolation, and that including quantum correlations with the source indeed lead to departures and benefits from a quantum driving.

6.3.4 *Phenomenological quantum source*

So far we have modeled the quantum source by describing it fully and self-consistently, coupling its output to a target through the cascaded formalism. The excitation of the source itself was achieved phenomenologically from the Lindblad formalism. One could also in principle take a simpler route by describing directly the quantum source through ad-hoc Lindblad terms. This is an expedient way to see whether quantum excitation can bring us to regions beyond those of access from the classical case, that lie in an ellipsoid of, for most of the cases, mixed states (not on the surface of the sphere). In particular, a common feature of all the kinds of excitation we have considered is that the state with population 1/2 is completely mixed, i.e., it is located at the origin of the sphere.

We now show how to drive the target 2LS to reach states with population 1/2 but with nonzero coherence. Specifically, we assume a source that emits photons in the state $|+\rangle_\phi = (|0\rangle + e^{i\phi}|1\rangle)/\sqrt{2}$. At the simplest level, the incoherent type of such an excitation is described with Lindblad terms in the master equation (1.28) of the type $(P^*/2)\mathcal{L}_x\rho$, where $x = |+\rangle_\phi\langle 0|$ is the operator that brings the vacuum state into $|+\rangle_\phi$ and P^* is the rate at which this excitation is enforced onto the target. The resulting population and coherence of the source 2LS in this case are given by:

$$n_\sigma^+ = \frac{P^*(P^* + 2\gamma_\sigma e^{i\phi})}{P^{*2} + 4\gamma_\sigma^2 + 4P^*\gamma_\sigma\cos 2\phi} \qquad \text{and} \qquad \langle\sigma\rangle^+ = \frac{2P^*\gamma_\sigma}{(P^* + \gamma_\sigma)(P^* e^{2i\phi} + 2\gamma_\sigma)}, \tag{6.10}$$

where the phase ϕ must be chosen so that $n_\sigma^+ \in \mathbb{R}$. The accessible volume with $\phi = 0$ is shown in Fig. 6.1(f). This case demonstrates a type of quantum excitation that drives the 2LS target into a volume of the Bloch sphere that strongly differs from the classical counterpart. The cw-excitation spoils the coherence, and even a source that explicitly drives the 2LS into the $|+\rangle$ state cannot sustain completely its coherence of the 2LS. Nevertheless, this indicates that the general case of quantum excitation does ultimately bring us further than the classical case, even though the SPS does not. Importantly, to clarify this point at this stage, we have assumed a simple phenomenological model for a particular case. It is not clear how such a source could be devised from an Hamiltonian in the first place before it is plugged to its target through the cascaded formalism. For instance, a close counterpart that emits photons in the state $|+\rangle_\phi = (|0\rangle + e^{i\phi}|1\rangle)/\sqrt{2}$ with a complex superposition ($\phi \notin \{0, \pi\}$), that is easily conceived conceptually, cannot be described in the above Lindblad form since this results in non-real coefficients of the master equation that yield unphysical density matrix (and, e.g., complex populations).

6.4 MOLLOW DRESSING

6.4.1 *Introduction*

In this Section, we go beyond which average quantum state a target 2LS can be driven into to consider instead some deeper structural aspect, namely, we describe the energy spectrum and its associated set of states. The naked 2LS has the simplest possible structure of a vacuum $|\mathrm{g}\rangle$ and an excited state $|\mathrm{e}\rangle$. When placed inside a cavity, in absence of dissipation, a new set of quantum states for the combined system takes over, which Jaynes and Cummings (1963) have shown are eigenvectors for the coupling Hamiltonian: $(|\mathrm{g}n\rangle + |\mathrm{e}, n-1\rangle)/\sqrt{2}$ at resonance with n the number of photons in the cavity. The respective pair of energies constitutes one stair of the Jaynes–Cummings ladder, that repeats this structure for each integer n. These states are entangled and go by the name of "polaritons" or "dressed states". In presence of dissipation, a notion of weak-coupling and strong-coupling emerges to distinguish cases where bare states $|\mathrm{g}, \mathrm{e}\rangle$ and $|n\rangle$ dominate the dynamics as dissipation destroyed their quantum superpositions. In the former case the coupling is classical while in the latter it binds the states through quantum nonlocality. This is a central concept of cavity QED but one that remains vaguely defined as rooted in the simple Hamiltonian framework. When including dissipation, the dressed-states energies become complex as a result of their finite lifetime, and acquire a broadening specific to their constitution in terms of bare states in addition to a renormalized energy. This has been explained for two coupled harmonic oscillators, but del Valle, Laussy, and Tejedor (2009) have shown that already the textbook case of the 2LS in a cavity displays a much less familiar structure, the so-called "dissipative Jaynes–Cummings ladder", with coexistence of weak and strong-coupling depending on the manifold of excitation. Such a description can be applied to other systems, as illustrated by Quesada (2012) with the dissipative Tavis–Cummings ladder. Besides, del Valle and Laussy (2011) demonstrated that when including, beyond mere decay, also an excitation scheme, the situation can become extremely complex. The simplest problem

Source	Target	Treated in
Classical laser	Mollow triplet	Section 6.4.3
2LS excited incoherently	Unresolved Mollow triplet	Section 6.4.4
2LS excited coherently	Mollow triplet with attenuated sidebands	Section 6.4.5
Cavity excited incoherently	Deformed singlet	Section 6.4.6
Cavity excited coherently	Mollow triplet	Section 6.4.7
One-atom laser	Quintuplet to Mollow triplet transition	Section 6.4.8
N-photon source	Quantum Mollow triplet	Chapter 8

Table 6.1: Classification of the shape of the emission of the target 2LS according to the source driving it.

of this type—the celebrated Mollow (1969) triplet— is the context for which Cohen-Tannoudji and Reynaud (1977) first spoke about the "dressed states". In this Chapter, where we study quantum driving of a 2LS, we are naturally brought to consider how the quantum features of light affect the 2LS target's state. In the limit where light is coherent, we expect to recover the conventional Mollow scenario, as is already known to be the case from the Jaynes–Cummings perspective where light is quantized, in agreement with the results from del Valle and Laussy (2010).

We will now turn to the more general problem of how a 2LS target becomes affected by quantum excitation without feedback, i.e., beyond the Hamiltonian formalism (the cases that will be dealt with are summarized in Table 6.1). This poses some immediate questions such as: Can a single-photon source dress a 2LS? Are Rabi oscillations—exchanges of excitation between the modes—necessary for state-dressing? If so, how can this be achieved in the cascaded formalism where feedback is precisely forbidden? Does the Mollow theory of a c-number description of the exciting laser break down in some regime, say of low excitation? These and other fundamental questions are answered in the remaining of this Chapter.

6.4.2 *Complex energy spectrum*

We define strong-coupling as the emergence of resonances in the system with real energies different from those of the bare states. Laussy, del Valle, and Tejedor (2009) showed that such resonances are obtained in a dissipative system from the eigenvalues D_p of the Liouvillian matrix M, which follows from writing Eq. (1.28) as:

$$\partial_t \{\rho\} = -M \{\rho\} \tag{6.11}$$

where $\{\rho\}$ is the density matrix laid out in vectorial form, namely,

$$\{\rho\} = (\rho_{11}, \rho_{21}, \cdots, \rho_{n1}, \rho_{21} \cdots \rho_{nn})^T , \tag{6.12}$$

for some truncation n that can be taken to go to ∞. This gives access to the "transitions" in the system, rather than directly to the energies of the states. Weisskopf and Wigner (1930) already identified this nuance in the first considerations of light-matter interactions. From the knowledge of the transitions, however, one can usually reconstruct the underlying energy structure of the system, that is, both the composition of the dressed states and their associated energies. A typical observable is the total emission emission spectrum that results from the combined emission between the various states:

$$S(\omega) = \frac{1}{\pi} \sum_p \frac{L_p(\gamma_p/2) - K_p(\omega_p - \omega)}{(\gamma_p/2)^2 + (\omega_p - \omega)^2} , \tag{6.13}$$

where $D_p \equiv \gamma_p/2 + i\omega_p$ is the pth resonance, i.e., eigenvalue of M, that defines the energy structure of the system, and L_p and K_p are the corresponding weights for this transition that

determine its prominence in the total emission accordingly with the state and dynamics of the system. The term L_p weights a pure Lorentzian emission, corresponding to spontaneous emission from the initial state towards the final one, while K_p brings a dispersive correction that is typical of coupled oscillators and that results in our case from interferences between transitions that overlap in energy. In finite-size Hamiltonian systems or those that can be decomposed into a direct sum of uncoupled manifolds, such as the Jaynes–Cummings Hamiltonian, the most important structure comes from D_p alone. In infinite-size systems where the system cannot be closed in a self-consistent way, for instance because an excitation term connects all the manifolds, one then needs to weight the transition D_p with $|L_p + iK_p|$ as otherwise different truncation schemes of M give different results for the complex energy spectrum, whereas the weighted transitions converge to a physical result. For this reason, the complex weight is fundamental as well. It is obtained, following Laussy, del Valle, and Tejedor (2009), as

$$L_p + iK_p = \frac{1}{n_\sigma}\mathrm{Tr}\left\{\sigma\Big(\!\Big(E_{ip}\sum_n E^{-1}_{pn}\{\rho_{ss}\sigma^\dagger\}_n\Big)\!\Big)\right\}, \tag{6.14}$$

where ρ_{ss} is the steady-state solution of the master equation, σ is the annihilation operator of the 2LS, $n_\sigma = \mathrm{Tr}(\sigma^\dagger\sigma\rho_{ss})$ is its population and E is the matrix of eigenvectors of M (i.e., $E^{-1}ME$ is the diagonal matrix of complex energies). Here $\{\mathcal{M}\}_n$ refers to the nth element of the flattened matrix $\mathcal{M}$ and $(\!(\mathcal{V})\!)$ refers to the reversed process that shapes the vector $\mathcal{V}$ (of size n^2) into a matrix as $((\mathcal{V}_1, \mathcal{V}_2, \cdots, \mathcal{V}_n), (\mathcal{V}_{n+1}, \mathcal{V}_{n+2}, \cdots \mathcal{V}_{2n}), \cdots)$.

In the following Sections, we start a comprehensive analysis of the complex energy spectrum, and the structure of states (bare and dressed) associated to it, for the configurations of excitation of a 2LS listed in Table 6.1. Namely, in Section 6.4.3 we start with the conventional Mollow triplet, where a classical field drives a 2LS, then in Section 6.4.4 we replace the classical field by the simplest quantum light, i.e., that emitted by a SPS; in Section 6.4.5, the SPS is brought itself in the Mollow triplet regime. Then we come back to the conventional Mollow configuration of light exciting a 2LS, but with light described by an operator rather than by a c-number. This will allow us to i) see what is lost in the approximation of describing the laser as a sine-wave and ii) consider classical excitation beyond merely a coherent state. Specifically, we consider in Section 6.4.6 a thermal state of the light-field (chaotic light), in Section 6.4.7 a coherent state (the closest to the conventional Mollow case), and, finally, in Section 6.4.8, we take an additional step in describing the quantum dynamics of an actual laser acting as the source to drive the 2LS, taking the simplest case of a one-atom laser to do so. All these cases bring some variations to the problem. Their common features give a picture of what constitutes the substance of the Mollow triplet.

6.4.3 *Excitation by a classical field*

The simplest classical excitation of a 2LS is that provided by a thermal source, or incoherent pumping, that brings the system into its excited state at a rate P_σ. For completeness, we address this case as well before we turn to coherent excitation that leads to Mollow physics. The 2LS incoherently pumped is described by the master equation:

$$\partial_t\rho = i[\rho, \omega_\sigma\sigma^\dagger\sigma] + \frac{\gamma_\sigma}{2}\mathcal{L}_\sigma\rho + \frac{P_\sigma}{2}\mathcal{L}_{\sigma^\dagger}\rho\,, \tag{6.15}$$

where ω_σ is the free energy of the 2LS and γ_σ its decay rate, with M-matrix (defined as in Eq. (6.11)):

$$M = \begin{pmatrix} P_\sigma & 0 & 0 & -\gamma_\sigma \\ 0 & \Gamma_\sigma/2 + i\omega_\sigma & 0 & 0 \\ 0 & 0 & \Gamma_\sigma/2 + i\omega_\sigma & 0 \\ -P_\sigma & 0 & 0 & \gamma_\sigma \end{pmatrix}, \tag{6.16}$$

where $\Gamma_\sigma \equiv \gamma_\sigma + P_\sigma$. The result is in this case trivial, as the only eigenvalue with nonzero weight is $D_1 = \Gamma_\sigma/2 + i\omega_\sigma$ with weight $L_1 + iK_1 = 1$, i.e., purely Lorentzian. Note how including the complex weight in the computation of the complex energy spectrum allows us to retain the one relevant resonance while the matrix M otherwise features four. As a conclusion, as expected, a 2LS excited incoherently is simply excited and release this excitation with the same energy by spontaneous emission, with a photoluminiscence spectrum given by:

$$S(\omega) = \frac{1}{\pi} \frac{\Gamma_\sigma/2}{(\Gamma_\sigma/2)^2 + (\omega_\sigma - \omega)^2} \,. \tag{6.17}$$

There are no dynamical effects, shifts, dressing, renormalization of any sort. We now see how this changes considerably when upgrading the incoherent excitation to a coherent one.

The excitation of the 2LS by a coherent classical field, i.e., a c-number $\Omega_\sigma \exp(i\omega_\mathrm{L} t)$ with Ω_σ^2 the intensity of the driving laser, brings us to the Mollow master equation shown in Eq. (1.44). In this case, and considering the laser resonant to the 2LS, the Liouvillian matrix becomes

$$M = \begin{pmatrix} 0 & -i\Omega_\sigma & i\Omega_\sigma & -\gamma_\sigma \\ -i\Omega_\sigma & \gamma_\sigma/2 & 0 & i\Omega_\sigma \\ i\Omega_\sigma & 0 & \gamma_\sigma/2 & -i\Omega_\sigma \\ 0 & i\Omega_\sigma & -i\Omega_\sigma & \gamma_\sigma \end{pmatrix}, \tag{6.18}$$

which has a more complex set of eigenvalues:

$$D_1 = 0 \,, \tag{6.19a}$$
$$D_2 = \gamma_\sigma/2 \,, \tag{6.19b}$$
$$D_\pm = \frac{1}{4}\left(3\gamma_\sigma \pm \sqrt{\gamma_\sigma^2 - 64\Omega_\sigma^2}\right) . \tag{6.19c}$$

The imaginary part of these quantities, that correspond to the energies of the transitions (real parts correspond to their broadening), are shown as a function of the intensity of the driving laser in Fig. 6.2(a). Their corresponding weight is encoded in the colour: positive weights have blue shade while negative ones have a red shade.

This simple structure subtends a complex and rich phenomenology. At low intensity, $D_\pm \approx \gamma_\sigma(3 \pm 1)/4$ and the emission spectrum is as shown in Fig. 6.2(b), where D_2 is shown as the blue lorentzian and D_- is shown as the red negative lorentzian. The peak due to D_1 corresponds to the light scattered by the 2LS from the laser (not shown) and is known as the Rayleigh peak. This peak has zero linewidth, and is involved in the Heitler (1944) process that generates antibunched photons with the coherence of the driving laser.

In this case, and as long as $\Omega_\sigma \leq \gamma_\sigma/8$, the spectrum consists of a single line as the eigenvalues' imaginary parts (that correspond to the states energies) are all degenerate. The combination of Eqs. (6.13) and (6.19) yields the emission spectrum of the 2LS:

$$S_\sigma(\omega) = \frac{1}{2\pi}\frac{\gamma_\sigma/2}{(\gamma_\sigma/2)^2 + \omega^2} + \frac{1}{4\pi\beta}\frac{(3\gamma_\sigma - \beta)/4}{[(3\gamma_\sigma - \beta)/4]^2 + \omega^2}\frac{8(\beta + 5\gamma_\sigma)\Omega_\sigma^2 - \gamma_\sigma^2(\gamma_\sigma + \beta)}{8\Omega_\sigma^2 + \gamma_\sigma^2} + \\ + \frac{1}{4\pi\beta}\frac{(3\gamma_\sigma + \beta)/4}{[(3\gamma_\sigma + \beta)/4]^2 + \omega^2}\frac{8(\beta - 5\gamma_\sigma)\Omega_\sigma^2 + \gamma_\sigma^2(\gamma_\sigma - \beta)}{8\Omega_\sigma^2 + \gamma_\sigma^2} \,, \tag{6.20}$$

where $\beta = \sqrt{\gamma_\sigma^2 - 64\Omega_\sigma^2}$, and which in the limit of vanishing driving, $\Omega_\sigma \to 0$, becomes as in Eq. (1.47). This total emission spectrum is shown with the black dashed line in Fig. 6.2(b) along with its decomposition into the underlying transitions (here not split). The dressed states, in red and blues, are largely compensating each other. This is the process of coherent absorption and re-emission that endows this regime with peculiar properties. Beside, in this regime the

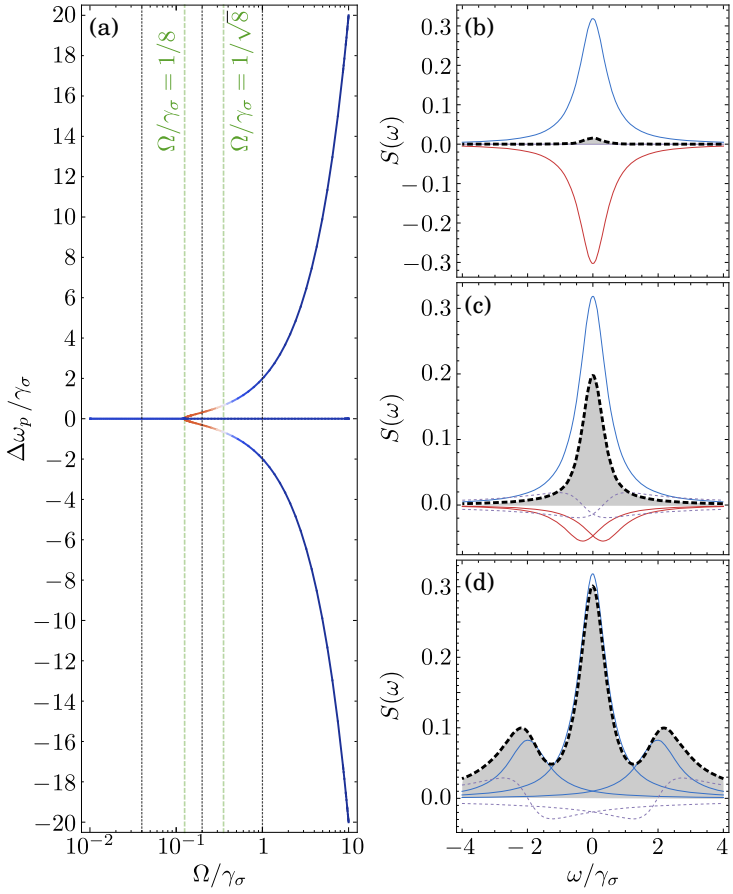

Figure 6.2: Excitation by a coherent source. (a) Energy spectrum of a coherently driven 2LS. The energies that contribute to the total emission spectrum with positive lorentzians are shown in blue, whereas those contributing as negative lorentzians are shown in red. (b-d) Emission spectra of the target 2LS (dashed, black lines) for the values $\Omega_\sigma/\gamma_\sigma$ marked by the vertical dashed lines in Panel (a). The total emission spectrum is made of the sum of positive (blue lines) and negative (red) lorentzians, and dispersive functions (dotted purple).

light emitted by the 2LS is essentially coming from the Rayleigh peak (not shown). As a result of this structure of emission from the 2LS, the light emitted is antibunched and originates mainly from the Rayleigh peak, that has the first-order coherence of the laser (it is a δ peak for a c-number driving field). This is a strong feature of resonance fluorescence that has been observed by several groups, including Nguyen et al. (2011), Matthiesen, Vamivakas, and Atatüre (2012), Proux et al. (2015), and Al-Khuzheyri et al. (2016). However, the discussion made in these works did not take into account the effect of the observation, as we have discussed in details in Chapter 3.

As far as strong-coupling is concerned, the situation of interest is that of energy splitting between the dressed states. This occurs when:

$$\Omega_\sigma > \gamma_\sigma/8\,, \tag{6.21}$$

and is shown in Figs. 6.2(a) and (c). Note that, strikingly, the split states have a negative weight, i.e., correspond to absorbing lines. While their position is consistent with the conventional dressed-state picture with energies $\omega_\pm = \pm\sqrt{64\Omega_\sigma^2 - \gamma_\sigma^2}/4$, the dynamics involved is opposite to that of new states radiating at their corresponding energy. Instead, they enter the scene by absorbing energy. They start to emit light instead of taking it away for the more stringent condition (cf. Eq. (6.21)):

$$\Omega_\sigma > \gamma_\sigma/\sqrt{8}\,, \tag{6.22}$$

Figure 6.2(d) shows the emission spectrum for $\Omega = \gamma_\sigma$ with, in this case, an active contribution from all the dressed states that result in the characteristic emission spectrum as a triplet that is clearly understood from the dressed state structure. In the limit of very large intensity, $D_\pm \approx 3\gamma_\sigma/4 \pm 2i\Omega_\sigma$, and the emission spectrum is the well-known Mollow (1969) triplet given in Eq. (1.49). The satellites contribute negatively to the total spectrum when they are close to the

center, with effect of trimming the fat tails of the central Lorentzian. As a result, the system emits with a sharper distribution of frequencies, typically a Student t distribution (that results from the difference of two Lorentzians, as shown in Fig. 6.2(b)). This allows to collect more easily all the emitted photon in a narrower window of detection and, therefore, to achieve better values of antibunching. On the opposite, when the Mollow triplet is largely split, it consists of essentially three non-overlapping Lorentzian lines (of linewidths $3\gamma_\sigma/4$ and γ_σ for the central and satellite peaks, respectively), its statistical properties recover those of an incoherently pumped 2LS. This understanding of the composition of the Mollow triplet, even before it is fully-formed, is important not only on fundamental grounds, but also since it can be used to engineer better single-photon sources, as we will see in Section 6.5.

6.4.4 *Excitation by a single-photon source*

In this and the following four Sections, we upgrade the source of excitation from a classical to a quantum field. The simplest quantum field is that provided by a single-photon source, which is modeled by an incoherently driven 2LS, as sketched in Fig. 6.1(a) with a thermal field (incoherent pumping) providing the classical excitation, and is described by Eq. (1.28) adding the lindblad term $(P_\sigma/2)\mathcal{L}_{\sigma^\dagger}\rho$. The resulting Liouvillian matrix M has dimension 16×16 but only four of the sixteen eigenvalues contribute to the steady-state emission spectrum. These eigenvalues are solutions to cubic equations that are too bulky to be written here. In Fig. 6.3(a-i), I show the weighted energy spectrum of the target 2LS as a function of the intensity of the incoherent driving. For clarity, I split the positive (1st column) and negative (2nd column) contributions that are shown together in the third column, with the same color code (blue,

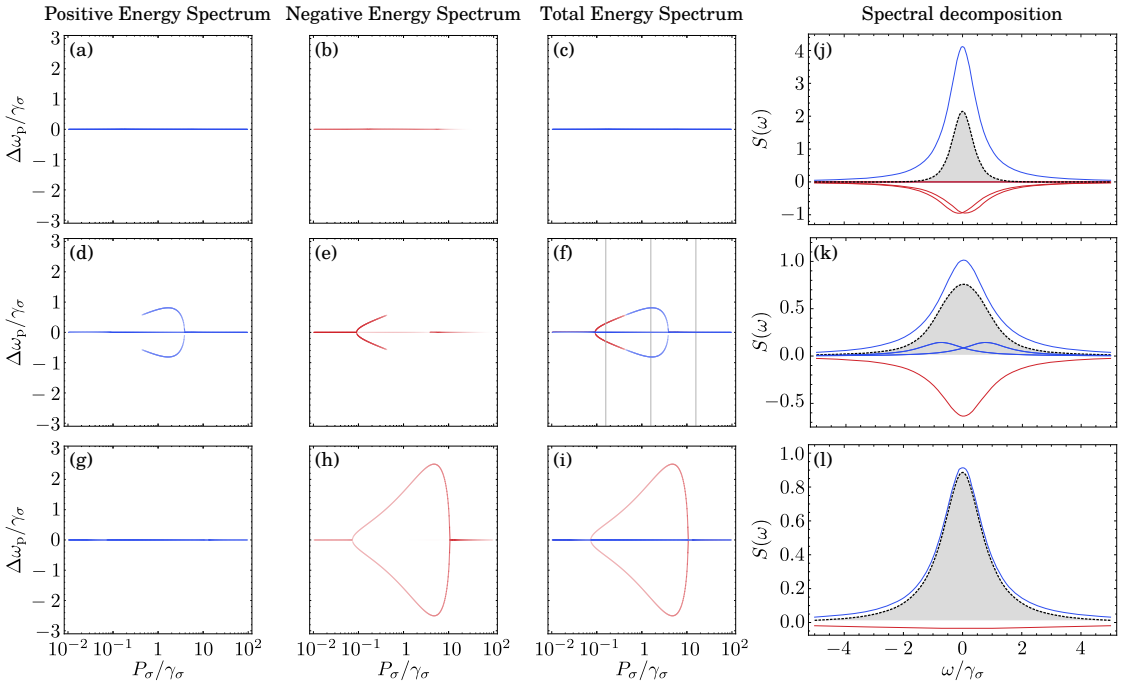

Figure 6.3: Excitation by a single–photon source. (a-i) Energy spectra of the target 2LS. The energies that contribute to the total emission spectrum with positive lorentzians are shown in blue, whereas those that contribute with negative lorentzians are shown in red. (j-l) Emission spectra of the target 2LS (dashed, black lines) for the values P_σ/γ_σ marked by the vertical dashed lines in Panel (f). The total emission spectrum is made of the sum of positive (blue lines) and negative (red lines) lorentzians. To compute the figures we set γ_σ as the unit, and set $\gamma_\xi/\gamma_\sigma = 0.1$ in Panels (a-c), $\gamma_\xi/\gamma_\sigma = 1$ in Panels (d-f), and $\gamma_\xi/\gamma_\sigma = 10$ in Panels (g-i).

overall positive; red, overall negative). The upper row, Figs. 6.3(a-c), shows the case where $\gamma_\xi/\gamma_\sigma = 0.1$ and the driving is too weak to dress the energies of the target 2LS: it behaves like its classical counterpart under incoherent pumping. Figure 6.3(d-f) shows the case where $\gamma_\xi/\gamma_\sigma = 1$, that results in a splitting of the energy levels, with a splitting that opens with absorbing lines before turning to emitting dressed states, as in the case of a 2LS driven by a coherent classical field. Unlike the latter, however, the splitting eventually quenches with increasing pumping rate. This can be explained by the fact that the target 2LS is not driven efficiently in the high excitation regime since the emission spectrum of the source 2LS broadens (cf. Eq. (6.17)), reducing the intensity at the frequency of the target 2LS. In Fig. 6.3(f), we select three values for P_σ/γ_σ for which the total emission spectrum (dashed black line) is decomposed into its dressed state emission (emitting in blue and absorbing in red), as shown in Fig. 6.3(j-l). The magnitude of the lorentzians at the splitted energies is not large enough to result in an observable splitting in the total emission spectrum of the target 2LS. Figure 6.3(g-i) shows the case where $\gamma_\xi/\gamma_\sigma = 10$, with a third scenario of an energy splitting that occurs *only* with absorbing dressed states, but with a magnitude of the splitting that is larger than in the previous case. This case also fails to produce an observable splitting in the total luminescence spectrum. Even though the power spectrum remains a single-peak throughout, one can still dress a 2LS with a SPS. The energy splitting of the target 2LS occurs when the following condition is satisfied:

$$\gamma_\xi/\gamma_\sigma \geq \left[\frac{P_\sigma^{*4} - 68P_\sigma^{*3} + 726P_\sigma^{*2} + 1 - 8\sqrt{-2P_\sigma^* \left(P_\sigma^{*2} - 16P_\sigma^* + 1\right)^3}}{P_\sigma^{*2} - 14P_\sigma^* + 1} \right]^{1/2} , \tag{6.23}$$

where I have introduced the unitless parameter $P_\sigma^* = P_\sigma/\gamma_\sigma$, and noting that the condition is valid only when the argument on the right-hand side (rhs) of the inequality is a real value. The lower bound for P_σ^* is the real-valued zero that cancels the rhs of Eq. (6.23), which is the solution of a polynomial of order 8 for which I give a numerical approximation. When the rhs of Eq. (6.23) is real, it ranges from zero to infinty, which translates to a condition on the population of the source $0.93 \gtrsim n_\sigma \gtrsim 0.88$. Equation (6.23) thus provides the criterion for strong-coupling of a 2LS with the light emitted in the CW regime by a SPS. While the criterion shows that this is possible with the source 2LS close to saturation, it also shows the conditions as required by the formula, are not particularly enlightening. Since the complex energy spectrum remains (relatively) simple, one can go in this case one stage deeper and reconstruct from the resonances the structure of the dressed states.

The archetype of the energy spectrum of a 2LS driven by a single-photon source, and the corresponding linewidths are shown in Fig. 6.4(a) and in Fig. 6.4(b), respectively. The black solid lines in the figures correspond to transitions between the bare modes, i.e., from $|1\rangle_\sigma |1\rangle_\xi = |1,1\rangle$ to either $|1,0\rangle$ or $|0,1\rangle$, and from either $|1,0\rangle$ or $|0,1\rangle$ to $|0,0\rangle$. The blue and red dashed lines correspond to transitions involving dressed states that we note as

$$\left|I_\pm\right\rangle = \alpha\,|0,1\rangle + \sqrt{1-\alpha^2}e^{\pm i\phi}\,|1,0\rangle\ , \tag{6.24}$$

where $0 \leq \alpha \leq 1$. However, the appearance of the dressed states do not imply the absence of the bare state. On the contrary they coexist giving rise to transitions from $|1,1\rangle$ to either $\left|I_+\right\rangle$ or $\left|I_-\right\rangle$, but only from $|0,1\rangle$ to $|0,0\rangle$: when the energy levels are splitted, the transition from $|1,0\rangle$ to $|0,0\rangle$ is suppressed as all the emission of the source 2LS is efficiently absorbed by the target 2LS, and instead takes place the coherent transfer from $|1,0\rangle$ to $|0,1\rangle$. Therefore, the schematic representation of the energy levels of a 2LS driven by a single-photon source is as shown in Fig. 6.4(c), where we show the coexistance of the bare and dressed states in the single-photon manifold.

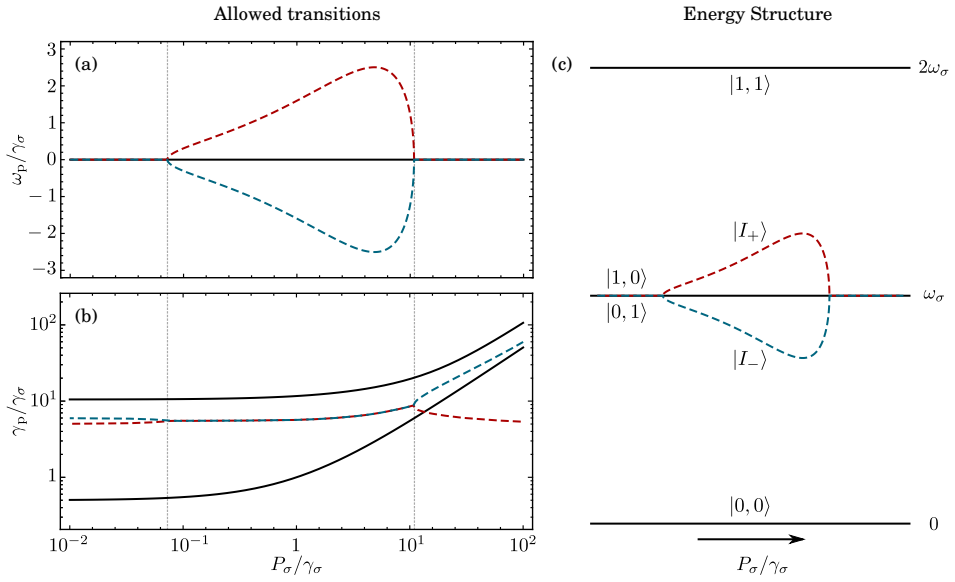

Figure 6.4: Energy structure of a 2LS driven by a single photon source. (a) Energy change in due to the allowed transitions in the 2LS. (b) Linewidth of the emission of the 2LS due to the allwed transitions. The transitions that involved the dressed states are shown by the dashed red and dashed blue lines. Panel (a) shows a splitting in the transition energies, while Panel (b) shows that those transitions have the same linewidth. (c) The energy structure of the 2LS driven by a single photon source is obtained from the allowed transitions in Panel (a).

6.4.5 *Excitation by a Mollow triplet*

In this Section, we keep the same source 2LS but we excite it coherently. This systematic study of all the possibilities of exciting a 2LS by quantum light thus brings us to this curious configuration of exciting a 2LS by the Mollow triplet. The system is described by Eq. (1.30), using two input channels for the source with $\epsilon_1 = \epsilon_2 = 1/2$, setting $H_\sigma = -i\sqrt{\epsilon_1\gamma_\sigma}\mathcal{E}(\sigma^\dagger - \sigma)$, and for simplicity we note $\Omega_\sigma \equiv \sqrt{\epsilon_1\gamma_\sigma}\mathcal{E}$ as the intensity of the coherent light that drives the source 2LS. As in the previous section, the Hilbert space has dimension 16×16, but in this case all the eigenvalues are involved in the energy spectrum of the target 2LS, as shown in Fig. 6.5 for several values of the ratio γ_ξ/γ_σ. The most obvious observation is the considerably higher complexity of the structure of the driven system. In this case, we will focus only on the resonances without making any attempt at reconstructing the underlying dressed states, as we did for the simplest configuration of exciting with a SPS. Panels (a-c) show the case for $\gamma_\xi/\gamma_\sigma = 0.1$. The splitting also starts with absorbing states and occurs for a driving intensity $\Omega_\sigma/\gamma_\sigma \approx 0.02$, that is is roughly one order of magnitude smaller than that required with a classical laser ($\Omega_\sigma/\gamma_\sigma = 1/8$). Other states do split at that usual threshold, suggesting that the target 2LS incorporates the energy structure of the source to its own. In fact, at large driving intensities, most of the energies converge to those of the source 2LS to provide a carbon copy of the conventional Mollow triplet, cf. Fig. 6.2. The most intense contributions to the total emission spectrum remain those provided by eigenvalues for which $|\Delta\omega_P/\gamma_\sigma| < 1$.

The total emission spectrum (dashed black lines) and its decomposition through dressed states emission (blue and red solid lines) are shown in Fig. 6.5(j-l) for the values of $\Omega_\sigma/\gamma_\sigma$ marked by the vertical dashed lines in panel (c). Panel (j) displays another case of emergence of the dressed states as absorbing lines, beside, in this case, also strongly interfering with important dispersive components (dotted lines). As a result, the total spectrum broadens as compared to the simple target-2LS emission (blue line). Panel (k) shows how the dressed states now fully formed contribute to the emission with enough energy splitting and weight

of the corresponding transition to produce a noticeable feature in the total emission spectrum (dotted black). However, negative contributions balance these peaks and the resulting emission spectrum only exhibits two "bumps" on its flanks. The target is resilient to developing a Mollow triplet, although its dressing is now unambiguous as observable directly in the luminescence. Panel (l) shows the quenching of the Mollow triplet at higher intensity of the source: the lateral peaks vanish and the remaining splitted energies lie close to the bare state, resulting in an emission spectrum with a single, heavily-tailed, line.

Panels (d-f) and (g-i) of Fig. 6.5 show the energy spectrum of the target 2LS for $\gamma_\xi/\gamma_\sigma = 1$ and $\gamma_\xi/\gamma_\sigma = 10$, respectively. Although most of the features of the energy spectrum of the target 2LS remain when we increase its decay rate, a notable feature is observed when $\gamma_\xi/\gamma_\sigma = 1$: there appears in this case dressed states that are split in energy at all driving intensities, as seen in Fig. 6.5(e) for $\Omega_\sigma/\gamma_\sigma < 10^{-1}$ through the asymptotic lines instead of the usual bifurcations. While the weights also vanish with decreasing driving intensity, they are never exactly zero and the structure of the dressed states is peculiar as they manifest including at vanishing driving field intensity. This is another manifestation of a behaviour first observed by Laussy, del Valle, and Finley (2012), in which equal decay rates in coupled quantum-optical systems lead to optimum strong-coupling conditions. In this case, such a behaviour opens a channel of excitation where the target 2LS can benefit from the strong-coupling of the source 2LS (that is in strong-coupling from the strong classical driving field) regardless of its driving intensity. The information of strong-coupling is therefore "encoded" in the photons emitted by the source and "restored" in the target. If the target and sources are different objects (due to mismatched decay rates), this information is lost.

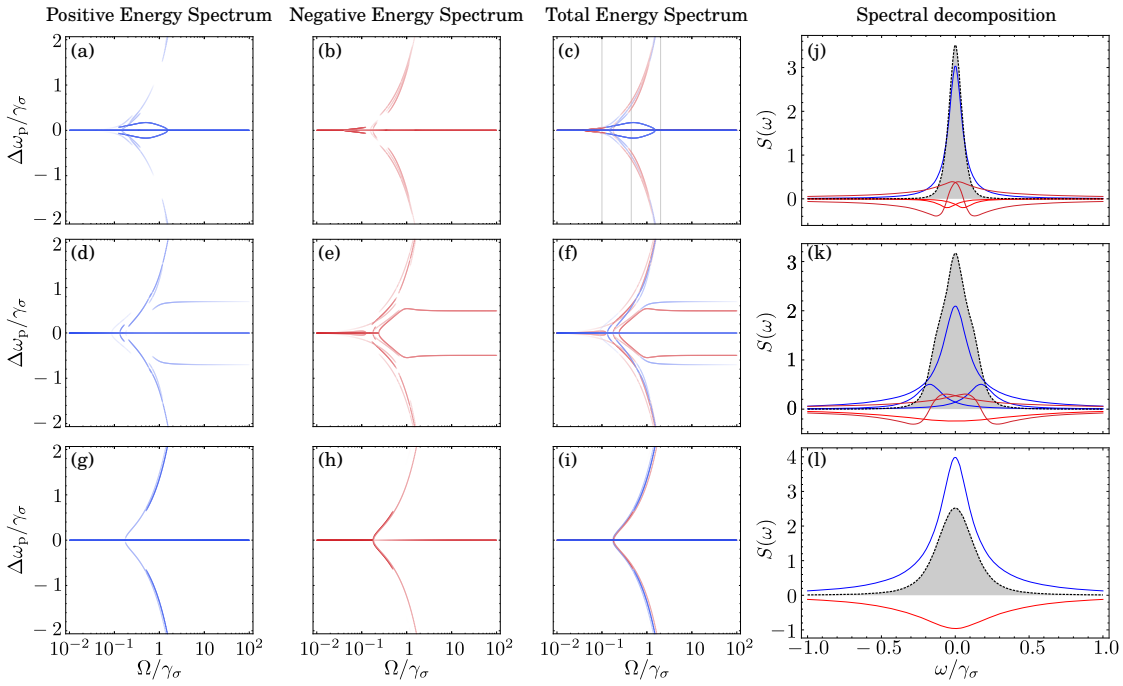

Figure 6.5: Excitation by a Mollow triplet. (a-i) Energy spectra of the target 2LS. The energies that contribute to the total emission spectrum with positive lorentzians are shown in blue, whereas those that contribute with negative lorentzians are shown in red. (j-l) Emission spectra of the target 2LS (dashed, black lines) for the values $\Omega_\sigma/\gamma_\sigma$ marked by the vertical dashed lines in Panel (c). The total emission spectrum is made of the sum of positive (blue lines) and negative (red lines) lorentzians. To compute the figures we set γ_σ as the unit, and set $\gamma_\xi/\gamma_\sigma = 0.1$ in Panels (a-c), $\gamma_\xi/\gamma_\sigma = 1$ in Panels (d-f), and $\gamma_\xi/\gamma_\sigma = 10$ in Panels (g-i).

6.4.6 *Excitation by an incoherently driven cavity*

In this and the following Section, we change the source of excitation for a driven cavity. Here, we discuss the case of an incoherently driven cavity. The system is described by Eq. (1.28) when replacing the parameters of the source (operators and associated variables), marked with the subindex σ, by those corresponding to a cavity, which we note with the subindex a (the operator a is a boson annihilation operator). The incoherent driving of the cavity is described by the lindblad term $(P_a/2)\mathcal{L}_{a^\dagger}\rho$ in the master equation. In contrast to the previous three Sections, the Hilbert space of the system is now infinite. To compute the energy spectrum, we need to truncate in the number of excitations. This is a difficult constrain for an incoherently driven cavity since its population $n_a = P_a/(\gamma_a - P_a)$ has thermal fluctuations. For this reason the energy spectra showed in Fig. 6.6 are computed up to $P_a/\gamma_a \approx 0.968$, with corresponding populations $n_a = 30$ for which we have checked convergence of the results. Panels (a-c) display the case with $\gamma_\xi/\gamma_a = 0.1$ and show that the energy spectrum is qualitatively similar to a 2LS driven by a classical laser (cf. Fig. 6.2(a)). The most notable features of this result are the following: first, weighting the transitions in a truncated Hilbert space is mandatory to reach convergence, as D_p alone do not yield a stable structure otherwise as not only the number of eigenvalues grows with the size of truncation, but their distribution also fails to settle to a consistent pattern. Second, the weighted complex energy spectrum, shown in Fig. 6.6, that is well-defined and for which we have checked convergence, reduces to a simple structure in the spectral shape but still exhibits some unexpected features, namely, up to three satellite energies visible on each flank of the central Lorentzian, as compared to the single line of the conventional Mollow triplet (cf. Fig. 6.2(a)). The system fluctuates so much that it cannot accommodate all the transitions with three energies only, but requires seven instead. Third, while the weighted structure is indeed similar to the classical excitation, the intensity of the satellite peaks is much smaller in comparison, so that the total emission spectrum is barely affected by them and is given essentially by a single lorentzian at the energy of the target 2LS, as shown in Fig. 6.6(g-h) for the values P_a/γ_a marked by the vertical dashed lines in Fig. 6.6(c). The excitation of a 2LS by

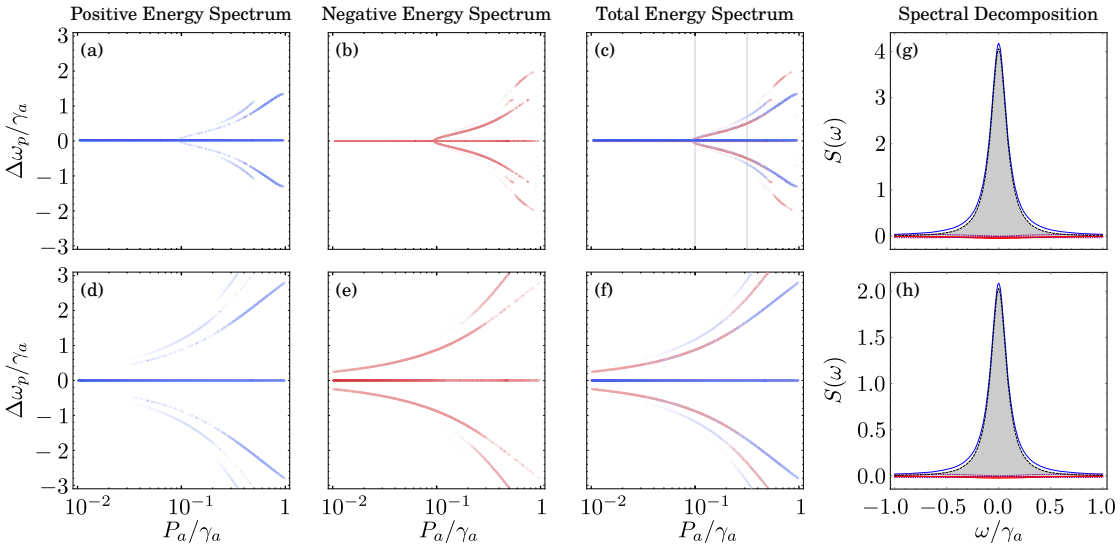

Figure 6.6: Excitation by an incoherently driven cavity. (a-f) Energy spectra of the target 2LS. The energies that contribute to the total emission spectrum with positive lorentzians are shown in blue, whereas those that contribute with negative lorentzians are shown in red. (g-h) Emission spectra of the target 2LS (dashed, black lines) for the values P_a/γ_σ marked by the vertical dashed lines in Panel (c). The total emission spectrum is made of the sum of positive (blue lines) and negative (red lines) lorentzians. To compute the figures we set γ_a as the unit, and set $\gamma_\xi/\gamma_a = 0.1$ in Panels (a-c), and $\gamma_\xi/\gamma_a = 1$ in Panels (d-f).

thermal light is therefore largely a case of fundamental interest that, for most purposes, can be approximated to an incoherently excited 2LS, despite this configuration yields a dressing of the target. Fourth, as in the previous case, setting the decay rate of the target 2LS equal to the decay rate of the cavity leads to energy-splitting at all values of pumping, while a mismatch leads to a bifurcation instead, as shown in Fig. 6.6(d-f). In summary for this configuration, there is little physics in the main observable, but much to be learned on the mechanisms of quantum excitation from a (quantized) thermal source.

6.4.7 *Excitation by a coherently driven cavity*

In this Section, we describe the energy splitting of a 2LS driven by the emission of a coherently driven cavity. The system is described by Eq. (1.30) with the changes of the previous Section, but now we use two input channels for the source with $\epsilon_1 = \epsilon_2 = 1/2$, we replace the incoherent pumping of the source by $H_a = -i\sqrt{\epsilon_1\gamma_a}\mathcal{E}(a^\dagger - a)$, and set the effective driving intensity of the source as $\Omega_a = \sqrt{\epsilon_1\gamma_a}\mathcal{E}$. This creates a coherent state $|2\Omega_a/\gamma_a\rangle$ that is dynamically coupled to the 2LS. The dimension of the Hilbert space is also infinite and must be truncated. In this case, however, Poissonian fluctuation of the cavity make the truncation manageable up to large populations.

The energy spectrum of the target 2LS are shown in Fig. 6.7(a-c) for $\gamma_\xi/\gamma_a = 0.1$, and in Fig. 6.7(d-f) for $\gamma_\xi/\gamma_a = 1$. The notable features here are direct counterparts of the incoherent excitation case: First, the weighted energy spectrum now fully reduces to the level of complexity of the conventional Mollow triplet, with exactly three resonances. Here it must be borne in mind that the underlying structure is that of a fully quantized 2LS-cavity system, with countably infinite complex eigenvalues (that fail to provide a converged structure if unweighted). In the Hamiltonian regime, del Valle and Laussy (2011) showed that the corresponding structure is extremely complicated and this is the cascaded feature (of no feedback from the target to its source) that brings such a simplification with an actual triplet structure down to the most

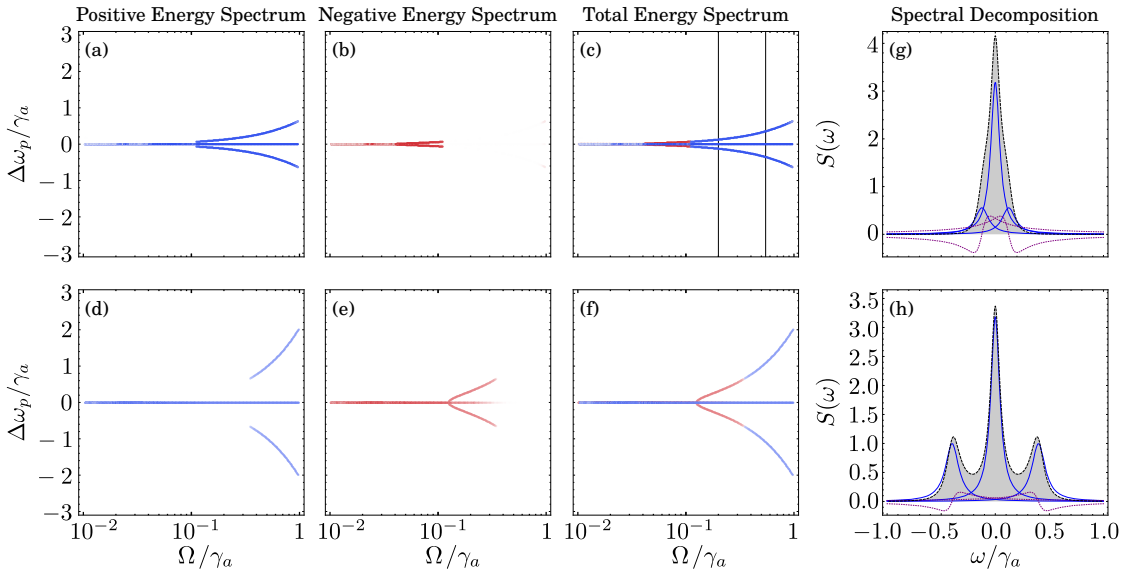

Figure 6.7: Excitation by a coherently driven cavity. (a-f) Energy spectra of the target 2LS. The energies that contribute to the total emission spectrum with positive lorentzians are shown in blue, whereas those that contribute with negative lorentzians are shown in red. (g-h) Emission spectra of the target 2LS (dashed, black lines) for the values Ω_a/γ_σ marked by the vertical dashed lines in Panel (c). The total emission spectrum is made of the sum of positive (blue lines) and negative (red lines) lorentzians. To compute the figures we set γ_a as the unit, and set $\gamma_\xi/\gamma_a = 0.1$ in Panels (a-c), and $\gamma_\xi/\gamma_a = 1$ in Panels (d-f).

fundamental level. This is not exactly the conventional Mollow case, however, since there is one additional parameter, the decay rate of the cavity γ_a, that cannot be zero as otherwise no photons are emitted by the source. This causes some differences between these two configurations: the c-field on the one-hand and the coherent-state cavity on the other. Figure 6.7 shows two cases for the later with different γ_ξ/γ_a. Interestingly, in this case, the configuration $\gamma_a = \gamma_\xi$ does not lead to an asymptotic loss of the splitting but to a bifurcation. This splitting from a single-line always occur before that of the conventional Mollow triplet. The energy spectra remain qualitatively very similar to that of the c-field driving (cf. Fig. 6.2). The agreement is recovered at large drivings where a mean-field approximation, that replaces the cavity operator a by $\sqrt{n_a}$ in Eq. (1.28), converges to the numerical solution. This approximation leads to the master equation of a 2LS driven by a laser with intensity $\Omega^* = \sqrt{(1-\epsilon_1)\gamma_\xi\gamma_a n_a} = \sqrt{\gamma_\xi\gamma_a n_a/2}$ so the agreement at large Ω_σ (where n_a is very large too) appears to be exact. The mean-field approximation does not hold however for small values of Ω_σ/γ_a and therefore fails to predict the splitting threshold. In this case, strong correlations between the 2LS and the few photons from the quantized driving field (albeit in a coherent state) exist that lead to differences from the c-field driving. We will come back to their importance in Section 6.5, where we turn to applied considerations of this physics.

6.4.8 *Excitation by a one-atom laser*

In this Section, we consider an actual laser as the source for the 2LS. Namely, we drive the 2LS with the coherent state generated by a device that creates this coherence from its internal dynamics, without inheriting it from another classical source (e.g., another laser, a classical field, etc.) This is the culminating point of our description of the Mollow physics in this Chapter, as there is nowhere a classical approximation that results in unphysical and/or pathological results, like the ones that González-Tudela et al. (2013) have shown can occur from the δ peak of the laser. There have been several efforts to go beyond the Mollow paradigm where the driving light is a perfect sine wave, for instance Zoller (1978a), Zoller (1978b), and Zoller and Ehlotzky (1978)'s earliest work (which was the topic of Zoller's Ph. D thesis), where the sought features of the driving field are enforced into the model. Here, in line with the cascaded formalism philosophy, we leave to the source to self-consistently develop and establish its lasing properties.

The simplest such laser is the one-atom laser, which was brought by Mu and Savage (1992) and has been observed by, e.g., McKeever et al. (2003), Nomura et al. (2010), and Gericke et al. (2017). This laser is based on the strong coupling between a 2LS and a cavity, in which the incoherent pumping of the 2LS is turned into a coherent state of the cavity. Its Hamiltonian is that of Jaynes and Cummings (1963):

$$H_s = \omega_\sigma \sigma^\dagger\sigma + \omega_a a^\dagger a + g(a^\dagger\sigma + \sigma^\dagger a)\,, \tag{6.25}$$

where, as before, σ is the fermionic operator describing the atom and a is the bosonic operator describing the cavity, with respective free energies ω_σ and ω_a. Now, however, they are coupled reversibly with strength g. The incoherent driving of the atom (P_σ), the decay processes and the cascaded coupling between the cavity and the target 2LS are included in the master equation:

$$\partial_t\rho = i[\rho, H_s + H_\xi] + \frac{P_\sigma}{2}\mathcal{L}_{\sigma^\dagger}\rho + \sqrt{\gamma_a\gamma_\xi}\left\{[a\rho, \xi^\dagger] + [\xi, \rho a^\dagger]\right\} + \sum_{k=\{\sigma,a,\xi\}}\frac{\gamma_k}{2}\mathcal{L}_k\rho\,. \tag{6.26}$$

Here, γ_σ, γ_a and γ_ξ are the decay rates of the atom inside the cavity, the cavity, and the target 2LS, respectively; and since there is no external coherent field driving the system we consider only one input channel for the source and for the target. In Fig. 6.8 we show the normalised emission spectra of a 2LS cascaded by a one atom laser (solid lines), and we compare it to the normalised emission spectra of a 2LS driven by a classical laser (dashed lines). In the bottom three lines of Fig. 6.8, the incoherent driving of the atom is so small that the one atom laser is not in the lasing regime. Therefore, the comparison of the spectra is made so that the population

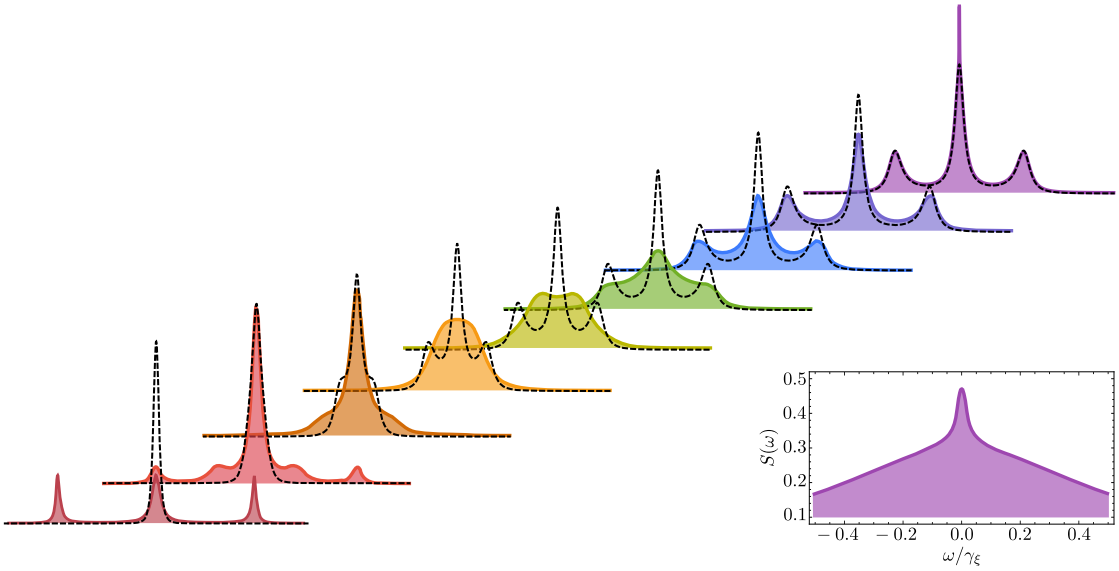

Figure 6.8: Dressing of the target 2LS with a one atom laser. We compare the normalised emission spectra of the a 2LS driven by the emission of a one atom laser (solid color lines) with the normalised emission spectra of a 2LS driven coherently by a classical laser (dashed black lines). The incoherent driving of the one atom laser increases towards the upper right corner of the figure, and makes the emission spectra of the target 2LS to change from a filter of the emission of the cavity, as is clear from the lateral peaks due to the strong coupling between the cavity and the atom inside, to the splitting of the emission line until it reaches a triplet shape equivalent to that of a coherently driven 2LS. To compute the figures we set the atom, the cavity and the target 2LS in resonance, and the rest of the parameters were as follows: γ_ξ was set as the unit, $\gamma_\sigma/\gamma_\xi = 10^{-2}$, $\gamma_a/\gamma_\xi = 1$, $g/\gamma_\xi = 10$. The incoherent driving rate P_σ is different for each spectrum, for the spectrum at the bottom we took the limit $P_\sigma/\gamma_\xi \to 0$. For the next seven lines we used the P_σ such that $\Omega/\gamma_\xi = \sqrt{\gamma_a\gamma_\xi n_a}/\gamma_\xi = 0.5$, 1.0, 1.5, 2.0, 2.5, 3.0, and 3.5. The last spectrum, at the top right of the figure, was obtained for a cavity with $\gamma_a/\gamma_\xi = 0.1$ and $P_\sigma/\gamma_\xi = 20.115$, so that the population in the cavity was 100 photons. The inset shows a zoom on this last spectrum very close to the resonance of the target 2LS, to show the Rayleigh peak due to the driving by a laser.

in the target 2LS and in the coherently driven 2LS are the same. In all the other cases, when the one atom laser is in the lasing regime, the comparison of the spectra is made so that the driving intensity is the same, i.e., we compare the spectra of the target 2LS with that of a 2LS driven coherently with intensity $\Omega^* = \sqrt{\gamma_\xi\gamma_a n_a}$, where n_a is the population of the cavity. Figure 6.8 shows neatly the splitting of the energy levels of the target 2LS as a function of the rate of incoherent driving of the atom inside the cavity. At the lowest P_σ, the spectrum of the target 2LS is the one at the left bottom part of the figure. There we see clearly that the target 2LS is acting as filter of the emission of the cavity: the central peak corresponds to the resonance of the target 2LS, while the other two peaks reveal the Rabi doublet due to the strong coupling between the cavity and the atom inside. As the incoherent driving of the atom increases, the peaks corresponding to the Rabi doublet become less dominant, and the emission spectrum of the target 2LS tends to merge into a broad single line. Increasing even further the incoherent driving, the emission line of the target 2LS begins to split again, but in a different way than the coherently driven 2LS: while the splitting of the target 2LS seems to be a doublet as e.g. in the light green line, the spectrum of the coherently driven 2LS has clearly a triplet shape. At large driving rates the emission of the target 2LS converges to that of the coherently driven 2LS. In fact, in the uppermost spectrum the cavity has 100 photons, its statistics is coherent (that is $\langle a^\dagger a^\dagger aa\rangle/n_a^2 = 1$), and the two spectra are exactly the same. In Fig. 6.9 we show a density plot of the photoluminiscence spectrum of the target 2LS driven by all the sources of light that we have considered in this Section, and summarized in its caption. At the highest

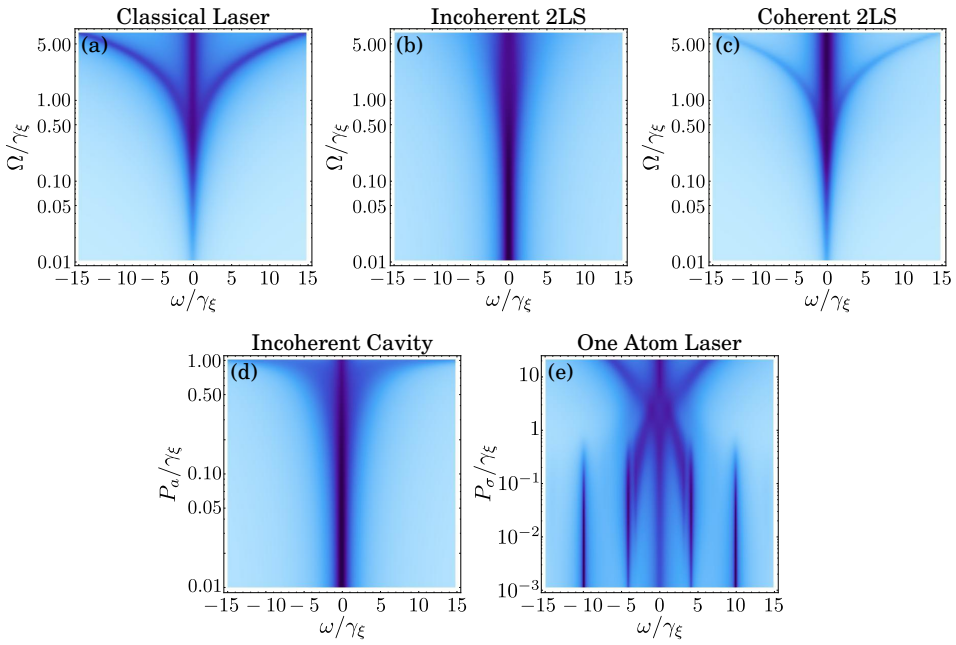

Figure 6.9: Photoluminescence spectra of the two-level system driven by all the sources studied in the chapter: (a) A classical laser resulting in the conventional Mollow Triplet. (b) An incoherent 2LS providing a single line that merely broadens. (c) A coherent 2LS providing a Mollow splitting but of weak intensity and that vanishes with increasing driving intensity. (d) A Thermal cavity providing a single line whose broadening is reminiscent of the Mollow structure. (e) A one-atom laser showing the transition from the non-lasing regime of the driving source to the exact recovering of the conventional Mollow triplet. At low driving, the target echoes the structure from a Jaynes-Cummings-like coupling with the source.

intensity shown in Fig. 6.8 the triplet structure sits below a narrow line due to the photons that are scattered by the two-level system rather than absorbed and later re-emitted. This peak is evidence of the so-called Rayleigh scattering, and it is observed even when considering the excitation of a two-level system with a classical laser (in fact, I have discussed this process in details in Chapter 3. However, for the classical case, one assumes that the laser is perfectly monochromatic and therefore the linewidth of this peak is exactly zero. In contrasts, the peak that arises in this spectrum has the natural linewidth of the laser (which this time is physical, and no approximation has been made to describe it), which is shown in the inset of Fig. 6.8.

6.5 CASCADED SINGLE PHOTON SOURCES

6.5.1 *Introduction*

Cascading is a powerful concept that allows to achieve extremely high end values from a moderate initial input, with such compelling examples as the domino effect, which Whitehead (1983) has shown can amplify energy by over two billions in a basement, to Lindeman (1942)'s trophic cascade that can lead to extinction of species. It acts in several key processes of various areas of science, e.g., with chemical and nuclear reactions, as reported by Bodenstein (1913) and Anderson, Fermi, and Szilard (1939), respectively. In optics, through stimulated emission, Dicke (1954) show that it underpins basic phenomena such as supperradiance and Schawlow and Townes (1958) did accordingly with lasing. With the advent of heterostructures, it became possible to engineer more elaborate schemes to better control the chain reaction. A highlight is the proposal by Kazarinov and Suris (1971) of energy staircases in a superlattice leading to the successive creations of an increasing number of photons by a single initial electron, a scheme

that Faist et al. (1994) realized a quarter of a century later under the name of a quantum cascade laser. Recently, Liew et al. (2013) made another proposal with cascades between condensates and extremely high correlations in the form of superbunching, which according to Liew et al. (2016) occur as a result of the cascading.

6.5.2 *Driving the cascaded SPS*

In this Section, I propose the application of such a principle to quantum light, and with the aim of increasing not the intensity of light but a quality dear to quantum engineers, namely, antibunching. In the race to build always better sources, in particular in the semiconductor community (cf. the work of Rau et al. (2014), Schlehahn et al. (2015), and Ding et al. (2016)), where such devices would furthermore have a large economic and technological potential. Kuhlmann et al. (2015) recently showed that the Fourier transform limit for single photon emission and there is now much efforts to combine and enhance other features such as brightness, efficiency and, of course, antibunching, as has been done, e.g. by Unsleber et al. (2016), Somaschi et al. (2016), and Loredo et al. (2016). My proposal takes a new direction and rather than improving the engineering and the implementation, I turn to a different mechanism to increase the quality of SPS by magnitudes not accessible only with a better technology. Namely, I propose to cascade the output of a chain of single photon sources (SPS), with effect of a profound restructuring of their spectral emission, bringing the initial Lorentzian shape of a single SPS to grow into a Student t lineshape of order $2k$ after k iterations of the cascade. I show that such a spectral engineering that trims the fat Lorentzian tails is accountable for increased antibunching. As the iterations converge towards a Normal distribution, this scheme allows to engineer extremely antibunched single photon sources that could power quantum logic with the repetition rates necessary for their successful operations at a large scale. In essence, my results remove the constrain of spectral broadening associated to short lifetimes. Stated otherwise, it achieves at the single-photon emission level what a laser does in the Schallow-Townes limit by narrowing the line with increasing signal.

My proposal consists of an array of consecutive SPS, in which the first SPS is excited externally while the rest of them are excited by the fluorescence of the previous SPS. I will consider cascades of up to three emitters but the scheme can be continued indefinitely. The underlying principle is that exciting with quantum light allows to access new regimes that neither classical excitations nor reversible (Hamiltonian) coupling can provide. This is thanks to the added degrees of freedom of quantum light on the one hand (such as reduced fluctuations) and the one-way transfer of energy on the other hand that removes the effective decay implied by strong-coupling oscillating the excitation back to its source.

Here more than in the other cases discussed so far, a fully-integrated approach might be desirable to realize a device. The scheme consists in feeding the output field of the i-th system to the input field of the $(i+1)$-th system, with no feedback. This could be achieved by unidirectional couplers in the laboratory or, as already commented in Chapter 5, by using chiral waveguides to assemble the whole architecture compactly on the same chip, as shown by Petersen, Volz, and Rauschenbeutel (2014) and Coles et al. (2016). It could also be possible to use a highly directional source of excitations, as Ma et al. (2015) did, or a direct photonic coupling following the work of Meyer et al. (2015). A schematic representation is shown in Fig. 6.10(a) and reads as follows: the first SPS is driven by an external pumping, and the emission of SPS1 is then sent to SPS2, and so on and so forth as more stages of the cascaded are arranged. An array of N SPS

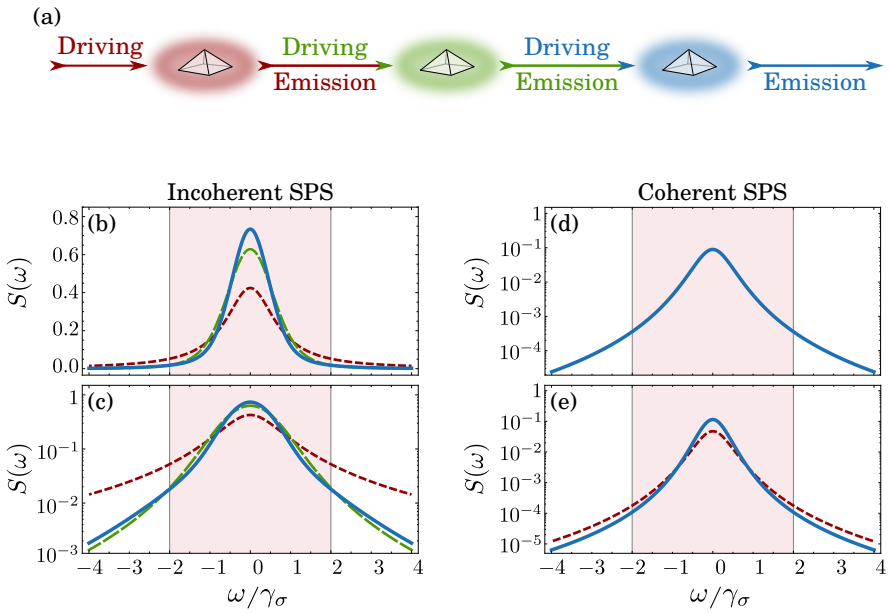

Figure 6.10: Scheme of the cascaded single-photon sources. (a) A series of SPS is connected through a cascaded architecture. In each step of the cascade a SPS is driven by the emission of the previous SPS. (b–d) Emission spectra of the initial SPS (red, dotted), the first (green, dashed), and second (blue, solid) cascade steps. In each step of the cascade, the emission line becomes narrower and more peaked around the central frequency. Panels (b) and (c) were made with $\gamma_\xi/\gamma_\sigma = P_\sigma/\gamma_\sigma = 1$. Panel (d) shows the case for the coherent excitation of *all* the SPS by the coherent field, whereas Panel (e) shows the case for the excitation by only the emission of the quantum source, i.e., the excitation of the target is done through a different channel than the one used to drive coherently the source.

with annihilation operators σ_i, Hamiltonian H_i, and decay rate γ_i can then be described by a master equation in the form:

$$\partial_t \rho = \sum_{j=1}^{N} \left(i[\rho, H_j] + \frac{\gamma_j}{2}\mathcal{L}_{c_j}\rho - \sqrt{\gamma_j}\left[\mathcal{E}c_j^\dagger - \mathcal{E}^* c_j, \rho\right]\right) + \\ + \sum_{j=2}^{N}\sum_{l=1}^{j-1}\sqrt{\gamma_j\gamma_l}\left\{[c_l\rho, c_j^\dagger] + [c_j, \rho c_l^\dagger]\right\} + \frac{P_{c_1}}{2}\mathcal{L}_{c_1^\dagger}\rho\,, \quad (6.27)$$

where $\mathcal{E}$ is the amplitude of the coherent field incident upon SPS1. The justification for this master equation is given in the Appendices B.2 and B.3, and I have featured explicitly an incoherent pumping of the first SPS at the rate P_{c_1}, that can be set to zero to consider the effect of the coherent driving only. The antibunching of a two-level system is, ideally, exactly zero. An actual experiment will detect two photons, even in absence of noise and extraneous emitters, from the SPS itself. This is due to time uncertainty that can bring together two photons close enough in time to exhibit photon bunching. For some fixed time unit set by the detector, the larger the emission rate, the more likely are such spurious coincidences. In the frequency space, this is linked to tail events that are not detected, for instance because the detector's bandwidth Γ is finite. Accordingly, the theory of frequency-resolved correlation of del Valle et al. (2012) predicts that while detecting all photons at all frequencies, $\Gamma \to \infty$, produces the ideal $g^{(2)}_\infty(\tau = 0) = 0$, failure to do so results in bunching. The fastest is the source, the broader is the spectrum and the more difficult it becomes to collect all the photons. Crucially, the spectrum is a Lorentzian and consequently has fat tails. This means that outliers are frequent, unlike a Normal distribution where they are exponentially suppressed until they become safely completely negligible. A fat-tail distribution can never safely exclude all its outliers, regardless

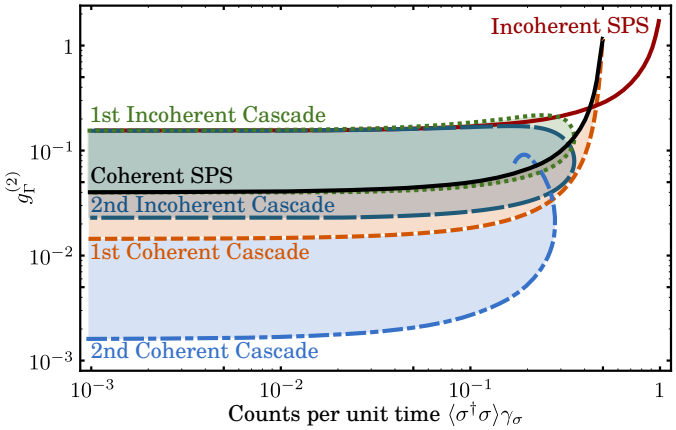

Figure 6.11: Improvement in the $g_\Gamma^{(2)}$ due to the cascaded scheme. Once we fixed the linewidth of the first SPS, the degree of freedom of the second SPS spans a new accessible region shown by the colour shading. The antibunching provided by a incoherent SPS is enhanced by the cascaded scheme, but for a wide range of parameter it is overcome by the antibunching provided by the coherent SPS. However, by allowing all the SPS in the cascade to be driven by a coherent field, a destructive interference sets a limits the enhancement of the $g_\Gamma^{(2)}$ at the first step. The enhancement on the second cascaded is obtained by driving the cascade with only the emission of the coherent SPS. In the axis, γ_σ has the dimension of inverse time and its numerical value sets the unit.

of the filters bandwidth. There would therefore appear to be an intrinsic limitation between emission rate and photon antibunching. We now show how to thwart such a predicament by trimming the fat tails. Figure 6.11 shows the combined emission rate and antibunching $g_\Gamma^{(2)}$ for a SPS that is excited either incoherently (solid red) or coherently (solid black) as pumping is varied (dummy parameter on the curve). This figure is for a detector bandwidth $\Gamma = 4\gamma_\sigma$. Increasing Γ, one both betters the emission rate and antibunching, towards their ideal values of γ_σ and 0, respectively. However, this is a slow convergence that requires unpractical large filters at a disadvantage with the fat Lorentzian tails. The exact functions of Γ and other parameters are given by, in the case of incoherent pumping at rate P_σ:

$$I_\sigma^{\text{inc}} = \gamma_\sigma P_\sigma / \left(\gamma_\sigma + P_\sigma\right) \int_{-\Gamma/2}^{\Gamma/2} S(\omega)\, d\omega\,, \tag{6.28a}$$

$$g_\sigma^{(2),\text{inc}} = \frac{2}{1 + 3\tan\left[\pi \left(\gamma_\sigma + P_\sigma\right) I_\sigma^{\text{inc}} / \left(2\gamma_\sigma P_\sigma\right)\right]}\,, \tag{6.28b}$$

where Eq. (6.28b) is valid for $I_\sigma^{\text{inc}} \leq \gamma_\sigma P_\sigma / \left(\gamma_\sigma + P_\sigma\right)$. The coherent counterpart is given by:

$$I_\sigma^{\text{coh}} = \frac{4\gamma_\sigma \Omega_\sigma^2}{\gamma_\sigma^2 + 8\Omega_\sigma^2} \int_{-\Gamma/2}^{\Gamma/2} S(\omega)\, d\omega\,, \tag{6.29a}$$

$$\begin{aligned} g_\sigma^{(2),\text{coh}} = {} & \{2\gamma_{\widetilde{11}}(\gamma_{\widetilde{01}}^2 + 8\Omega_\sigma^2)(\gamma_{\widetilde{11}}\gamma_{\widetilde{12}} + 16\Omega_\sigma^2)\times \\ & \times [\gamma_{\widetilde{11}}^2\gamma_{\widetilde{21}}\gamma_{\widetilde{31}}\gamma_{\widetilde{12}}\gamma_{\widetilde{32}}(9\gamma_{\widetilde{10}}^2 + 7\gamma_{\widetilde{10}}\gamma_{\widetilde{01}} + \gamma_{\widetilde{01}}^2) + 4\gamma_{\widetilde{11}}\gamma_{\widetilde{32}}(84\gamma_{\widetilde{10}}^4 + 16\gamma_{\widetilde{10}}^3\gamma_{\widetilde{01}} + 118\gamma_{\widetilde{10}}^2\gamma_{\widetilde{01}}^2 + \\ & + 31\gamma_{\widetilde{10}}\gamma_{\widetilde{01}}^3 + 2\gamma_{\widetilde{01}}^4)\Omega_\sigma^2 + 32\gamma_{\widetilde{10}}(51\gamma_{\widetilde{10}}^3 + 75\gamma_{\widetilde{10}}^2\gamma_{\widetilde{01}} + 38\gamma_{\widetilde{10}}\gamma_{\widetilde{01}}^2 + 8\gamma_{\widetilde{01}}^3)\Omega_\sigma^4 + 768\gamma_{\widetilde{10}}^2\Omega_\sigma^6]\}/ \\ & \left\{3\gamma_{\widetilde{31}}(\gamma_{\widetilde{11}}\gamma_{\widetilde{21}} + 4\Omega_\sigma^2)(\gamma_{\widetilde{11}}\gamma_{\widetilde{21}} + 8\Omega_\sigma^2)(\gamma_{\widetilde{31}}\gamma_{\widetilde{32}} + 16\Omega_\sigma^2)(\gamma_{\widetilde{11}}^2\gamma_{\widetilde{12}} + 8\gamma_{\widetilde{10}}\Omega_\sigma^2)^2\right\}\,, \end{aligned} \tag{6.29b}$$

where we have used again the compact notation $\gamma_{\widetilde{nm}}^k = (n\Gamma + m\gamma_\sigma)^k$. From these results, and as is apparent on Fig. 6.11, one sees that the coherent driving provides better antibunching than its incoherent counterpart, with plateaus of

$$g_\sigma^{(2),\text{coh}} = 2\gamma_{\widetilde{01}}^2(9\gamma_{\widetilde{10}}^2 + 7\gamma_{\widetilde{01}}\gamma_{\widetilde{10}} + \gamma_{\widetilde{01}}^2)/3\gamma_{\widetilde{11}}^2\gamma_{\widetilde{21}}\gamma_{\widetilde{31}}\,, \tag{6.30}$$

and $g_\sigma^{(2),\mathrm{inc}} = 2\gamma_{\widetilde{01}}/\gamma_{\widetilde{31}}$, which for $\Gamma = 4\gamma_\sigma$ reduce to $346/8775 \approx 0.039$ and $2/13 \approx 0.154$ respectively. The maximum emission rate, however, is smaller. This is due to stimulated emission induced by the coherent driving that Rabi oscillates back the excited state to the ground state and thus saturates the SPS to at most half its full occupancy. In contrast, the incoherent driving can saturate the two-level system to its excited state and can thus emit twice as much. The reason for a better antibunching of the coherent driving has already been discussed above in relation to the Heitler effect. It is related to the spectral shape that trims its fat tails by destructive interferences. In the case of the Mollow triplet, we have shown above that it consists of three Lorentzians centered at $\omega = 0$, and $\omega = \pm\sqrt{64\Omega_\sigma^2 - \gamma_\sigma^2}$ as shown in Eq. (1.49). In the limit of vanishing driving, the resulting lineshape thus concentrates its emission to the central peak with a distribution of the type:

$$S(\omega) = \frac{1}{\pi}\frac{32\gamma_\sigma\Omega_\sigma^2}{(\gamma_\sigma^2+\omega^2)^2}\,, \tag{6.31}$$

which is proportional to a Student's t–distribution or order 3. The tails of this distribution vanish faster than those of a Lorentzian distribution. A given frequency windows collects more photons from the SPS and its antibunching is therefore more like that of the full spectrum, that provides the exact zero.

We can extend this principle to cascaded systems, where the driving of the SPS is not from an external classical laser (which, since it does not get feedback, can be seen as a particular case of cascading) but from another 2LS. For the case of incoherent pumping, we observe a similar behavior in the emission spectrum, as a difference of lorentzians leads to a distribution with faster decaying tails. Namely, the emission spectrum of the first cascade reads at vanishing pumping:

$$\begin{aligned} S_\xi(\omega) &= \frac{1}{2\pi}\frac{\gamma_\sigma\gamma_\xi}{\gamma_\xi-\gamma_\sigma}\left[\frac{1}{(\gamma_\sigma/2)^2+\omega^2} - \frac{1}{(\gamma_\xi/2)^2+\omega^2}\right], \\ &= \frac{1}{2\pi}\frac{\gamma_\sigma\gamma_\xi\left(\gamma_\sigma+\gamma_\xi\right)}{(\gamma_\sigma^2+4\omega^2)(\gamma_\xi^2+4\omega^2)}\,, \end{aligned} \tag{6.32}$$

which is a Student t distribution of order 3. In the next stage in the cascade, the resulting distribution is a Student t of order 5.

There is a trade-off between the antibunching and the intensity of the emission of the cascaded single-photon source. The improvement of the value of $g_\Gamma^{(2)}$ is maximum when all the SPS have the same decay rate. In Fig. 6.11 I show the antibunching as a function of the emission rate of the cascaded SPS at various steps of the cascade, and for both the coherent and the incoherent driving. The coherent (solid, black line) and incoherent (solid, red line) are simply a SPS driven by a classical field. In the first step of the cascade we obtain a large enhancement in the antibunching: for a wide range of intensities, the antibunching for the first step in the incoherent cascade (dotted, green line) matches the antibunching obtained with the coherent SPS, which shows again how driving a system with a classical laser can be seen as cascade. On the other hand, the antibunching for the first step in the coherent cascade (dashed, orange line) shows a huge enhancement, which for a large range of intensities is even better that the antibunching for the second step in the incoherent cascade (large-dashed, blue line). However, the second step in the coherent cascade shows the same antibunching as the coherent SPS, thus effectively reducing its antibunching. In fact, if all the SPS in the cascade have the same decay rate, then all the even steps in the coherent cascade have the antibunching of the coherent SPS, whereas the odd steps have the antibunching of the first step in the coherent cascade. Another possible configuration for the coherent cascade provides a gain in the $g^{(2)}$ in the second step of

the cascade. Namely, removing the coherent excitation from all the SPS except for the first one. This is achieved in the same way as in Section 6.2, for which Eq. (6.27) is modified to:

$$\partial_t \rho = \sum_{j=1}^{N} \left(i[\rho, H_j] + \frac{\gamma_k}{2} \mathcal{L}_{c_k} \right) \rho - \sqrt{\epsilon \gamma_1} \left[\mathcal{E} c_1^\dagger - \mathcal{E}^* c_1, \rho \right] + \\ + \sum_{j=3}^{N} \sum_{l=2}^{j-1} \sqrt{\gamma_j \gamma_l} \left\{ [c_l \rho, c_j^\dagger] + [c_j, \rho c_l^\dagger] \right\} + \sum_{j=2}^{N} \sqrt{(1-\epsilon)\gamma_1 \gamma_j} \left\{ [c_1 \rho, c_j^\dagger] + [c_j, \rho c_1^\dagger] \right\} . \quad (6.33)$$

The coherent SPS provided by Eq. (6.33) has the same antibunching as the one provided by Eq. (6.27), but requires a larger amplitude of the coherent field $\mathcal{E}$ as it is effectively reduced by a factor $\sqrt{\epsilon}$. For a large range of values of the emission rate, the antibunching of the first step in the cascade coincides with the values obtained with Eq. (6.27). However, only a fraction $(1-\epsilon)$ of the light emitted by the coherent SPS is transmitted to the cascade, and the emission rate of the cascade is reduced by that factor. This is shown by the dashed, golden line in Fig. 6.11. The antibunching for the second step in the cascade, as opposed to what is obtained with Eq. (6.27), improves vastly as shown by the dashed, blue line in Fig. 6.11. Considering, e.g., a typical lifetime of $\tau_\sigma = 1$ ns for a self-assembled quantum dot, which transform-limit turns into a PL line of $\gamma_\sigma = \hbar/\tau_\sigma = 666$ eV, that is, furthermore, power-broadened by pumping, one gets emission rates of ten million counts per second with an antibunching of $\approx 3.5 \times 10^{-3}$ in a frequency window of $4\gamma_\sigma$ with two cascades under incoherent pumping, and one order of magnitude better antibunching with coherent pumping. The cascading can be iterated further and by turning to shorter lived two-level emitters, since we have removed the spectral constrain of outliers spoiling the antibunching, we can reach extremely bright antibunched single photon sources. To appreciate these results, one can stress the saturated antibunching for the incoherent (red) an coherent (black) uncascaded SPS while those in the cascades improve their antibunching, albeit at the cost of diminished emission rates. This is because the first SPS sets the unit of time. In fact, the envelope of the first cascade, in the units fixed by the first SPS, is the same as the envelope of this first SPS . As a consequence, what one achieves already at the first case of the cascade is to increase the decay rate of the SPS for a given value of the antibunching, thereby achieving brighter single single photon sources. Next stages in the cascade further improve the situation.

6.5.3 *Comparison with the excitation of an harmonic oscillator*

In the previous Chapter, I treated the excitation of an harmonic oscillator by a quantum source. Such excitation allowed the harmonic oscillator to cover some area in the $(n_a, g_a^{(2)})$ space, shown in green in Fig. 6.12(a). Since this was some distance away from physical limit, a natural question is whether other quantum sources could access more territory. I now show how, indeed, the emission from a cascaded SPS indeed achieves that goal, although still far from yet touching the boundary. In the case of driving the oscillator with cascaded SPS, the excitation is obtained through Eq. (1.28). In this configuration, the accessible area expands to the orange region of Fig. 6.12. Inspired by the positive results obtained using a second cascade to excite the harmonic oscillator, one might think that further cascading the source could move the border of the accessible states closer to the limit set by the Fock duo. However, covering all the possible values for all the free parameters (driving intensity, decay rates and frequencies) grows exponentially with the number of cascades in the hypothetical device. It remains an open question at the time of writing whether further cascades, or for that matter another quantum source, can get closer or even reach the frontier.

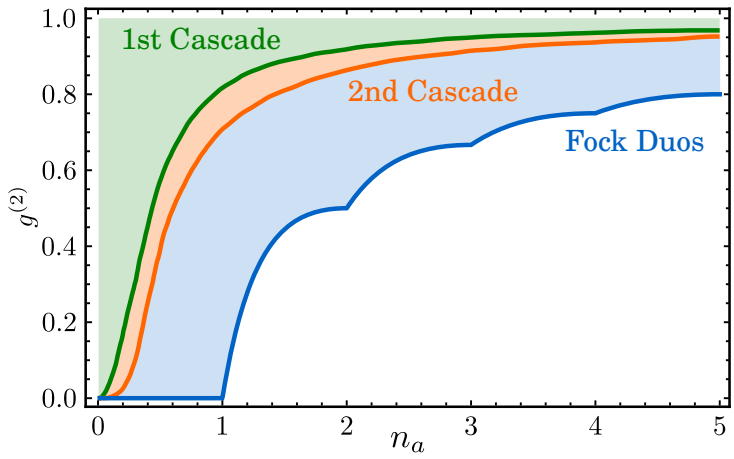

Figure 6.12: Getting closer to the limit: adding a cascade step to excite an harmonic oscillator pushed the border of the accessible states from the green (1st Cascade) to the orange (2nd Cascade) region. Adding more steps to the cascade could take the accessible region closer to the Fock Duos limit.

6.6 CONCLUSIONS

I have studied in detail several aspects as well as several configurations of the driving of a two-level system (2LS) by quantum light (and classical light for comparison). I have shown that the 2LS is "quantum-enough" not to benefit by itself from the excitation by quantum light as far as the quantum state is concerned, since classical excitation can drive it in the same steady state. However, when granted together with its source, with which it can enter in strong-coupling, or when considering dynamical aspects of its emission, quantum driving of a SPS can result in new regimes for its dynamics. This led us to a discussion of the meaning and definition of strong-coupling between states in absence of feedback and, therefore, of oscillations. At a fundamental level, I have meticulously discussed all the main possibilities to drive a 2PS with various types of light, yielding a series of Mollow triplets that are summarized in Fig. 6.9. As the most elaborate description, I have presented a full quantized model where the lasing is self-consistently formed out of incoherent excitation through the one-atom lasing mechanism. This allows to consider aspects such as the question of the optical phase and the nature of the Rayleigh peak in absence of any c-number in the Hamiltonian. At an applied level, I have shown how the quality of the reduction of multiple-photon emission (antibunching) can be understood as linked to the spectral tails. I identified in this way why coherent pumping (resonance fluorescence) overtakes its incoherent counterpart and discussed the counter-intuitive Heitler effect of antibunched scattered photons off a laser. Namely, the coherent driving leads, in the weak-coupling of the Mollow triplet, to interferences that turn the luminescence line into a Student-t distribution with weaker fat tails than the Lorentzian profile of spontaneous emission. This allows to collect more easily all the signal that, when taken in its entirety, contrives to result in a single emitted photon by destructive interferences of the possible emissions. I have shown how a similar and even further trimming of fat tails can be achieved by cascading SPS with the effect of yielding increasingly antibunched emitters with decreasing tails, ultimately converging towards a normal distribution (with no outliers), making it realistic to thus design *perfect* single photon sources, i.e., that yield exactly zero coincidence and perfect antibunching, $g^{(2)} = 0$, by considering, say, the emission in five standard deviations of the cascaded SPS with enough stages to approach a Gaussian. This would provide one spurious coincidence in 3.5 millions repetitions, making any departure from exactly zero to any other factor in the experiment than the source itself. These results should stimulate experiments on new approaches to design better single photon sources.

7 EXCITATION OF POLARITONS

No, no! The adventures first, explanations take such a dreadful time.

— Lewis Carroll
Alice's Adventures in Wonderland
& Through the Looking-Glass

7.1 INTRODUCTION

The previous two chapters were devoted to the excitation with quantum light of the most fundamental targets: a boson and a fermion. In this Chapter, we upgrade the target of the excitation to a quantum superposition of two bosonic particles, of which one is weakly interacting. Exciton-polaritons—from here on simply *polaritons*—are the archetype of such a class of superposition, arising from the strong coupling between a photon and an exciton in a quantum well. While their full 2D structure can be described microscopically—in which case we have to invoke the many electronic modes involved in the excitons and their coupling to the photonic field, as discussed in Section 7.2.2—for this first part of the discussion we will follow the work of Verger, Ciuti, and Carusotto (2006) which captures the microscopic description in a simple model, in which a couple of harmonic oscillators are strongly coupled, and one of them has a Kerr-like nonlinearity. Namely, the Hamiltonian describing the polaritons is given by

$$H_p = \omega_a a^\dagger a + \omega_b b^\dagger b + g(a^\dagger b + b^\dagger a) + U b^\dagger b^\dagger b b \,, \tag{7.1}$$

where a and b are the annihilation operators for the photonic and excitonic field, with bare frequencies ω_a and ω_b respectively. The coupling between them has a strength g and the interaction between excitons (which arises from the Coulomb force) is given by U. The dissipative aspect of polaritons is taken into account through a master equation as in Eq. (1.20), the spontaneous decay of the photon and the exciton, given by γ_a and γ_b, respectively. In the strong coupling regime, obtained when the coupling strength, g in Eq. (7.1), satisfies the relation $g > |\gamma_a - \gamma_b|/4$, the system is not governed by the bare states anymore, and instead the dynamics is better described through the dressed states. In the context of polaritons, these states are referred to as the "lower" and "upper" polariton branches, which I have introduced and shown in Fig. 1.17, and their energies are related to the energy, coupling strength and decay rates of the bare modes as follows:

$$\omega_{LP/UP} = \frac{\omega_a + \omega_b}{2} \mp \sqrt{g^2 - \left(\frac{\gamma_a - \gamma_b}{4}\right)^2} \,. \tag{7.2}$$

When driven classically with a laser, the response of the polaritons is as shown in Fig. 7.1. The strong coupling makes the occupation of the photonic field go towards the frequencies of the polariton branches, while leaving a dip of population at the frequency of the bare modes. Figure 7.1(b) shows the second-order correlation functions, as defined in Eq. (1.33), of both the photonic field (blue line) and the lower polariton (orange). In the correlations of the photonic field one sees the evidence of both the conventional (at the frequencies of the polaritons) and the unconventional photon blockade (close to the frequencies of the bare modes), which, for polaritons, were first predicted theoretically by Verger, Ciuti, and Carusotto (2006) and Liew and Savona (2010), respectively. These two blockade effects have been recently been measured by Muñoz-Matutano et al. (2019) and Delteil et al. (2019) in the conventional version and by Snijders et al. (2018) and Vaneph et al. (2018) in the unconventional one. However, the experiments above had to be done in the regime in which the excitation is very small—as

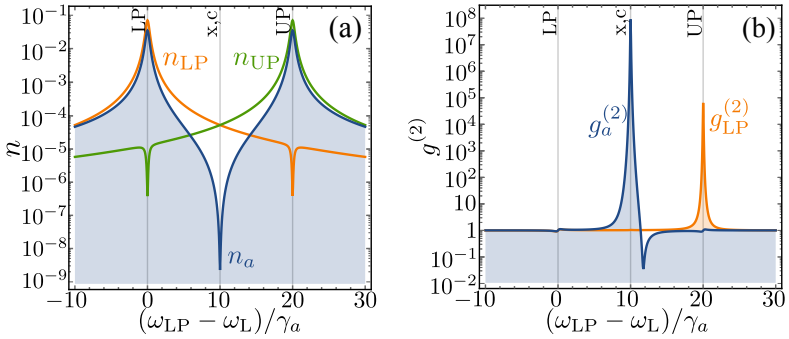

Figure 7.1: Response of polaritons to coherent driving. (a) Mean occupation of the cavity n_a (blue), the lower n_{LP} (orange) and upper n_{UP} (green) polariton branches as a function of the detuning between the lower polariton branch and the driving laser. The strong coupling yields the suppression of the occupation at the frequencies of the bare modes, while pushing it to the frequencies of the polariton branches. (b) Second-order correlation function for the cavity (blue) and the lower polariton branch (orange), displaying the conventional and unconventional photon blockade at the frequencies of the bare modes and of the polaritons, respectively.

Messin et al. (2001) showed that stronger excitations lead to blueshift and bistability—and the observed antibunching remains relatively small.

In this Chapter, I undertake a different approach to observe quantum behaviours from polaritons. Instead of using classical excitation and expecting the quantumness to arise from the interaction between excitons, I will inject it from outside, and study the subsequent internal quantum dynamics. While I will consider the polaritons as the optical target throughout this Chapter, I will consider the quantum light from two types of sources: the Mollow (1969) triplet, introduced in Section 1.2.6, and entangled pairs of single photons

7.2 EXCITING WITH THE MOLLOW TRIPLET

With the ever increasing availability of quantum emitters, the question of their effect on a target is one of increasing theoretical interest. In the wake of Kira and Koch (2006)'s proposal for quantum optical spectroscopy, it has been shown thoroughly by Kira et al. (2011), Carmele, Knorr, and Richter (2009), and Aßmann and Bayer (2011) that the statistics of the light affects strongly the response of a system. In our case, the excitation is the output from a two-level system driven by a laser with an intensity such that the emission spectrum is a Mollow (1969) triplet. This is described through the Hamiltonian H_σ given in Eq. (1.45). The target, on the other hand, are polaritons described through the Hamiltonian H_p in Eq. (7.1) referring the frequencies of the photon and the exciton to the frequency of the driving laser. Furthermore, the dissipation of the two systems and the cascaded coupling from the 2LS to the photonic field are given by the master equation (1.28), which in this context becomes

$$\partial_t \rho = i[\rho, H_\sigma + H_p] + \frac{\gamma_\sigma}{2}\mathcal{L}_\sigma + \frac{\gamma_a}{2}\mathcal{L}_a + \frac{\gamma_b}{2}\mathcal{L}_b - \sqrt{\gamma_\sigma \gamma_a}\left\{[\sigma^\dagger, a\rho] + [\rho a^\dagger, \sigma]\right\} . \tag{7.3}$$

7.2.1 *Mollow Spectroscopy*

We now turn to a specific application of the excitation with quantum light, tackling the excitation of a system of interacting polaritons with the emission from a 2LS driven coherently in the Mollow (1969) regime. In chapters 1 and 2 I have discussed how the photons from various frequency windows of the Mollow triplet have different types of statistics, ranging from the expected antibunching (stemming from the fermionic character of the 2LS) from the lateral peaks, up to superbunching from the leapfrog processes (introduced in Chapter 2) that lead to the emission of photon pairs, a higher-still photon-bundle,, which Sánchez Muñoz et al. (2014b)

have shown violate Cauchy-Schwartz and Bell's inequalities, passing through intermediate cases in other frequency windows. Thus, we can use this rich variety of quantum light (from a single source) to scan over the target to probe its response to all types of input: from antibunched single-photons, to superbunched highly correlated photon-pairs. This gives rise to a new type of spectroscopy based on photon correlations, to which I refer as "Mollow spectroscopy".

The response of weakly interacting polaritons, described with a Hamiltonian as in Eq. (7.1), to classical light shows that antibunching is extremely small and requires vanishing excitations, as stronger excitations lead to blueshift and bistability. For this reason, unconventional polariton blockade mechanisms are favored, although these still require small pumping. In contrast, excitation with quantum light allows a strong response in statistics with small populations for all ranges of excitation and values of the ratio U/γ_a. Figure 7.2(a) shows the lower polariton population n_{LP} (the dot-dashed yellow line) and its second order correlation function $g^{(2)}_{\mathrm{LP}}$ (the blue line) as the quantum source is scanned over the lower polariton (LP) branch, at energy ω_{LP} as defined in Eq. (7.2). Both the population and the statistics of the Mollow triplet are transferred to the polaritons, but with some deviations due to their interactions. These deviations are particularly marked in the polariton statistics, even down to very small values of U/γ_a, as seen in Fig. 7.2(b), where I plot the L^2 norm $\|g^{(2)}_{U=0} - g^{(2)}_{U\neq 0}\|_2$, i.e., integrating over frequencies the differences of photon statistics with and without nonlinearities. Variations of about one percent are obtained for $U/\gamma_a = 10^{-2}$. For even lower values, this becomes a delicate measurement but still one within reach of state-of-the-art experiments, such as the one conducted by Peiris et al. (2015). The higher sensitivity of the nonlinearity in statistics than in population comes from the strongly correlated character of the leapfrog photon pairs, which optimize the effect of the interaction by consistently using the ideal number of photons (two) needed for it to manifest. The tunability of statistics from the Mollow triplet allows us, in particular, to extract the numerical value of the nonlinearity. This is achieved by measuring the change in photon statistics with the frequency of excitation. The maximum of the bunching is obtained at the frequencies of the two-photon leapfrogs, namely at the frequency halfway between the central and the satellite peaks. Photon pairs closer to the satellites lose their bunching faster than those closer to the central peak. Comparing the response of the system when going in these two directions allows us to quantify small nonlinearities that are otherwise hidden within the radiative broadening. Thanks to the symmetry of the Mollow triplet, such a comparison can be conveniently implemented without the need for a calibration of the frequencies by using directly both sides of the triplet, rather than both sides of the superbunching peak. One can

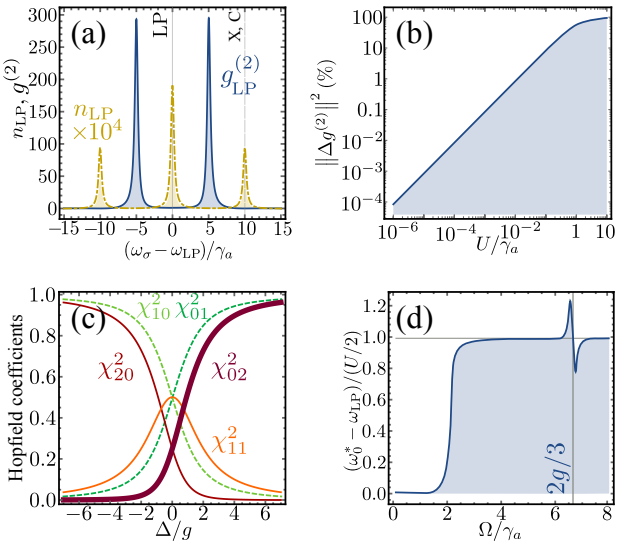

Figure 7.2: Mollow spectroscopy of weakly interacting polaritons. (a) Population (dot-dashed yellow line) and photon-statistics (solid blue line) when scanning the Mollow triplet onto the lower polariton branch. (b) Magnitude of the deviation from the noninteracting polariton statistics as a function of U/γ_a. (c) Hopfield coefficients χ_{nm} of relative light (n)-matter (m) content, as a function of detuning. (d) Mollow splitting required for the measurement of ω_0 to be Ω_σ independent, allowing an absolute measurement of U.

simply sweep the Mollow line shape onto the target and record its photon statistics. From these measurements, one then defines f for the autoconvolution of the correlation function

$$f(\omega) = \int_{-\infty}^{+\infty} g^{(2)}(\omega - \nu) g^{(2)}(\nu)\, d\nu\,. \tag{7.4}$$

The triangle inequality places the maximum of $f(\omega)$ at the values ω_0^* that minimizes the asymmetry of $g^{(2)}$ around $\omega - \omega_{\mathrm{LP}}$. When the leapfrog processes are sufficiently well defined (see below), we find that the shift is precisely given by the two-polariton interaction:

$$\omega_0^* = \omega_{\mathrm{LP}} + 2U\chi_{02}^2\,, \tag{7.5}$$

where χ_{02} is the two-polariton Hopfield coefficient for the state $|02\rangle$ of two excitons and zero photons. The closed-form expression of χ_{02} in terms of the detuning is too cumbersome to be given here, but the values is straightforwardly obtained by diagonalization of the Hamiltonian in Eq. (7.1) and, as shown in Fig. 7.2(c), it is in excellent approximation given by χ_{01}^2. In the case of an anharmonic oscillator with no exciton-photon structure, the shift would be directly given by $2U$. There is thus no dependence of the measurement of ω_0^* on the population or other dynamical variables and it is therefore absolute, unlike the blueshift from a classical driving that requires knowledge of the effective laser intensity. This is not the only advantage that powers Mollow spectroscopy. A strong pumping of polaritons lead to several complications that hinder full or compelling information: Schmitt-Rink, Chemla, and Miller (1985) have shown the effects of heating and phase space filling, Houdré et al. (1995) reported on the loss of strong coupling, Ferrier et al. (2011) and Christmann et al. (2012) observed a contribution to the blueshift coming from the population of the exciton reservoir, and Kartashov, Konotop, and Torner (2012) discuss the effect of the exciton-photon fraction deviating from the Hopfield coefficients.

Since polariton interactions provide the foundation for nonlinear effects that constitute much of the polariton literature, the question of their nature and magnitude could be regarded as one of the most important open problems of the field (cf. the work of Rossbach et al. (2013), Cilibrizzi et al. (2014), Sun et al. (2017), and Walker et al. (2017)). In contrast, the excitation of the same system with the Mollow triplet is clean of all such complications of high densities. Since it recourses to the minimum amount of polaritons required to poke the interaction (two), Mollow spectroscopy acts as a "probe" in the ultimate sense of the term, with as little disturbance as possible. For Eq. (7.5) to hold, the Mollow triplet must be such that leapfrog processes are not mixed with other types of less correlated emission, leading to some departure from a shift ruled wholly by the two-polariton interaction. Figure 7.2(d) shows the splitting required for Eq. (7.5) to be accurate, namely, in the plateau when $\Omega \geq 3\gamma_a$ Even at low splitting, from power dependence, once can estimate the nonlinearity. For large Mollow splittings, against the Rabi splitting, there is a resonance in $g^{(2)}$ at $\Omega/\gamma_a = 3g/2$ when the lower leapfrog excites the lower polariton branch, while the upper Mollow satellite excites the upper polariton branch.

7.2.2 *Beyond the single-mode approximation of the polariton*

In the previous section, I have reduced the problem of exciting polariton with quantum light, to probing a single mode. While this describes a system on its own—a single anharmonic oscillator—in principle, polaritons are made of continuous rather than discrete fields, and the full Hamiltonian describing them features such fields:

$$H_{\mathrm{P}} = \int \hat{\psi}^\dagger(x) \left[-\frac{\hbar^2 \nabla^2}{2m} + U\hat{\psi}^\dagger(x)\hat{\psi}(x) \right] \hat{\psi}(x)\, dx\,, \tag{7.6}$$

where $\hat{\psi}(x)$ is an operator (I have kept here explicitly the $\hat{}$ symbol to highlight that), an is a function of the continuous variable x (assuming here a 1D case, where $x \in \mathbb{R}$, in 2D it would be a function of $\mathbf{r} \in \mathbb{R}^2$). For simplicity, here we also consider the polariton field directly, without

the underlying exciton-photon structure as is done in the main text. The corresponding master equation including polariton lifetime reads:

$$\partial_t \rho = i[\rho, H_{\mathrm{P}}] + \frac{\gamma}{2} \int \left(2\hat{\psi}(x)\rho\hat{\psi}^\dagger(x) - \hat{\psi}^\dagger(x)\hat{\psi}(x)\rho - \rho\hat{\psi}^\dagger(x)\hat{\psi}(x) \right) dx \,, \tag{7.7}$$

where $\gamma = (\gamma_a + \gamma_b)/2$ at the bottom of the polariton branch. A convenient procedure at this point is to turn to the reciprocal space, with the opportunity to introduce some details on the space structure. Namely, the link between real and reciprocal space is made through the Fourier transform, which yields a relation of the type:

$$\hat{\psi}(x) = \sum_k \hat{a}_k \phi_k(x) \,, \tag{7.8}$$

with $\hat{a}_k$ Bose operators satisfying $[\hat{a}_k^\dagger, \hat{a}_q] = \delta_{k,q}$ (and zero in all other cases). The function $\phi_k(x)$ translates the hypotheses one makes on the nature of space. For instance, if in free space, $\phi_k(x) = e^{ikx}/\sqrt{L}$, in terms of a "quantization" length L that can be made to go to infinity and turn the sum of reciprocal space into an integral. In this case, $\hbar k$ has the full meaning of a momentum. Substituting Eq. (7.8) into Eq. (7.6) yields the k-space Hamiltonian (from here onward we drop the $\hat{}$ notation):

$$H_{\mathrm{P}} = \sum_{k\in\mathbb{K}} \frac{\hbar^2 k^2}{2m} {a^\dagger}_k a_k + \frac{U}{L} \sum_{k_1,k_2,q\in\mathbb{K}} {a^\dagger}_{k_1+q} {a^\dagger}_{k_2-q} a_{k_1} a_{k_2} \,, \tag{7.9}$$

where the sum runs over $\mathbb{K} = \{\pm n\pi/L \,;\, n \in \mathbb{N}\}$ (in 1D; in 2D, the sum would be over $\mathbb{K}^2$). This is the Hamiltonian one should use to describe a continuous, weakly interacting polariton gas (neglecting other ingredients such as coupling to phonon fields). Physically, this is achieved by impinging the light from the two-level system at an angle on the microcavity. In this way, one can apply the principle of Mollow spectroscopy along the dispersion, similarly to classical spectroscopy.

An important point is that although the incoming light couples to one mode only, the mode itself is coupled through the interaction U to other modes. I will consider here the case where the quantum light impinges onto the ground state of the polariton dispersion, namely letting $c_2 = a_0$ in the master equation (1.28), for which the interaction part of the Hamiltonian (7.9) reduces to:

$$H_{q\in\mathbb{K}} = \frac{U}{L} \left(\sum_{q\in\mathbb{K}} a_q^\dagger a_{-q}^\dagger a_0 a_0 + \text{h.c.} + \sum_{q\in\mathbb{K}^*} a_q^\dagger a_q^\dagger a_q a_q + \sum_{q\in\mathbb{K}^*} a_q^\dagger a_q^\dagger a_q a_{-q} \right) , \tag{7.10}$$

since the exciting light is on the vacuum of the system and states that are not populated get decoupled from the dynamics (with $\mathbb{K}^* = \mathbb{K} - \{0\}$). Although the main coupling term $a_q^\dagger a_{-q}^\dagger a_0 a_0$ does not conserve energy (two particles from the ground state are scattered to two excited states), the term can still play a role in cases such as large occupancy of the modes (condensation), coherent driving, etc. Also, the smaller is the energy gap, the larger is the relevance of such terms, which is precisely our concern in the case of continuous fields, since some excited states lie arbitrarily near the ground state. This term remains complicated to treat exactly. In the previous section I have restricted the description to the case $\mathbb{K} = \{0\}$, and now I justify the validity of such an approximation and go beyond it by considering additional terms.

Figure 7.3 shows two cases of Eq. (7.9) as a function of the quantization length L. The energy difference between the ground state polariton at $k = 0$ and the first excited polariton state at $k = \pm\pi/L$ is $\Delta E = \pi^2\hbar^2/(2mL^2)$. For small enough L the discretization becomes meaningful, as spacing between successive states becomes larger that the other energy scales. Assuming that the first excited state dominates the dynamics of Eq. (7.10), one can describe the effect of the continuous-field nature of polaritons by solving for the case:

$$\begin{aligned} H_{\mathrm{P},\pm q} = {} & \omega_q \left(a_q^\dagger a_q + a_{-q}^\dagger a_{-q} \right) + \\ & + \frac{U}{L} \left(a_0^\dagger a_0^\dagger a_0 a_0 + a_q^\dagger a_{-q}^\dagger a_0 a_0 + a_0^\dagger a_0^\dagger a_q a_{-q} + a_q^\dagger a_q^\dagger a_q a_q + a_{-q}^\dagger a_{-q}^\dagger a_{-q} a_{-q} + a_q^\dagger a_{-q}^\dagger a_q a_{-q} \right) \end{aligned} \tag{7.11}$$

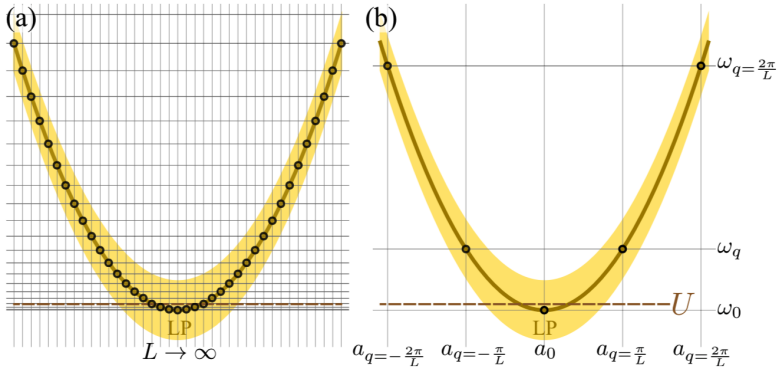

Figure 7.3: Quantization of the lower polariton (LP) branch in 1D reciprocal space, for two sizes L of "space". The shadowed area shows the radiative broadening of the line and a brown dashed line shows the interaction strength U. (a) quasi-continuum approximation with a plethora of modes, in particular in between the ground state and the interaction line. (b) for small quantization areas, the first excited state lies a sizable distance away allowing a few modes approximation. Further excited states can be neglected.

where q is now understood as π/L, and $\omega_q = \hbar^2\pi^2/(2mL^2)$ is the energy of the excited states, with the ground state ω_a setting the zero of energy. Although this looks a strong simplification, one must bear in mind that we are solving a full quantum system, including the dynamics of the source. The total Hilbert space to describe the quantum excitation by resonance fluorescence of Eq. (7.11) is $\mathcal{H}_\sigma \otimes \mathcal{H}_0 \otimes \mathcal{H}_q \otimes \mathcal{H}_{-q}$ (here we are considering the Hilbert space of the 2LS, the ground state of the polaritons and two excited states with momentum $\pm q$) which—for a truncation of the Bosonic spaces at five particles (which I have checked assures convergence)—has dimension $2 \times (2^6)^3 = 2^{19}$, i.e, of magnitude half-a-million. There are dedicated methods to efficiently address such problems numerically. Since I do not undertake a comprehensive analysis of this case at this stage but merely wish to explore the boundaries of its validity, I also studied (with more data points) a case with the further simplification:

$$H_{\mathrm{P},q} = \omega_q a_q^\dagger a_q + \frac{U}{L}\left(a_0^\dagger a_0^\dagger a_0 a_0 + a_q^\dagger a_q^\dagger a_0 a_0 + a_0^\dagger a_0^\dagger a_q a_q + a_q^\dagger a_q^\dagger a_q a_q\right), \tag{7.12}$$

which has dimension 2^{13} only, i.e., less than 10000, which can be readily computed on a desktop computer. Results of both cases, Eq. (7.11) and (7.12), are shown in Fig. 7.4. The horizontal green dashed line is the shift given by Eq. (7.5), i.e., assuming no perturbation from the excited states. The solid blue line corresponds to the more realistic case, Eq. (7.11) and is interpolating between 12 data points. The dashed red line corresponds to the reduced Hilbert space approximated version Eq. (7.12), and has enough data points that it can be assumed continuous from the numerical calculation. Interestingly, the crudest version yields stronger deviations from the single-mode approximation. In both cases, these results show that Mollow spectroscopy as presented in the previous section remains accurate within a 10% error margin, and becomes exact for energy splitting between the polariton ground state and its closest state is $\gtrsim 10\gamma_a$. The figure also implies that the approximation is good again when the first excited state lies close to the ground state. This is however not trustful since another excited state will then lie at the energy of the resonance and take the place of the first excited state. At this stage of the work, it remains an open question whether in such a case the dynamics will be given in good approximation by the same effective reduced Hamiltonian, with all other excited states (many between the ground and resonant excited state) playing a minor role as suggested by this figure. While this is an appealing and, on physical grounds, likely scenario, I cannot support that this is the case and a full investigation is called for. For the time being, I focus on the region $\omega_q - \omega_0 \gtrsim 10\gamma_a$. For the inverse lifetime of the polaritons of $\gamma_a = 0.1\,\mathrm{ps}^{-1}$ that we can assume for today's sample, i.e., $\gamma_a \approx 66\,\mu\mathrm{eV}$, the energy difference required to justify the single-mode approximation is thus $\Delta E \sim 0.6\,\mathrm{meV}$. For a typical GaAs cavity with a polariton

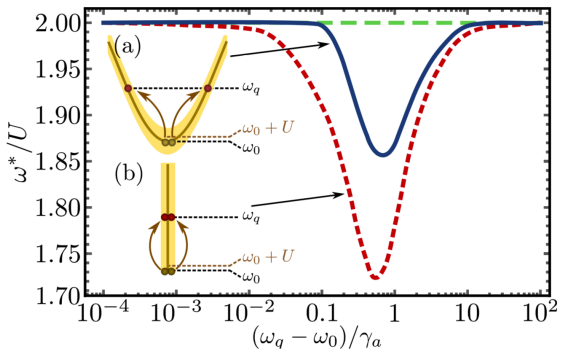

Figure 7.4: Shift of the photon statistics ω^* due to the first excited state in (a) two degenerate excited states, Eq. (7.11) and (b) only one excited state. The green dashed line corresponds to the single-mode approximation. At spacing ten times the radiative lifetime, the effect of excited states is negligible.

mass of the order of $m = 5 \times 10^{-5} m_e$ (m_e being the free electron mass), this means a quantization size of the order:

$$L = \sqrt{\frac{\pi^2 \hbar^2}{2m\Delta E}} \sim 3.5\,\mu\text{m}\,. \tag{7.13}$$

This size could be met experimentally by using laser spot of this dimension, assuming no drift or diffusion of the polaritons in the sample. The resulting spread in k-space of the laser spot is still small enough ($1/L$ as compared to π/L) to be neglected in the Hamiltonian. It could also be filtered out in energy with a mask, or one could consider the coupling of the quantum light to three modes, which would not change the algorithmic complexity of the problem. Clearly, however, this brings the discussion to another regime, with the dependence of the shift on the spot radius. If the laser spot size, that is achievable experimentally, would appear too compelling, one can also enforce quantization directly on the sample, by etching a portion out for characterization. This is the strategy of Verger, Ciuti, and Carusotto (2006) (considering various geometries) to reach the regime of polariton blockade. In this case, assuming an infinite square well potential of size L, one has $\phi_k(x) = \sqrt{2/L}\sin(k\pi x/L)$ for $k \in \mathbb{Z}$ and the same procedure now yields

$$H_{\text{E}} = \sum_{k\in\mathbb{Z}} \frac{\pi^2}{L^2}\frac{\hbar^2 k^2}{2m} a_k^\dagger a_k + \frac{3U}{2L}\sum_{k\in\mathbb{Z}} a_k^\dagger a_k^\dagger a_k a_k + \\ + \frac{U}{L}\sum_{q,k\in\mathbb{Z}} a_k^\dagger a_k^\dagger a_q a_q + \frac{U}{2L}\sum_{k_1,k_2,q\neq k_2} a_{k_1+q}^\dagger a_{k_2-q}^\dagger a_{k_1} a_{k_2}\,. \tag{7.14}$$

This Hamiltonian yields the same energy difference $\Delta E = \pi^2\hbar^2/(2mL^2)$ between the ground state at $k = 0$ and its closes neighbour (note that in this case the summation is over $\mathbb{Z}$, not $\mathbb{K}$), but enhances the values of the self-interaction of the polaritons by a factor of 1.5 and decreases the scattering term by a factor 2. In addition of justifying the approximation of a single-mode, this also makes it better, as the detrimental effect of scattering to the excited states is weaker.

As a conclusion, the trend of the impact of excited states is qualitatively clear: it produces a small departure (at most 10%) from the single-mode approximation that I have used in Section 7.2.1, which can be circumvented experimentally. More interestingly, however, such deviations should not be regarded as detrimental but as opening new directions of applying the technique. For instance, one can show that the dip in Fig. 7.4 is given precisely by the scattering process, in the sense that without self-interaction, the shift in the photon statistics of the pumped state is negative and accounts for the observed depletion in the numerical computation. Therefore, once the full theoretical analysis of this wider problem is made, one can hope to extend the method of Mollow spectroscopy to systems with closely excited states, and certainly also to continuous fields, where methods of quantum field theory are however called for to undertake such calculations. This is a topic for future works. For our purpose, it is enough to conclude from this analysis that the principle of Mollow spectroscopy as given in closed-form in the previous section can already be applied in the laboratory, to provide precise information on the polariton interaction not reachable by conventional methods, and that an

intense field of research lays open to tackle more complicated systems, not only regarding vacuum of more complex geometries, but also probing their excited states.

7.3 EXCITING WITH ENTANGLED PHOTONS

The spectroscopic technique that I introduced in Section 7.2.1 requires to fine-tune the emission of a 2LS with the absorption lines of the polariton systems. While in theory this is done in a straightforward way, doing it in the laboratory is a challenging task, which cannot be done with the state-of-the-art samples. However, there are other types of sources of Quantum Light that can be readily interfaced with today's polariton samples. In this section, I will discuss the case of excitation of polaritons with single photons, and address two questions of paramount relevance: can the polaritons display truly quantum behaviour? And are the interactions between polaritons strong enough to modify their quantum state?

7.3.1 *Experimental setup*

The source of individual photons is a periodically poled KTP (PPKTP) crystal[1] driven by a continuous wave laser of wavelength $\lambda = 405\,\text{nm}$. Following the setup of Fedrizzi et al. (2007), these photons impinge onto the PPKTP crystal, where they are downconverted to a pair of entangled photons, with a bandwidth sufficiently narrow so that they can be coupled to our microcavity (the description of which is given in Appendix C). The PPKTP crystal is introduced inside a Sagnac interferometer (see the sketch in Fig. 7.5) which allows to create polarization entangled photons in a state of the form

$$|\Psi\rangle = \frac{1}{\sqrt{2}}\left(|\text{HV}\rangle + e^{i\varphi}\,|\text{VH}\rangle\right)\,, \tag{7.15}$$

where $|\text{H}\rangle$ ($|\text{V}\rangle$) stands for a horizontally (vertically) polarized photon. The relative phase between the two superposed states φ can be manipulated, by placing a liquid crystal in one of the arms of the interferometer, to generate Bells states

$$\left|\Psi^{\pm}\right\rangle = \frac{1}{\sqrt{2}}\left(|\text{HV}\rangle \pm |\text{VH}\rangle\right)\,. \tag{7.16}$$

At the end of the interferometer, we have a pair of non-degenerate entangled photons travelling in different directions and with different wavelengths: one—to which I will refer to as the *idler*—matching the polariton resonance ($\lambda \approx 830\,\text{nm}$) and the other—*the signal*—with the wavelength required to conserve energy ($\lambda \approx 790\,\text{nm}$). The idler photon is directed towards the microcavity, where it excites a single polariton which is stored in the cavity until its spontaneous decay. Then, the photon is retrieved and sent to a tomography stage, where it meets the signal photon (which comes there straight from the interferometer).

The tomography stage is sketched in Fig. 7.5. It consists of a quarter waveplate (QWP) followed by a half waveplate (HWP), a polarizing beamsplitter (PBS) and a single-photon detector (APD). The coincidence counts from the two single-photon detectors are measured in a 4 ns window with a home-made coincidence unit. By making such measurements for all the combinations of polarizations on each detector (that makes 6×6 possibilities for the three polarization bases: circular, vertical and diagonal), we are able to determine whether the idler—which transformed into a polariton and was later re-emitted as a photon—retained the nonlocal quantum correlations of a Bell state, as suggested by James et al. (2001). If this were the case, it would mean that the polariton state that inherited and later transmitted this information was itself in a genuine one-particle quantum state, which was furthermore entangled with the

1 Potassium titanyl phosphate, or simply KTP, is a compound with chemical formula $KTiOPO_4$, and it is a white solid with nonlinear optical properties.

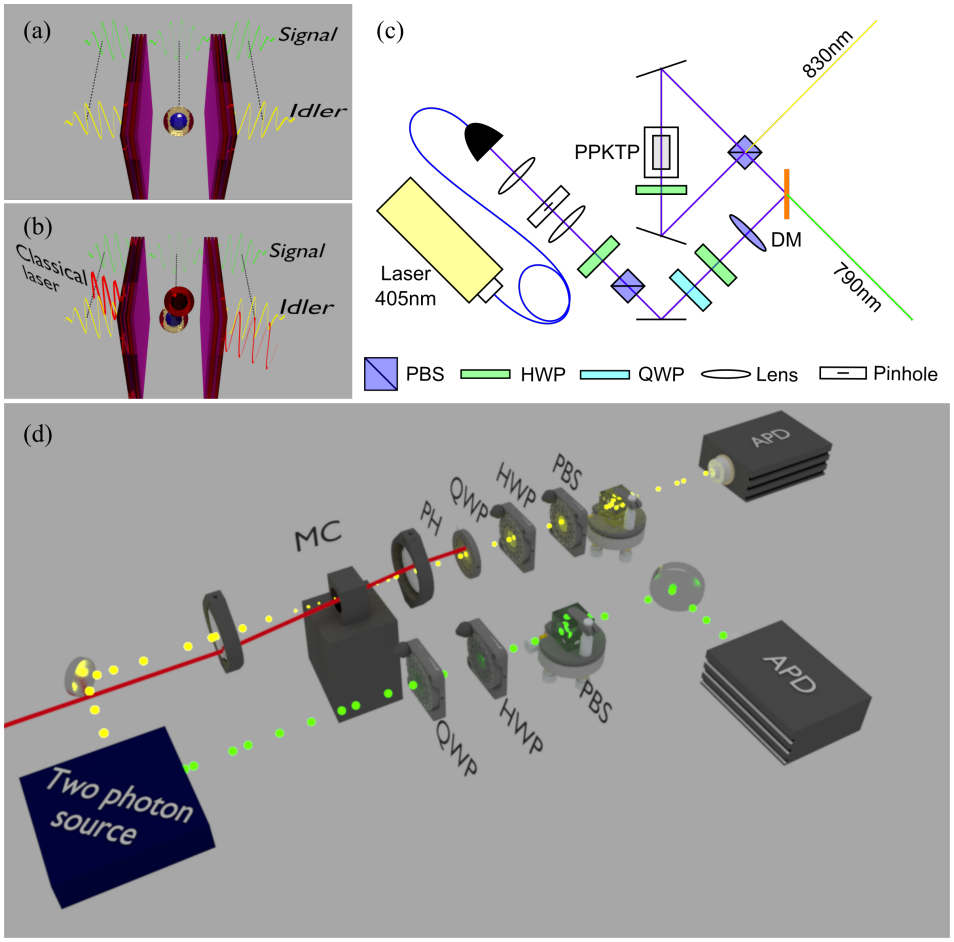

Figure 7.5: Sketch of the behaviour inside the microcavity: (a) Linear regime: a single photon (yellow, idler) gets into the microcavity where it becomes a polariton, that is later reconverted into an external photon. When this photon is entangled with another one (green, signal), we show that the entanglement is preserved throughout. (b) Interacting regime: a single photon (yellow, idler) enters the microcavity along with photons from a classical laser (red). The polaritons in the microcavity interact. This affects the entanglement of the single-polariton in a way that allows to measure the polariton-polariton interaction. (c) Sketch of the Sagnac interferometric source. (d) Sketch of the setup implementing these configurations.

signal photon propagating on the other side of the setup. Namely, it would prove that we have created the state

$$|\Psi^{\pm}\rangle = \frac{1}{\sqrt{2}}\left(a_{\mathrm{H}}^{\dagger}p_{\mathrm{V}}^{\dagger} \pm a_{\mathrm{V}}^{\dagger}p_{\mathrm{H}}^{\dagger}\right)|0\rangle\ , \tag{7.17}$$

where p_{H} and p_{V} are the boson annihilation operators for the horizontally and vertically polarized polaritons and a_{H} and a_{V} for the signal photon, respectively. While this could be well expected from a standard linear theory of light propagating through resonant dielectrics, the failures of polaritons to demonstrate other expected quantum correlations, such as in the OPO (optical parametric oscillator) scattering, show that it is not obvious whether polaritons are proper carriers of quantum features. In particular, their composite nature and large exciton component could lead to fast decoherence (e.g., via phonon scattering). The spectral shape of the idler state is shown in Fig. 7.6(a). Using single mode laser excitation of the PPKTP crystal, the bandwidth of the entangled photon pairs is reduced to 0.46 nm, which is only 35% wider than the polariton state. Varying the temperature of the PPKTP crystal one can modify the wavelengths of the downconverted photons from 825 nm to 831 nm. In order to check that the entangled idler is indeed transferred into the polariton state and not merely

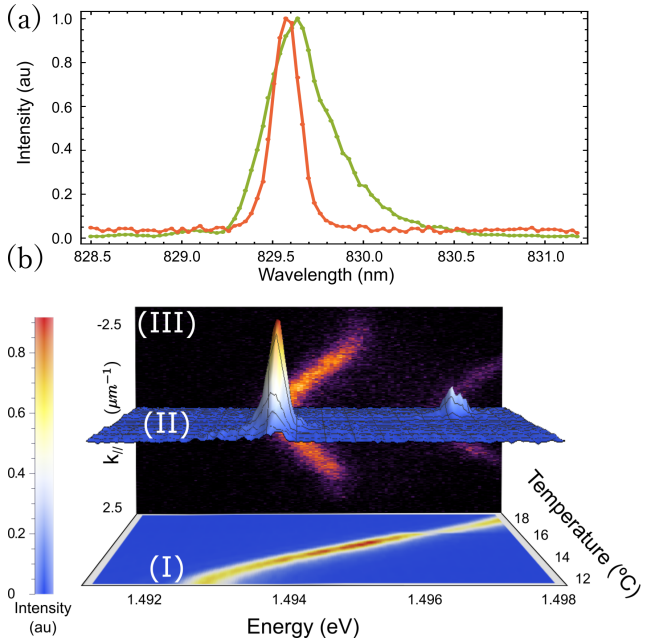

Figure 7.6: (a) Green: normalized emission of the PPKTP crystal. Orange: normalized transmission of the emission of the PPKTP crystal through the LPB. (b) Changes on the resonance as a function of the temperature of the two-photon source. I: 2D map of the emission of the crystal outside of the microcavity. II: transmitted intensity as a function of the energy as the temperature varies. Two peaks can be identified that correspond to the resonances with one of the two polariton branches. The color-bar corresponds to both I & II. III: far field of the emission under non-coherent pumping.

passing through the cavity mode—as they would while propagating through a slab of glass—we performed transmission measurements while scanning the energy of the idler from below the lower polariton branch (LPB) to above the upper polariton branch (UPB). In Fig. 7.6(b), the effect of the microcavity on the idler state shows that no light is transmitted when the idler is out-of-resonance with the polaritons. This means that every photon that passes through the sample has been converted into a polariton. If this were not be the case, we would have observed a finite signal at the energy of the cavity (which lies between the LPB and the UPB), but it is completely absent even in logarithmic scale (not shown).

7.3.2 *Entanglement and nonlocality*

The tomography procedure outlined in the previous section, yields the state of the pair of photons, even after one of them has been absorbed and later re-emitted by the microcavity. The 36 measurements in all the possible combinations of polarization allows us to reconstruct the density matrix describing the state of the two photons. It then reads

$$\rho \equiv \frac{1}{\mathcal{K}} \begin{pmatrix} \mathrm{HHHH} & \mathrm{HHVH} & \mathrm{HHHV} & \mathrm{HHVV} \\ h.c. & \mathrm{HVVH} & \mathrm{HVHV} & \mathrm{HVVV} \\ h.c. & h.c. & \mathrm{VHHV} & \mathrm{VHVV} \\ h.c. & h.c. & h.c. & \mathrm{VVVV} \end{pmatrix}, \tag{7.18}$$

where $\mathcal{K}$ is a constant so that $\mathrm{Tr}(\rho) = 1$ and, e.g., VHHV stands for:

$$\langle \psi | \, c_{\mathrm{V}}^{\dagger} q_{\mathrm{H}}^{\dagger} q_{\mathrm{H}} c_{\mathrm{V}} \, | \psi \rangle \, , \tag{7.19}$$

where $|\psi\rangle$ are the states seen by the pair of photons when one of them reaches the cavity. From the density matrix in Eq. (7.18) we can quantify the degree of entanglement between the two photons through the "*concurrence*", a measure of entanglement proposed by Hill and Wootters (1997), which is defined as

$$C[\rho] \equiv \max(0, \lambda_1 - \lambda_2 - \lambda_3 - \lambda_4) \tag{7.20}$$

where the λ_i are the eigenvalues in decreasing order of the matrix $\sqrt{\sqrt{\rho}\tilde{\rho}\sqrt{\rho}}$, where we have defined

$$\tilde{\rho} \equiv (\sigma_y \otimes \sigma_y) \rho^T (\sigma_y \otimes \sigma_y) \, , \tag{7.21}$$

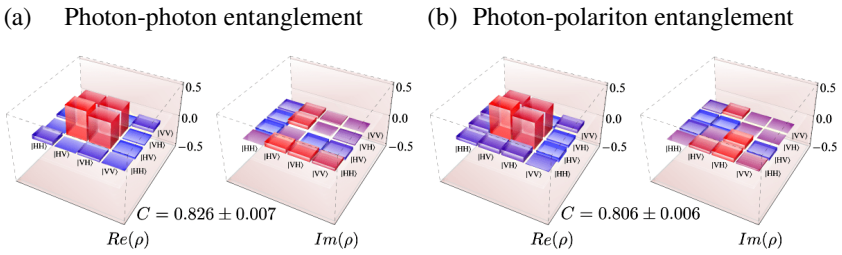

Figure 7.7: Tomography measured between the signal and idler photons. The signal is sent directly towards the detector while the idler photon becomes a polariton when entering the sample. (a) Real (left) and imaginary (right) components of the density matrix for the source of photon-pairs without the sample. The concurrence is not one because the operation wavelength is not optimal for the source. (b) Real (left) and imaginary (right) components of the density matrix when passing through the microcavity. The concurrence of 0.806 shows that polaritons retain the entanglement.

and σ_y is a Pauli spin matrix. The concurrence is a monotonous quantity ranging from zero for classically correlated or uncorrelated states and approaching one as the quantum entanglement increases.

To study the transfer of the entanglement into the polariton field, I compare the entanglement of the pair of photons in two configurations:

- when the photons are measured immediately after being emitted, thus guaranteeing to be as entangled as they get, and
- when one of the two photons passes through the cavity, becomes a polariton, and is later re-emitted as a photon.

Figure 7.7 shows the density matrices and the computed concurrence for the two cases. Panel (a) shows the photon-photon entanglement, which is topped at 0.826 (it is not exactly one because the entangled state is not optimized at the operation at the wavelength to interface with the cavity). Panel (b) shows that, although one of the photons has gone through the cavity, the quantum entanglement has only reduced marginally to 0.806. This result is a direct proof that was generated experimentally a single polariton within the microcavity and that it existed there as a quantum state with no classical counterpart. If the single photon had been lost in the polariton thermal noise or coupled to a collection of other polariton states, no entanglement would have been observed. This transfer of the photon to and from a polariton state has shown to conserve almost entirely the original degree of entanglement. This is an encouraging result for a future exploitation of quantum polaritonics.

Beyond the preservation of concurrence, we also demonstrated the nonlocality between the signal photon and the polariton created by the idler photon. We did so by probing the classical Clauser et al. (1969)—also known as the CHSH—inequality $S \leq 2$ where:

$$S = |E(a,b) - E(a,b') + E(a',b) + E(a',b')|\,, \tag{7.22}$$

and

$$E(x,y) = \frac{C_{++}(x,y) + C_{--}(x,y) - C_{+-}(x,y) - C_{-+}(x,y)}{C_{++}(x,y) + C_{--}(x,y) + C_{+-}(x,y) + C_{-+}(x,y)}\,, \tag{7.23}$$

is a function of the coincident counts $C_{pq}(x,y)$ between the two measurement ports of our tomography setup, for the photons with polarization $p,q \in \{-,+\}$ in the bases $x = a, a'$ and $y = b, b'$ where $a = -\pi/8$, $a' = \pi/8$, $b = 0$ and $b' = \pi/4$ are the combinations of polarization angles that maximize the Bell's inequality violation. This can be obtained by rotating the tomography HWPs in $a/2$, $a'/2$, $b/2$ and $b'/2$. Figure 7.8 displays the measured Bell curves, which show the photon coincidences associated to these bipartite polarization measurements, along with the continuous correlated oscillations predicted by the theory. In the optimum

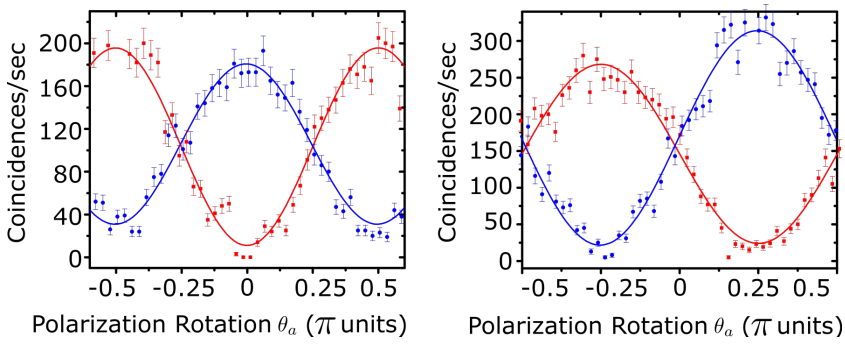

Figure 7.8: Coincidences as a function of the polarization between the external photons and the polaritons. Left: Bell curves for a polarization angle $b = 0$. Right: Bell curves for $b = -\pi/4$. Red squares and blue circles denote the ++ and +− coincidences, respectively.

configuration, we obtain a value of $S = (2.463 \pm 0.007)$ which unambiguously violates the CHSH inequality and proves the nonlocal character of the photon-polariton system.

The experimental results shown above demonstrate clearly that, although polaritons are quasi-particles in a solid-state system with complex and yet-to-be-fully-characterized interactions with their matrix and other polaritons, as reviewed by Deveaud (2016), they can be used as quantum bits maintaining almost unvaried their quantum state and can transfer it back and forth to an external photon. In particular, this shows that several effects, such as pure dephasing, coupling to phonons, radiative lifetime, etc., are not detrimental to quantum coherence.

7.3.3 *Nonlinearity at the single polariton level*

Now that I have demonstrated that one can inject quantum states in a polariton system, and that polaritons are able to maintain and transfer quantum information, I will address the question of whether the quantum state of polaritons can be affected and ultimately controlled. Thus, we need to go into the nonlinear regime and study the effect of polariton interactions. To observe such nonlinearities within our available equipment, we repeated the experiment with the cavity in a non polariton-vacuum configuration: instead of exciting the sample only with a single photon coming from the PPKTP crystal, we add the excitation from a classical laser, which is the most common way to drive a microcavity (cf. Fig. 7.5). The driving from the laser induces a macroscopic (and classical) state of the polaritons inside the microcavity, which we want to use to modify the state of the entangled photon. Since the polaritons from the classical state and the single polariton need to be distinguishable, they are put in the cavity with different wavevectors (which in practice means that they are shone onto the sample at different angles). Moreover, to avoid the effects of relaxation from the classical state to lower energy states, we sent the laser in resonance to the lower polariton branch, while the entangled photons is sent in resonance to the upper polariton branch. Note, however, that polariton-phonon interaction and Auger processes, although minimized at low temperature and low power of excitation, cannot be completely avoided.

The Hamiltonian governing the dynamics of the polaritons within the microcavity has been written by Kavokin et al. (2017), where the description is made directly from the photonic and excitonic modes present in the sample. This Hamiltonian reads

$$H = H_0 + H_{\text{shift}} + H_{\text{scat}}\,, \tag{7.24}$$

where the components are defined as

$$H_0 = \sum_{\mathbf{k},\sigma=\uparrow,\downarrow} \omega_{a,\mathbf{k}}\, a^\dagger_{\sigma,\mathbf{k}} a_{\sigma,\mathbf{k}} + \omega_{b,\mathbf{k}}\, b^\dagger_{\sigma,\mathbf{k}} b_{\sigma,\mathbf{k}} + g_{\mathbf{k}}(a^\dagger_{\sigma,\mathbf{k}} b_{\sigma,\mathbf{k}} + b^\dagger_{\sigma,\mathbf{k}} a_{\sigma,\mathbf{k}})\,, \tag{7.25a}$$

$$H_{\text{shift}} = \sum_{\mathbf{k},\sigma=\uparrow,\downarrow} V^{(1)}_{\mathbf{k},\mathbf{k},0}\, b^\dagger_{\sigma,\mathbf{k}} b^\dagger_{\sigma,\mathbf{k}} b_{\sigma,\mathbf{k}} b_{\sigma,\mathbf{k}} + V^{(2)}_{\mathbf{k},\mathbf{k},0}\, b^\dagger_{\sigma,\mathbf{k}} b^\dagger_{\sigma,\mathbf{k}} b_{-\sigma,\mathbf{k}} b_{-\sigma,\mathbf{k}}\,, \tag{7.25b}$$

$$\begin{aligned} H_{\text{scat}} = {} & \sum_{\substack{\mathbf{k},\mathbf{k}'\neq\mathbf{k}\\ \sigma=\uparrow,\downarrow}} V^{(1)}_{\mathbf{k},\mathbf{k}',0}\, b^\dagger_{\sigma,\mathbf{k}} b^\dagger_{\sigma,\mathbf{k}'} b_{\sigma,\mathbf{k}} b_{\sigma,\mathbf{k}'} + V^{(2)}_{\mathbf{k},\mathbf{k}',0}\, b^\dagger_{\sigma,\mathbf{k}} b^\dagger_{-\sigma,\mathbf{k}'} b_{\sigma,\mathbf{k}} b_{-\sigma,\mathbf{k}'} + \\ & + \frac{1}{4} \sum_{\substack{\mathbf{k},\mathbf{k}'\neq\mathbf{k}\\ \sigma=\uparrow,\downarrow}} \exp(i\Delta_{\mathbf{k},\mathbf{k}',\delta\mathbf{k}} t)\big(V^{(1)}_{\mathbf{k},\mathbf{k}',\delta\mathbf{k}}\, b^\dagger_{\sigma,\mathbf{k}+\delta\mathbf{k}} b^\dagger_{\sigma,\mathbf{k}'-\delta\mathbf{k}} b_{\sigma,\mathbf{k}} b_{\sigma,\mathbf{k}'} + \\ & \qquad + 2V^{(2)}_{\mathbf{k},\mathbf{k}',\delta\mathbf{k}}\, b^\dagger_{\sigma,\mathbf{k}+\delta\mathbf{k}} b^\dagger_{-\sigma,\mathbf{k}'-\delta\mathbf{k}} b_{\sigma,\mathbf{k}} b_{-\sigma,\mathbf{k}'} + \text{h.c.}\big)\,, \end{aligned} \tag{7.25c}$$

where $a_{\sigma,\mathbf{k}}$ ($b_{\sigma,\mathbf{k}}$) is the annihilation operator of the photon (exciton) with polarization σ, momentum $\mathbf{k}$, energy $\omega_{a,\mathbf{k}}$ ($\omega_{b,\mathbf{k}}$) and $\Delta_{\mathbf{k},\mathbf{k}',\delta\mathbf{k}} = (E(\mathbf{k}) + E(\mathbf{k}') - E(\mathbf{k}+\delta\mathbf{k}) - E(\mathbf{k}'-\delta\mathbf{k}))/\hbar$.
Here H_0 describes the linear coupling between photons and excitons, which occurs when the two particles have the same polarization and the same momentum. H_{shift} describes the interactions between excitons with the same momentum but possibly different polarizations, and H_{scat} describes the scattering between excitons with different momenta. The matrix elements $V^{(1)}_{\mathbf{k},\mathbf{k}',\delta\mathbf{k}}$ and $V^{(2)}_{\mathbf{k},\mathbf{k}',\delta\mathbf{k}}$ describe the scattering of two polaritons in the triplet and the singlet configurations, respectively. The experimental evidence allows us to reduce the number of terms that play a role in the dynamics of an ideal system, namely

(a) The lower polariton branch is completely empty, except at the wavevector $\mathbf{k} = \mathbf{k_0}$ where the laser creates a polariton condensate. Here we assume that the condensate is in a coherent state which allows us to do a mean field approximation replacing the operators of the lower polariton branch for complex numbers.

(b) The upper polariton branch is empty, except for the single photon that enters at $\mathbf{k} = \mathbf{0}$. This means that the nonlinear terms of the Hamiltonian for the upper polariton branch always evaluate to zero.

The latter condition implies that Eq. (7.25b) does not contribute to the dynamics, and that Eq. (7.25c) reduces to

$$\begin{aligned} H_{\text{scat}} = {} & 3V^{(1)}(b^\dagger_{\uparrow,\mathbf{0}} b_{\uparrow,\mathbf{0}} b^\dagger_{\uparrow,\mathbf{k_0}} b_{\uparrow,\mathbf{k_0}} + b^\dagger_{\downarrow,\mathbf{0}} b_{\downarrow,\mathbf{0}} b^\dagger_{\downarrow,\mathbf{k_0}} b_{\downarrow,\mathbf{k_0}}) + 2V^{(2)} b^\dagger_{\downarrow,\mathbf{0}} b_{\downarrow,\mathbf{0}} b^\dagger_{\uparrow,\mathbf{k_0}} b_{\uparrow,\mathbf{k_0}} + \\ & + 2V^{(2)} b^\dagger_{\uparrow,\mathbf{0}} b_{\uparrow,\mathbf{0}} b^\dagger_{\downarrow,\mathbf{k_0}} b_{\downarrow,\mathbf{k_0}} + V^{(2)}(b^\dagger_{\uparrow,\mathbf{0}} b_{\downarrow,\mathbf{0}} + b^\dagger_{\downarrow,\mathbf{0}} b_{\uparrow,\mathbf{0}})(b^\dagger_{\uparrow,\mathbf{k_0}} b_{\downarrow,\mathbf{k_0}} + b^\dagger_{\downarrow,\mathbf{k_0}} b_{\uparrow,\mathbf{k_0}})\,, \end{aligned} \tag{7.26}$$

where I have assumed that the interaction energies do not depend on the wavevectors. The lower and upper polaritons are related to the photon and exciton through the transformation,

$$a_{\sigma,\mathbf{k}} = \cos\theta_{\mathbf{k}}\, q_{\sigma,\mathbf{k}} + \sin\theta_{\mathbf{k}}\, p_{\sigma,\mathbf{k}} \qquad \text{and} \qquad b_{\sigma,\mathbf{k}} = \sin\theta_{\mathbf{k}}\, q_{\sigma,\mathbf{k}} - \cos\theta_{\mathbf{k}}\, p_{\sigma,\mathbf{k}}\,, \tag{7.27}$$

where $p_{\sigma,\mathbf{k}}$ and $q_{\sigma,\mathbf{k}}$ are the annihilation operators of the lower and upper polaritons, respectively; and σ is the polarization of the particles. Since the dispersion relation of the photon and of the exciton do not have the same curvature (cf. Fig 1.17), their contribution to the lower and upper polariton is different at each $\mathbf{k}$. This variation is taken into account through the Hopfield coefficient,

$$\sin\theta_{\mathbf{k}} = \sqrt{\frac{\xi^2_{\mathbf{k}}}{1+\xi^2_{\mathbf{k}}}} \qquad \text{with} \qquad \xi_{\mathbf{k}} = \frac{(\omega_{b,\mathbf{k}} - \omega_{a,\mathbf{k}}) + \sqrt{4g^2_{\mathbf{k}} + (\omega_{b,\mathbf{k}} - \omega_{a,\mathbf{k}})^2}}{2g_{\mathbf{k}}}\,. \tag{7.28}$$

In the lower and upper polariton basis, the Hamiltonian in Eq. (7.25a) becomes

$$H_0 = \sum_{\mathbf{k},\sigma=\uparrow,\downarrow} q^\dagger_{\sigma,\mathbf{k}} q_{\sigma,\mathbf{k}} \left(\omega_{b,\mathbf{k}} \sin^2\theta_\mathbf{k} + \omega_{a,\mathbf{k}} \cos^2\theta_\mathbf{k} + g_\mathbf{k} \cos\theta_\mathbf{k} \sin\theta_\mathbf{k}\right) + \\ + p^\dagger_{\sigma,\mathbf{k}} p_{\sigma,\mathbf{k}} \left(\omega_{b,\mathbf{k}} \cos^2\theta_\mathbf{k} + \omega_{a,\mathbf{k}} \sin^2\theta_\mathbf{k} - g_\mathbf{k} \cos\theta_\mathbf{k} \sin\theta_\mathbf{k}\right) , \quad (7.29)$$

whereas Eq. (7.26) becomes,

$$H_{\text{scat}} = 3V^{(1)}(q^\dagger_{\uparrow,\mathbf{0}} q_{\uparrow,\mathbf{0}} p^\dagger_{\uparrow,\mathbf{k_0}} p_{\uparrow,\mathbf{k_0}} + q^\dagger_{\downarrow,\mathbf{0}} q_{\downarrow,\mathbf{0}} p^\dagger_{\downarrow,\mathbf{k_0}} p_{\downarrow,\mathbf{k_0}}) \cos^2\theta_{\mathbf{k_0}} \sin^2\theta_\mathbf{0} + \\ + 2V^{(2)}(q^\dagger_{\downarrow,\mathbf{0}} q_{\downarrow,\mathbf{0}} p^\dagger_{\uparrow,\mathbf{k_0}} p_{\uparrow,\mathbf{k_0}} + q^\dagger_{\uparrow,\mathbf{0}} q_{\uparrow,\mathbf{0}} p^\dagger_{\downarrow,\mathbf{k_0}} p_{\downarrow,\mathbf{k_0}}) \cos^2\theta_{\mathbf{k_0}} \sin^2\theta_\mathbf{0} + \\ + V^{(2)}(q^\dagger_{\uparrow,\mathbf{0}} q_{\downarrow,\mathbf{0}} + q^\dagger_{\downarrow,\mathbf{0}} q_{\uparrow,\mathbf{0}})(p^\dagger_{\uparrow,\mathbf{k_0}} p_{\downarrow,\mathbf{k_0}} + p^\dagger_{\downarrow,\mathbf{k_0}} p_{\uparrow,\mathbf{k_0}}) \cos^2\theta_{\mathbf{k_0}} \sin^2\theta_\mathbf{0} , \quad (7.30)$$

where I have taken into account that at $\mathbf{k} = \mathbf{k_0}$, only the lower polariton branch is populated, whereas at $\mathbf{k} = \mathbf{0}$ only the upper polariton branch is populated. Resorting again to the fact that the condensate in the lower polariton branch is in a coherent state, the operators for the lower polariton at any given wavevectors can be replaced by the square root of the population at such wavevector, namely $p_{\sigma,\mathbf{k}} = \sqrt{n_\sigma}\delta_{\mathbf{k},\mathbf{k_0}}$, where n_σ is the mean number of particles with polarization σ in the lower polariton branch at $\mathbf{k} = \mathbf{k_0}$, and δ is the Kronecker delta. At last, we include a spin-orbit coupling term that enters into the Hamiltonian as an effective magnetic field that couples polaritons with the same momenta but opposite spins as introduced by Kavokin et al. (2017):

$$H_{\text{so}} = g_{\text{so}}(q^\dagger_{\uparrow,\mathbf{0}} q_{\downarrow,\mathbf{0}} + q^\dagger_{\downarrow,\mathbf{0}} q_{\uparrow,\mathbf{0}}) . \quad (7.31)$$

The magnitude of the coupling is given by the imbalance of polaritons with spin +1 and those with spin −1, and the polariton interaction strength, namely $g_{\text{so}} = 2\big(V^{(1)} - V^{(2)}\big)(n_\uparrow - n_\downarrow) \cos^2\theta_{\mathbf{k_0}} \sin^2\theta_\mathbf{0}$. After applying the mean field approximation, the resulting Hamiltonian has a simple form,

$$H = \omega_\uparrow q^\dagger_\uparrow q_\uparrow + \omega_\downarrow q^\dagger_\downarrow q_\downarrow + g_{\uparrow\downarrow}(q^\dagger_\uparrow q_\downarrow + q^\dagger_\downarrow q_\uparrow) , \quad (7.32)$$

with

$$\omega_\uparrow = \cos^2\theta_{\mathbf{k_0}} \sin^2\theta_\mathbf{0}\big(3n_\uparrow V^{(1)} + 2n_\downarrow V^{(2)}\big) + \omega_0 , \quad (7.33a)$$

$$\omega_\downarrow = \cos^2\theta_{\mathbf{k_0}} \sin^2\theta_\mathbf{0}\big(3n_\downarrow V^{(1)} + 2n_\uparrow V^{(2)}\big) + \omega_0 , \quad (7.33b)$$

$$g_{\uparrow\downarrow} = \big[2\sqrt{n_\uparrow n_\downarrow} V^{(2)} + 2\big(V^{(1)} - V^{(2)}\big)(n_\uparrow - n_\downarrow)\big] \cos^2\theta_{\mathbf{k_0}} \sin^2\theta_\mathbf{0} , \quad (7.33c)$$

$$\omega_0 = \sin^2\theta_\mathbf{0}\omega_{b,\mathbf{0}} + \cos^2\theta_\mathbf{0}\omega_{a,\mathbf{0}} + g_\mathbf{0} \cos\theta_\mathbf{0} \sin\theta_\mathbf{0} . \quad (7.33d)$$

In the sample used for the experiment, the photon-exciton detuning was 2.3 meV at $\mathbf{k} = \mathbf{0}$, zero at $\mathbf{k} = \mathbf{k_0}$ and the Rabi coupling (half Rabi splitting) was 1.6 meV at $\mathbf{k} = \mathbf{0}$. Therefore the Hopfield coefficients are

$$\cos^2\theta_{\mathbf{k_0}} = \frac{1}{2} \qquad \text{and} \qquad \cos^2\theta_\mathbf{0} \approx 0.21 . \quad (7.34)$$

The classical pumping power is changed from having only the vacuum state up to an average estimated at 380 polaritons at any given time, with a density still below 1 polariton/μm². The calibration of the population is explained in Appendix C.

The nonlinear crystal emits pairs of photons entangled in their polarization degree of freedom, that can be described through the wavefunction

$$|\psi_0\rangle = \frac{1}{\sqrt{2}}\big(\,|\mathrm{H},\mathrm{V}\rangle + |\mathrm{V},\mathrm{H}\rangle\,\big) \equiv \frac{1}{\sqrt{2}}\big(c^\dagger_\mathrm{H} q^\dagger_\mathrm{V} + c^\dagger_\mathrm{V} q^\dagger_\mathrm{H}\big)\,|0\rangle , \quad (7.35)$$

where $c^\dagger_\phi$ is the creation operator of the single photon with polarization ϕ that goes directly to the detector, whereas $q^\dagger_\phi$ is the creation operator of the photon with polarization ϕ that impinges

onto the upper polariton branch at $\mathbf{k} = \mathbf{0}$. The latter, when inside the cavity, evolves according to the Schrödinger equation with the Hamiltonian in Eq. (7.32) for the duration t of the mean polariton lifetime, producing as the output wavefunction

$$|\psi(t)\rangle = e^{-iHt}\,|\psi_0\rangle\ . \tag{7.36}$$

Note, however, that the parameters of the Hamiltonian depend on the mean number of particles in the lower polariton branch, cf. Eq. (7.33). Such a population is build by a laser. The Poissonian fluctuations in the intensity of the laser induces a fluctuation in the number of particles in the condensate. Using the Quantum Monte Carlo method introduced by Mølmer, Castin, and Dalibard (1993), I was able to go beyond a mean-field description and take into account these fluctuations by sampling randomly the state of the condensate when the upper single-polariton is created. Figure 7.9 shows the number of particles as a function of time, with the "jumps" due to the pouring and leakage of photons in and out of the microcavity, respectively. The Poissonian distribution corresponding to each mean number of particles is shown on the right with colors matching the trajectories. Before one of the entangled photons is sent to the cavity, the state of the lower and upper polariton branches can be written as

$$|\psi_0\rangle = \left|n_\uparrow, n_\downarrow\right\rangle \otimes \frac{i}{\sqrt{2}}(|\uparrow,\uparrow\rangle - |\downarrow,\downarrow\rangle)\,, \tag{7.37}$$

where $n_\uparrow$ ($n_\downarrow$) is the macroscopic population of the lower branch with spin $\sigma =\uparrow$ ($\downarrow$) and $(|\uparrow,\uparrow\rangle - |\downarrow,\downarrow\rangle)/\sqrt{2}$ is the state in Eq. (7.35) written in the basis of circular polarization. The state after one of the single photons has passed through the cavity is obtained simply by propagating the initial state with the Hamiltonian in Eq. (7.32), from which I obtain

$$|\psi(t)\rangle = e^{-iHt/\hbar}\,|\psi_0\rangle = \left|n_\uparrow, n_\downarrow\right\rangle \otimes \left[c_{\uparrow,\uparrow}(t)\,|\uparrow,\uparrow\rangle + c_{\downarrow,\downarrow}(t)\,|\downarrow,\downarrow\rangle + c_{\uparrow,\downarrow}\big(\,|\uparrow,\downarrow\rangle - |\downarrow,\uparrow\rangle\,\big)\right]. \tag{7.38}$$

where the coefficients are related to the detuning and the coupling strength through the following relations,

$$c_{\uparrow,\uparrow}(t) = \frac{1}{\sqrt{2}R}\left[\Delta \sin\left(\frac{Rt}{2}\right) + iR\cos\left(\frac{Rt}{2}\right)\right], \quad c_{\downarrow,\downarrow}(t) = c^*_{\uparrow,\uparrow}(t)\,, \quad \text{and} \quad c_{\uparrow,\downarrow}(t) = \sqrt{2}\frac{g_{\uparrow,\downarrow}}{R}\sin\left(\frac{Rt}{2}\right), \tag{7.39}$$

where I have used the shorthand notation $\Delta = \omega_\uparrow - \omega_\downarrow$ and $R = \sqrt{4g^2_{\uparrow,\downarrow} + \Delta^2}$. The final state of the system is obtained by averaging over many realizations. Because of the fluctuations

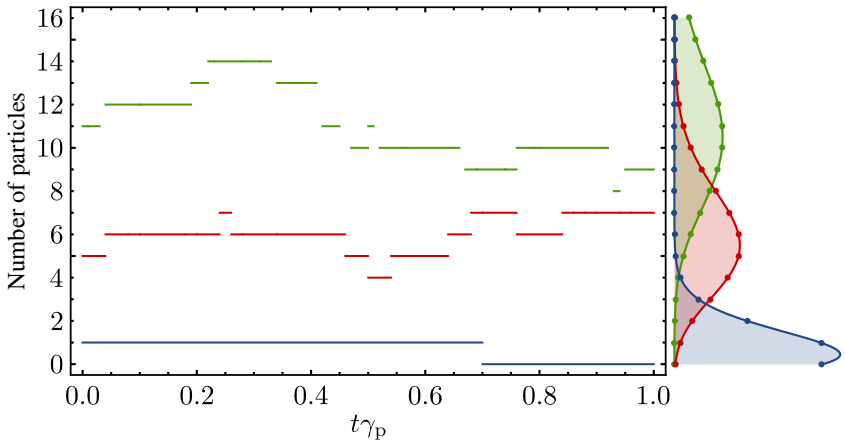

Figure 7.9: Fluctuations of the condensate in the lower polariton branch in a time equivalent to one tenth of the polariton lifetime γ_p. The speed and amplitude of the fluctuations increases with the mean number of particles in the condensate.

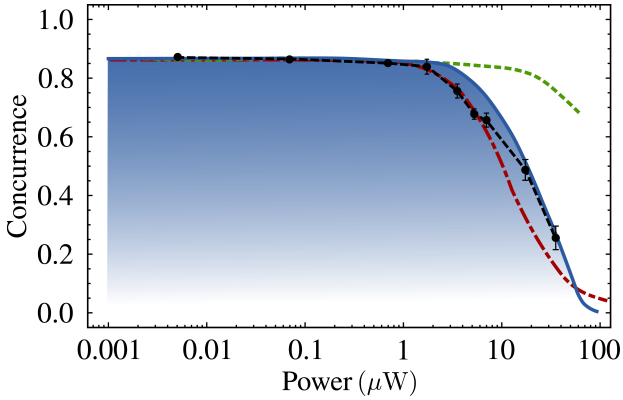

Figure 7.10: Concurrence between the external photons and the polaritons as a function of the power of the classical laser impinging onto the sample. Each data point (black bullet) is obtained from the 36 measurements of coincidences in all the combinations of polarization (the dotted line serves as a guide). The solid blue line is a theoretical simulation for a model of fluctuating polarized lower polaritons that interact with the single upper polariton injected by the quantum source with an interaction strength of 0.9% of the radiative broadening, and which is in excellent quantitative agreement with the observation. The red, dashed-dotted line shows the theoretical simulation for a model of a condensate assuming thermal fluctuations, which gives a worst fit of the experimental observation and suggests that, as expected, the condensate has Poissonian fluctuations. The green, dashed line shows the loss of concurrence without polariton interactions, i.e., due only to the polaritons scattered to the state to which the single photon arrives, confirming that the amount of noise in the experiment is small enough to observe the effects of interactions on a single polariton.

in the number of polaritons that each single photon sees when they arrive to the cavity, the reconstructed state of the polaritons becomes mixed and the photon correlations are washed out. In fact, if the factor $Rt/2$ is uniformly distributed around an interval δ_θ the purity is given by

$$\mathrm{Tr}(\rho^2) = \frac{1}{2} + \frac{1-\cos\delta_\theta}{\delta_\theta^2} \geq \frac{1}{2}\,. \tag{7.40}$$

The effect of the condensate in the lower branch on the state of the single photon that impinges onto the upper branch, can be obtained by propagating the initial state of the single photon, i.e., $|\psi(0)\rangle = i(|\uparrow\rangle - |\downarrow\rangle)/\sqrt{2}$, with the effective Hamiltonian in Eq. (7.32):

$$\begin{aligned}|\psi(t)\rangle &= e^{-iHt/\hbar}\,|\psi(0)\rangle = \\ &\frac{1}{\sqrt{2}}\left[i\cos\left(\frac{Rt}{2}\right) - \frac{2g_{\uparrow,\downarrow}+\Delta}{R}\sin\left(\frac{Rt}{2}\right)\right]|\uparrow\rangle - \frac{1}{\sqrt{2}}\left[i\cos\left(\frac{Rt}{2}\right) - \frac{2g_{\uparrow,\downarrow}-\Delta}{R}\sin\left(\frac{Rt}{2}\right)\right]|\downarrow\rangle\,,\end{aligned} \tag{7.41}$$

and the probability to measure the single photon in the state $|\varphi\rangle = (\alpha\,|\uparrow\rangle + \beta e^{i\theta}\,|\downarrow\rangle)/\mathcal{N}$ with $\mathcal{N} = \sqrt{\alpha^2+\beta^2}$ is given by,

$$\begin{aligned}P_\varphi = |\langle\varphi|\psi(t)\rangle|^2 = \frac{1}{2\mathcal{N}R^2}\Big[&R^2\left(\mathcal{N}^2 - 2\alpha\beta\cos\theta\right)\cos^2\left(\frac{Rt}{2}\right) + 4\alpha\beta R\Delta\sin\theta\cos\left(\frac{Rt}{2}\right)\sin\left(\frac{Rt}{2}\right) + \\ &+ \left(R^2\mathcal{N}^2 + 4(\alpha^2-\beta^2)g_{\uparrow,\downarrow}\Delta - 2\alpha\beta(R^2-2\Delta^2)\cos\theta\right)\sin^2\left(\frac{Rt}{2}\right)\Big]\,,\end{aligned} \tag{7.42}$$

where R and Δ are as in Eq. (7.39). The theory models the experiment by feeding Hamiltonian (7.32) with the initial state in Eq. (7.35) and acquiring statistics over repetitions of this scenario with coefficients (7.33) fluctuating with Poissonian distributions with a mean $n_{\uparrow\downarrow}$, thus describing a polariton condensate beyond mean-field.

7.3.4 *Loss of concurrence*

Measuring the concurrence as a function of the intensity of the driving laser (or equivalently, the number of polaritons on the classical state occupying the lower polariton branch), we observe a decay of the entanglement when the polariton density increases, as shown in the data points of Fig. 7.10. While the evolution of the wavefunction is expected, the loss of concurrence seems to suggest a decoherence of the single polariton when it is made interact with the classical state. There are several reasons why the concurrence is apparently lost. Some of them are related to the presence of the condensate in the system, and are completely independent of the strength (or even existence) of the interactions. The spread of the condensate, both in real and in momentum space, yields to a complex redistribution of polaritons on their branch and scattering processes start to occur to the state to which the single photon arrives. However, as I will show in the next section, such a "noise" induced by the scattered polaritons is small enough to allow us to resolve the effect of interactions. The complexity of the situation increases when the interactions are taken into account, as they induce an effective coupling between the two branches. Specifically, the lower polaritons of a given polarization are coupled to the upper polaritons with the opposite polarization, and such a coupling breaks the quantum superposition of the single polariton into a (disentangled) product state. Furthermore, as has been observed by Love et al. (2008), the lower polariton condensate fluctuates with Poissonian statistics, and each pair of entangled photons finds the microcavity in an instantaneously different state, which inevitably propagates their wavefunction in a different way. Thus, in the final observation, which is reconstructed by averaging over many of such individual realizations, we observe that the entanglement—measured through the correlations in polarization between the pair of photons, after one of them has passed through the microcavity—is spoiled and that the state of the photon pair becomes mixed.

To describe the experiment, I included all these effects, and I was able to reproduce theoretically the empirical observation with an excellent agreement (cf. the blue solid line in Fig. 7.10). For the model, I assumed that the polaritons on the lower branch are in a coherent state with a single wavevector $\mathbf{k}$ of the single-mode ground state system, and that the laser confines them to a finite extension in space of $A = 706\,\mu m^2$. Furthermore, the spot on which the single photon impinges on the sample has a radius three times smaller. In a different setup, we observe that mean lifetime of the microcavity is 3 ps, thus we assume that the time that each polariton remains inside the microcavity follows a Poissonian distribution with such a mean value. With these conditions, I fit the observation with a same-spin interaction between excitons of $V^{(1)} = 73.9\,\mu eV\mu m^2$ and with opposite spin of $V^{(2)} = -0.1V^{(1)}$, which, although larger than the estimate given by Tassone and Yamamoto (1999) using microscopic theories, are consistent with other recent observations, such as the one made by Walker et al. (2017) that attribute such high values to the presence of an exciton reservoir, which undoubtedly could be excited by thermal processes and Auger effects that, in addition to the background noise, would also be detrimental to the concurrence. While the magnitude of this interaction remains to be asserted and further studied, my calculation shows that the wavefunction of a single-polariton Fock state is indeed affected by its interactions with the condensate in the lower polariton branch, albeit in a random way as ruled by fluctuations currently beyond our control.

7.3.5 *Noise in the measurement*

The behaviour shown in Figure 7.10 was obtained by following the work of Altepeter et al. (2003), thus performing a *hyper-complete tomography* of the state of the pair of entangled photons. This tomographic process, which was proposed by James et al. (2001), consists of counting the coincidences of the photons in a combination of three bases of polarization (logical, diagonal, and circular). Therefore, the noise in the form of accidental coincidences from any source not related to the entangled photons can be corrected *on average* by subtracting the background coincidences measured in absence of the quantum source. There is, however, another form

of noise that cannot be corrected in this way when the condensate is present. The increasing power on the x-axis of Fig. 7.10 corresponds to more populated polariton condensates in the microcavity, which collectively affects the single polariton sent by the nonlinear crystal: the denser the condensate, the larger is its effect on the concurrence. The interpretation for this observation is that more polariton in the condensate lead to stronger shifts to the energy of the single polariton due to the polariton-polariton interaction, thus spoiling the concurrence through the fluctuation of the number of condensed polaritons. Another factor that would affect the concurrence, even in the absence of the interaction, is if the condensate, at $\mathbf{k} = \mathbf{k_0}$ on the lower branch, would scatter polaritons to the mode excited by the quantum source (e.g., to the upper polariton branch at $\mathbf{k} = \mathbf{0}$), thus introducing indistinguishable but uncorrelated polaritons to the mode from which we measure the correlations. Being indistinguishable from the "real" signal, this noise cannot be corrected by simple subtraction of a background, as it is related to the signal. For instance, if a scattered polariton and one of the entangled photons are present simultaneously in the cavity, we should expect coalescence effects such as Bose stimulation, which is in fact, additional physics rather than noise. The respective rates at which the mode is populated by scattered polaritons, on the one hand, and by the quantum source, on the other hand, suggest that the effect should however be very small. But since the effect on the concurrence could be large, we have to account for it in the theoretical modelling. We now discuss how doing so allows us to rule out that our observation is dominated by scattered polaritons from the condensate and that the observation is explained instead by direct interactions of the single upper polariton at $k = 0$ with the rest of the lower-polariton condensate at $k = k_0$. To quantify the amount of polaritons that are scattered to the wavevector of the single polariton, we measured the luminescence from the cavity. The wavevector selection was made by spatially filtering the emission with a pinhole. Then, the energy resolution was obtained by passing the light through a monochromator. In Figure 7.11, I show the intensity of the emission at the wavevector from which we collected the photons to count the coincidences with the single photon. There, I show in red the emission without filtering in energy (as the APD is not sensible to the energy of the photons that it collects), and in green and blue the contribution from only the lower and upper polariton branch, respectively. The latter polaritons are in fact populating the state to which the single photon arrives, and thus they are reducing the amount of correlated signal.

Figure 7.12 shows, for the various power of the laser that creates the condensate in the lower polariton branch, the coincidences between the photons emitted by the cavity with vertical polarisation and photons from the nonlinear crystal with horizontal polarisation going directly to the APD. This basis corresponds to a state in which the pair of photons are generated by the nonlinear crystal, and therefore provide the higher visibility for the signal. In panel (a), I show the case in which the power of the driving laser was set at 50 nW. There, the signal (the peak at zero delay) can be clearly distinguished from the accidental coincidences that constitute the constant background. However, such a distinction becomes less clear as the power of the

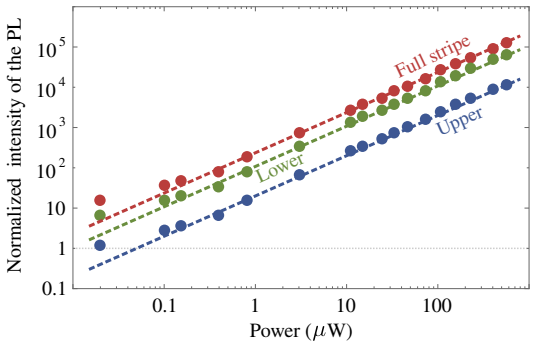

Figure 7.11: Luminescence of the sample at the wavevector at which the single photon impinges, normalized to the intensity of the single polariton. The colour lines corresponds to the full stripe (red), i.e., without filtering in energy the emission of the sample, the light emitted from the lower branch (green) and from the upper branch (blue). The measured values are shown by the dots, while the dotted lines represent the linear fit of the data. Note that when the concurrence of the entangled photons starts to fall (at about 1 µW) the intensity of the luminescence from the lower branch is about 200 times as larger as the single photons.

driving laser increases and the amount of accidental coincidences is comparable to the amount of correlated signal, as shown in Panels (b-d). To accommodate the noise into the description of the experiment, we need to upgrade the theoretical model. The scattering of polaritons to the wavevector to which we sent the single photon can be modelled as an incoherent continuous driving. The intensity of such a driving can be deduced from the luminescence of the microcavity, shown in Fig. 7.11. For instance, when the intensity of the driving laser is 20 µW, the intensity of the luminescence from the lower polariton branch is about 2000 times larger than the intensity due to the single polariton, which comes with a repetition rate of 500 000 photon pairs per second. Since the cavity has a lifetime of 3 ps, the average number of photons at the wavevector where the single polariton impinges is thus 0.003. The description of the system is therefore upgraded to a master equation, in which the rate of the incoherent pumping is chosen so that the steady state population of the cavity is equal to the average population estimated from the luminescence. To take into account only the coincidental detection, I use the Quantum Monte Carlo method developed by Mølmer, Castin, and Dalibard (1993) and compute the quantum trajectories of the experiment. In them, the Hamiltonian propagation is still done by Eq. (7.32), while the decay and incoherent driving are taken into account as quantum jumps. After many such trajectories, I reconstruct the state of the entangled photons by performing the tomography, in the same way that I reconstruct the state form the actual experiment. In Fig. 7.10 I show the dependence of the concurrence on the intensity of the laser

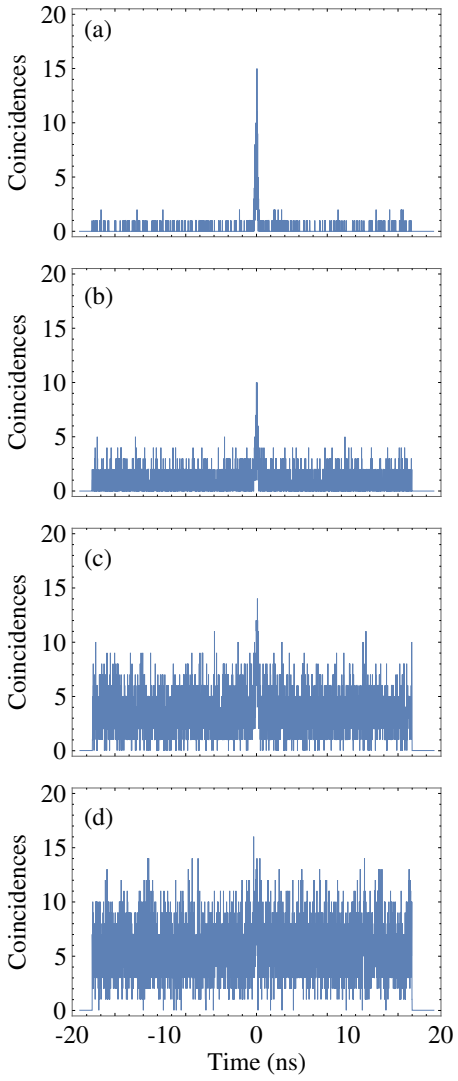

Figure 7.12: Counting photon coincidences, as a function of pumping power. The photon that passes through the cavity and becomes a polariton is detected with vertical polarization. The other one, that goes directly from the nonlinear crystal to the APD is measured in with horizontal polarization. The laser sustaining the polariton condensate impinges onto the cavity has a power of (a) 50 nW, (b) 5 µW, (c) 16 µW and (d) 26 µW. In all the panels the background noise follows a Poissonian distribution. As the power of the driving laser increases, the amount of coincidences due to the entangled single polariton are not simply added on top of the background noise, but instead they remain constant. This follows from the "noise" produced by scattered polaritons from the condensate to the mode excited by the quantum source, being indistinguishable with the signal, and requiring being included in the model rather than subtracted from the data.

driving in the lower branch, taking into account the noise due to the scattered polaritons (green, dashed line) and both the noise and the interactions (blue, solid line). It is clear that if the state to which the entangled polariton arrives is largely populated, the tomography of the pair of photons becomes spoiled and the concurrence drops. However, the noise due to the scattered polaritons from the condensate is far from enough to account for our observations. This assures that interactions are the dominating effect.

7.3.6 *Quantum Spectroscopy*

Using quantum light as the driving field provides new methods to gain information on the condensate itself, which is able to affect the quantum correlations between two particles in a measurable way without producing any sizable change to the single-photon observables such as the luminescence. For instance, we can go beyond simply characterizing the underlying Hamiltonian by mapping its effect on *all* the possible polarization states; namely, the way in which the condensate transforms the Poincaré sphere. In the cases where one deals with entangled states, as we do in our experiment, this can be achieved using the technique introduced by Altepeter et al. (2003), known as the *Ancilla Assisted Quantum Process Tomography* (AAQPT). The protocol consists of characterizing the action of an unknown map (to which the pioneering authors refer to as the "*black box*") acting on one of two entangled qubits. Because of the intrinsic correlations on the bipartite system, the map can be recreated using only one input and its corresponding output state (instead of having to measure *all* the combinations).

The characterization of the state of the qubit is done through the Stokes decomposition, by which the density matrix of a qubit is written as

$$\rho = \frac{1}{2}\vec{r}\cdot\vec{\sigma} = \frac{1}{2}(r_0\mathbf{1} + r_1\sigma_1 + r_2\sigma_2 + r_3\sigma_3)\,, \tag{7.43}$$

where $\vec{r}$ is the Stokes vector and $\vec{\sigma}$ is the vector of Pauli matrices. The AAQPT allows to obtain the black box (in our case, the microcavity with a lower polariton condensate) map χ from the expression $\vec{r}_{\text{out}} = \chi\vec{r}_{\text{in}}$ where $\vec{r}_{\text{in}}$ and $\vec{r}_{\text{out}}$ are the Stokes parameterization of the state of the single photon before and after it goes through the cavity, respectively. The numerical calculation of χ is obtained by the linear decomposition $\chi = (A^{-1}B)^{\text{T}}$ with A and B matrices obtained from the state of the pair of entangled photons before and after one of the photons has gone though the cavity and are defined as

$$A_{i,j} = \text{Tr}[(\sigma_i \otimes \sigma_j)\rho_{\text{out}}] \qquad \text{and} \qquad B_{i,j} = \text{Tr}[(\sigma_i \otimes \sigma_j)\rho_{\text{in}}]\,. \tag{7.44}$$

In the experiment, where errors and noise could lead to a non-physical result, the map is best estimated by a *Maximum Likelihood* process over χ, which provides a trace preserving and completely positive map χ_{physical} that minimizes the statistical dispersion of the expectation values of the measured map χ_{raw}. An intuitive representation of χ that facilitate its interpretation is given through the Poincaré sphere, where any qubit is mapped as a point on the surface, using (r_1, r_2, r_3) as Cartesian coordinates, and it is shown in Fig. 7.13 for three powers of the driving laser. There, r_0 represents the intensity of the field, r_1 the degree of linear polarization, r_2 that of diagonal polarization and r_3 that of circular polarization. In essence, the sphere rotates under unitary transformation and shrinks under the effect of decoherence. Our joint experimental/theoretical analysis shows that the sphere does not rotate, although it experiences some wobbling, until at larger pumping, it shrinks into a spindle. The experimental tomography obtained directly from the post-processing of the data. The theory applies the same procedure to input states (7.35) undergoing the evolution of Hamiltonian (7.32). We find that the shrinking into a spindle, also due to the fluctuating condensate that causes the loss of concurrence, can be obtained with no rotation of the sphere with increasing pumping when $\omega_\uparrow - \omega_\downarrow$ and $g_{\uparrow\downarrow}$ remain constant on average (although they are subject to fluctuations). In these conditions, both polarization states at the extremities of the spindle have a constant energy shift and there is no admixture of polarization. This results in the decoherence of all polarization states except for the eigenstates $\uparrow, \downarrow$, while not producing a unitary rotation.

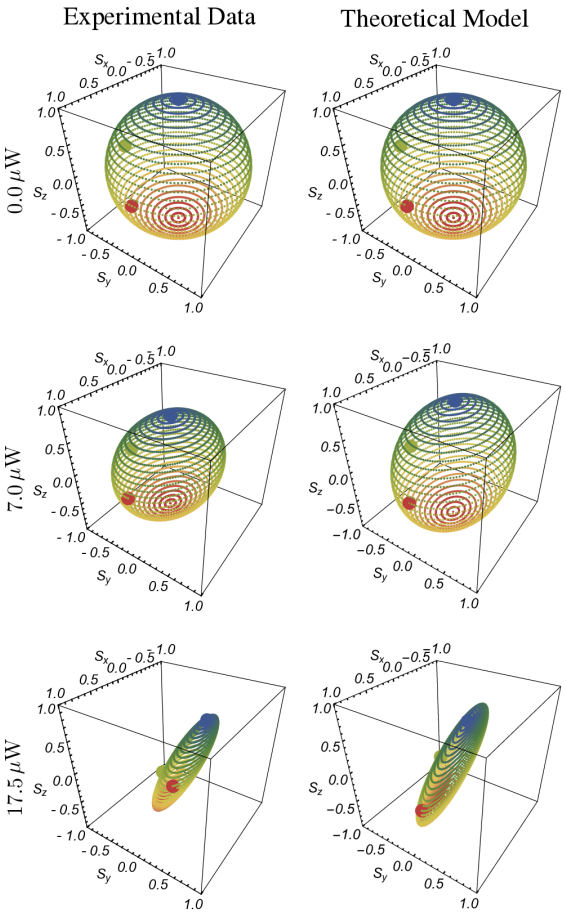

Figure 7.13: Ancilla assisted quantum process tomography. Our technique allows us to observe the effect of the lower polariton condensate on the polarization of an upper polariton qubit, as a function of the increasing pumping (left column). The shrinking of the Poincaré sphere into a spindle confirms that the qubit is affected by its interaction with the lower condensate, whose fluctuations lead to an effective decoherence when averaging. The theoretical model leads to an excellent agreement of the observed phenomenology (right column) and points at future methods for characterizing also the condensate itself.

7.4 CONCLUSIONS

I have shown how exciting a system of weakly interacting particles with Quantum Light allows us to obtain information about the internal structure of the systems. In particular, we have seen that exciting a system of polaritons with the emission of a 2LS coherently driven in the Mollow triplet regime, allows to map the photoluminescence and the photon correlations of the 2LS to the polaritons. While the polaritons are the target of the excitation, they also behave as a colour filter of the Mollow triplet, and they are able to observe the whole landscape of correlations that the photons emitted by the triplet have. I have shown how exposing the polariton dispersion relation to the various types of light allows us to determine the strength of the interactions between polaritons, thus demonstrating an implementation of a spectroscopic technique, to which I refer as *Mollow Spectroscopy*. These results suggest numerous other applications, including the spin, performing quantum pump-probe and two-colour spectroscopy with delay between quantum correlated beams, probing and exciting continuous fields or their resonant configurations such as optical parametric oscillators, and driving other quantum systems, e.g., two-level systems, coupled cavities, polariton circuits, etc., each of them amenable to several types of quantum light. The emitter of Fock states recently proposed by Sánchez Muñoz et al. (2014a), releasing all its energy in bundles of N photons, should be a key resource for quantum excitation. Beyond the exotic states of light already alluded to, this may open the door to new classes of excitations, such as the correlated electron-hole clusters, the so-called dropletons, discovered by Almand-Hunter et al. (2014) within the limitations of classical excitations by theoretical deduction.

As the state-of-the-art polariton samples are not ready yet to implement Mollow Spectroscopy, we turned their excitation with simpler but still quantum sources of light, namely, a source

of pairs of entangled photons. Using such a source, we drove polaritons a little step closer to the realization of a quantum computer, and demonstrated for the first time the generation of a genuinely quantum state of the polariton field, by observing one of the entangled photons being absorbed by the microcavity, becoming a single polaritons, being re-emitted as a photon and keeping its quantum correlations during the whole process. Repeating the experiment with the single photon impinging onto a microcavity containing a polariton condensate allowed us to show that the quantum correlations between the photons are maintained and their state can be manipulated through the interaction between polaritons, which I have been able to estimate from fitting the experimental observation with a full quantum mechanical model. Further and systematic investigations using these techniques will allow placements of stricter boundaries around the strengths that I have reported and clarify the nature of the strongly correlated gas that is formed at high densities. These current results have obvious implications for the design and implementation of a new generation of quantum gates, routing interacting polaritons in predetermined landscapes. Polaritons thus appear to be the possible precursors of the long-sought strongly interacting photons needed for the realization of scalable and efficient quantum computers.

8 EXCITATION WITH THE BUNDLER

Under the trees of England I meditated
on this lost and perhaps mythical labyrinth...
I thought of a maze of mazes, of a sinuous,
ever growing maze which would take me in
both past and future and would somehow involve the stars

— Jorge Luis Borges

8.1 INTRODUCTION

The Bundler is a device proposed by Sánchez Muñoz et al. (2014a) already discussed several times in the previous chapters. As a short reminder, it is a source which emits packets—or simply, *bundles*—of exactly N-photons. These photons are the result of a relaxation process that takes place involving virtual (rather than real) energy levels, and are therefore highly quantum-correlated. The device is based on the Mollow (1969) triplet, which has also been widely discussed in the previous chapters. Here, we are interested in the photons that are emitted from frequencies in between the central and lateral peaks of the triplet. As the emission from these frequencies is considerably low as compared to the emission at the frequencies from the peaks, the emission is enhanced by coupling a cavity to the 2LS at the frequency of interest. In general, the bundles are composed of N photons and they are obtained when the cavity is resonant to the N-photon transition of the Mollow ladder, i.e., $\omega_a = \omega_L \pm \Omega_+/N$, where Ω_+ is the splitting between the central and the lateral peaks of the triplet. The photon bundles are emitted with a particular temporal structure, which Sánchez Muñoz et al. (2014a) identified as a geometric series as a result of the spontaneous emission of a Fock state of N photons. Such a structure is not visible from the density matrix in the steady-state, but can only be observed in an experiment, either on a computer (with a Monte Carlo simulation) or in a laboratory. The fact that the photons of a bundle are not emitted simultaneously poses an important question: how far apart can a pair of photons be, so that they still constitute a photon bundle? The answer to this question lies at the heart of the definition of the bundle and is a key element to the definition of the *purity* of the bundles. The shape of the emission spectrum of the Bundler's cavity depends on the intensity with which it is coupled to the 2LS, and the intensity at which the latter is driven by a laser: while a larger driving intensity increases the splitting between the various N-photon resonances, it also reduces the amount of signal that the 2LS emits. Figure 8.1 shows a prototypical example of the emission spectrum of the $N = 1$ bundler when the cavity is resonant to the two-photon transition. Note that the largest contribution, both in height and intensity corresponds precisely to the light coming from the two-photon transition. The latter indicates that the emission of the Bundler is dominated by photon pairs rather than single-photons. Sánchez Muñoz et al. (2018) proposed a way to estimate the purity of the N-photon emission directly from the density matrix. It relies on obtaining the eigenvalues of the Liouvillian describing the system, in the same way that we did in Section 6.4 when we discussed the dressing of a 2LS when driven by a Mollow triplet. The method allows us to obtain the frequencies at which the system emits and the intensity of such an emission. Thus, one can estimate the N-photon purity by summing the contributions from all the emission in a frequency window neighbouring the N-photon resonance and comparing it with the total emission. In the late 2000s, del Valle, Laussy, and Tejedor (2009) showed that the emission

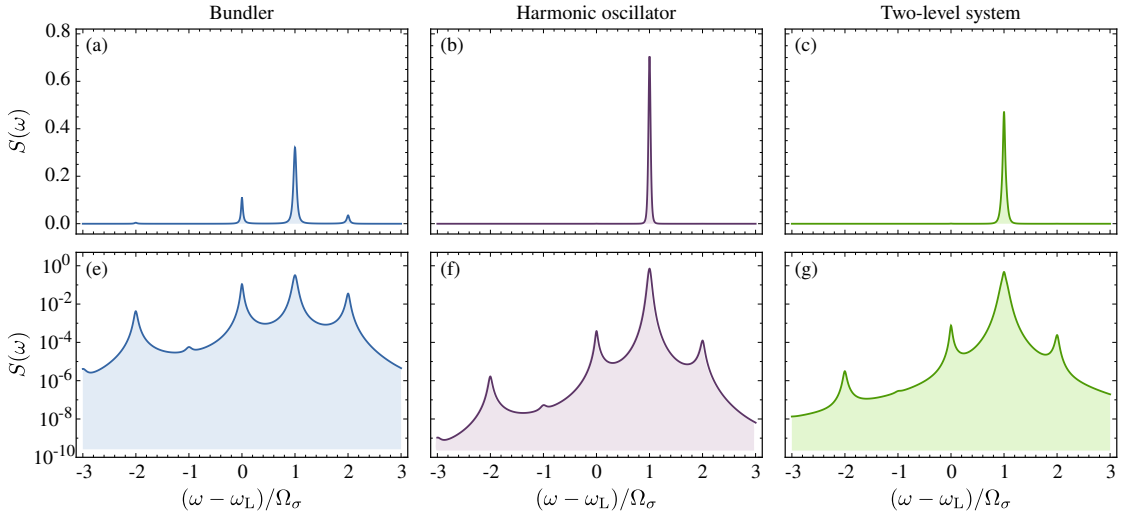

Figure 8.1: Emission spectra of the Bundler, the Harmonic oscillator and the two-level system driven by the Bundler. (a) The cavity of the Bundler displays the triplet structure—whose peaks are located at $\omega = \omega_\sigma$ and $\omega = \omega_\sigma \pm 2\Omega_\sigma$—inherited from its coupling to the 2LS driven by the laser, but the dominant emission comes at the frequency corresponding to the 2-photon transition—which is $\omega = \omega_\sigma + \Omega_\sigma$— to which the cavity is resonant. (b) and (c) show the emission spectrum of a harmonic oscillator and a two-level system, respectively, when they are driven by the Bundler and are set in resonance with the 2-photon transition too. In both cases the emission is predominantly at the frequency of the Bundler. (e-g) show the figures in panels (a-c) in logarithmic scale to unveil the structure hidden in linear scale. The figures were obtained by setting γ_σ, the decay rate of the two-level system driven by the classical laser, as the unit; $\gamma_a = 2\gamma_\sigma$, $\gamma_b = 2\gamma_\sigma$, $g = 2\gamma_\sigma$, $\Omega_\sigma = 2\gamma_\sigma$, $\omega_a = \omega_b = \omega_\sigma + \Omega_\sigma$, and $\Omega_\sigma = 25\gamma_\sigma$.

spectrum of a quantum system can be written as the sum of Lorentzians with amplitude L_p and dispersive components with amplitude K_p:

$$S(\omega) = \frac{1}{\pi}\frac{1}{n_a}\sum_p \left[L_p \frac{(\gamma_p/2)}{(\gamma_p/2)^2 + (\omega - \omega_p)^2} - K_p \frac{(\omega - \omega_p)}{(\gamma_p/2)^2 + (\omega - \omega_p)^2} \right], \tag{8.1}$$

where the functions in the sum are described by the frequency ω_p at which they are centered and their widths γ_p, respectively. Thus, one can estimate the purity of the N photon emission by summing all the amplitudes L_p such that their associated frequency ω_p satisfies the condition

$$|\omega_p - \omega_N| \leq \frac{\gamma_a}{2}, \tag{8.2}$$

where ω_N is the frequency of each photon from the N-photon transition and γ_a is the linewidth of the cavity.

8.2 PHENOMENOLOGICAL BUNDLER

The full description of the Bundler—the strong coupling between a two-level system and a cavity—requires a very large Hilbert space. In fact, in regimes of interest where the emission of the cavity consists of N-photon bundles, the computational effort becomes quickly unmanageable for regular computers and one would have to turn either to dedicated algorithms or computing clusters. To study the effect of the Bundler on an optical target, it is therefore impractical to have to start with already extremely heavy problems. Another route, is to describe the emission of the Bundler from a phenomenological point of view. In this section, I turn to the latter and explore possible *toy models* describing simple systems that behave like the Bundler. A

very crude description of the Bundler consists of a single mode (with annihilation operator d, for which I still do not assume any type of statistics) obeying a master equation of the type

$$\partial_t \rho = i\left[\rho, \Omega_d\left(d^{\dagger N} + d^N\right)\right] + \frac{\gamma_d}{2}\mathcal{L}_d\rho + \frac{P_d}{2}\mathcal{L}_{d^{\dagger N}}\rho\,, \tag{8.3}$$

where the lindblad terms $\mathcal{L}_c\rho$ are defined as in Eq. (1.21). Here, the driving from a N-photon laser is done with intensity Ω_d and we assume that the system is driven in resonance, namely that $\omega_d = N\omega_{\rm L}$, and the incoherent driving is done at a rate P_d. In the following, the coherent and incoherent drivings will be described through Eq. (8.3) by setting $P_d = 0$ and $\Omega_d = 0$, respectively. I now tackle several cases of interest, starting with the simplest Bundler, namely letting $N = 2$ in Eq. (8.3).

The accuracy with which the toy models of the Bundler emit photon-bundles can be quantified by the N-photon purity, introduced by Sánchez Muñoz et al. (2014a) in the seminal paper of the Bundler. There, the authors observe that even when the Bundler was operating in the regime of N-photon bundles, sometimes it also emits single photons. These astray photons spoil the quality of the emission—since by definition the Bundler should emit N-photon bundles every time—and reduce its purity. The quantification of the purity of the emission is done assuming that it is the result of various competing mechanisms of emission which i) are independent from each other and ii) follow a particular probability distribution. Thus, in general and operating in the regime of N-photon bundles, the probability to obtain n photons can be obtained as

$$p_N(n) = \frac{1}{n!}\frac{\partial^n}{\partial s^n}\Pi_{x_1+x_2+\cdots+x_N}(s)\Big|_{s=0}\,, \tag{8.4}$$

where $\Pi_{x_1+x_2+\cdots+x_N} = \Pi_{x_1}\Pi_{x_2}\cdots\Pi_{x_N}$ is the generating function, which can be broken down into the generating functions of the independent underlying processes. In the original paper, Sánchez Muñoz et al. (2014a) assumed that the emission was made of N-photon bundles and individual photons, each of them following a Poissonian distribution with mean value λ_1 and λ_N, respectively. Thus, the generating function entering into Eq. (8.4) was simply

$$\Pi_{x_1+x_N} = \Pi_{x_1}\Pi_{x_N} = e^{-\lambda_1(1-s)}e^{-\lambda_N(1-s^N)}\,, \tag{8.5}$$

where we have assumed the generating function $\Pi_{x_k} = \langle s^{x_k}\rangle = e^{-\lambda_k(1-s^k)}$, which corresponds to a Poissonian distribution. Replacing the generating function from Eq. (8.5) into Eq. (8.4) yields the probability distribution (there is a typo of an extra $n!$ factor in Sánchez Muñoz et al. (2014a)'s paper, the correct expression is given here)

$$p_N(n) = e^{-(\lambda_1+\lambda_N)}\sum_{k=0}^{n/N}\frac{\lambda_1^{n-kN}\lambda_N^k}{k!(n-kN)!}\,. \tag{8.6}$$

Thus, the purity π_N of the N-photon bundle emission is defined as the ratio of N-photon emission as compared to the total emission, namely

$$\pi_N = \frac{\lambda_N}{\lambda_1+\lambda_N}\,. \tag{8.7}$$

The probability distribution of the observed photons cannot be accessed through the density matrix, as the latter provides statistical averages only. Thus, one has to turn to, e.g., Monte Carlo simulations like the one that I presented in Chapter 2. Furthermore, recently Diaz-Camacho et al. (2019) have shown that even in the regime of N-photon emission, the light coming from the Bundler spoiled by individual photons, but also by bundles of two photons, bundles of three photons and so on. Thus, the probability distribution presented in Eq. (8.6) is only accurate for the case $N = 2$. The sources that I will discuss in the following three subsections have regimes of operation for which the purity of the two-photon emission is greater than 99%, provided that the intensity of the driving is small (but not necessarily vanishing small).

8.2.1 *Three-level system with coherent two-photon driving*

This scenario is described through the master equation (8.3) setting $P_d = 0$ and changing the generic operator d for an operator b truncated at two excitations, thus becoming a three-level system (3LS). In the steady-state, the population of the 3LS is given by

$$n_b = \frac{8\Omega_b^2}{\gamma_b^2 + 8\Omega_b^2}, \tag{8.8}$$

which saturates to 1 in the limit of very intense driving (a very intense one-photon laser driving a N-level system yields a population equal to $N/2$, evidencing the Rabi oscillations. Interestingly, the counterpart with a N-photon laser yields populations smaller than $N/2$). At the two-photon level, the emission spectrum is given by a superposition of a pair of lorentzians centered at the natural frequency of the 3LS:

$$\begin{aligned} S_b(\omega) = \frac{1}{16\pi\Omega_b} \frac{\gamma_b + \beta_-/2}{(\gamma_b + \beta_-/2)^2 + \omega^2} \Bigg\{ & \frac{\gamma_b(\gamma_b - \beta_-) + 4(\beta_- - 2\gamma_b)\Omega_b + 4\Omega_b^2}{\beta_-} \\ & - \frac{\gamma_b(\gamma_b - \beta_+) - 4(\beta_+ - 2\gamma_b)\Omega_b + 4\Omega_b^2}{\beta_+} \Bigg\} + \\ + \frac{1}{16\pi\Omega_b} \frac{\gamma_b - \beta_+/2}{(\gamma_b + \beta_+/2)^2 + \omega^2} \Bigg\{ & \frac{\gamma_b(\gamma_b + \beta_+) + 4(\beta_+ + 2\gamma_b)\Omega_b + 4\Omega_b^2}{\beta_+} \\ & - \frac{\gamma_b(\gamma_b + \beta_-) - 4(\beta_- + 2\gamma_b)\Omega_b + 4\Omega_b^2}{\beta_-} \Bigg\}, \end{aligned} \tag{8.9}$$

where $\beta_\pm = \sqrt{\gamma_b^2 \pm 8\gamma_b\Omega_b - 8\Omega_b^2}$. The correlations between pairs of individual photons, defined as in Eq. (1.33), are given by

$$g_b^{(2)}(\tau) = 1 - e^{-\gamma_b\tau}\left[\left(\frac{1}{2} - \frac{\gamma_b^2}{16\Omega_b^2}\right)\cos\left(2\sqrt{2}\Omega_b\tau\right) + \frac{\sqrt{2}\gamma_b}{4\Omega_b}\sin\left(2\sqrt{2}\Omega_b\tau\right)\right], \tag{8.10}$$

which is shown as a function of the intensity of the driving in Fig. 8.2(a). Here, the two-photon driving is shown in the argument of the oscillations, which are augmented by a factor $\sqrt{2}$ with respect to a 2LS driven coherently by a one-photon laser. The zero-delay correlation

$$g_b^{(2)}(\tau = 0) = \frac{1}{2} + \left(\frac{\gamma_b}{4\Omega_b}\right)^2, \tag{8.11}$$

reveals that the emission can be antibunched (albeit with a lower boundary at $1/2$) in the limit of very intense excitation, while in the regime of vanishing driving the correlations explode to an infinite superbunching. Furthermore, the correlations between two-photon bundles, as introduced in Eq. (4.6), are given by

$$g_{2\,b}^{(2)}(\tau) \equiv \frac{\langle b^{\dagger\,2}(0)b^{\dagger\,2}(\tau)b^2(\tau)b^2(0)\rangle}{\langle b^{\dagger\,2}b^2\rangle^2} = 2e^{-\gamma_b\tau}\left[\cosh(\gamma_b\tau) - \cos\left(2\sqrt{2}\Omega_b\tau\right)\right], \tag{8.12}$$

which always vanishes at zero-delay, but as the intensity of the driving increases the oscillatory behaviour dominates, as shown in Fig. 8.2(b). Thus, Eqs. (8.10–8.12) indicate that the bundles are obtained in the regime of low excitation where the $g_b^{(2)}(0) \gg 1$ while the $g_{2\,b}^{(2)}(0) \ll 1$.

Regardless of the regime of excitation, the state of the source is given by

$$\rho_b = \frac{1}{\gamma_b^2 + 8\Omega_b^2}\begin{pmatrix} \gamma_b^2 + 2\Omega_b^2 & 0 & i\sqrt{2}\gamma_b\Omega_b \\ 0 & 4\Omega_b^2 & 0 \\ -i\sqrt{2}\gamma_b\Omega_b & 0 & 2\Omega_b^2 \end{pmatrix}, \tag{8.13}$$

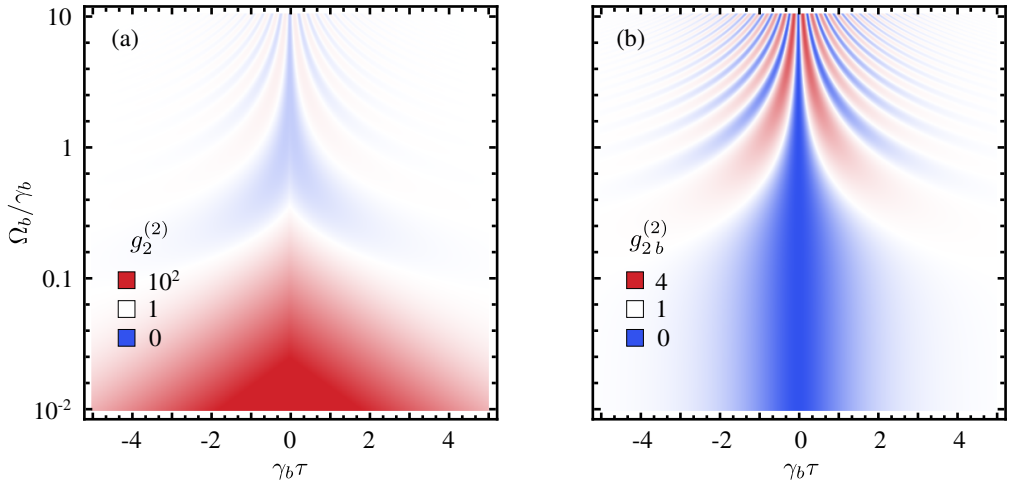

Figure 8.2: Photon correlations of a 3LS driven coherently by an N-photon laser. (a) Second-order correlation function between individual photons. (b) Second-order correlation function between two-photon bundles. The region with $\Omega_b\gamma_b < 0.1$ provides light which purity of two-photon emission is about 99%.

for which the probabilities of having one and two photons (in this system, the probability of having one photon is *always* twice the probability of having two) are maximized in the limit $\Omega_b/\gamma_b \to \infty$, where they become $p_b(1) = 1/2$ and $p_b(2) = 1/4$. However, in such a high-intensity driving regime, the off-diagonal terms in Eq. (8.13) vanish and the state becomes completely mixed. This can be nicely observed through the Wigner function of the state of light, which in phase-space with Cartesian coordinates (x, y) and for an arbitrary intensity Ω_b becomes

$$W_b(x,y) = \frac{2}{\pi}\frac{e^{-2r^2}}{\gamma_b^2 + 8\Omega_b^2}\left\{\gamma_b^2 + 16r^4\Omega_b^2 + 8r^2\gamma_b\Omega_b \sin\left[2\arg(x+iy)\right]\right\}, \tag{8.14}$$

where $r^2 = x^2 + y^2$, and which has a richer structure than the Bundler.

8.2.2 *Three-level system with incoherent two-photon driving*

This scenario is described through the master equation (8.3) by setting $\Omega_d = 0$ and changing the generic operator d for an operator b truncated at two excitations. In the steady-state, the population of an $(N+1)$-level system driven by a reservoir supplying its photons in packets of N photons is given by

$$n_b(N) = \frac{N!\,N\,P_b}{\gamma_b + p_b N![\gamma + \psi_0(N+1)]}, \tag{8.15}$$

where γ is the Euler-Mascheroni constant and $\psi_0(x)$ is the Digamma function, defined as the logarithmic derivative of the Gamma function

$$\psi_0(x) = \frac{\partial}{\partial x}(\ln\Gamma(x)) = \frac{\Gamma'(x)}{\Gamma(x)}. \tag{8.16}$$

In particular, considering the case for $N = 2$, Eq. (8.15) becomes simply

$$n_b(2) = \frac{4P_b}{\gamma_b + 3P_b}. \tag{8.17}$$

Similarly to the case with coherent excitation, the emission spectrum in this case is also given by the superposition of two Lorentzians centered at the frequency of the 3LS

$$S_b(\omega) = \frac{1}{2\pi}\frac{P_b - 2\gamma_b}{P_b - \gamma_b}\frac{P_b + \gamma_b/2}{(P_b + \gamma_b/2)^2 + \omega^2} + \frac{1}{2\pi}\frac{P_b}{P_b - \gamma_b}\frac{3\gamma_b/2}{(3\gamma_b/2)^2 + \omega^2}, \tag{8.18}$$

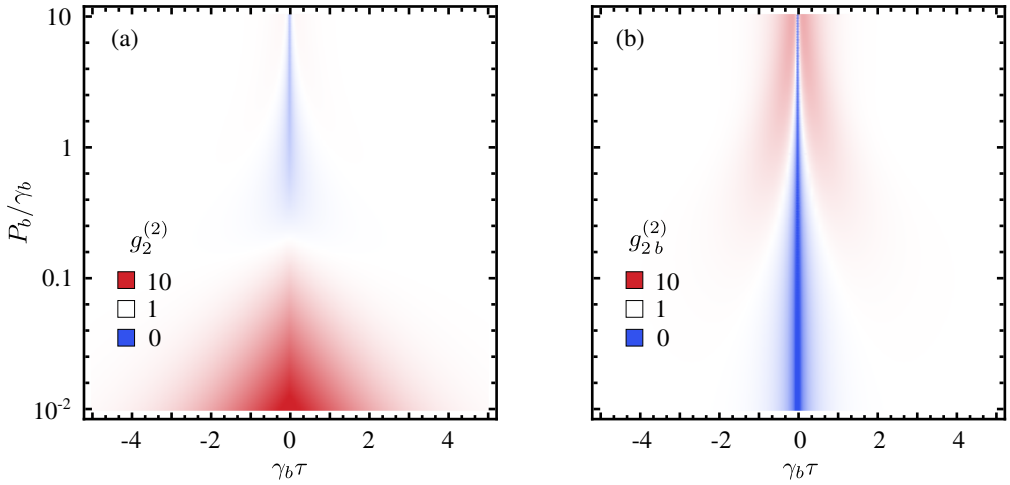

Figure 8.3: Photon correlations of a 3LS driven incoherently by a reservoir supplying the photons in packages of N-photons. (a) Second-order correlation function between individual photons. (b) Second-order correlation function between two-photon bundles. The region with $\Omega_b\gamma_b < 0.1$ provides light which purity of two-photon emission is about 99%.

which yields a single line of luminescence. Furthermore, the correlations between individual photons and between two-photon bundles are given by

$$g_b^{(2)}(\tau) = 1 + \left[\frac{14P_b^2 - 11P_b\gamma_b + \gamma_b^2}{8P_b\chi}\sinh\left(\frac{\chi\tau}{2}\right) - \frac{5P_b - \gamma_b}{8P_b}\cosh\left(\frac{\chi\tau}{2}\right)\right]e^{-(2P_b+3\gamma_b)\tau/2}, \tag{8.19a}$$

$$g_{2\,b}^{(2)}(\tau) = 1 + \left[\frac{10P_b + \gamma_b}{\chi}\sinh\left(\frac{\chi\tau}{2}\right) - \cosh\left(\frac{\chi\tau}{2}\right)\right]e^{-(2P_b+3\gamma_b)\tau/2}, \tag{8.19b}$$

where $\chi^2 = 4P_b^2 - 12P_b\gamma_b + \gamma_b^2$. They are shown as a function of the intensity of the incoherent driving in Fig. 8.3.

The density matrix of the source is

$$\rho_b = \frac{1}{3P_b + \gamma_b}\begin{pmatrix} \gamma_b & 0 & 0 \\ 0 & 2P_b & 0 \\ 0 & 0 & P_b \end{pmatrix}, \tag{8.20}$$

from where we know that the probability to obtaining one photon is *always* twice as large as the probability of having two photons.

The Wigner function in this case is

$$W_b(r) = \frac{2}{\pi}\frac{(8r^4 - 1)P_b + \gamma_b}{3P_b + \gamma_b}e^{-2r^2}, \tag{8.21}$$

where $r^2 = x^2 + y^2$, which becomes negative for $P_b/\gamma_b > 1/(1 - 8r^4)$. While in the limit of low excitation the Wigner function is given simply by a Gaussian, when the driving and decay rates are of the same magnitude, the function becomes a surface similar to a torus with the same radius as figure 8.9(c), albeit with a finite intensity of driving (in the case of the coherent driving, the torus was obtained in the limit of infinite driving). In the general case of a $(n+1)$-level

system in contact with a reservoir supplying the excitation in packages of N-photons, the probability to observe k photons in the system is given by

$$p_N(0) = \frac{\gamma_b}{\gamma_b + p_b N![\gamma + \psi_0(N+1)]}\,, \tag{8.22a}$$

$$p_N(k) = \frac{N!}{k}\frac{P_b}{\gamma_b + p_b N![\gamma + \psi_0(N+1)]} \quad \text{for} \quad 1 \leq k \leq N\,, \tag{8.22b}$$

and, as the incoherent driving does not grow coherence in the system, all the off-diagonal elements of the density matrix are zero and all the information of the state of the $(N+1)$-level system is given by the probabilities in Eq. (8.22a). For instance, the second order correlation function becomes simply

$$g_b^{(2)} = \frac{\gamma_b + p_b N![\gamma + \psi_0(N+1)]}{2(N-1)!N^2 P_b}\,. \tag{8.23}$$

8.2.3 *Harmonic oscillator with coherent two-photon driving*

A harmonic oscillator driven by a laser of N photons is described through Eq. (8.3), setting $P_d = 0$ and changing the operator d for an operator a of a bosonic particle, for which the energy levels are not truncated. For consistency in the notation, here I label the intensity of the driving laser as Ω_a. For $N = 2$, the observables can be found in closed form with standard methods, but for higher values of N the stimulated emission of the laser into the harmonic oscillator makes the population of the latter diverge even at very small driving intensities. Thus, in the rest of the section, I will restrict to the case $N = 2$.

The population of the harmonic oscillator is given by

$$n_a = \frac{8\Omega_a^2}{\gamma_a^2 - 16\Omega_a^2}\,, \tag{8.24}$$

where it is clear that the maximum driving intensity (to have physical results, with positive mean values of the population) is $\Omega_a = \gamma_a/4$. Furthermore, the emission spectrum can be written as the superposition of two Lorentzians centered at the frequency of the harmonic oscillator

$$S_a(\omega) = \frac{1}{4\pi\Omega_a}\left[\frac{(\gamma_a/2)^2 - 4\Omega_a^2}{(\gamma_a/2 - 2\Omega_a)^2 + \omega^2} - \frac{(\gamma_a/2)^2 - 4\Omega_a^2}{(\gamma_a/2 + 2\Omega_a)^2 + \omega^2}\right]. \tag{8.25}$$

Note that the Lorentzian that enters into the spectrum as a subtraction is broader than the other one, thus the tails of the emission line of the oscillator are thinner than they would be without the second term in the right-hand side of Eq. (8.25).

The correlations between individual photons are expressed as

$$g_a^{(2)}(\tau) = 1 + e^{-\gamma_a\tau}\left[\left(1 + \frac{\gamma_a^2}{16\Omega_a^2}\right)\cosh\left(4\Omega_a\tau\right) + \frac{\gamma_a}{2\Omega_a}\sinh\left(4\Omega_a\tau\right)\right], \tag{8.26}$$

which is always larger (or equal, in the limit of very large τ) than 1. Note that, while it is not apparent in Eq. (8.26), the intensity of the laser Ω_a cannot be taken arbitrarily large, as the population diverges at a finite value (even though the correlation does not). On the other hand, the correlations between two-photon bundles are also analytical but they are too cumbersome to be written here. However, at zero-delay the correlation reduces to

$$g_{2\,a}^{(2)}(\tau = 0) = 3\frac{3\gamma_a^4 + 384\gamma_a^2\Omega_a^2 + 2048\Omega_a^4}{\left(\gamma_a^2 + 32\Omega_a^2\right)^2}\,, \tag{8.27}$$

which is always larger than 9. Here, we find a fundamental difference between the toy model exciting a 3LS or a harmonic oscillator: while in the former one can obtain two-photon bundles

with sub-Poissonian statistics, the bundles emitted by the driven harmonic oscillator are always superbunched. Thus, using one model or the other will depend on the type of statistics that one is interested to simulate.

8.3 EXCITING A HARMONIC OSCILLATOR

Already in Chapter 5 we have seen the behaviour of a harmonic oscillator when it is driven with the correlated photons emitted by the leapfrog processes of a Mollow triplet. These results were shown in Fig. 5.7, and implied that the Bundler is not able to take the harmonic oscillator into highly populated and antibunched states, but into states close to vacuum for which the emission is scarce but highly correlated. Exciting a harmonic oscillator with the light emitted by toy-Bundler is done mixing the master equation for a cascaded coupling, given in Eq. (1.28), with the description of the source through the master equation of the toy model, given in Eq. (8.3). In the following, I will use the annihilation operator c for the target harmonic oscillator, and its observables will be noted accordingly, e.g., its decay rate will be noted as γ_c and its population n_c.

8.3.1 *Exciting with a three-level system*

The first question that we tackle regards the repetition rate of the emission and the efficiency with which it drives the harmonic oscillator. Given that the source of quantum light is a three-level system, the repetition rate of its emission is fundamentally truncated. Figure 8.4 shows the map of the population of the harmonic oscillator as a function of the repetition rate of the source (the intensity of the driving is the implicit variable) and the ratio between the linewidth of the harmonic oscillator and of the three-level system. Note that the repetition rate of the 3LS is truncated at 1 when the driving is done by a coherent source, while it is truncated at 4/3 when the driving is done by an incoherent source. However, given the same linewidth of the harmonic oscillator, the population is larger when it is driven with the coherent 3LS. In fact, for

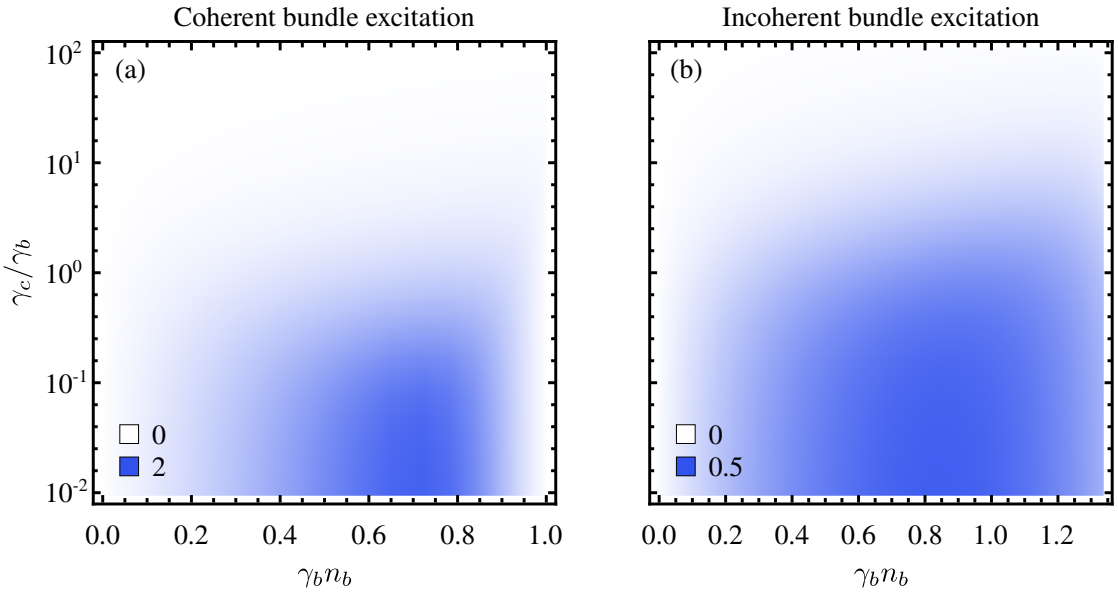

Figure 8.4: Population induced on a harmonic oscillator when it is excited by a three-level system, itself drive by (a) a coherent two-photon laser and (b) a thermal reservoir supplying the photons in packages of two photons. The population of the target is optimized, in both cases, when the intensity of the driving is either $\Omega_b/\gamma_b = 0.567$ or $P_b/\gamma_b = 0.567$, and the linewidth of the target is well below the linewidth of the source.

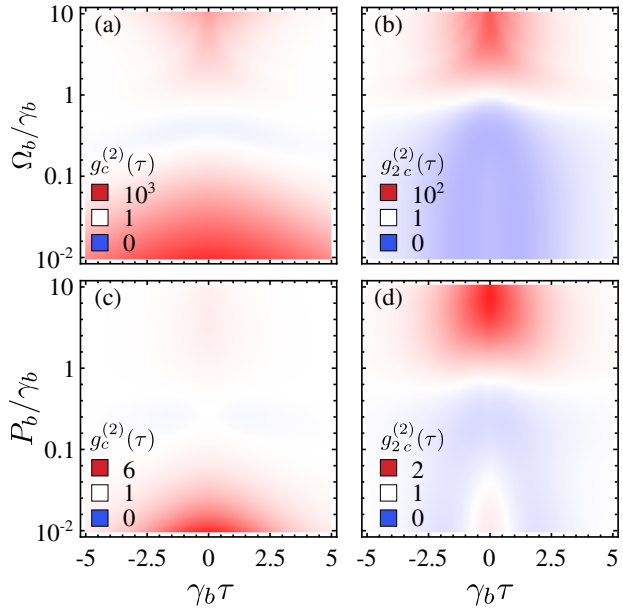

Figure 8.5: Photon correlations of the photons emitted by a harmonic oscillator driven by a three level system. (a, b) Correlations between pairs of single photons and between pairs of two-photon bundles, respectively; for the case in which the driving of the 3LS is done coherently. (c, d) Same as the upper row for the case in which the excitation of the 3LS is done incoherently. The figures were obtained using γ_b as the unit and $\gamma_c/\gamma_b = 1$. In both rows, the regions where the $g_c^{(2)}(\tau)$ is bunched while the $g_{2c}^{(2)}(\tau)$ is antibunched suggests that the emission from the harmonic oscillator is done as two-photon bundles.

the range of linewidths shown in Fig. 8.4, the maximum population that the harmonic oscillator reaches when the excitation comes from the coherent 3LS is up to four times larger than when it comes from the incoherent one. However, the purity of the two-photon bundles emitted by the 3LS is not optimum for the driving intensity that maximizes the population in the cavity. Thus, one has to compromise the population of the target for the purity of the emission.

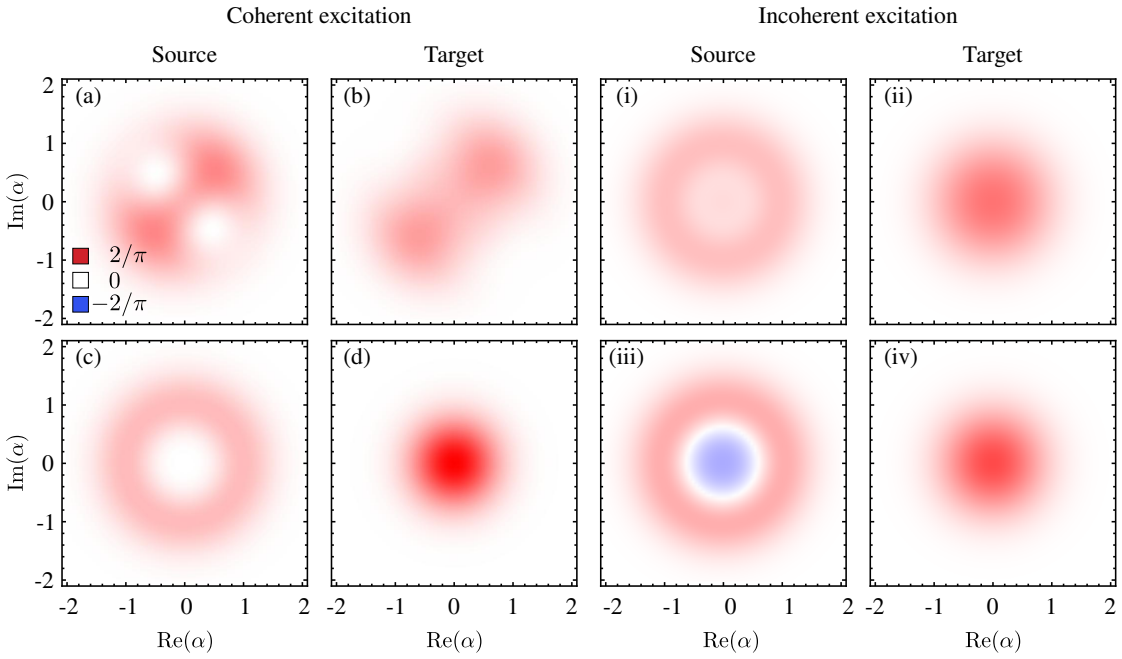

Figure 8.6: Wigner function for a harmonic oscillator driven by a three-level system, for two types of excitation and two intensities of the driving: The panels show the cases in which the excitation is coherent (a-d) and incoherent (i-iv). The upper row shows the case in which the probability of having a single photon in the target is maximum, where one can appreciate the appearance of lobes in phase-space for the coherent excitation. The bottom row shows the case in which the intensity of the excitation is very large. For the figures, I used γ_b as the unit and set $\gamma_c/\gamma_b = 1$.

The photon correlations on the target harmonic oscillator, both for pair of single photons and pairs of two-photon bundles, are shown in Figure 8.5 for the case in which its linewidth is equal to the the linewidth of the source. Panels (a, b) show the case in which the 3LS is driven coherently, while panels (c, d) show the incoherent counterpart. The correlations are stronger (specially the bunching) when the excitation is done coherently. Furthermore, all the figures suggest that there are regions of excitation in which the emission of the harmonic oscillator takes place as bundles rather than as individual photons.

As it is the case when exciting with quantum light, the target of the excitation inherits some of the properties of the source. As such, the state of light imprinted on the target resembles the state of light of the source. This is particularly notable in the Wigner function, shown in Fig. 8.6, where I compare the phase-space distribution of the source and of the target for the two types of excitation and for two intensities. The upper row shows the Wigner functions for the parameters that maximize the probability to have a single photon in the harmonic oscillator: for the coherent excitation, panels (a) and (b), the distribution consists of two lobes that blur on the target. For the incoherent excitation, the distribution for the source resembles a torus, however in the harmonic oscillator the state remains a large portion of vacuum and the distribution is roughly given by a Gaussian. The bottom row shows the cases in which the excitation is very large. In this case, the state of the coherently driven 3LS becomes mixed and the distribution (panel (c)) resembles the torus obtained for the incoherent excitation in panel (i). In contrast, the Wigner function of the incoherently driven 3LS becomes negative around the origin of the phase space, thus evidencing the quantum character of the state. In both cases, the Wigner function of the target is dominated by the vacuum.

8.3.2 *Exciting with a harmonic oscillator*

For the target the observables are given by

$$n_c = \frac{8\Omega_a^2}{\gamma_a^2 - 16\Omega_a^2}\frac{\gamma_a(2\gamma_a+\gamma_c)}{(\gamma_a+\gamma_c)^2-16\Omega_a^2} = n_a\frac{\gamma_a(2\gamma_a+\gamma_c)}{(\gamma_a+\gamma_c)^2-16\Omega_a^2} = \frac{n_a\gamma_a(2\gamma_a+\gamma_c)(1+2n_a)}{(\gamma_a+\gamma_c)^2(1+2n_a)-2n_a\gamma_a^2}, \tag{8.28}$$

where in the rightmost term of Eq. (8.28) I eliminated the explicit dependence of the population on the intensity of the driving. Furthermore, the emission spectrum of the target harmonic

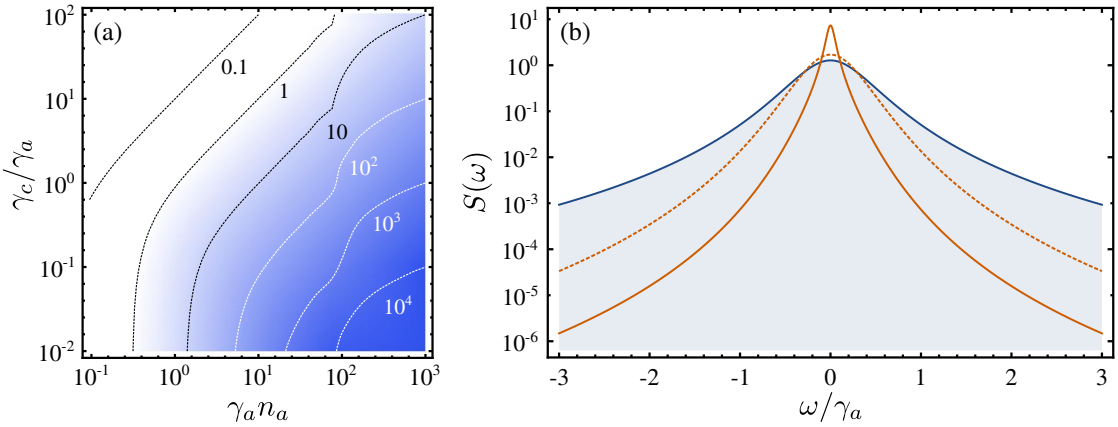

Figure 8.7: (a) Population induced in a harmonic oscillator when driven by a cavity toy-model for the Bundler. For a fixed intensity of the Bundler, the population of the target is the largest in the region where its linewidth is well below the linewidth of the bundler. (b) Emission spectra for the source and the target. The solid blue line corresponds to the emission line of the source, which is given by Eq. (8.25). The orange lines correspond to the emission from the target using $\gamma_c/\gamma_a = 0.1$ (solid) and $\gamma_c/\gamma_a = 1$ (dashed). In the limit in which $\gamma_c/\gamma_a \to \infty$ the emission spectrum of the target matches the spectrum from the source.

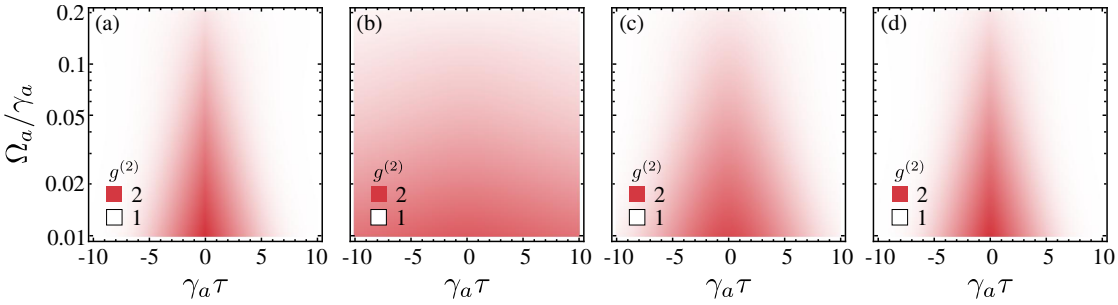

Figure 8.8: Photon correlations induced by a cavity emitting two-photon bundles. (a) Correlations of the source, displaying antibunching in the regime of large intensity of the driving laser. (b–d) Correlations of the target for $\gamma_c/\gamma_b = 0.1$, 1 and 10, respectively. In the limit in which the linewidth of the target cavity is much larger than the linewidth of the source, the photon correlations of the target match the correlations of the source.

oscillator is given by the superposition of three Lorentzians centered at the natural frequency of the harmonic oscillator

$$S_c(\omega) = \frac{1}{\pi}\frac{(\gamma_c/2)}{(\gamma_c/2)^2+\omega^2}\frac{2\gamma_a(\gamma_a^2-16\Omega_a^2)}{(2\gamma_a+\gamma_c)[(\gamma_a-\gamma_c)^2-16\Omega_a^2]} + \\ + \frac{1}{\pi}\frac{\gamma_a/2+2\Omega_a}{(\gamma_a/2+2\Omega_a)^2+\omega^2}\frac{\gamma_c(\gamma_a-4\Omega_a)(\gamma_a+\gamma_c-4\Omega_a)}{8\Omega_a(2\gamma_a+\gamma_c)(\gamma_a-\gamma_c+4\Omega_a)} - \\ - \frac{1}{\pi}\frac{\gamma_a/2-2\Omega_a}{(\gamma_a/2-2\Omega_a)^2+\omega^2}\frac{\gamma_c(\gamma_a+4\Omega_a)(\gamma_a+\gamma_c+4\Omega_a)}{8\Omega_a(2\gamma_a+\gamma_c)(\gamma_a-\gamma_c-4\Omega_a)}, \quad (8.29)$$

which in the limit of $\gamma_c/\gamma_a \to \infty$ becomes the emission spectrum of the source, as expected. Figure 8.7(a) shows the population of the harmonic oscillator as a function of the repetition rate of the Bundler and the ration between the linewidth of the osciillator and the cavity of the Bundler, while Fig. 8.7(b) shows the emission spectrum of the source (solid, blue line) and of the target (orange lines) for two linewidths of the target, demonstrating that the tails of the emission form the cavity are trimmed in a process akin to spectral filtering. The photon correlations of

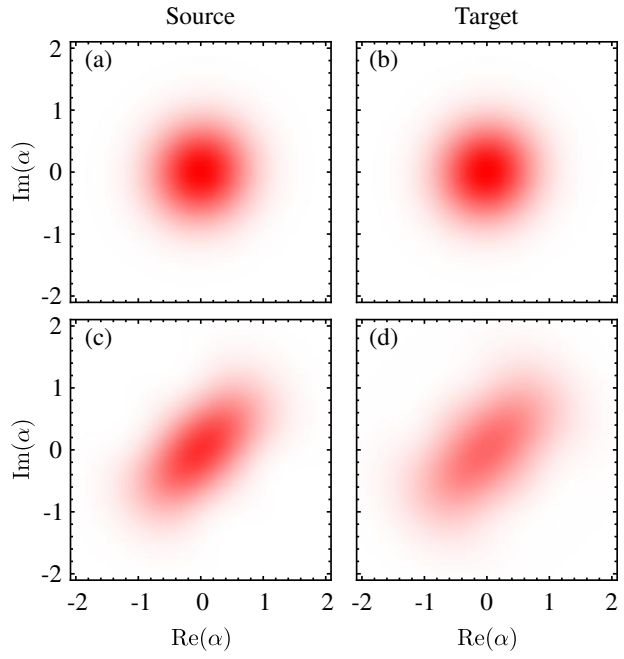

Figure 8.9: Wigner functions for the source and the target at two regimes of excitation. (a, b) show the case in which the probability of having a single photon in the target is maximum, where one can appreciate the appearance of lobes in phase-space. (c, d) show the case in which the excitation is very intense, the state of light of the source is completely mixed and the target is mostly in vacuum. The former regime provides the antibunching shown in Fig. 8.2(c). In all the cases, the distribution has always non-negative values. For the figures I used γ_b as the unit and set $\gamma_c/\gamma_b = 1$.

the target harmonic oscillator resemble those of the source. In Fig. 8.8, I show the correlations of (a) the source and (b-d) the target harmonic oscillator for various linewidths: as the linewidth of the target becomes small, the correlation thermalizes and the structure is blurred. Furthermore, the photon correlations of the target are also always bunched. Considering the state of the harmonic oscillator, I turn to the Wigner function, shown in Fig. 8.9. In agreement with the fact that the source is *always* bunched, the Wigner function is also always positive, and the target harmonic oscillator inherits the classicality of the state (albeit with a larger dispersion in the phase space). In the case of very intense excitation, the source harmonic oscillator becomes a squeezed state, which transpires to the state of the target harmonic oscillator.

8.4 EXCITING A TWO-LEVEL SYSTEM

Exciting a two-level system with the light emitted by toy-Bundler is done mixing the master equation for a cascaded coupling, given in Eq. (1.28), with the description of the source through the master equation of the toy model, given in Eq. (8.3). In the following, I will use the annihilation operator σ for the target two-level system, and its observables will be noted accordingly, e.g., its decay rate will be noted as γ_σ and its population n_σ.

8.4.1 *Exciting with a three-level system*

Considering a two-level system as the optical target also requires to study the ability and efficiency of the Bundler to excite it. Thus, I also consider the population of the two-level system as a function of the intensity of the emission from the Bundler and the linewidth of the two-level system. The results are shown in Fig. 8.10 for a three-level system driven coherently in panel (a) and driven incoherently in panel (b). In the same way as in with the excitation of a harmonic oscillator, the mean occupation of the target is larger when the 3LS is itself driven coherently. Note that the maximum population that the 2LS can reach, within the range of parameters considered in the figure, is still below $1/2$, which is a threshold easily surpassed with classical

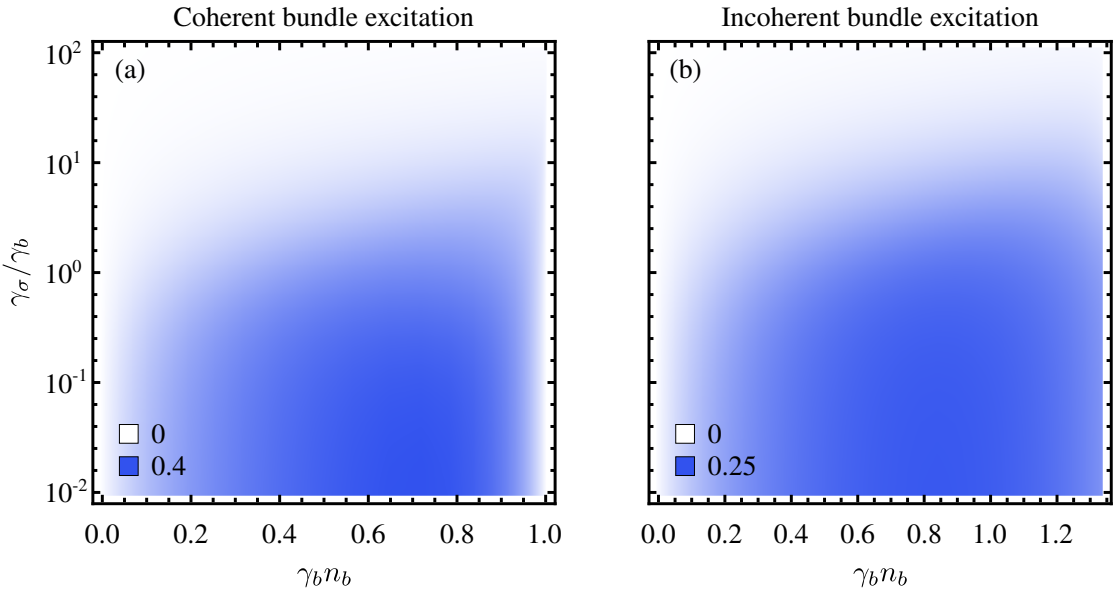

Figure 8.10: Population induced on a two-level system when it is excited by a three-level system, itself drive by (a) a coherent two-photon laser and (b) a thermal reservoir supplying the photons in packages of two photons. The population of the target is optimized, in both cases, when the intensity of the driving is either $\Omega_b/\gamma_b = 0.567$ or $P_b/\gamma_b = 0.567$, and the linewidth of the target is well below the linewidth of the source.

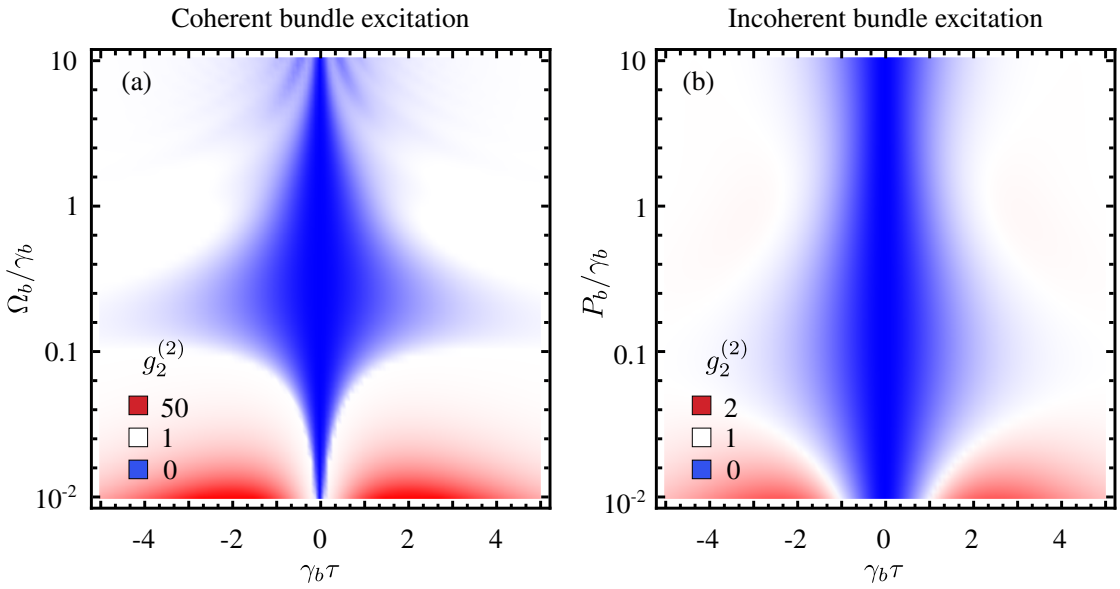

Figure 8.11: Photon correlations of a two-level system driven by a three-level system, itself driven (a) coherently and (b) incoherently. In the case with the coherently driven 3LS the correlations are enormous in the regime of vanishing driving, in which the antibunching (due to the fermionic character of the two-level system) quickly becomes bunched. In the opposite regime, where the driving laser is very intense, the emission from the two-level system undergoes oscillations but maintaining its antibunching character. The figures were obtained using $\gamma_\sigma = \gamma_b$.

excitation. The correlations between the photons emitted by the two-level system are shown in Fig. 8.11 for the coherently driven 3LS in panel (a) and for the incoherently driven 3LS in panel (b). Due to the fermionic character of the two-level system, without filtering one cannot possibly observe photon bundles and therefore the correlation between bundles is not defined. In Fig. 8.11 it is interesting that in the regime in which the three-level system is driven weakly, the photon correlations of the target quickly go form antibunching to bunching (in the case of the coherent excitation, the correlations become superbunched). In the opposite regime, with large intensity of the excitation one observes oscillations in the correlations for the coherent excitation, which are a consequence of Rabi oscillations in the source. However, note that in the case of incoherent driving the coherence time of the correlations are not broadened by the excitation rate, as occurs with the classical excitation of a two-level system. Because the population of the target 2LS is never larger than $1/2$, then the vacuum state is *always* dominant over the Fock state with one photon, which implies that regardless of the type of excitation, the Wigner function of the target 2LS is always completely positive.

8.5 CONCLUSIONS

In this chapter I have presented the excitation of a harmonic oscillator and a two-level system by a Bundler. Given the computational complexity of simulating the real device, I turned to toy-models that provide similar type of emission without the intricate underlying structure. I considered three models: a three-level system or a harmonic oscillator driven either coherently or incoherently by sources providing their photons two by two. The various types of excitations and the system on which they act, allow the emission of photons bundles with various types of statistics, thus making each of them more appealing depending on the type of correlations in which one is interested.

9 CONCLUSIONS

La sabiduría nos llega cuando ya no nos sirve de nada

— Gabriel García Márquez

9.1 ENGLISH

In this Thesis, I have tackled the problem of exciting optical targets with Quantum Light. To do so, I was first called to describe various sources of Quantum Light, which provide their emission either as single-photons or as N-photon bundles, and then I have used them to excite the most fundamental systems: a harmonic oscillator (the archetype of bosonic particles), a two-level system (the prototype of fermionic particles) and polaritons (particles that arise from the strong coupling between a boson and a fermion). The main results of my work can be summarized as follows.

The desiderata for a single-photon source comprises a very extensive list, although some of the most wanted characteristics of a such a source are its ability to suppress multi-photon emission, the indistinguishability of the emitted photons, and its repetition rate. While many experimental groups are striving to optimize the behaviour of this type of sources, they also neglect a key fact of quantum mechanics: the observation. I have shown that when the detection of the light is taken into account self-consistently, some single-photon sources behave in unexpected ways. The resolution in frequency that one gains by filtering the emission induces an indeterminacy in the time at which the photons are detected. Filtering the light emitted by a two-level system spoils its perfect antibunching. Thus, a criterion to identify single-photon sources, and classify their performance regarding multi-photon emission, has to involve the effect of detection. As such, I have proposed a criterion—the N-norm—which quantifies how well the photon correlations are suppressed to all orders (instead of only to order two, $g^{(2)} \ll 1$, which is what is typically considered), and shown its application to various mechanisms that provide antibunched light. Using this, I have shown that a two-level system driven coherently is the best single-photon source when one considers classical excitation only. However, I have also shown that using the emission of such a two-level system to excite yet another two-level system enhances the single-photon character of the emitted light. Furthermore, I have tackled the problem of a two-level system driven by a weak laser into the Heitler regime. While several experimental groups have claimed that in such a system the emission is monochromatic and antibunched, one finds that the two properties do not coexist when considering their detection simultaneously. However, I have shown that one can overcome the negative effect of filtering by making an interference of the emitted light with a coherent field. Performing the interference in an adequate manner, one can restore the lost antibunching even when filtering below the natural linewidth of the two-level system.

Using the fact that filtering the emission from a single-photon source spoils the correlations between photons, thus making it possible for the source to emit more that one photon at the same time, we turn to sources of N photons. In particular, I focused on the light emitted from resonance fluorescence in the Mollow triplet regime. Building onto the proposal of Sánchez Muñoz et al. (2014a) for a source of N-photon bundles, I considered the correlations between single photons emitted at a given frequency ω_1 and N-photon bundles emitted at another frequency ω_2. I presented a systematic analysis of these correlations, considering all the possible configurations for $N = 2$, thus finding the frequencies ω_1 and ω_2 that maximize the correlations. Increasing the number of photons involved in the scheme also expands the amount of possible configurations in which the photons can be emitted. As particular cases, I also considered the

processes involving four photons (the general case involving N photons can also be tackled, but at this stage it does not bring much to the discussion): a two-photon bundle heralding another two-photon bundle, or a single photon heralding the emission of a three-photon bundle. In both cases, I show the particular set of frequencies that maximize the correlations and therefore the heralding process. This paves the way towards the development of an efficient source of *heralded* N-photon bundles.

When considering the effect that the process of detecting the light has on the light itself, one must bear in mind that the spectral resolution of the detector induces a temporal uncertainty, which results in a shuffling of the detection times of the photons. Such a temporal scrambling cannot be assessed through the density matrix formalism, as is consists of an statistical average over many realizations, which wash out the variations in the detection times from the individual quantum trajectories. Instead, I turned to the Quantum Monte Carlo technique introduced by Mølmer, Castin, and Dalibard (1993) and upgraded it to account for the detection process. In doing so, I verified the reality of the photon correlations obtained through del Valle et al. (2012)'s *Theory of Frequency-filtered and Time-resolved Correlations*. This tool becomes particularly important for the design of heralded N-photon sources.

After considering the sources of Quantum Light, I discussed their effect on fundamental optical targets, namely a harmonic oscillator, a two-level system and weakly interacting bosonic particles. I established the ways in which it was advantageous for these targets to be excited with quantum rather than classical light. While the Hilbert space of the two-level system is finite and can be readily mapped through the Bloch sphere, the counterpart for the harmonic oscillator is infinite and there is not a standard map to chart the regions of the Hilbert space that are accessible to the harmonic oscillator. I showed that a way to chart such a space is to consider the mean occupation of the harmonic oscillator and the N-order correlations among the photons emitted by it. Already in this case, I showed that there is a fundamental limit, beyond which no states of the harmonic oscillator are allowed. The states at the boundary are given by a superposition of two Fock states of consecutive number of photons, which are the generalization of Fock states to non-integer mean population. Using the photon correlations and the mean population as charting rulers, I was able to determine the region of the Hilbert space that the harmonic oscillator can access when it is excited, and then to show the gain that one obtains when the excitation is done by the light emitted by a two-level system. In particular, I have shown that there is a large region of the Hilbert space of the harmonic oscillator for which the mean population lies between one and two, while the second-order correlation function lies below $1/2$. This observation implies that the commonly used criterion that affirms that whenever the photon correlation of the emitted light satisfies $g^{(2)} < 1/2$, then the light has been emitted by a single-photon source, is incorrect and should not be used as such. Regarding the two-level system as a target, I have shown that exciting it with classical light already lets it access all its Hilbert space, and therefore there is no advantage in using Quantum Light. However, I proceeded to study systematically the question of strong coupling between the source of quantum light and the driven two-level system, increasing the level of complexity of the driven mechanism. Namely, starting with a two-level system driven by a thermal reservoir, or a laser (driving it into the Heitler or the Mollow regime), then considering a cavity under either incoherent or coherent excitation, and finishing with a one-atom laser as the most realistic model for a classical source of light. With these sources, I showed the various regimes in which the target two-level system is dressed and how the rich structure of energy transitions is weighted. Finally, I have shown that the single-photon character of the two-level system can be enhanced when it is excited with antibunched light: the value of the filtered photon correlations are reduced as compared to what one would obtain when exiting the two-level system classically.

Afterwards, I considered the excitation of weakly interacting particles, taking as an example exciton polaritons. I showed that the emission from a Mollow triplet, with its rich underlying structure, can be used as a versatile source of Quantum Light providing light with all types of statistical properties, depending on the frequency at which one collects it. Sweeping the Mollow

triplet around the resonance frequency of polaritons, I showed that the latter accommodates the properties of the emitted light, i.e., the triplet structure is mapped onto the populations, and the statistical properties of the light are transposed to the photon correlations of the polaritons, which also vary across frequencies. While the population is symmetric with respect to the resonance frequency of the polariton, the photon correlations display a slight asymmetry due to the interacting character of the polaritons. I have shown that such an asymmetry, which can be quantified and extracted through a convolution of the photon correlations, is directly proportional to the interaction strength of the polaritons, thus rendering the excitation with the Mollow triplet a novel spectroscopic technique, that I have named "*Mollow Spectroscopy*" and which can be applied to a wide range of systems of interacting particles.

The state-of-the-art polariton samples are still not ready to interface with quantum dots, and therefore the spectroscopic technique cannot be implemented yet. However, they can be coupled to single photons emitted by, e.g., nonlinear crystals emitting pairs of entangled photons. Sending one of these entangled photons onto the polariton sample, letting it evolve in the cavity until its eventual re-emission, and then measuring the correlations between the photon emitted by the cavity and the other entangled photon, experimentalist implementing this scheme were able to demonstrate for the first time the generation of a genuine quantum state of the polariton field, and to show that, despite their highly dissipative character, polaritons are suitable to maintain quantum correlations. Furthermore, sending the single photon to the polariton sample already containing a condensate of particles, I showed that the number of polaritons in the condensate and the interaction among them allows to shift the phase of the photon that goes through the cavity, while still maintaining the quantum correlations. Thus, I have demonstrated that polaritons are, in principle, a suitable platform for the development of quantum technologies leading towards the implementation of a quantum computer.

9.2 ESPAÑOL

En esta Tesis abordé el problema de excitar objetivos ópticos mediante Luz Cuántica. Para hacer esto, primero tuve que describir varios tipos de fuentes de Luz Cuántica, cuya emisión consiste bien en fotones individuales o en paquetes de N fotones, y luego los he usado para excitar los sistemas más fundamentales: un oscilador armónico (el arquetipo de las partículas bosónicas) un sistema de dos niveles (el prototipo de las partículas fermionicas) y polaritones (partículas que se originan del acoplo fuerte entre un bosón y un fermión). Los resultados principales de mi trabajo se pueden resumir de la siguiente manera.

Aunque las expectativas de una fuente de fotones individuales comprenden una lista muy larga, algunas de las características más importantes de tal fuente son su capacidad de suprimir la emisión de multiples fotones, la indistinguibilidad de los fotones emitidos y su tasa de repetición. Mientras que muchos grupos experimentales están esforzando para optimizar el comportamiento de este tipo de fuentes, ellos también omiten un punto fundamental de la mecánica cuántica: la medida. He mostrado que cuando la detección de la luz es tenida en cuenta de manera auto-consistente, algunas de las fuentes de fotones individuales se comportan de maneras inesperadas. La resolución en frecuencia que se gana al filtrar la emisión induce una indeterminación en el tiempo en el que dichos fotones han sido detectados. Al filtrar la emisión de un sistema de dos niveles, se estropea su perfecto anti-agrupamiento. Así, un criterio para identificar fuentes de fotones individuales, y para clasificar su desempeño en relación con la supresión de la emisión de multiples fotones, tiene que incluir el efecto de la detección. De esta manera, he propuesto un criterio—la norma-N—la cual cuantifica que tanto se suprimen las correlaciones entre fotones a todos los órdenes (en lugar de considerar simplemente el segundo orden, $g^{(2)} \ll 1$, que es el criterio usado comúnmente), y he mostrado su aplicación a varios mecanismos que proporcionan luz anti-agrupada. Usando este criterio, he mostrado que un sistema de dos niveles excitado coherentemente es la mejor fuente de fotones individuales que se puede obtener considerando únicamente la excitación clásica. Sin embargo, también he mostrado que usando la emisión de dicho sistema de dos niveles para excitar otro

sistema de dos niveles mejora la calidad de los fotones individuales de la luz emitida. Por otra parte, he considerado el problema de un sistema de dos niveles excitado débilmente por un laser, entrando así en el régimen de Heitler. A pesar de que varios grupos experimentales han afirmado que la emisión de uno de estos sistemas es monocromática y anti-agrupada, es fácil ver que estas dos propiedades no coexisten cuando se considera la detección. Sin embargo, he mostrado que el efecto negativo de la detección se puede superar haciendo una interferencia entre la luz emitida y un campo coherente. Haciendo la interferencia de la manera adecuada se puede reestablecer el anti-agrupamiento perdido, incluso luego de filtrar en un rango menor al ancho de banda natural del sistema de dos niveles.

Usando el hecho de que filtrar la emisión de una fuente de fotones individuales dañan las correlaciones entre los fotones, haciendo posible que estas fuentes emitan más de un fotón a la vez, volcamos nuestra atención a las fuentes de N fotones. En particular, me concentré en la luz emitida por la fluorescencia resonante en el régimen de Mollow. Elaborando sobre la propuesta de Sánchez Muñoz et al. (2014a) para una fuente de paquetes de N fotones, consideré las correlaciones entre fotones individuales emitidos a una frecuencia ω_1 y un paquete de N fotones a otra frecuencia ω_2. Presenté un análisis sistemático de estas correlaciones, considerando todas las posibles configuraciones para $N = 2$, encontrando así las frecuencias ω_1 y ω_2 que maximizan las correlaciones. Al aumentar el número de fotones involucrados en el esquema también expande el número de configuraciones en las que los fotones pueden ser emitidos. Como casos particulares, también consideré los procesos que relacionan cuatro fotones (el caso general para N fotones también se puede abordar, pero en este punto no son útiles para la discusión): un paquete de dos fotones anunciando la emisión de otro paquete de dos fotones, o un fotón individual anunciando la emisión de un paquete de tres fotones. En ambos casos, mostré el grupo de frecuencias que maximiza las correlaciones y el proceso de anunciamiento. Esto cementa las fundaciones para el desarrollo de fuentes eficiente de paquetes de N fotones anunciados.

Al considerar el efecto que tiene la detección sobre la luz, hay que tener en cuenta que la resolución espectral del detector induce una indeterminación temporal, la cual resulta en el reordenamiento de los tiempos en los que los fotones son detectados. Este reacomodamiento temporal no se puede acceder mediante el formalismo de la matriz densidad, pues este consiste en un promedio estadístico sobre muchas realizaciones, el cual difumina las variaciones en los tiempos de detecciones de las trayectorias cuánticas individuales. En cambio, consideré la técnica de Monte Carlo Cuántico introducida por Mølmer, Castin, and Dalibard (1993), y la mejoré incluyendo en ella el proceso de detección. Al hacer esto, verifiqué la veracidad de las correlaciones obtenidas por la *Teoría de Correlaciones filtradas en frecuencia y resueltas en tiempo* de del Valle et al. (2012). Esta herramienta es particularmente importante para el diseño de fuentes de N fotones anunciados.

Después de considerar las fuentes de Luz Cuántica, discutí su efecto en objetivos ópticos fundamentales: un oscilador armónico, un sistema de dos niveles y partículas bosónicas levemente interactuantes. Establecí las maneras en las que resulta ventajoso para estos objetivos el ser excitados por luz cuántica en vez de luz clásica. Mientas que el espacio de Hilbert del sistema de dos niveles es finito y puede mapearse fácilmente en la esfera de Bloch, la contraparte para el oscilador armónico es infinito y no hay una manera estándar de trazar las regiones del espacio de Hilbert que pueden ser accedidas por el oscilador armónico. Mostré que una manera de mapear este espacio es considerar la ocupación media y la función de correlación de orden N de los fotones emitidos por el oscilador. Incluso en este caso mostré que hay un límite fundamental, más allá del cual no hay estados accesibles por el oscilador. Los estados en la frontera están dados por una superposición de estados de Fock con número de fotones consecutivos, los cuales proveen la generalización de los estados de Fock para ocupaciones medias dadas por números no enteros. Usando las funciones de correlación y la población media como medidas del mapa, pude determinar las regiones del espacio de Hilbert que el oscilador armónico puede acceder al ser excitado, y luego mostrar la ganancia que se obtiene cuando la excitación se hace mediante la emisión de un sistema de dos niveles. En particular, mostré que

hay una región enorme del espacio de Hilbert del oscilador armónico en el que la ocupación media es entre uno y dos, mientras que la función de correlación de segundo orden es menor que 1/2. Esta observación implica que el criterio ampliamente usado, que afirma que cuando las correlaciones entre fotones satisfacen la condición $g^{(2)} < 1/2$, entonces la luz ha sido emitida por una fuente de fotones individuales, es incorrecto y no debe seguir usándose. Con relación al sistema de dos niveles como objetivo, he mostrado que excitándolo mediante luz clásica ya lo deja acceder todo el espacio de Hilbert, de manera que en este aspecto no hay ninguna ganancia al usar luz cuántica. Sin embargo, procedí a estudiar sistemáticamente el problema del acoplo fuerte entre la fuente de luz cuántica y el sistema de dos niveles bajo excitación, aumentando progresivamente la complejidad del mecanismo de excitación. Así, comencé por un sistema de dos niveles excitado por un reservorio térmico o un laser (haciéndolo entrar ya sea en el régimen de Heitler o de Mollow), luego consideré una cavidad bajo excitación coherente o incoherente, y terminé con el laser de un átomo como el modelo más realista de una fuente de luz clásica. Con estas fuentes, mostré los varios regímenes en los que el sistema de dos niveles puede ser vestido y como la rica estructura energética es pesada. Finalmente, mostré que la calidad de los fotones individuales emitidos por un sistema de dos niveles aumenta cuando este último es excitado mediante luz anti-agrupada: el valor de las correlaciones filtradas es reducido a comparación del que se obtendría al excitar el sistema de dos niveles clásicamente.

Luego, consideré la excitación de partículas levemente interactuantes, usando como ejemplo los polaritones excitónicos. Mostré que la emisión de un triplete de Mollow, con su rica estructura subyacente, puede ser usada como una fuente versátil de luz cuántica capaz de proveer todos los tipos de propiedades estadísticas, dependiendo de la frecuencia a las que se observe. Barriendo el triplete de Mollow alrededor de la frecuencia de resonancia de los polaritones, mostré que este último toma las propiedades de la luz emitida, i.e., la estructura del triplete es mapeada en la población, y las propiedades estadísticas de la luz emitida se transmiten a las correlaciones entre los polaritones, las cuales también cambian con la frecuencia. Mientras que la población es simétrica con respecto a la frecuencia de los polaritones, las correlaciones tienen una pequeña asimetría debida a la interacción entre polaritones. Mostré que esta asimetría, que puede ser cuantificada y extraída mediante una convolución de las correlaciones, es directamente proporcional a la fuerza de la interacción de los polaritones, lo cual convierte a la excitación con el triplete de Mollow en una técnica espectroscópica, la cual he denominado "*espectroscopía de Mollow*" y la cual puede aplicarse a una gran variedad de sistemas de partículas interactuantes.

Las muestras de polaritones más avanzadas aún no están preparadas para ser acopladas con puntos cuánticos, y por lo tanto la técnica espectroscópica no puede ser implementada todavía. Sin embargo, ellas pueden ser acopladas con fotones individuales emitidos por, e.g., cristales no-lineales que emiten pares de fotones entrelazados. Enviando uno de estos fotones a la muestra de polaritones, dejándolo evolucionar dentro de la cavidad hasta que eventualmente es re-emitido, y luego midiendo las correlaciones entre este fotón y el otro fotón entrelazado, un grupo de experimentalistas que implementó este esquema demostraron por primera vez la generación de un estado genuinamente cuántico del campo de polaritones, y mostraron que, a pesar de su carácter disipativo, los polaritones son idóneos para mantener correlaciones cuánticas. Además, enviando el fotón individual a una muestra de polaritones que ya albergaba un condensado de partículas, mostré que el número de polaritones en el condensado y la interacción entre ellos permite rotar la fase del fotón que atraviesa la cavidad, a la vez que mantiene las correlaciones cuánticas. Así, he demostrado que los polaritones son, en principio, una plataforma adecuada para el desarrollo de tecnologías cuánticas que lleven a la implementación de un computador cuántico.

A

THEORETICAL TOOLS

A.1 OBSERVABLES AND THE QUANTUM REGRESSION THEOREM

A.1.1 *The Liouvillian and the Steady-state*

The Master equation (1.20) is a first order differential equation, which can always be written in a matrix form:

$$\partial_t \vec{\rho} = \mathcal{L}\,\vec{\rho}\,, \tag{A.1}$$

where $\vec{\rho}$ is the vector representation of the density matrix ρ and $\mathcal{L}$ is the *Liouvillian* associated to the Master equation under consideration. Formally, the solution to the Eq. (A.1) is obtained by direct integration

$$\vec{\rho}(t) = \exp\left[\int_0^t \mathcal{L}\,dt\right]\vec{\rho}_0\,, \tag{A.2}$$

where $\vec{\rho}_0$ is the density matrix at the initial time, and we have not made any assumptions regarding the temporal dependence of the Liouvillian. Once the state of the system is known as a function of time, we have all the information about it. In particular, we can obtain the mean value of any operator of the system, which is given by the average of the operator weighted by the density matrix. Thus, if $\hat{O}$ is an operator of the system, its mean value due to the dynamics induced by the Master equation (A.1) will be given by

$$\langle\hat{O}\rangle(t) = \mathrm{Tr}\left(\hat{O}\rho(t)\right)\,, \tag{A.3}$$

where $\rho(t)$ is the density matrix of Eq. (A.2) in its matrix representation. The description of the state of the system as a function of time is specially relevant when the transient state is important, as is the case when excitation of the system also depends on time, e.g., when the driving is pulsed. Conversely, when the excitation is done through a continuous wave, the Master equation (1.20) takes the state into a unique and non-trivial (non-vacuum) steady-state. Such a state becomes independent of the time, and therefore it follows the equation

$$\mathcal{L}\vec{\rho} = 0\,, \tag{A.4}$$

which becomes an algebraic problem of finding a non-trivial solution for $\vec{\rho}$. The solution to Eq. (A.4) is given by some density matrix ρ_{ss}, with which the mean value of the operators of the system become independent of the time

$$\langle\hat{O}\rangle = \mathrm{Tr}\left(\hat{O}\rho_{\mathrm{ss}}\right)\,, \tag{A.5}$$

where the mean value $\langle\cdot\rangle$ has no dependence on the time, thus indicating that it is taken on the steady-state. From an experimental point of view, the relevant mean values are those that are *observable*, namely, those that correspond to hermitian operators for which the mean values are real-valued. For instance, we will use repeatedly observables such as the population of a field and its second-order correlation function, defined as in Eq. (1.32).

A.1.2 *Quantum Regression Theorem*

The solution of the Master equation gives us all the information about the system. In particular, computing the steady-state of the system, one is able to obtain time-independent mean values for any operator of the system. However, with the formalism descried so far, we are not able to

evaluate correlations involving two times. In particular, the first- and second-order correlation functions of the field

$$G^{(1)}(t, t+\tau) \propto \langle a^\dagger(t) a(t+\tau) \rangle \,, \tag{A.6a}$$

$$G^{(2)}(t, t+\tau) \propto \langle a^\dagger(t) a^\dagger(t+\tau) a(t+\tau) a(t) \rangle \,, \tag{A.6b}$$

are specially important, as they are related to the emission spectrum and the photon statistics of the emission, respectively. The method to compute the correlations of the type of Eq. (A.6) was found by Lax (1963) and Lax (1967) and it is known as the *Quantum Regression formula*. In his book, Carmichael (2008) demonstrates that the two-times correlations can be obtained directly from the density matrix at some time t and the Liouvillian that generates the dynamics as

$$\langle \hat{O}_1(t+\tau) \hat{O}_2(t) \rangle = \mathrm{Tr} \left\{ \hat{O}_1(0) e^{\mathcal{L}\tau} [\hat{O}_2(0) \rho(t)] \right\} \,, \tag{A.7a}$$

$$\langle \hat{O}_1(t) \hat{O}_2(t+\tau) \rangle = \mathrm{Tr} \left\{ \hat{O}_2(0) e^{\mathcal{L}\tau} [\rho(t) \hat{O}_1(0)] \right\} \,, \tag{A.7b}$$

$$\langle \hat{O}_1(t) \hat{O}_2(t+\tau) \hat{O}_3(t) \rangle = \mathrm{Tr} \left\{ \hat{O}_2(0) e^{\mathcal{L}\tau} [\hat{O}_3 \rho(t) \hat{O}_1] \right\} \,, \tag{A.7c}$$

where $\hat{O}_j$ are operators of the system, with $j = 1, 2, 3$, and in all cases we have taken $\tau \geq 0$. In the steady-state, the dependence on the time t vanishes and we are left with correlations that depend solely on the time-delay τ.

The method described above is particularly useful when one looks for numerical results, rather than for analytical expressions, and when the dimensions of the Liouvillian are not so large as to make the calculation of its exponential intractable. An alternative approach to compute the correlations consists on searching a full set of operators that contains the dynamics of the correlator of interest. Oftentimes, the dimension of such a set of operators is smaller than the dimensions of the Liouvillian. Following the steps of Carmichael (2008) we start with assuming that for any arbitrary operator $\hat{O}$ there exists a set of operators $\{\hat{A}_\mu\}$ such that

$$\mathrm{Tr} \left[\hat{A}_\mu (\mathcal{L} \hat{O}) \right] = \sum_\lambda M_{\mu\lambda} \mathrm{Tr} (\hat{A}_\lambda \hat{O}) \,, \tag{A.8}$$

where $M_{\mu\lambda}$ are constants. The equation above implies, in particular, that the temporal dynamics of the set of operators $\{\hat{A}_\mu\}$ is given by a reduced matrix, to which we will refer as the *regression matrix*, with a smaller dimension than th Hilbert space:

$$\partial_t \langle \hat{A}_\mu \rangle = \sum_\lambda M_{\mu\lambda} \hat{A}_\lambda \,. \tag{A.9}$$

This relation can be written in a matrix form as

$$\partial_t \vec{A} = M \vec{A} \tag{A.10}$$

where $\vec{A} = (\hat{A}_1, \hat{A}_2, \cdots)^T$. Then, using the results from Eq. (A.7), we find that the two-times correlators follow the differential equation (now for the delay τ instead of the time t)

$$\partial_\tau \langle \hat{O}(t) \hat{A}_\mu (t+\tau) \rangle = \sum_\lambda M_{\mu\lambda} \langle \hat{O}(t) \hat{A}_\lambda (t+\tau) \rangle \,, \tag{A.11}$$

which in matrix form reads

$$\partial_\tau \langle \hat{O}(t) \vec{A}(t+\tau) \rangle = M \langle \hat{O}(t) \vec{A}(t+\tau) \rangle \,, \tag{A.12}$$

where the matrix M is the same that generates the t-dynamics of the set of operators $\{\hat{A}_\mu\}$, as shown in Eq. (A.10). Analogously, it is easy to show that the two-time correlators involving three operators are given by

$$\partial_\tau \langle \hat{O}_1(t) \vec{A}(t+\tau) \hat{O}_2(t) \rangle = M \langle \hat{O}_1(t) \vec{A}(t+\tau) \hat{O}_2(t) \rangle \,. \tag{A.13}$$

In both cases the two-time correlators can obtained formally by integrating the differential equation, which then leaves us with

$$\langle \hat{O}(t)\vec{A}(t+\tau)\rangle = e^{M\tau}\langle \hat{O}(t)\vec{A}(t)\rangle\,, \tag{A.14a}$$

$$\langle \hat{O}_1(t)\vec{A}(t+\tau)\hat{O}_2(t)\rangle = e^{M\tau}\langle \hat{O}_1(t)\vec{A}(t)\hat{O}_2(t)\rangle\,, \tag{A.14b}$$

which also involves computing the exponential of a matrix, which is general is smaller than the Liouvillian.

A.1.3 *Delayed correlations*

Using the methods described in the previous section, we are ready to compute the temporal correlations of the field, as given by Eq. (A.6). From them, we can extract the information regarding the energy profile and the temporal structure with which the photons are emitted from the system.

The emission spectrum of the system described with annihilation operator c, which could be either bosonic or fermionic, is obtained from the real part of the Fourier transform of the first-order correlation function:

$$S(\omega) = \frac{1}{\pi}\frac{1}{n_c}\Re\int_0^\infty \langle c^\dagger c(\tau)\rangle e^{i\omega\tau}d\tau\,. \tag{A.15}$$

where $n_c = \langle c^\dagger c\rangle$ is the mean population of the system in the steady-state. We can use the formal solution to the τ-correlators in Eq. (A.7) or Eq. (A.14) to simplify the expression for the spectrum. For instance, the correlator $\langle c^\dagger c(\tau)\rangle$ is given by

$$\langle c^\dagger c(\tau)\rangle = \mathrm{Tr}\left[ce^{\mathcal{L}\tau}(\rho_{ss}c^\dagger)\right]\,, \tag{A.16}$$

where ρ_{ss} is the density matrix in the steady-state. Replacing this expression on the spectrum we obtain

$$S(\omega) = \frac{1}{\pi}\frac{1}{n_c}\mathrm{Tr}\left[c\int_0^\infty e^{\mathcal{L}\tau}e^{i\omega\tau}(\rho_{ss}c^\dagger)d\tau\right]\,, \tag{A.17}$$

which can be integrated formally to yield

$$S(\omega) = -\frac{1}{\pi}\frac{1}{n_c}\mathrm{Tr}\left[c\frac{1}{\mathcal{L}+i\omega\mathbb{1}}(\rho_{ss}c^\dagger)\right]\,, \tag{A.18}$$

where $\mathbb{1}$ is the identity matrix and we have assumed that the integral becomes zero in the limit of infinite delay. Note that now the problem has been reduced to obtain the inverse of the matrix $(\mathcal{L}+i\omega\mathbb{1})$ instead of computing the exponential of the Liouvillian.

Similarly, we can use the expression of either Eq. (A.7) or Eq. (A.14) to generalize the second-order correlation function defined in Eq. (1.32) to include finite delays as

$$g^{(2)}(\tau) = \frac{\langle c^\dagger(c^\dagger c)(\tau)c\rangle}{\langle c^\dagger c\rangle^2} = \frac{\mathrm{Tr}\left\{c^\dagger ce^{\mathcal{L}\tau}[c\rho_{ss}c^\dagger]\right\}}{\mathrm{Tr}\left\{c^\dagger c\rho_{ss}\right\}^2}\,, \tag{A.19}$$

where c is the annihilation operator of the mode under investigation.

A.2 NUMERICAL METHODS FOR THE REGRESSION MATRIX

This first appendix is devoted to the numerical methods I have used to obtain the results shown in this Thesis.

The solutions to the Master equations of the type given in Eq. (1.20), are commonly obtained numerically, finding directly the density matrix ρ that satisfies the equation. However, while the numerical solutions are readily obtained, finding analytic expressions is a rather complicated

task. Conversely, one can obtain the solution to the equation, by computing the differential equation that rule the behaviour of the mean values of the operators of interest, e.g., $\langle\hat{O}\rangle(t) = \mathrm{Tr}(\rho(t)\hat{O})$.

Such a differential equation is obtained directly from the Master equation, taking into account the linearity of the derivatives and the trace:

$$\partial_t\langle\hat{O}\rangle = \partial_t\mathrm{Tr}(\rho\hat{O}) = \mathrm{Tr}(\partial_t\rho\hat{O})\,. \tag{A.20}$$

Note that the rightmost term of Eq. (A.20) includes explicitly the term $\partial_t\rho$, which is exactly the left-hand side of the Master equation in Eq. (1.20). Thus, replacing the right-hand side of the master equation onto Eq. (A.20), we have

$$\begin{aligned}
\partial_t\langle\hat{O}\rangle &= \mathrm{Tr}(\partial_t\rho\hat{O})\,, && \text{(A.21a)}\\
&= \frac{i}{\hbar}\mathrm{Tr}\left\{[\rho,H]\hat{O}\right\} + \sum_k \frac{\gamma_k}{2}\mathrm{Tr}\left\{\left(2L_k\rho L_k^\dagger + L_k^\dagger L_k\rho + \rho L_k^\dagger L_k\right)\hat{O}\right\}\,, && \text{(A.21b)}\\
&= \frac{i}{\hbar}\mathrm{Tr}\left(\rho H\hat{O} - \rho\hat{O}H\right) + \sum_k \frac{\gamma_k}{2}\mathrm{Tr}\left(2\rho L_k^\dagger\hat{O}L_k - \rho\hat{O}L_k^\dagger L_k - \rho L_k^\dagger L_k\hat{O}\right)\,, && \text{(A.21c)}\\
&= \frac{i}{\hbar}\left\langle[H,\hat{O}]\right\rangle + \sum_k \frac{\gamma_k}{2}\left(2\left\langle L_k^\dagger\hat{O}L_k\right\rangle - \left\langle\hat{O}L_k^\dagger L_k\right\rangle - \left\langle L_k^\dagger L_k\hat{O}\right\rangle\right)\,, && \text{(A.21d)}
\end{aligned}$$

where we have used the cyclic property of the trace and in Eq. (A.21c) we have placed the density matrix on the leftmost part of each term. Thus, the most general term that one can write to study a system made of N quantum objects—each of which modelled with annihilation operator c_j—is given by replacing

$$\hat{O} = {c_1^\dagger}^{\mu_1}c_1^{\nu_1}{c_2^\dagger}^{\mu_2}c_2^{\nu_2}\cdots{c_N^\dagger}^{\mu_N}c_N^{\nu_N}\,, \tag{A.22}$$

where μ_k and ν_k are integers for all k, and which may take values as large as the truncation of the Hilbert space of their respective quantum object. Therefore, Eq. (A.22) provides a set of coupled equations, that can be condensed as

$$\partial_t\vec{v} = \mathcal{M}\vec{v}\,, \tag{A.23}$$

where $\vec{v} = \{1\,,\langle c_1^\dagger\rangle\,,\langle c_1^\dagger c_1\rangle\,,\cdots\langle{c_1^\dagger}^{\mu_1}c_1^{\nu_1}{c_2^\dagger}^{\mu_2}c_2^{\nu_2}\cdots\,,{c_N^\dagger}^{\mu_N}c_N^{\nu_N}\rangle\}^{\mathrm{T}}$ is a vector containing all the mean values, and $\mathcal{M}$ is a matrix containing all the coefficients of the coupled equations. As the matrix $\mathcal{M}$ can also be used to compute the delayed-correlations—using the Quantum Regression Theorem showed in section A.1.2—it is commonly referred to as the *Regression Matrix*. In the following subsections we will show the sets of equations that result from the Master equation of some of the fundamental systems discussed on this Thesis.

A.2.1 *Incoherently driven harmonic oscillator*

The master equation of a harmonic oscillator with annihilation operator a and driven incoherently is given by (we set $\hbar = 1$)

$$\partial_t\rho = i[\rho,\omega_a a^\dagger a] + \frac{\gamma_a}{2}\mathcal{L}_a\rho + \frac{P_a}{2}\mathcal{L}_{a^\dagger}\rho\,, \tag{A.24}$$

where ω_a is the frequency of the harmonic oscillator, which leaks and receives photons at rates γ_a and P_a, respectively, and $\mathcal{L}_c\rho = (2c^\dagger\rho c - c^\dagger c\rho - \rho c^\dagger c)$.

In this case, the general equation is yields the following term

$$\partial_t\left\langle{a^\dagger}^\mu a^\nu\right\rangle = \left\{i\omega_a(\mu-\nu) - \frac{\gamma_a - P_a}{2}(\mu+\nu)\right\}\left\langle{a^\dagger}^\mu a^\nu\right\rangle + P_a\mu\nu\left\langle{a^\dagger}^{\mu-1}a^{\nu-1}\right\rangle\,, \tag{A.25}$$

from which it is already clear that i) the incoherently driving cannot build coherence on the harmonic oscillator (as the off-diagonal elements only decay from their initial condition), and ii) the harmonic oscillator is left in a thermal state, for which the Nth-order correlation function, defined in Eq. (1.32), is given by $g_a^{(N)} = N!$.

A.2.2 *Coherently driven harmonic oscillator*

The master equation of a harmonic oscillator with annihilation operator a and driven incoherently is given by (we set $\hbar = 1$)

$$\partial_t \rho = i[\rho, (\omega_a - \omega_{\mathrm{L}})a^\dagger a + \Omega_a(a^\dagger + a)] + \frac{\gamma_a}{2}\mathcal{L}_a\rho\,, \tag{A.26}$$

where ω_a is the frequency of the harmonic oscillator, which leaks photons at a rate γ_a, and ω_{L} and Ω_a are the frequency and intensity of the coherent field driving the harmonic oscillator.

In this case, the general equation is yields the following term

$$\partial_t \left\langle a^{\dagger\,\mu} a^\nu \right\rangle = \left\{ i(\omega_a - \omega_{\mathrm{L}})(\mu - \nu) - \frac{\gamma_a}{2}(\mu + \nu) \right\} \left\langle a^{\dagger\,\mu} a^\nu \right\rangle + i\Omega_a \left(\mu \left\langle a^{\dagger\,\mu-1} a^\nu \right\rangle - \nu \left\langle a^{\dagger\,\mu} a^{\nu-1} \right\rangle \right)\,. \tag{A.27}$$

This time, the analysis is not trivial, but with a bit of care one can notice that the harmonic oscillator is left in a coherent state, for which the Nth-order correlation function is given by $g_a^{(N)} = 1$.

A.2.3 *Incoherently driven two-level system*

The master equation of a two-level system with annihilation operator σ and driven incoherently is given by (we set $\hbar = 1$)

$$\partial_t \rho = i[\rho, \omega_\sigma \sigma^\dagger \sigma] + \frac{\gamma_\sigma}{2}\mathcal{L}_\sigma\rho + \frac{P_\sigma}{2}\mathcal{L}_{\sigma^\dagger}\rho\,, \tag{A.28}$$

where ω_σ is the frequency of the two-level system, which leaks and receives photons at rates γ_σ and P_σ, respectively, and $\mathcal{L}_c\rho = (2c^\dagger\rho c - c^\dagger c\rho - \rho c^\dagger c)$.

In this case, the general equation is yields the following term

$$\partial_t \left\langle \sigma^{\dagger\,\mu} \sigma^\nu \right\rangle = \left\{ i\omega_\sigma(\mu - \nu) - \frac{\gamma_\sigma + P_\sigma}{2}(\mu + \nu) \right\} \left\langle \sigma^{\dagger\,\mu} \sigma^\nu \right\rangle + P_\sigma \mu\nu \left\langle \sigma^{\dagger\,1-\mu} \sigma^{1-\nu} \right\rangle\,. \tag{A.29}$$

As in the case of the excitation of a harmonic oscillator, the incoherent driving is unable to build coherence on the density matrix of the two-level system. Also, note that the steady-state solution for the population bounded by 1, to which it goes asymptotically as the rate of driving becomes larger than the decay rate. Besides, note that all the N-photon correlation function vanish, but the reason is the fermionic character of the two-level system: the operator σ is nilpotent, meaning that, regardless of the driving scheme, it always satisfies $\sigma^2 = 0$.

A.2.4 *Coherently driven two-level system*

The master equation of a two-level system with annihilation operator σ and driven coherently is given by (we set $\hbar = 1$)

$$\partial_t \rho = i[\rho, (\omega_\sigma - \omega_{\mathrm{L}})\sigma^\dagger \sigma + \Omega_\sigma(\sigma^\dagger + \sigma)] + \frac{\gamma_\sigma}{2}\mathcal{L}_\sigma\rho\,, \tag{A.30}$$

where ω_σ is the frequency of the harmonic oscillator, which leaks photons at a rate γ_σ, and ω_{L} and Ω_σ are the frequency and intensity of the coherent field driving the harmonic oscillator.

In this case, the general equation is yields the following term

$$\begin{aligned}\partial_t \left\langle \sigma^{\dagger\,\mu} \sigma^\nu \right\rangle = &\left\{ i(\omega_\sigma - \omega_{\mathrm{L}})(\mu - \nu) - \frac{\gamma_\sigma}{2}(\mu + \nu) \right\} \left\langle \sigma^{\dagger\,\mu} \sigma^\nu \right\rangle + \\ &+ i\Omega_\sigma \left\{ [\mu + 2\nu(1 - \mu)] \left\langle \sigma^{\dagger\,1-\mu} \sigma^\nu \right\rangle - [\nu + 2\mu(1 - \nu)] \left\langle \sigma^{\dagger\,\mu} \sigma^{1-\nu} \right\rangle \right\}\,.\end{aligned} \tag{A.31}$$

A.2.5 *Cascaded excitation*

Using the emission from a quantum source to drive another system is done through the Cascaded coupling, which modifies the Master equation of the system to

$$\partial_t \rho = i[\rho, H] + \frac{\gamma_\sigma}{2}\mathcal{L}_\sigma \rho + \frac{\gamma_a}{2}\mathcal{L}_a \rho + \frac{\sqrt{\alpha\gamma_\sigma\gamma_a}}{2}\left\{[\sigma\rho, a^\dagger] + [a, \rho\sigma^\dagger]\right\} . \tag{A.32}$$

Here, H is the Hamiltonian describing the *free evolution* of the two quantum systems under consideration, of which we have given particular cases in the previous subsections. Furthermore, the source of the quantum light is described with the annihilation operator σ, and set to decay spontaneously at a rate γ_σ. The target of the quantum excitation, on the other hand, is described through the annihilation operator a and set to decay with rate γ_a. The rightmost term of Eq. (A.32) describes the unidirectional coupling between the source and the target. López Carreño, del Valle, and Laussy (2018) showed that the factor $\alpha = (1-\chi_1)(1-\chi_2)$ takes into account the amount of the light that i) the source (σ) and the target (a) are allows to emit to free space (with fractions χ_1 and χ_2, respectively) and ii) the fraction of the light that is emitted by the system as a whole, i.e., the exact source cannot be distinguished. Such an amount of light corresponds to a fraction $(1-\chi_1)(1-\chi_2)$ of the total light.

Following the procedure done in Eq. (A.21), we find that the contribution from the cascaded coupling to the general differential equation for the correlators is give by

$$\partial_t \langle \hat{O} \rangle = \sqrt{\alpha\gamma_\sigma\gamma_a}\left(\left\langle a^\dagger \sigma \hat{O}\right\rangle - \left\langle \sigma^\dagger a \hat{O}\right\rangle + \left\langle \hat{O} a^\dagger \sigma\right\rangle + \left\langle \hat{O}\sigma^\dagger a\right\rangle\right) . \tag{A.33}$$

Note that the complete differential equation needs to include the terms coming from the Hamiltonian and the independent decay of the source and the target of the excitation.

Depending on the type of object that we are using as the source and the target, whether they follow the Fermi or the Bose-Einstein statistics, the equation ruling the dynamics of the correlators is different:

1. Bosonic source & bosonic target:

$$\partial_t \left\langle \sigma^{\dagger\,\mu}\sigma^\nu a^{\dagger\,m} a^n\right\rangle = -\sqrt{\alpha\gamma_\sigma\gamma_a}\left(m\left\langle \sigma^{\dagger\,\mu+1}\sigma^\nu a^{\dagger\,m-1}a^n\right\rangle + n\left\langle \sigma^{\dagger\,\mu}\sigma^{\nu+1}a^{\dagger\,m}a^{n-1}\right\rangle\right) . \tag{A.34}$$

2. Bosonic source & fermionic target:

$$\begin{aligned}\partial_t \left\langle \sigma^{\dagger\,\mu}\sigma^\nu a^{\dagger\,m} a^n\right\rangle = -\sqrt{\alpha\gamma_\sigma\gamma_a}\Big(&m\left\langle \sigma^{\dagger\,\mu+1}\sigma^\nu a^{\dagger\,1-m}a^n\right\rangle + n\left\langle \sigma^{\dagger\,\mu}\sigma^{\nu+1}a^{\dagger\,m}a^{1-n}\right\rangle - \\ &-2m(1-n)\left\langle \sigma^{\dagger\,\mu+1}\sigma^\nu a^{\dagger\,m}a^{1-n}\right\rangle - 2n(1-m)\left\langle \sigma^{\dagger\,\mu}\sigma^{\nu+1}a^{\dagger\,1-m}a^n\right\rangle\Big) .\end{aligned} \tag{A.35}$$

3. Fermionic source & bosonic target:

$$\begin{aligned}\partial_t \left\langle \sigma^{\dagger\,\mu}\sigma^\nu a^{\dagger\,m} a^n\right\rangle = -\sqrt{\alpha\gamma_\sigma\gamma_a}\Big(&m(1-\mu)\left\langle \sigma^{\dagger\,1-\mu}\sigma^\nu a^{\dagger\,m-1}a^n\right\rangle + \\ &+ n(1-\nu)\left\langle \sigma^{\dagger\,\mu}\sigma^{1-\nu}a^{\dagger\,m}a^{n-1}\right\rangle\Big) .\end{aligned} \tag{A.36}$$

4. Fermionic source & fermionic target:

$$\begin{aligned}\partial_t \left\langle \sigma^{\dagger\,\mu}\sigma^\nu a^{\dagger\,m} a^n\right\rangle = -\sqrt{\alpha\gamma_\sigma\gamma_a}\Big(&m(1-\mu)\left\langle \sigma^{\dagger\,1-\mu}\sigma^\nu a^{\dagger\,1-m}a^n\right\rangle + n(1-\nu)\left\langle \sigma^{\dagger\,\mu}\sigma^{1-\nu}a^{\dagger\,m}a^{1-n}\right\rangle - \\ &- 2m(1-n)(1-\mu)\left\langle \sigma^{\dagger\,1-\mu}\sigma^\nu a^{\dagger\,m}a^{1-n}\right\rangle - 2n(1-m)(1-\nu)\left\langle \sigma^{\dagger\,\mu}\sigma^{1-\nu}a^{\dagger\,1-m}a^n\right\rangle\Big) .\end{aligned} \tag{A.37}$$

B

MATHEMATICAL DEMONSTRATIONS

B.1 PROOF THAT FOCK DUOS BOUND THE $(n_a, g_a^{(2)})$ SPACE

We prove mathematically that there are no states below the boundary set by Eq. (5.4) but at least one for every point above, thus showing that our charting of the Hilbert space in the $(n_a, g_a^{(2)})$ space as defined by this boundary is complete.

proposition: *For a given population $n_a \in \mathbb{R}$, the maximum antibunching is given by a superposition of at most two consecutive Fock states.* □

First, for any $n_a \in \mathbb{R}$, there exists a superposition of at most two consecutive Fock states that provides this population, namely:

$$\sqrt{\lfloor n_a \rfloor - n_a + 1}\,\big|\lfloor n_a \rfloor\big\rangle + \sqrt{n_a - \lfloor n_a \rfloor}\,\big|\lfloor n_a \rfloor + 1\big\rangle\,. \tag{B.1}$$

We can write without loss of generality the generic state (5.1) as:

$$\sum_{k=-\lfloor n_a \rfloor}^{\infty} \sqrt{p(\lfloor n_a \rfloor + k)}\,\big|\lfloor n_a \rfloor + k\big\rangle\,, \tag{B.2}$$

where we remind that $p(n) = |\alpha_n|^2$ and is such that $\sum_{n=0}^{\infty} p(n) = 1$. Restricting ourselves to states with the same population implies:

$$\sum_{k=-\lfloor n_a \rfloor}^{\infty} p(\lfloor n_a \rfloor + k)(\lfloor n_a \rfloor + k) = n_a\,. \tag{B.3}$$

The second order correlation function for such states is then found as:

$$g_a^{(2)} = \sum_{k=-\lfloor n_a \rfloor}^{\infty} (\lfloor n_a \rfloor + k)(\lfloor n_a \rfloor + k - 1)p(\lfloor n_a \rfloor + k)/n_a^2\,. \tag{B.4}$$

Since n_a is the same for both states (B.1) and (B.2) when Eq. (B.3) is satisfied, it is enough for the comparison of their antibunching to consider the difference of their $n_a^2 g_a^{(2)}$ (effectively getting rid of the denominator, which simplifies the notations). We call this difference $\Delta G_a^{(2)}$ and find, from Eq. (5.4) and (B.4):

$$\begin{aligned}
\Delta G_a^{(2)} &= \sum_{k=-\lfloor n_a \rfloor}^{\infty} (\lfloor n_a \rfloor + k)(\lfloor n_a \rfloor + k - 1)p(\lfloor n_a \rfloor + k) - \\
&\qquad - \lfloor n_a \rfloor(\lfloor n_a \rfloor - 1)(\lfloor n_a \rfloor - n_a + 1) - \lfloor n_a \rfloor(\lfloor n_a \rfloor + 1)(n_a - \lfloor n_a \rfloor)\,, \\
&= \left[\sum_{k\neq\{0,1\}} (\lfloor n_a \rfloor + k)(\lfloor n_a \rfloor + k - 1)p(\lfloor n_a \rfloor + k)\right] + \\
&\quad + \lfloor n_a \rfloor(\lfloor n_a \rfloor - 1)(p(\lfloor n_a \rfloor) - \lfloor n_a \rfloor + n_a) + \lfloor n_a \rfloor(\lfloor n_a \rfloor + 1)(p(\lfloor n_a \rfloor + 1) - (n_a - \lfloor n_a \rfloor))\,,
\end{aligned}$$

where we have separated the terms $k = 0, 1$ from the sum and re-arranged the factors. Now, since $p(\lfloor n_a \rfloor + 1) = 1 - p(\lfloor n_a \rfloor) - \sum_{k\neq\{0,1\}} p(\lfloor n_a \rfloor + k)$ from the probability normalization, we arrive to:

$$\Delta G_a^{(2)} = \left[\sum_{k\neq\{0,1\}} (k-1)(2\lfloor n_a \rfloor + k)p(\lfloor n_a \rfloor + k)\right] - 2\lfloor n_a \rfloor(p(\lfloor n_a \rfloor) - \lfloor n_a \rfloor + n_a - 1)\,. \tag{B.5}$$

On the other hand, from Eq. (B.3), we can isolate:

$$p(\lfloor n_a \rfloor) = \lfloor n_a \rfloor - n_a + 1 + \sum_{k \neq \{0,1\}} (k-1) p(\lfloor n_a \rfloor + k)\,, \tag{B.6}$$

which, injected back in Eq. (B.5), yields:

$$\Delta G_a^{(2)} = \sum_{k \neq \{0,1\}} k(k-1) p(\lfloor n_a \rfloor + k)\,.$$

This is the final result, since all the terms in the sum are non-negative, we can conclude that $\Delta G_a^{(2)} \geq 0$. The inequality is maximized when *all* the probabilities $p(\lfloor n_a \rfloor + k) = 0$ for $k \neq \{0, 1\}$, i.e., for the states of type (B.1). When n_a is an integer, i.e., $\lfloor n_a \rfloor = n_a$, the maximum antibunching is obtained with the Fock state $|n_a\rangle$. QED.

proposition: *For a given population $n_a \in \mathbb{R}$ and any positive real number δ, there is at least one state such that $\Delta G^{(2)} = \delta$.* □

Let us consider the set of states with population $n_a = \sum_n np(n)$. We can construct a state ρ_0 with population n_a in the following way:

$$\rho_0 = p(0)\,|0\rangle\langle 0| + p(\lfloor n_a \rfloor)\,|\lfloor n_a \rfloor\rangle\langle \lfloor n_a \rfloor| + (1 - p(0) - p(\lfloor n_a \rfloor))\,|k\rangle\langle k|\ .$$

Imposing the population constraint, we obtain the following condition:

$$p(0) = \left(\frac{k - n_a}{k}\right) - p(\lfloor n_a \rfloor)\left(\frac{k - \lfloor n_a \rfloor}{k}\right)\,,$$

where we have assumed that $\lfloor n_a \rfloor < k \in \mathbb{N}$. The $g_a^{(2)} = g_{a*}^{(2)} + \delta$ of this state is given by:

$$g_a^{(2)} n_a^2 = \lfloor n_a \rfloor(\lfloor n_a \rfloor - 1) p(\lfloor n_a \rfloor) + k(k-1)(1 - p(0) - p(\lfloor n_a \rfloor))\,,$$

from which we can obtain $p(\lfloor n_a \rfloor)$:

$$p(\lfloor n_a \rfloor) = \frac{n_a\left(k - 1 - n_a g_a^{(2)}\right)}{\lfloor n_a \rfloor(k - \lfloor n_a \rfloor)}\,.$$

If $\delta > 0$ we can find an integer number $k > \max(n_a g_a^{(2)}, \lfloor n_a \rfloor)$ such that $0 \leq p(\lfloor n_a \rfloor) \leq 1$. Considering that this state is not made of two consecutive Fock states, the accessible $g_a^{(2)}$s are larger than $g_{a*}^{(2)}$. Of course, when $p(0) = 0$ and $k = \lfloor n_a \rfloor + 1$, ρ_0 is the maximally antibunched state and $g_a^{(2)} = g_{a*}^{(2)}$. When $n_a < 1$, $\lfloor n_a \rfloor = 0$, and the procedure above fails. In such case, we can build another state,

$$\rho_1 = p(0)\,|0\rangle\langle 0| + p(1)\,|1\rangle\langle 1| + (1 - p(0) - p(1))\,|k\rangle\langle k|\ ,$$

such that $n_a = p(1) + k(1 - p(0) - p(1))$. From this constraint we obtain the following condition:

$$p(1) = \frac{k(1 - p(0)) - n_a}{k - 1}\,.$$

The $g_a^{(2)}$ of this state is given by:

$$\begin{aligned} g_a^{(2)} n_a^2 &= k(k-1)(1 - p(0) - p(1))\,, \\ &= k(n_a + p(0) - 1)\,, \end{aligned}$$

from which we conclude that:

$$p(0) = \frac{g_a^{(2)} n_a^2 + k(1 - n_a)}{k}\,.$$

Again, we can always find an integer $k > 1$, such that $0 \leq p(0) \leq 1$.

B.2 MASTER EQUATION FOR THE CASCADE OF TWO SYSTEMS

The theory of cascaded systems developed by Gardiner and Zoller (2000) allows to couple unidirectionally two quantum systems, so that one of them can be regarded as the source of the excitation that the other one receives, thus behaving as an optical target. The formalism is based on writting the Langevin equation for the operators of the two systems:

$$\dot{a}_1 = i[a_1, H_{\text{sys}}] - [a_1, c_1^\dagger]\left\{\frac{\gamma_1}{2}c_1 + \sqrt{\gamma_1}b_{\text{in}}^{(1)}\right\} + \left\{\frac{\gamma_1}{2}c_1^\dagger + \gamma_1 b_{\text{in}}^{\dagger(1)}\right\}[a_1, c_1]\,, \tag{B.7a}$$

$$\dot{a}_2 = i[a_2, H_{\text{sys}}] - [a_2, c_2^\dagger]\left\{\frac{\gamma_2}{2}c_2 + \sqrt{\gamma_2}b_{\text{in}}^{(2)}\right\} + \left\{\frac{\gamma_2}{2}c_2^\dagger + \gamma_2 b_{\text{in}}^{\dagger(2)}\right\}[a_2, c_2]\,, \tag{B.7b}$$

where a_k is any operator of system k that decays at a rate γ_k, $H_{\text{sys}} = H_1 + H_2$ is the total Hamiltonian, describing the *independent* dynamics of the two systems, and $b_{\text{in}}^{(k)}$ is the input field of system k. Since we are considering that the system 2 (the target) is the driven by the emission of system 1 (the source), is clear that the input field of system 2 corresponds to the output field of system 1:

$$b_{\text{in}}^{(2)} = b_{\text{in}}^{(1)} + \sqrt{\gamma_1}c_1\,, \tag{B.8}$$

where the last term of the rhs describe the emission of system 1, due only to its internal dynamics. Converting Eq. (B.7) to a Quantum Ito equation and assuming that the input field has an amplitude $\mathcal{E}$, we can obtain a master equation for the operator $\rho(t)$ describing the cascaded system, which takes the form:

$$\partial_t\rho = i[\rho, H_1 + H_2] - \left[\mathcal{E}(\sqrt{\gamma_1}c_1^\dagger + \sqrt{\gamma_2}c_2^\dagger) - \mathcal{E}^*(\sqrt{\gamma_1}c_1 + \sqrt{\gamma_2}c_2), \rho\right] + \\ + \frac{\gamma_1}{2}\mathcal{L}_{c_1}\rho + \frac{\gamma_2}{2}\mathcal{L}_{c_2}\rho + \sqrt{\gamma_1\gamma_2}\left\{[c_1\rho, c_2^\dagger] + [c_2, \rho c_1^\dagger]\right\}\,, \tag{B.9}$$

which is the equation to which we refer to in Section 6.2. We note that the last term of the firs line in Eq. (B.11) is a Hamilonian–like term, that describes the coherent driving of the two systems in the cascade.

B.3 MASTER EQUATION FOR THE CASCADE OF AN ARBITRARY NUMBER OF SYSTEMS

The formalism presented in Appendix B.2 can be generalized to the cascade of an arbitrary number of systems. In such case, each operator of the kth system would satisfy the Langevin equation,

$$\dot{a}_k = i[a_k, H_{\text{sys}}] - [a_k, c_k^\dagger]\left\{\frac{\gamma_k}{2}c_k\sqrt{\gamma_k}b_{\text{in}}^{(k)}\right\} + \left\{\frac{\gamma_k}{2}c_k^\dagger + \gamma_k b_{\text{in}}^{\dagger(k)}\right\}[a_k, c_k]\,, \tag{B.10}$$

where now the input field of the kth system corresponds to the output field of the $(k-1)$th system, i.e., $b_{\text{in}}^{(k)} = b_{\text{in}}^{(1)} + \sum_{j=1}^{k-1}\sqrt{\gamma_j}c_j$. As in the Appendix B.2, we can derive the master equation for operator $\rho(t)$ describing the cascaded system,

$$\partial_t\rho = \sum_{j=1}^{N}\left(i[\rho, H_j] + \frac{\gamma_k}{2}\mathcal{L}_{c_k}\rho - \sqrt{\gamma_j}\left[\mathcal{E}c_j^\dagger - \mathcal{E}^*c_j, \rho\right]\right) + \sum_{j=2}^{N}\sum_{l=1}^{j-1}\sqrt{\gamma_j\gamma_l}\left\{[c_l\rho, c_j^\dagger] + [c_j, \rho c_l^\dagger]\right\}\,, \tag{B.11}$$

which is the equation that we refer to in Section 6.5.

C

SAMPLE & SETUP USED FOR THE EXPERIMENTS IN CHAPTER 8

The microcavity used for the experiments is made of two sets of distributed Bragg mirrors—each of them made of 20 layers—confining light, and one $In_{0.05}Ga_{0.95}As$ quantum well confining excitons. The quantum well is placed at the antinode of the cavity to maximize the interaction between the light and the exciton, and thus allowing the access into the strong coupling regime, as seen three decades ago by Weisbuch et al. (1992). The experiment can be understood as four parts: the generation of the entangled photons, the measurement of the signal-photon tomography, the (classical) excitation of the polaritons, and the measurement of the polariton-photon tomography. The first part is accomplished with a Sagnac interferometer, excited with a single-mode diode laser at 405 nm, which is pumped with a power of 6.5 mW and bandwidth FWHM < 5 pm. The power selection is achieved by fixing a half-wave plate (HWP) before a polarizing beam splitter (PBS), and the horizontal output polarization is again rotated in a desired arbitrary polarization before a dichronic mirror (DM). In order to increase the efficiency of the PPKTP crystal, we introduced a lens to focalize the diode right on top of the crystal. The second and the fourth sections of the setup are used for the tomography measurement. The idler photon goes through the polariton source, which consists on a cryostat at 20 K and a pressure of 100 mbar. The single-photon is focused on the surface of the microcavity and the emitted photons are recollected with a second lens sending them directly to the fourth stage (the idler's tomography stage). In the experiment measuring nonlinear effects, an additional laser is sent to the microcavity at a particular angle. The transmitted photons given by the laser are covered with a diaphragm (pinhole, PH) at the Fourier plane of the recollection lens.

The entanglement measurement is made following the work of Altepeter, Jeffrey, and Kwiat (2005), performing a tomographic analysis. In our case, we apply a hypercomplete tomography by projecting the bipartite state onto a combination set of three bases: logical ($|H\rangle$ & $|V\rangle$), diagonal ($|+\rangle = (|H\rangle + |V\rangle)/\sqrt{2}$ & $|-\rangle = (|H\rangle - |V\rangle)/\sqrt{2}$), and circular ($|R\rangle = (|H\rangle + i|V\rangle)/\sqrt{2}$ & $|L\rangle = (|H\rangle - i|V\rangle)/\sqrt{2}$). Each local projection is done by applying a rotation in a QWP and a HWP, followed by a PBS as polarization filter (see Fig 7.5). Finally, the remaining photons belonging to the qubit of both the signal and the idler are coupled to a single-mode optical fiber, connected to an avalanche photo-detector (APD). The reconstruction of the state sees the relative coincident count events among all the mentioned projections during the desired integration time. In that way, we measure the state by projecting many copies of the same. The measurements corresponding to the results reported in Fig. 8.1 were unavoidably affected by the presence of the classical continuous-wave laser which was minimised by momentum selection of the polariton signal (as shown in Fig. 7.5d). The contribution of this noise, however, was subtracted from the raw data by performing desynchronised tomography for each power of the external laser. The calibration of the population and density in presence of the classical laser was obtained by means of four different parameters: the pumping power, the photon energy, the polariton lifetime and the laser spot size. The amount of photons/sec delivered by the laser to the microcavity were calculated as the ratio Power/Energy. Given the transmission of the microcavity and assuming the same amount of photons to be emitted on both sides of the sample, only 0.5% of the photons become polaritons. Multiplying this rate of polaritons/sec by the lifetime of a polariton (measured as 3 ps), gives a maximum of 380 polaritons for the highest power used. The polariton density was obtained by dividing by the spot area of the driving laser ($A = 706\,\mu m^2$).

BIBLIOGRAPHY

Aaronson, S. and A. Arkhipov (2011). "The computational complexity of linear optics". In: *Proceedings of the 43rd Annual ACM Symposium on Theory of Computing*, p. 333. DOI: 10.1145/1993636.1993682.

Aerts, S., P. Kwiat, J.-Å. Larsson, and M. Żukowski (1999). "Two-Photon Franson-Type Experiments and Local Realism". In: *Phys. Rev. Lett.* 83, p. 2872. DOI: 10.1103/PhysRevLett.83.2872.

Agarwal, G. S. (1976). "Exact Solution for the Influence of Laser Temporal Fluctuations on Resonance Fluorescence". In: *Phys. Rev. Lett.* 37, p. 1383. DOI: 10.1103/PhysRevLett.37.1383.

Aharonovich, I., D. Englund, and M. Toth (2016). "Solid-state single-photon emitters". In: *Nat. Photon.* 10, p. 631. DOI: 10.1038/nphoton.2016.186.

Al-Khuzheyri, R., A. C. Dada, J. Huwer, T. S. Santana, J. Skiba-Szymanska, et al. (2016). "Resonance fluorescence from a telecom-wavelength quantum dot". In: *Appl. Phys. Lett.* 109, p. 163104. DOI: 10.1063/1.4965845.

Allen, L. and J. H. Eberly (1987). *Optical Resonance and Two-Level Atoms*. Dover.

Almand-Hunter, A. E., H. Li, S. T. Cundiff, M. Mootz, M. Kira, and S. W. Koch (2014). "Quantum droplets of electrons and holes". In: *Nature* 506, p. 471. DOI: 10.1038/nature12994.

Altepeter, J. B., D. Branning, E. Jeffrey, T. C. Wei, P. G. Kwiat, R. T. Thew, J. L. O'Brien, M. A. Nielsen, and A. G. White (2003). "Ancilla-Assisted Quantum Process Tomography". In: *Phys. Rev. Lett.* 90, p. 193601. DOI: 10.1103/PhysRevLett.90.193601.

Altepeter, J.B., E.R. Jeffrey, and P. G. Kwiat (2005). "Photonic State Tomography". In: *Advances in Atomic, Molecular, and Optical Physics* 52, p. 105. DOI: 10.1016/S1049-250X(05)52003-2.

Anderson, H. L., E. Fermi, and Leo Szilard (1939). "Neutron Production and Absorption in Uranium". In: *Phys. Rev.* 56, p. 284. DOI: 10.1103/PhysRev.56.284.

Apanasevich, P.A. and S. Ya. Kilin (1977). "Light-induced correlations in spontaneous emission". In: *Phys. Lett. A* 62, p. 83. DOI: 10.1016/0375-9601(77)90956-2.

Arnoldus, H. F. and G. Nienhuis (1984). "Photon correlations between the lines in the spectrum of resonance fluorescence". In: *J. Phys. B.: At. Mol. Phys.* 17, p. 963. DOI: 10.1088/0022-3700/17/6/011.

Aspect, A., G. Roger, S. Reynaud, J. Dalibard, and C. Cohen-Tannoudji (1980). "Time Correlations between the Two Sidebands of the Resonance Fluorescence Triplet". In: *Phys. Rev. Lett.* 45, p. 617. DOI: 10.1103/PhysRevLett.45.617.

Aßmann, M. and M. Bayer (2011). "Nonlinearity sensing via photon-statistics excitation spectroscopy". In: *Phys. Rev. A* 84, p. 053806. DOI: 10.1103/PhysRevA.84.053806.

Badano, A. and J. Kanicki (2001). "Monte Carlo analysis of the spectral photon emission and extraction efficiency of organic light-emitting devices". In: *J. Appl. Phys.* 90, p. 1827. DOI: 10.1063/1.1385571.

Bamba, M., A. Ĭmamoḡlu, I. Carusotto, and C. Ciuti (2011). "Origin of strong photon antibunching in weakly nonlinear photonic molecules". In: *Phys. Rev. A* 83, 021802(R). DOI: 10.1103/PhysRevA.83.021802.

Baym, G. (1998). "The Physics of Hanbury Brown–Twiss Intensity Interferometry: from Stars to Nuclear Collisions". In: *Acta Physica Polonica B* 29, p. 1839.

Bengtsson, I. and K. Życzkowski (2008). *Geometry of Quantum States*. Cambridge Univ. Press.

Bodenstein, M. (1913). "Eine Theorie der photochemischen Reaktionsgeschwindigkeiten". In: *Z. Phys. Chem.* 85, p. 390. DOI: 10.1515/zpch-1913-8512.

Bondurant, R. S. and J. H. Shapiro (1984). "Squeezed states in phase-sensing interferometers". In: *Phys. Rev. D* 30, p. 2548. DOI: 10.1007/978-1-4757-0605-5_91.

Brannen, E. and H. I. S. Ferguson (1956). "The question of correlations between photons in coherent light rays". In: *Nature* 178, p. 481. DOI: 10.1038/178481a0.

Brassard, G., N. Lütkenhaus, T. Mor, and B. C. Sanders (2000). "Limitations on Practical Quantum Cryptography". In: *Phys. Rev. Lett.* 85, p. 1330. DOI: 10.1103/PhysRevLett.85.1330.

Broome, M.A., A. Fedrizzi, S. Rahimi-Keshari, J. Dove, S. Aaronson, T.C. Ralph, and A.G. White (2013). "Photonic boson sampling in a tunable circuit". In: *Science* 15, p. 794. DOI: 10.1126/science.1231440.

Carmele, A., A. Knorr, and M. Richter (2009). "Photon statistics as a probe for exciton correlations in coupled nanostructures". In: *Phys. Rev. B* 79, p. 035316. DOI: 10.1103/PhysRevB.79.035316.

Carmichael, H. J. (1985). "Photon Antibunching and Squeezing for a Single Atom in a Resonant Cavity". In: *Phys. Rev. Lett.* 55, p. 2790. DOI: 10.1103/PhysRevLett.55.2790.

— (1993a). "An open systems approach to Quantum Optics". In: Springer. Chap. 6 Photoelectric Detection II, p. 110. DOI: 10.1007/978-3-540-47620-7.

— (1993b). "Quantum trajectory theory for cascaded open systems". In: *Phys. Rev. Lett.* 70, p. 2273. DOI: 10.1103/PhysRevLett.70.2273.

— (2008). *Statistical methods in quantum optics 1*. Springer.

Carmichael, H. J., R. J. Brecha, and P. R. Rice (1991). "Quantum interference and collapse of the wavefunction in cavity QED". In: *Opt. Commun.* 82, p. 73. DOI: 10.1016/0030-4018(91)90194-I.

Carmichael, H. J., S. Singh, R. Vyas, and P. R. Rice (1989). "Photoelectron waiting times and atomic state reduction in resonance fluorescence". In: *Phys. Rev. A* 39, p. 1200. DOI: 10.1103/PhysRevA.39.1200.

Ceperley, D. and B. Alder (1986). "Quantum Monte Carlo". In: *Science* 231, p. 555. DOI: 10.1126/science.231.4738.555.

Christmann, G., G. Tosi, N. G. Berloff, P. Tsotsis, P. S. Eldridge, Z. Hatzopoulos, P. G. Savvidis, and J. J. Baumberg (2012). "Polariton ring condensates and sunflower ripples in an expanding quantum liquid". In: *Phys. Rev. B* 85, p. 235303. DOI: 10.1103/PhysRevB.85.235303.

Cilibrizzi, P., H. Ohadi, T. Ostatnicky, A. Askitopoulos, W. Langbein, and P. Lagoudakis (2014). "Linear Wave Dynamics Explains Observations Attributed to Dark Solitons in a Polariton Quantum Fluid". In: *Phys. Rev. Lett.* 113, p. 103901. DOI: 10.1103/PhysRevLett.113.103901.

Cirac, J. I., P. Zoller, H. J. Kimble, and H. Mabuchi (1997). "Quantum State Transfer and Entanglement Distribution among Distant Nodes in a Quantum Network". In: *Phys. Rev. Lett.* 78, p. 3221. DOI: 10.1103/PhysRevLett.74.4091.

Clauser, J. F., M. A. Horne, A. Shimony, and R. A. Holt (1969). "Proposed Experiment to Test Local Hidden-Variable Theories". In: *Phys. Rev. Lett.* 23, p. 880. DOI: 10.1103/PhysRevLett.23.880.

Cohen-Tannoudji, C. N. and S. Reynaud (1977). "Dressed-atom description of resonance fluorescence and absorption spectra of a multi-level atom in an intense laser beam". In: *J. Phys. B.: At. Mol. Phys.* 10, p. 345. DOI: 10.1088/0022-3700/10/3/005.

— (1979). "Atoms in Strong Light-Fields: Photon Antibunching in Single Atom Fluorescence". In: *Phil. Trans. R. Soc. Lond. A* 293, p. 223. DOI: 10.1098/rsta.1979.0092.

Coles, R. J., D. M. Price, J. E. Dixon, B. Royall, E. Clarke, P. Kok, M. S. Skolnick, A. M. Fox, and M. N. Makhonin (2016). "Chirality of nanophotonic waveguide with embedded quantum emitter for unidirectional spin transfer". In: *Nat. Comm.* 7, p. 11183. DOI: 10.1038/ncomms11183.

Collet, M. J. and C. W. Gardiner (1984). "Squeezing of intracavity and travelling-wave light fields produced in parametric amplification". In: *Phys. Rev. A* 30, p. 1386. DOI: 10.1103/PhysRevA.30.1386.

Crespi, A., R. Osellame, R. Ramponi, D. J. Brod, E. F. Galvão, N. Spagnolo, C. Vitelli, E. Maiorino, P. Mataloni, and F. Sciarrino (2013). "Integrated multimode interferometers

with arbitrary designs for photonic boson sampling". In: *Nat. Photon.* 7, p. 545. DOI: 10.1038/nphoton.2013.112.

Cresser, J. D. (1987). "Intensity correlations of frequency-filtered light fields". In: *J. Phys. B.: At. Mol. Phys.* 20, p. 4915. DOI: 10.1088/0022-3700/20/18/027.

Cuevas, Á., J. C. López Carreño, B. Silva, M. De Giorgi, D. G. Suárez-Forero, et al. (2018). "First observation of the quantized exciton-polariton field and effect of interactions on a single polariton". In: *Science Advances* 4, eaao6814. DOI: 10.1126/sciadv.aao6814.

Dada, A. C., T. S. Santana, R. N. E. Malein, A. Koutroumanis, Y. Ma, J. M. Zajac, J. Y. Lim, J. D. Song, and B. D. Gerardot (2016). "Indistinguishable single photons with flexible electronic triggering". In: *Optica* 3, p. 493. DOI: 10.1364/OPTICA.3.000493.

Dalibard, J., Y. Castin, and K. Mølmer (1992). "Wave-function approach to dissipative processes in quantum optics". In: *Phys. Rev. Lett.* 68, p. 580. DOI: 10.1103/PhysRevLett.68.580.

Dalibard, J. and S. Reynaud (1983). "Correlation signals in resonance fluorescence : interpretation via photon scattering amplitudes". In: *J. Phys. France* 44, p. 1337. DOI: 10.1051/jphys:0198300440120133700.

Daveau, R. S., K. C. Balram, T. Pregnolato, J. Liu, E. H. Lee, et al. (2017). "Efficient fiber-coupled single photon source based on quantum dots in a photonic crystal waveguide". In: *Optica* 4, p. 178. DOI: 10.1364/OPTICA.4.000178.

del Valle, E. (2013). "Distilling one, two and entangled pairs of photons from a quantum dot with cavity QED effects and spectral filtering". In: *New J. Phys.* 15, p. 025019. DOI: 10.1088/1367-2630/15/2/025019.

del Valle, E. and F. P. Laussy (2010). "Mollow Triplet under Incoherent Pumping". In: *Phys. Rev. Lett.* 105, p. 233601. DOI: 10.1103/PhysRevLett.105.233601.

— (2011). "Regimes of strong light-matter coupling under incoherent excitation". In: *Phys. Rev. A* 84, p. 043816. DOI: 10.1103/PhysRevA.84.043816.

del Valle, E., F. P. Laussy, and C. Tejedor (2009). "Luminescence spectra of quantum dots in microcavities. II. Fermions". In: *Phys. Rev. B* 79, p. 235326. DOI: 10.1103/PhysRevB.79.235326.

del Valle, E., A. González-Tudela, F. P. Laussy, C. Tejedor, and M. J. Hartmann (2012). "Theory of Frequency-Filtered and Time-Resolved N-Photon Correlations". In: *Phys. Rev. Lett.* 109, p. 183601. DOI: 10.1103/PhysRevLett.109.183601.

del Valle, E., B. Silva, C. Sánchez Muñoz, J. C. López Carreño, and F.P. Laussy (2018). "Loss of antibunching". In: *In preparation*.

Delteil, A., T. Fink, A. Schade, S. Höffling, C. Schneider, and A. Ĭmamoğlu (2019). "Towards polariton blockade of confined exciton-polaritons". In: *Nat. Mater.* 18, p. 219. DOI: 10.1038/s41563-019-0282-y.

Deutsch, D. (1985). "Quantum theory, the Church-Turing Principle and the universal quantum computer". In: *Proc. R. Soc. Lond. A* 400, p. 97. DOI: 10.1098/rspa.1985.0070.

Deveaud, B. (2016). "Polariton interactions in semiconductor microcavities". In: *C. R. Physique* 17, p. 874. DOI: 10.1016/j.crhy.2016.05.004.

di Martino, G., Y. Sonnefraud, S. Kéna-Cohen, M. Tame, Ş. K. Özdemir, M. S. Kim, and S. A. Maier (2012). "Quantum Statistics of Surface Plasmon Polaritons in Metallic Stripe Waveguides". In: *Nano Lett.* 12, p. 2504. DOI: 10.1021/nl300671w.

Diaz-Camacho, G., E. Zubizarreta Casalengua, J. C. López Carreño, E. del Valle, and F. P. Laussy (2019). "Herealded N-photon source". In: *In preparation*.

Dicke, R. H. (1954). "Coherence in Spontaneous Radiation Processes". In: *Phys. Rev.* 93, p. 99. DOI: 10.1103/PhysRev.93.99.

Dietrich, A., M. Bürk, E. S. Steiger, L. Antoniuk, T. T. Tran, M. Nguyen, I. Aharonovich, F. Jelezko, and A. Kubanek (2018). "Obsevation of Fourier transform limited lines in hexagonal boron nitride". In: *Phys. Rev. B* 98, 081414(R). DOI: 10.1103/PhysRevB.98.081414.

Ding, X., Y. He, Z.-C. Duan, N. Gregersen, M.-C. Chen, et al. (2016). "On-Demand Single Photons with High Extraction Efficiency and Near-Unity Indistinguishability from a Resonantly

Driven Quantum Dot in a Micropillar". In: *Phys. Rev. Lett.* 116, p. 020401. DOI: 10.1103/PhysRevLett.116.020401.

Dominici, L., D. Colas, S. Donati, J. P. Restrepo Cuartas, M. De Giorgi, et al. (2014). "Ultrafast Control and Rabi Oscillations of Polaritons". In: *Phys. Rev. Lett.* 113, p. 226401. DOI: 10.1103/PhysRevLett.113.226401.

Dong, S., T. Huang an Y. Liu, J. Wang, Liantuan Xiao G. Zhang, and S. Jia (2007). "Fast recognition of single molecules based on single-event photon statistics". In: *Phys. Rev. A* 76, p. 063820. DOI: 10.1103/PhysRevA.76.063820.

Dory, C., K. A. Fischer, K. Müller, K. G. Lagoudakis, T. Sarmiento, A. Rundquist, J. L. Zhang, Y. Kelaita, N. V. Sapra, and J. Vučković (2017). "Tuning the photon statistics of a strongly coupled nanophotonic system". In: *Phys. Rev. A* 95, p. 023804. DOI: 10.1103/PhysRevA.95.023804.

Downing, C. A., J. C. López Carreño, F. P. Laussy, E. del Valle, and A. I. Fernández-Domínguez (2019). "Quasichiral Interactions between Quantum Emitters at the Nanoscale". In: *Phys. Rev. Lett.* 122, p. 057401. DOI: 10.1103/PhysRevLett.122.057401.

Dum, R., A. S. Parkins, P. Zoller, and C. W. Gardiner (1992). "Monte Carlo simulation of master equations in quantum optics for vacuum, thermal, and squeezed reservoirs". In: *Phys. Rev. A* 46, p. 4382. DOI: 10.1103/PhysRevA.46.4382.

Eberly, J.H. and K. Wódkiewicz (1977). "The time-dependent physical spectrum of light". In: *J. Opt. Soc. Am.* 67, p. 1252. DOI: 10.1364/JOSA.67.001252.

Einstein, A. (1905). "Concerning an Heuristic Point of View Toward the Emission and Transformation of Light". In: *Annalen der Physik* 17, p. 132. DOI: 10.1002/andp.19053220607.

Eisaman, M. D., J. Fan, A. Migdall, and S. V. Polyakov (2011). "Single-photon sources and detectors". In: *Rev. Sci. Instrum.* 82, p. 071101. DOI: 10.1063/1.3610677.

Faist, J., F. Capasso, D. L. Sivco, C. Sirtori, A. L. Hutchinson, and A. Y. Cho (1994). "Quantum Cascade Laser". In: *Science* 264, p. 553. DOI: 10.1126/science.264.5158.553.

Fedrizzi, A., T. Herbst, A. Poppe, T. Jennewein, and A. Zeilinger (2007). "A wavelength-tunable fiber-coupled source of narrowband entangled photons". In: *Opt. Express* 15, p. 15377. DOI: 10.1364/OE.15.015377.

Ferrier, L., E. Wertz, R. Johne, D. D. Solnyshkov, P. Senellart, I. Sagnes, A. Lemaître, G. Malpuech, and J. Bloch (2011). "Interactions in Confined Polariton Condensates". In: *Phys. Rev. Lett.* 106, p. 126401. DOI: 10.1103/PhysRevLett.106.126401.

Feynman, R. (1998). *Statistical Mechanics*. 2nd ed. Advanced Book Classics. Perseus Books.

Feynman, R. P., Jr. F. L. Vernon, and R. W. Hellwarth (1957). "Geometrical Representation of the Schrödinger Equation for Solving Maser Problems". In: *J. Appl. Phys.* 28, p. 49. DOI: 10.1063/1.1722572.

Feynman, R. P., R. B. Leighton, and M. Sands (1971). *Feynman Lectures on Physics*. Vol. III. Addison Wesley.

Filip, R. and Jr. L. Mišta (2011). "Detecting Quantum States with a Positive Wigner Function beyond Mixtures of Gaussian States". In: *Phys. Rev. Lett.* 106, p. 200401. DOI: 10.1103/PhysRevLett.106.200401.

Flayac, H. and V. Savona (2014). "Heralded Preparation and Readout of Entangled Phonons in a Photonic Crystal Cavity". In: *Phys. Rev. Lett.* 113, p. 143603. DOI: 10.1103/PhysRevLett.113.143603.

Gardiner, C. W. (1993). "Driving a quantum system with the output field from another driven quantum system". In: *Phys. Rev. Lett.* 70, p. 2269. DOI: 10.1103/PhysRevLett.70.2269.

Gardiner, C. W. and A. S. Parkins (1994). "Driving atoms with light of arbitrary statistics". In: *Phys. Rev. A* 50, p. 1792. DOI: 10.1103/PhysRevA.50.1792.

Gardiner, C. W. and C. M. Savage (1984). "A multimode quantum theory of a degenerate parametric amplifier in a cavity". In: *Opt. Commun.* 59, p. 173. DOI: 10.1016/0030-4018(84)90342-0.

Gardiner, G. W. and P. Zoller (2000). *Quantum Noise*. 2nd. Springer-Verlag, Berlin.

Garraway, B.M., M.S. Kim, and P.L. Knight (1995). "Quantum jumps, atomic shelving and Monte Carlo fluorescence spectra". In: *Opt. Commun.* 117, p. 560. DOI: 10.1016/0030-4018(95)00231-V.

Gericke, C. Gies F., L. Gartner, S. Holzinger, C. Hopfmann, T. Heindel, et al. (2017). "Strons light-matter coupling in the presence of lasing". In: *Phys. Rev. A* 96, p. 023806. DOI: 10.1103/PhysRevA.96.023806.

Gerry, C. C. and P. L. Knight (2005). *Introductory Quantum Optics*. Cambridge University Press.

Glasserman, P. (1994). *Monte Carlo methods in Financial engineering*. Springer-Verlag.

Glauber, R. J. (1963). "Photon Correlations". In: *Phys. Rev. Lett.* 10, p. 84. DOI: 10.1103/PhysRevLett.10.84.

Golubev, N. V. and A. I. Kuleff (2014). "Control of populations of two-level systems by a single resonant laser pulse". In: *Phys. Rev. A* 90, p. 035401. DOI: 10.1103/PhysRevA.90.035401.

Gonzalez-Ballestero, C., A. Gonzalez-Tudela, F. J. Garcia-Vidal, and E. Moreno (2015). "Chiral route to spontaneous entanglement generation". In: *Phys. Rev. B* 92, p. 155304. DOI: doi:10.1103/PhysRevB.92.155304.

Gonzalez-Ballestero, C., E. Moreno, F. J. García-Vidal, and A. Gonzalez-Tudela (2016). "Non-reciprocal few-photon devices based on chiral waveguide-emitter couplings". In: *Phys. Rev. A* 94, p. 063817. DOI: 10.1103/PhysRevA.94.063817.

González-Tudela, A., E. del Valle, and F. P. Laussy (2015). "Optimization of photon correlations by frequency filtering". In: *Phys. Rev. A* 91, p. 043807. DOI: 10.1103/PhysRevA.91.043807.

González-Tudela, A., F. P. Laussy, C. Tejedor, M. J Hartmann, and E. del Valle (2013). "Two-photon spectra of quantum emitters". In: *New J. Phys.* 15, p. 033036. DOI: 10.1088/1367-2630/15/3/033036.

Grange, T., N. Somaschi, C. Antón, L. De Santis, G. Coppola, V. Giesz, A. Lemaître, I. Sanges, A. Auffèves, and P. Senellart (2017). "Reducing phonon-induced decoherence in solid-state single-photon sources with cavity quantum electrodynamics". In: *Phys. Rev. Lett.* 118, p. 253602. DOI: 10.1103/PhysRevLett.118.253602.

Groove, R. E., F. Y. Wu, and S. Ezekial (1977). "Measurement of the spectrum of resonance fluorescence from a two-level atom in an intense monochromatic field". In: *Phys. Rev. A* 16, p. 227. DOI: 10.1103/PhysRevA.15.227.

Grosso, G., H. Moon, B. Lienhard, S. Ali, D. K. Efetov, M. M. Furchi, P. Jarillo-Herrero, M. J. Ford, I. Aharonovich, and D. Englund (2017). "Tunable and high-purity room temperature single-photon emission from atomic defects in hexagonal boron nitride". In: *Nat. Comm.* 8, p. 705. DOI: 10.1038/s41467-017-00810-2.

Grundmann, M., O. Stier, and D. Bimberg (1995). "InAs/GaAs pyramidal quantum dots: Strain distribution, optical phonons, and electronic structure". In: *Phys. Rev. B* 52, p. 11969. DOI: 10.1103/PhysRevB.52.11969.

Guimond, P. O., H. Pichler, A. Rauschenbeutel, and P. Zoller (2016). "Chiral quantum optics with V-level atoms and coherent quantum feedback". In: *Phys. Rev. A* 94, p. 033829. DOI: 10.1103/PhysRevA.94.033829.

Hanbury Brown, R. (1991). *Boffin: A Personal Story of the Early Days of Radar, Radio Astronomy and Quantum Optics*. CRC Press.

Hanbury Brown, R. and R. Q. Twiss (1956a). "Correlation between Photons in two Coherent Beams of Light". In: *Nature* 177, p. 27. DOI: 10.1038/177027a0.

— (1956b). "The Question of Correlation between Photons in Coherent Light Rays". In: *Nature* 178, p. 1447. DOI: 10.1038/1781447a0.

Hanschke, L., K. A. Fischer, S. Appel, D. Lukin, J. Wierzbowski, S. Sun, R. Trivedi, J. Vučković, J. J. Finley, and K. Müller (2018). "Quantum dot single-photon sources with ultra-low multi-photon probability". In: *npj Quantum Information* 4, p. 43. DOI: 10.1038/s41534-018-0092-0.

Haroche, S. and J.-M. Raimond (2006). *Exploring the Quantum: Atoms, Cavities, and Photons*. Oxford University Press.

He, Y.-M., J. Liu, S. Maier, M. Emmerling, S. Gerhardt, M. Davanço, C. Schneider, and S. Höfling (2017). "Deterministic implementation of a brigth, on-demand single-photon source with near-unity indistinguishability via quantum dot imaging". In: *Optica* 4, p. 802. DOI: 10.1364/OPTICA.4.000802.

Hegerfeldt, G. C. and M. B. Plenio (1996). "Conditional resonance-fluorescence spectra of single atoms". In: *Phys. Rev. A* 53, p. 1164. DOI: 10.1103/PhysRevA.53.1164.

Heitler, W. (1944). *The Quantum Theory of Radiation*. Oxford University Press.

Hill, S. and W. K. Wootters (1997). "Entanglement of a Pair of Quantum Bits". In: *Phys. Rev. Lett.* 78, p. 5022. DOI: 10.1103/PhysRevLett.78.5022.

Hong, C. K., Z. Y. Ou, and L. Mandel (1987). "Measurement of subpicosecond time intervals between two photons by interference". In: *Phys. Rev. Lett.* 59, p. 2044. DOI: 10.1103/PhysRevLett.59.2044.

Houdré, R., J. L. Gibernon, P. Pellandini, R. P. Stanley, U. Oesterle, C. Weisbuch, J. O'Gorman, B. Roycroft, and M. Ilegems (1995). "Saturation of the strong-coupling regime in a semiconductor microcavity: Free-carrier bleaching of cavity polaritons". In: *Phys. Rev. B* 52, p. 7810. DOI: 10.1103/PhysRevB.52.7810.

Ishii, A., T. Uda, and Y. K. Kato (2017). "Room-temperature single-photon emission from micrometer-long air-suspended carbon nanotubes". In: *Phys. Rev. Appl.* 8, p. 054039. DOI: 10.1103/PhysRevApplied.8.054039.

Jakeman, E., E. R. Pike, P. N. Pusey, and J. M. Vaughan (1977). "The effect of atomic number fluctuations on photon antibunching in resonance fluorescence". In: *J. Phys. A.: Math. Gen.* 10, p. L257. DOI: 10.1088/0305-4470/10/12/010.

James, D. F. V., P. G. Kwiat, W. J. Munro, and A. G. White (2001). "Measurement of qubits". In: *Phys. Rev. A* 64, p. 52312. DOI: 10.1103/PhysRevA.64.052312.

Jaynes, E.T. and F.W. Cummings (1963). "Comparison of Quantum and Semiclassical Radiation Theory with Application to the Beam Maser". In: *Proc. IEEE* 51, p. 89. DOI: 10.1109/PROC.1963.1664.

Ježek, M., I. Straka, M. Mičuda, M. Dušek, J. Fiurášek, and R. Filip (2011). "Experimental Test of the Quantum Non-Gaussian Character of a Heralded Single-Photon State". In: *Phys. Rev. Lett.* 107, p. 213602. DOI: 10.1103/PhysRevLett.107.213602.

Jogenfors, J., A. Cabello, and J.-Å Larsson (2017). "Comment on "Franson Interference Generated by a Two-Level System"". In: *arXiv:1703.05055*.

Jogenfors, J., A. Mohamed Elhassan, J. Ahrens, M. Bourennane, and J.-Å. Larsson (2015). "Hacking the Bell test using classical light in energy-time entanglement-based quantum key distribution". In: *Science Advances* 1, e1500793. DOI: 10.1126/sciadv.1500793.

Kaneda, F., B. G. Christensen, J. J. Wong, H. S. Park, K. T. McCuster, and P. G. Kwiat (2015). "Time-multiplexed heralded single-photon source". In: *Optica* 2, p. 1010. DOI: 10.1364/OPTICA.2.001010.

Kartashov, Y. V., V. V. Konotop, and L. Torner (2012). "Compactons and bistability in exciton-polariton condensates". In: *Phys. Rev. B* 86, p. 205313. DOI: 10.1103/PhysRevB.86.205313.

Kavokin, A., J. J. Baumberg, G. Malpuech, and F. P. Laussy (2017). *Microcavities*. 2nd ed. Oxford University Press.

Kazarinov, R. F. and R.A. Suris (1971). "Possibility of amplification of electromagnetic waves in a semiconductor with a superlattice". In: *Fizika i Tekhnika Poluprovodnikov* 5, p. 797.

Kazimierczuk, T., J. Schmutzler, M. Aßmann, C. Schneider, M. Kamp, S. Höfling, and M. Bayer (2015). "Photon-Statistics Excitation Spectroscopy of a Quantum-Dot Micropillar Laser". In: *Phys. Rev. Lett.* 115, p. 027401. DOI: 10.1103/PhysRevLett.115.027401.

Kim, J.-H., T. Cai, C. J. K. Richardson, R. P. Leavitt, and E. Waks (2016). "Two-photon interference from a bright single-photon source at telecom wavelengths". In: *Optica* 3, p. 577. DOI: 10.1364/OPTICA.3.000577.

Kimble, H. J., M. Dagenais, and L. Mandel (1977). "Photon Antibunching in Resonance Fluorescence". In: *Phys. Rev. Lett.* 39, p. 691. DOI: 10.1103/PhysRevLett.39.691.

Kimble, H. J. and L. Mandel (1976). "Theory of resonance fluorescence". In: *Phys. Rev. A* 13, p. 2123. DOI: 10.1103/PhysRevA.13.2123.

Kira, M. and S. W. Koch (2006). "Quantum-optical spectroscopy of semiconductors". In: *Phys. Rev. A* 73, p. 013813. DOI: 10.1103/PhysRevA.73.013813.

Kira, M., S. W. Koch, R. P. Smith, A. E. Hunter, and S. T. Cundiff (2011). "Quantum spectroscopy with Schrödinger-cat states". In: *Nat. Phys.* 7, p. 799. DOI: 10.1038/nphys2091.

Knöll, L., W. Vogel, and D. G. Welsch (1986). "Quantum noise in spectral filtering of light". In: *J. Opt. Soc. Am. B* 3, p. 1315. DOI: 10.1364/JOSAB.3.001315.

Knöll, L. and G. Weber (1986). "Theory of N-fold time-resolved correlation spectroscopy and its application to resonance fluorescence radiation". In: *J. Phys. B.: At. Mol. Phys.* 19, p. 2817. DOI: 10.1088/0022-3700/19/18/012.

Knöll, L., G. Weber, and T. Schafer (1984). "Theory of time-resolved correlation spectroscopy and its application to resonance fluorescence radiation". In: *J. Phys. B.: At. Mol. Phys.* 17, p. 4861. DOI: 10.1088/0022-3700/17/24/020.

Kolobov, M.I. and I.V. Sokolov (1987). "Interference of a physical radiation field and of vacuum fluctuations at a light-source output". In: *Opt. Spectrosk.* 62, p. 112.

Kuhlmann, A. V., J. H. Prechtel, J. Houel, A. Ludwig, D. Reuter, A. D. Wieck, and R. J. Warburton (2015). "Transform-limited single photons from a single quantum dot". In: *Nat. Comm.* 6, p. 8204. DOI: 10.1038/ncomms9204.

Laussy, F. P., E. del Valle, and J.J. Finley (2012). "Universal signatures of lasing in the strong coupling regime". In: *Proc. SPIE* 8255, 82551G. DOI: 10.1117/12.912732.

Laussy, F. P., E. del Valle, and C. Tejedor (2009). "Luminescence Spectra of Quantum Dots in Microcavities. I. Bosons". In: *Phys. Rev. B* 79, p. 235325. DOI: 10.1103/PhysRevB.79.235325.

Laussy, F. P., I. A. Shelykh, G. Malpuech, and A. Kavokin (2006). "Effects of Bose–Einstein condensation of exciton polaritons in microcavities on the polarization of emitted light". In: *Phys. Rev. B* 73, p. 035315. DOI: 10.1103/PhysRevB.73.035315.

Laussy, F. P., E. del Valle, M. Schrapp, A. Laucht, and J. J. Finley (2012). "Climbing the Jaynes–Cummings ladder by photon counting". In: *J. Nanophoton.* 6, p. 061803. DOI: 10.1117/1.JNP.6.061803.

Lax, M. (1963). "Formal Theory of Quantum Fluctuations from a Driven State". In: *Phys. Rev.* 129, p. 2342. DOI: 10.1103/PhysRev.129.2342.

— (1967). "Quantum Noise. X. Density-Matrix Treatment of Field and Population-Difference Fluctuations". In: *Phys. Rev.* 157, p. 213. DOI: 10.1103/PhysRev.157.213.

Leifgen, M., T. Schröder, F. Gädeke1, R. Riemann, V. Métillon, E. Neu, C. Hepp, C. Arend, C. Becher, and K. Lauritsen (2014). "Evaluation of nitrogen- and silicon-vacancy defect centres as single photon sources in quantum key distribution". In: *New J. Phys.* 16, p. 023021. DOI: 10.1088/1367-2630/16/2/023021.

Lemonde, M.-A., N. Didier, and A. A. Clerk (2014). "Antibunching and unconventional photon blockade with Gaussian squeezed states". In: *Phys. Rev. A* 90, p. 063824. DOI: 10.1103/PhysRevA.90.063824.

Liew, T. C. H. and V. Savona (2010). "Single Photons from Coupled Quantum Modes". In: *Phys. Rev. Lett.* 104, p. 183601. DOI: 10.1103/PhysRevLett.104.183601.

Liew, T. C. H., M. M. Glazov, K. V. Kavokin, I. A. Shelykh, M. A. Kaliteevski, and A. V. Kavokin (2013). "Proposal for a Bosonic Cascade Laser". In: *Phys. Rev. Lett.* 110, p. 047402. DOI: 10.1103/PhysRevLett.110.047402.

Liew, T. C. H., Y. G. Rubo, A. S. Sheremet, S. De Liberato, I. A. Shelykh, F. P. Laussy, and A. V. Kavokin (2016). "Quantum statistics of bosonic cascades". In: *New J. Phys.* 18, p. 023041. DOI: 10.1088/1367-2630/18/2/023041.

Lin, X., X. Dai, C. Pu, Y. Deng, Y. Niu, L. Tong, W. Fang, Y. Jin, and X. Peng (2017). "Electrically-driven single-photon sources based on colloidal quantum dots with near -optimal antibunching at room temperature". In: *Nat. Comm.* 8, p. 1132. DOI: 10.1038/s41467-017-01379-6.

Lindeman, R. L. (1942). "The Trophic-Dynamic Aspect of Ecology". In: *Ecology* 23, p. 399. DOI: 10.2307/1930126.

Lodahl, P., S. Mahmoodian, S. Stobbe, P. Schneeweiss, J. Volz, A. Rauschenbeutel, H. Pichler, and P. Zoller (2016). "Chiral Quantum Optics". In: *Nature* 541, p. 473. DOI: 10.1038/nature21037.

López Carreño, J. C., E. del Valle, and F. P. Laussy (2017). "Photon correlations from the Mollow Triplet". In: *Laser Photon. Rev.* 11, p. 1700090. DOI: 10.1002/lpor.201700090.

— (2018). "Frequency-resolved Monte Carlo". In: *Sci. Rep.* 8, p. 6975. DOI: 10.1038/s41598-018-24975-y.

López Carreño, J. C. and F. P. Laussy (2016). "Excitation with quantum light. I. Exciting a harmonic oscillator". In: *Phys. Rev. A* 94, p. 063825. DOI: 10.1103/PhysRevA.94.063825.

López Carreño, J. C., C. Sánchez Muñoz, D. Sanvitto, E. del Valle, and F. P. Laussy (2015). "Exciting Polaritons with Quantum Light". In: *Phys. Rev. Lett.* 115, p. 196402. DOI: 10.1103/PhysRevLett.115.196402.

López Carreño, J. C., E. Zubizarreta Casalengua, E. del Valle, and F. P. Laussy (2016a). "Criterion for Single Photon Sources". In: *arXiv:1610.06126*.

López Carreño, J. C., C. Sánchez Muñoz, E. del Valle, and F. P. Laussy (2016b). "Excitation with quantum light. II. Exciting a two-level system". In: *Phys. Rev. A* 94, p. 063826. DOI: 10.1103/PhysRevA.94.063826.

López Carreño, J. C., E. Zubizarreta Casalengua, F. P. Laussy, and E. del Valle (2018). "Joint subnatural-linewidth and single-photon emission from resonance fluorescence". In: *Quantum Sci. Technol.* 3, p. 045001. DOI: 10.1088/2058-9565/aacfbe.

— (2019). "Impact of detuning and dephasing on a laser-corrected subnatural-linewidth single-photon source". In: *J. Phys. B.: At. Mol. Phys.* 52, p. 035504. DOI: 10.1088/1361-6455/aaf68d.

Loredo, J. C., N. A. Zakaria, N. Somaschi, C. Anton, L. de Santis, et al. (2016). "Scalable performance in solid-state single-photon sources". In: *Optica* 3, p. 433. DOI: 10.1364/OPTICA.3.000433.

Loredo, J. C., M. A. Broome, P. Hilare, O. Gazzano, I. Sagnes, A. Lemaitre, M. P. Almeida, P. Senellart, and A. G. White (2017). "Boson sampling with Single-photon Fock states from a Bright Solid-State source". In: *Phys. Rev. Lett.* 118, p. 120503. DOI: 10.1103/PhysRevLett.118.130503.

Love, A. P. D., D. N. Krizhanovskii, D. M. Whittaker, R. Bouchekioua, D. Sanvitto, et al. (2008). "Intrinsic Decoherence Mechanisms in the Microcavity Polariton Condensate". In: *Phys. Rev. Lett.* 101, p. 067404. DOI: 10.1103/PhysRevLett.101.067404.

Lu, Z. H., S. Bali, and J. E. Thomas (1998). "Observation of Squeezing in the Phase-Dependent Fluorescence Spectra of Two-Level Atoms". In: *Phys. Rev. Lett.* 81, p. 3635. DOI: 10.1103/PhysRevLett.81.3635.

Lukishova, S. G., L. J. Bissell, J. Winkler, and C. R. Stroud (2012). "Resonance in quantum dot fluorescence in a photonic bandgap liquid crystal host". In: *Opt. Lett.* 37, p. 1259. DOI: 10.1364/OL.37.001259.

Lvovsky, A. I. (2015). "Fundamentals of Photonics and Physics". In: Wiley-Blackwell. Chap. 5. Squeezed light.

Ma, Y., G. Ballesteros, J. M. Zajac, J. Sun, and D. B. Gerardot (2015). "Highly directional emission from a quantum emitter embedded in a hemispherical cavity". In: *Opt. Lett.* 40, p. 2373. DOI: 10.1364/OL.40.002373.

Mahmoodian, S., P. Lodahl, and A. S. Sorensen (2016). "Quantum networks with chiral light-matter interaction in waveguides". In: *Phys. Rev. Lett.* 117, p. 240501. DOI: 10.1103/PhysRevLett.117.240501.

Maiman, T. H. (1960). "Stimulated Optica Radiation in Ruby". In: *Nature* 187, p. 493. DOI: 10.1038/187493a0.

Mandel, L. (1982). "Squeezed States and Sub-Poissonian Photon Statistics". In: *Phys. Rev. Lett.* 49, p. 136. DOI: 10.1103/PhysRevLett.49.136.

Marte, P., R. Dum, R. Taïeb, P. D. Lett, and P. Zoller (1993). "Quantum wave function simulation of the resonance fluorescence spectrum from one-dimensional optical molasses". In: *Phys. Rev. Lett.* 71, p. 1335. DOI: 10.1103/PhysRevLett.71.1335.

Matthiesen, C., A. N. Vamivakas, and M. Atatüre (2012). "Subnatural Linewidth Single Photons from a Quantum Dot". In: *Phys. Rev. Lett.* 108, p. 093602. DOI: 10.1103/PhysRevLett.108.093602.

McCormick, C. F., V. Boyer, E. Arimondo, and P. D. Lett (2007). "Strong relative intensity squeezing by four-wave mixing in rubidium vapor". In: *Opt. Lett.* 32, p. 178. DOI: 10.1364/OL.32.000178.

McCormick, C. F., A. M. Marino, V. Boyer, and P. D. Lett (2008). "Strong low-frequency quantum correlations from a four-wave mixing amplifier". In: *Phys. Rev. A* 78, p. 043816. DOI: 10.1103/PhysRevA.78.043816.

McKeever, J., A. Boca, A. D. Boozer, J. R. Buck, and H. J. Kimble (2003). "Experimental realization of a one-atom laser in the regime of strong coupling". In: *Nature* 425, p. 268. DOI: 10.1038/nature01974.

Messikh, A., R. Tanaś, and Z. Ficek (2000). "Response of a two-level atom to a narrow-bandwidth squeezed-vacuum excitation". In: *Phys. Rev. A* 61, p. 033811. DOI: 10.1103/PhysRevA.61.033811.

Messin, G., J. Ph. Karr, A. Baas, G. Khitrova, R. Houdré, R. P. Stanley, U. Oesterle, and E. Giacobino (2001). "Parametric Polariton Amplification in Semiconductor Microcavities". In: *Phys. Rev. Lett.* 87, p. 127403. DOI: 10.1103/PhysRevLett.87.127403.

Mesta, M., M. Carvelli, R. J. de Vries, H. van Eersel, J. J. M. van der Holst, et al. (2013). "Molecular-scale simulaton of electroluminescence in a multilayer white organic light-emitting diode". In: *Nat. Mater.* 12, p. 652. DOI: 10.1038/nmat3622.

Meyer, H. M., R. Stockill, M. Steiner, C. Le Gall, C. Matthiesen, E. Clarke, A. Ludwig, J. Reichel, M. Atatüre, and M. Köhl (2015). "Direct Photonic Coupling of a Semiconductor Quantum Dot and a Trapped Ion". In: *Phys. Rev. Lett.* 114, p. 123001. DOI: 10.1103/PhysRevLett.114.123001.

Michler, P., A. Kiraz, C. Becher, W. V. Schoenfeld, P. M. Petroff, Lidong Zhang, E. Hu, and A. Ĭmamoḡlu (2000). "A Quantum Dot Single-Photon Turnstile Device". In: *Science* 290, p. 2282. DOI: 10.1126/science.290.5500.2282.

Mollow, B. R. (1969). "Power Spectrum of Light Scattered by Two-Level Systems". In: *Phys. Rev.* 188, p. 1969. DOI: 10.1103/PhysRev.188.1969.

Mølmer, K. and Y. Castin (1996). "Monte Carlo wavefunctions in quantum optics". In: *Quantum Semiclass. Opt.* 8, p. 49. DOI: 10.1088/1355-5111/8/1/007.

Mølmer, K., Y. Castin, and J. Dalibard (1993). "Monte Carlo wave-function method in quantum optics". In: *J. Opt. Soc. Am. B* 10, p. 524. DOI: 10.1364/JOSAB.10.000524.

Mu, Y. and C. M. Savage (1992). "One-atom lasers". In: *Phys. Rev. A* 46, p. 5944. DOI: 10.1103/PhysRevA.46.5944.

Mukamel, S. and K. E. Dorfman (2015). "Nonlinear fluctuations and dissipation in matter revealed by quantum light". In: *Phys. Rev. A* 91, p. 053844. DOI: 10.1103/PhysRevA.91.053844.

Müller, K., A. Rundquist, K. A. Fischer, T. Sarmiento, K. G. Lagoudakis, Y. A. Kelaita, C. Sánchez Muñoz, E. del Valle, F. P. Laussy, and J. Vučković (2015). "Coherent generation of nonclassical light on chip via detuned photon blockade". In: *Phys. Rev. Lett.* 114, p. 233601. DOI: 10.1103/PhysRevLett.114.233601.

Müller, K., K. A. Fischer, C. Dory, T. Sarmiento, K. G. Lagoudakis, A. Rundquist, Y. A. Kelaita, and J. Vučković (2016). "Self-homodyne-enabled generation of indistinguishable photons". In: *Optica* 3, p. 931. DOI: 10.1364/OPTICA.3.000931.

Muñoz-Matutano, G., A. Wood, M. Johnsson, X. Vidal, B Q. Baragiola, et al. (2019). "Emergence of quantum correlations from interacting fibre-cavity polaritons". In: *Nat. Mater.* 18, p. 213. DOI: 10.1038/s41563-019-0281-z.

Nguyen, H. S., G. Sallen, C. Voisin, Ph. Roussignol, C. Diederichs, and G. Cassabois (2011). "Ultra-coherent single photon source". In: *Appl. Phys. Lett.* 99, p. 261904. DOI: 10.1063/1.3672034.

Nieto, M. M. (1997). "Displaced and squeezed number states". In: *Phys. Lett. A* 229, p. 135. DOI: 10.1016/S0375-9601(97)00183-7.

Nomura, M., N. Kumagai, S. Iwamoto, Y. Ota, and Y. Arakawa (2010). "Laser oscillation in a strongly coupled single-quantum-dot–nanocavity system". In: *Nat. Phys.* 6, p. 279. DOI: 10.1038/nphys1518.

O'Brien, J. L., A. Furusawa, and J. Vučković (2009). "Photonic quantum technologies". In: *Nat. Phys.* 3, p. 687. DOI: 10.1038/nphoton.2009.229.

Ourjoumtsev, A., A. Kubanek, M. Koch, C. Sames, P. W. H. Pinkse, G. Rempe, and K. Murr (2011). "Observation of squeezed light from one atom excited with two atoms". In: *Nature* 474, p. 623. DOI: 10.1038/nature10170.

Palacios-Berraquero, C., M. Barbone, D. M. Kara, X. Chen, I. Goykhman, et al. (2016). "Atomically thin quantum light-emitting diodes". In: *Nat. Comm.* 7, p. 12978. DOI: 10.1038/ncomms12978.

Paul, H. (1982). "Photon antibunching". In: *Rev. Mod. Phys.* 54, p. 1061. DOI: 10.1103/RevModPhys.54.1061.

Peiris, M., K. Konthasinghe, and A. Muller (2017). "Franson Interference Generated by a Two-Level System". In: *Phys. Rev. Lett.* 118, p. 030501. DOI: 10.1103/PhysRevLett.118.030501.

Peiris, M., B. Petrak, K. Konthasinghe, Y. Yu, Z. C. Niu, and A. Muller (2015). "Two-color photon correlations of the light scattered by a quantum dot". In: *Phys. Rev. B* 91, p. 195125. DOI: 10.1103/PhysRevB.91.195125.

Petersen, J., J. Volz, and A. Rauschenbeutel (2014). "Chiral nanophotonic waveguide interface based on spin-orbit interaction of light". In: *Science* 346, p. 67. DOI: 10.1126/science.1257671.

Pichler, H., T. Ramos, A. J. Daley, and P. Zoller (2015). "Quantum optics of chiral spin networks". In: *Phys. Rev. A* 91, p. 042116. DOI: doi:10.1103/PhysRevA.91.042116.

Pittman, T. B., B. C. Jacobs, and J. D. Franson (2002). "Single photons on pseudodemand from stored parametric down-conversion". In: *Phys. Rev. A* 66, p. 042303. DOI: 10.1103/PhysRevA.66.042303.

Plenio, M. B. (1996). "Narrow absorption lines induced by electron shelving". In: *J. Mod. Opt.* 43, p. 753. DOI: 10.1080/09500349608232781.

Plenio, M. B. and P. L. Knight (1998). "The quantum-jump approach to dissipative dynamics in quantum optics". In: *Rev. Mod. Phys.* 70, p. 101. DOI: 10.1103/RevModPhys.70.101.

Proux, R., M. Maragkou, E. Baudin, C. Voisin, P. Roussignol, and C. Diederichs (2015). "Measuring the Photon Coalescence Time Window in the Continuous-Wave Regime for Resonantly Driven Semiconductor Quantum Dots". In: *Phys. Rev. Lett.* 114, p. 067401. DOI: 10.1103/PhysRevLett.114.067401.

Purcell, E. M. (1956). "The Question of Correlation between Photons in Coherent Light Rays". In: *Nature* 178, p. 1449. DOI: 10.1038/1781449a0.

Quesada, N. (2012). "Strong coupling of two quantum emitters to a single light mode: The dissipative Tavis–Cummings ladder". In: *Phys. Rev. A* 86, p. 013836. DOI: 10.1103/PhysRevA.86.013836.

Raizen, M. G., L. A. Orozco, M. Xiao, T. L. Boyd, and H. J. Kimble (1987). "Squeezed-State Generation by the Normal Modes of a Coupled System". In: *Phys. Rev. Lett.* 69, p. 198. DOI: 10.1103/PhysRevLett.59.198.

Rau, M., T. Heindel, S. Unsleber, T. Braun, J. Fischer, et al. (2014). "Free space quantum key distribution over 500 meters using electrically driven quantum dot single-photon sources—a proof of principle experiment". In: *New J. Phys.* 16, p. 043003. DOI: 10.1088/1367-2630/16/4/043003.

Reynaud, S. (1983). "La fluorescence de résonance: étude par la méthode de l'atome habillé". In: *Annales de Physique* 8, p. 315. DOI: 10.1051/anphys/198308080315.

Rodiek, B., M. Lopez, H. Hofer, G. Porrovecchio, M. Smid, et al. (2017). "Experimental realization of an absolute single-photon source base on a single nitrogen vacancy center in a nanodiamond". In: *Optica* 4, p. 71. DOI: 10.1364/OPTICA.4.000071.

Rogers, D. W. O. (2006). "Fifty years of Monte Carlo simulations for medical physics". In: *Phys. Med. Biol.* 51, R287. DOI: 10.1088/0031-9155/51/13/R17.

Rossbach, G., J. Levrat, E. Feltin, J.-F. Carlin, R. Butté, and N. Grandjean (2013). "Impact of saturation on the polariton renormalization in III-nitride based planar microcavities". In: *Phys. Rev. B* 88, p. 165312. DOI: 10.1103/PhysRevB.88.165312.

Sánchez Muñoz, C. (2016). "Generation of Nonclassical States of Light". PhD thesis. Universidad Autónoma de Madrid.

Sánchez Muñoz, C., E. del Valle, A. González Tudela, K. Müller, S. Lichtmannecker, M. Kaniber, C. Tejedor, J.J. Finley, and F.P. Laussy (2014a). "Emitters of N-photon bundles". In: *Nat. Photon.* 8, p. 550. DOI: 10.1038/nphoton.2014.114.

Sánchez Muñoz, C., E. del Valle, C. Tejedor, and F.P. Laussy (2014b). "Violation of classical inequalities by photon frequency filtering". In: *Phys. Rev. A* 90, p. 052111. DOI: 10.1103/PhysRevA.90.052111.

Sánchez Muñoz, C., F. P. Laussy, C. Tejedor, and E del Valle (2015). "Enhanced two-photon emission from a dressed biexciton". In: *New J. Phys.* 17, p. 123021. DOI: 10.1088/1367-2630/17/12/123021.

Sánchez Muñoz, C., F. P. Laussy, E. del Valle, C. Tejedor, and A. González-Tudela (2018). "Filtering multiphoton emission from state-of-the-art cavity quantum electrodynamics". In: *Optica* 5, p. 14. DOI: 10.1364/OPTICA.5.000014.

Santana, T. S., Y. Ma, R. N. E. Malein, F. Bastiman, E. Clarke, and B. D. Gerardot (2017). "Generating indistinguishable photons from a quantum dot in a noisy environment". In: *Phys. Rev. B* 95, 201410(R). DOI: 10.1103/PhysRevB.95.201410.

Schack, R., T. A. Brun, and I. C. Percival (1996). "Quantum-state diffusion with a moving basis: Computing quantum-optical spectra". In: *Phys. Rev. A* 53, p. 2694. DOI: 10.1103/PhysRevA.53.2694.

Schawlow, A. L. and C. H. Townes (1958). "Infrared and Optical Masers". In: *Phys. Rev.* 112, p. 1940. DOI: 10.1103/PhysRev.112.1940.

Schlehahn, A., M. Gaafar, M. Vaupel, M. Gschrey, P. Schnauber, et al. (2015). "Single-photon emission at a rate of 143 MHz from a deterministic quantum-dot microlens triggered by a mode-locked vertical-external-cavity surface-emitting laser". In: *Appl. Phys. Lett.* 107, p. 041105. DOI: 10.1063/1.4927429.

Schlehahn, A., S. Fischbach, R. Schmidt, A. Kaganskiy, A. Strittmatter, S. Rodt, T. Heindel, and S. Reitzenstein (2018). "A stand-alone fiber-coupled single-photon source". In: *Sci. Rep.* 8, p. 1340. DOI: 10.1038/s41598-017-19049-4.

Schmitt-Rink, S., D. S. Chemla, and D. A. B. Miller (1985). "Theory of transient excitonic optical nonlinearities in semiconductor quantum-well structures". In: *Phys. Rev. B* 32, p. 6601. DOI: 10.1103/PhysRevB.32.6601.

Schrama, C. A., G. Nienhuis, H. A. Dijkerman, C. Steijsiger, and H. G. M. Heideman (1992). "Intensity correlations between the components of the resonance fluorescence triplet". In: *Phys. Rev. A* 45, p. 8045. DOI: 10.1103/PhysRevA.45.8045.

Schulte, C. H. H., J. Hansom, A. E. Jones, C. Matthiesen, C. Le Gall, and M. Atatüre (2015). "Quadrature squeezed photons from a two-level system". In: *Nature* 525, p. 222. DOI: 10.1038/nature14868.

Schweickert, L., K. D. Jöns, K. D. Zeuner, S. F. Couvre da Silva, H. Huang, et al. (2018). "On-demand generation of background-free single photons from a solid-state source". In: *Appl. Phys. Lett.* 112, p. 093106. DOI: 10.1063/1.5020038.

Senellart, P., G. Solomon, and A. White (2017). "High-performance semiconductor quantum-dot single-photon sources". In: *Nat. Nanotech.* 12, p. 1026. DOI: 10.1038/nnano.2017.218.

Shatokhin, V. N. and S. Ya. Kilin (2001). "Correlation measurements in resonance fluorescence with spectral resolution and atomic inversion via detection of a spectrally filtered photon". In: *Phys. Rev. A* 63, p. 023803. DOI: 10.1103/PhysRevA.63.023803.

— (2002). "Atomic state reduction and energy balance relation in spectrally resolved resonance fluorescence". In: *Opt. Commun.* 210, p. 291. DOI: 10.1016/S0030-4018(02)01819-9.

— (2016). "Correlation functions in resonance fluorescence with spectral resolution: Signal-processing approach". In: *Phys. Rev. A* 94, p. 033835. DOI: 10.1103/PhysRevA.94.033835.

Shatokhin, V.N. and S.Ya. Kilin (2000). "Second-order coherence and state reduction in resonance fluorescence with spectral resolution". In: *Opt. Commun.* 174, p. 157. DOI: 10.1016/S0030-4018(99)00678-1.

Slusher, R. E., L. W. Hollberg, B. Yurke, J. C. Mertz, and J. F. Valley (1985). "Observation of Squeezed States Generated by Four-Wave Mixing in an Optical Cavity". In: *Phys. Rev. Lett.* 55, p. 2409. DOI: 10.1103/PhysRevLett.55.2409.

Smyth, W. S. and S. Swain (1999). "Complete quenching of fluorescence from a two-level atom driven by a weak, narrow-band, nonclassical light field". In: *Phys. Rev. A* 59, R2579(R). DOI: 10.1103/PhysRevA.59.R2579.

Snijders, H. J., J. A. Frey, H. Flayac J. Norman, V. Savona, A. C. Gossard, J. E. Bowers, M. P. van Exter, D. Bouwmeester, and W. Löffler (2018). "Observation of the Unconventional Photon blockade". In: *Phys. Rev. Lett.* 121, p. 043601. DOI: 10.1103/PhysRevLett.121.043601.

Somaschi, N., V. Giesz, L. De Santis, J. C. Loredo, M. P. Almeida, et al. (2016). "Near-optimal single-photon sources in the solid state". In: *Nat. Photon.* 10, p. 340. DOI: 10.1038/nphoton.2016.23.

Spring, J. B., B. J. Metcalf, P. C. Humphreys, W. S. Kolthammer, X.-M. Jin, et al. (2013). "Boson Sampling on a Photonic Chip". In: *Science* 339, p. 798. DOI: 10.1126/science.1231692.

Stoler, D., B.E.A. Saleh, and M.C. Teich (1985). "Binomial States of the Quantized Radiation Field". In: *Opt. Acta* 32, p. 345. DOI: 10.1080/713821735.

Stryer, L. (1981). *Biochemistry*. W.H. Freeman and Company. DOI: 10.1016/0307-4412(81)90224-7.

Sudarshan, E. C. G. (1963). "Equivalence of Semiclassical and Quantum Mechanical Descriptions of Statistical Light Beams". In: *Phys. Rev. Lett.* 10, p. 277. DOI: 10.1103/PhysRevLett.10.277.

Sun, Y., P. Wen, Y. Yoon, G. Liu, M. Steger, L. N. Pfeiffer, K. West, D. W. Snoke, and K. A. Nelson (2017). "Bose–Einstein Condensation of Long-Lifetime Polaritons in Thermal Equilibrium". In: *Phys. Rev. Lett.* 118, p. 016602. DOI: 10.1103/PhysRevLett.118.016602.

Tassone, F. and Y. Yamamoto (1999). "Exciton-exciton scattering dynamics in a semiconductor microcavity and stimulated scattering into polaritons". In: *Phys. Rev. B* 59, p. 10830. DOI: 10.1103/PhysRevB.59.10830.

Tian, L. and H. J. Carmichael (1992). "Quantum trajectory simulations of two-state behavior in an optical cavity containing one atom". In: *Phys. Rev. A* 46, R6801(R). DOI: 10.1103/PhysRevA.46.R6801.

Tillmann, M., B. Dakić, R. Heilmann, S. Nolte, A. Szameit, and P. Walther (2013). "Experimental boson sampling". In: *Nat. Photon.* 7, p. 540. DOI: 10.1038/nphoton.2013.102.

Tinsley, J. N., M. I. Molodtsov, R. Prevedel, D. Wartmann, J. Espigulé-Pons, M. Lauwers, and A. Vaziri (2016). "Direct detection of a single photon by humans". In: *Nat. Comm.* 7, p. 12172. DOI: 10.1038/ncomms12172.

Tomasin, M., E. Mantoan, J. Jogenfors, G. Vallone, J.-Å. Larsson, and P. Villoresi (2017). "High-visibility time-bin entanglement for testing chained Bell inequalities". In: *Phys. Rev. A* 95, p. 032107. DOI: 10.1103/PhysRevA.95.032107.

Ulam, S. M. (1991). *Adventures of a mathematician*. University of California Press.

Ulhaq, A., S. Weiler, S. M. Ulrich, R. Roßbach, M. Jetter, and P. Michler (2012). "Cascaded single-photon emission from the Mollow triplet sidebands of a quantum dot". In: *Nat. Photon.* 6, p. 238. DOI: 10.1038/nphoton.2012.23.

Unsleber, S., Y.-M. He, S. Gerhardt, S. Maier, C.-Y. Lu, J.-W. Pan, N. Gregersen, M. Kamp, C. Schneider, and S. Höfling (2016). "Highly indistinguishable on-demand resonance fluorescence photons from a deterministic quantum dot micropillar device with 74% extraction efficiency". In: *Opt. Express* 24, p. 8539. DOI: 10.1364/OE.24.008539.

Vaneph, C., A. Morvan, G. Aiello, M. Fechant, M. Aprili, J. Gabelli, and J. Esteve (2018). "Observation of the Unconventional Photon Blockade in the Microwave regime". In: *Phys. Rev. Lett.* 121, p. 043602. DOI: 10.1103/PhysRevLett.121.043602.

Verger, A., C. Ciuti, and I. Carusotto (2006). "Polariton quantum blockade in a photonic dot". In: *Phys. Rev. B* 73, p. 193306. DOI: 10.1103/PhysRevB.73.193306.

Verma, V. B., M. J. Stevens, K. L. Silverman, N. L. Dias, A. Garg, J. J. Coleman, and R. P. Mirin (2011). "Photon antibunching from a single lithographically defined InGaAs/GaAs quantum dot". In: *Opt. Express* 19, p. 4182. DOI: 10.1364/OE.19.004182.

Vogel, W. (1991). "Squeezing and Anomalous Moments in Resonance Fluorescence". In: *Phys. Rev. Lett.* 67, p. 2450. DOI: 10.1103/PhysRevLett.67.2450.

— (1995). "Homodyne correlation measurements with weak local oscillators". In: *Phys. Rev. A* 51, p. 4160. DOI: 10.1103/PhysRevA.51.4160.

Vogel, W. and D.-G. Welsch (2006). *Quantum Optics*. 3: Wiley-VCH.

Walker, P. M., L. Tinker, B. Rotall, D. V. Skryabin, I. Farrer, D. A. Ritcher, M. S. Skolnick, and D. N. Krizhanovskii (2017). "Dark Solitons in High Velocity Waveguide Polariton Fluids". In: *Phys. Rev. Lett.* 119, p. 097403. DOI: 10.1103/PhysRevLett.119.097403.

Walker, T., K. Miyanishi, R. Ikuta, H. Takanashi, S. V. Kashanian, Y. Tsujimoto, K. Hayasaka, T. Yamamoto, N. Imoto, and M. Keller (2018). "Long-distance single photon transmission from a trapped ion via quantum frequency conversion". In: *Phys. Rev. Lett.* 120, p. 203601. DOI: 10.1103/PhysRevLett.120.203601.

Walls, D. F. (1983). "Squeezed states of light". In: *Nature* 306, p. 141. DOI: 10.1038/306141a0.

Wang, H., Z.-C. Duan, Y.-H. Li, S. Chen, J.-P. Li, et al. (2016). "Near-Transform-Limited Single Photons from an Efficient Solid-State Quantum Emitter". In: *Phys. Rev. Lett.* 116, p. 213601. DOI: 10.1103/PhysRevLett.116.213601.

Weisbuch, C., M. Nishioka, A. Ishikawa, and Y. Arakawa (1992). "Observation of the coupled exciton-photon mode splitting in a semiconductor quantum microcavity". In: *Phys. Rev. Lett.* 69, p. 3314. DOI: 10.1103/PhysRevLett.69.3314.

Weisskopf, W. and E. Wigner (1930). "Calculation of the Natural Line Width on the Basis of Dirac's Theory of Light (as translated by J. B. Sykes)". In: *Zeitschrift für Physik* 63, p. 54. DOI: 10.1007/BF01336768.

Whitehead, L. A. (1983). "Domino "chain reaction"". In: *Am. J. Phys.* 51, p. 182. DOI: 10.1119/1.13456.

Wu, F. Y., R. E. Grove, and S. Ezekiel (1975). "Investigation of the Spectrum of Resonance Fluorescence Induced by a Monochromatic Field". In: *Phys. Rev. Lett.* 35, p. 1426. DOI: 10.1103/PhysRevLett.35.1426.

Yurke, B. (1984). "Use of cavities in squeezed-state generation". In: *Phys. Rev. A* 29, 408(R). DOI: 10.1103/PhysRevA.29.408.

Zoller, P. (1978a). "Atomic relaxation and resonance fluorescence in intensity and phase-fluctuating laser light". In: *J. Phys. B.: At. Mol. Phys.* 11, p. 2825. DOI: 10.1088/0022-3700/11/16/010.

— (1978b). "Emission spectra of atoms strongly driven by finite bandwidth laser light". In: *J. Phys. B.: At. Mol. Phys.* 11, p. 805. DOI: 10.1088/0022-3700/11/5/014.

Zoller, P. and F. Ehlotzky (1978). "Resonance fluorescence in phase-frequency modulated laser fields". In: *Z. Phys. A* 285, p. 245. DOI: 10.1007/BF01408234.

Zoller, P., M. Marte, and D. F. Walls (1987). "Quantum jumps in atomic systems". In: *Phys. Rev. A* 35, p. 198. DOI: 10.1103/PhysRevA.35.198.

Zou, X. T. and L. Mandel (1990). "Photon-antibunching and sub-Poissonian photon statistics". In: *Phys. Rev. A* 41, p. 475. DOI: 10.1103/PhysRevA.41.475.

Zubizarreta Casalengua, E., J. C. López Carreño, E. del Valle, and F. P. Laussy (2017). "Structure of the harmonic oscillator in the space of N-particle Glauber correlators". In: *J. Math. Phys.* 58, p. 062109. DOI: 10.1063/1.4987023.

Zubizarreta Casalengua, E., J. C. López Carreño, F. P. Laussy, and E. del Valle (2019). "Conventional and Unconventional Photon Statistics". In: *arXiv:1901.09030*.